

博士論文

**Mechanical Properties of Soil Subjected to Internal Erosion  
Initiated by Suffusion**

細粒分の流出を伴う内部侵食作用を受けた土の力学特性

**Santa Spitia Luisa Fernanda**

サンタ スピティア ルイサ フェルナンダ

2017 年 9 月

Institute of Industrial Science  
The University of Tokyo  
Japan



## Abstract

Internal erosion is an important cause of failure in hydraulic structures such as levees, dikes and embankment dams. This study focuses particularly on a case of internal erosion called suffusion in which the fine particles migrate through the voids between the coarse particles under seepage flow, leaving behind the coarse skeleton. This process may have an effect on the mechanical behavior of the soil. Thus, the main objective of this research is to evaluate the mechanical properties of a soil subjected to suffusion

In this study, red-colored Silica sand No.5 ( $D_{50}=0.5\text{mm}$ ) and a non-plastic silt called DL-Clay ( $D_{50}=23\mu\text{m}$ ) were used. Both soils (Silica sand and DL-clay) were mixed using various percentage combinations based on the study made by Kenney (1985), in which the author suggested the maximum content of detached particles that a granular soil can contain, and therefore the maximum possible loss. Based on this, the percentages of Silica sand (primary fabric) and DL-clay (detached particles) were estimated considering the void ratio and average porosity.

In order to understand the influence of water penetration on the suffusion of the soil, a series of permeability tests has been performed, applying water with various hydraulic gradients from the top part of specimens with different densities, and letting fine particles drain out. Additionally, a series of torsional tests were done to evaluate the effect of suffusion on the shear strength, and the variation of shear modulus at different stages before and during shearing.

As a result of the experiments described above, it can be concluded that the erodability of a soil depends not only on the particle size distribution, but also depends on the density,

initial fines content and hydraulic gradient. The peak shear strength, shear modulus  $G_{50}$ , small strain stiffness, and friction angle are found to be lower in the eroded specimens.



## Acknowledgement

Firstly, I would like to express my most sincere gratitude to my supervisor, Professor Reiko Kuwano, Institute of Industrial Science, The University of Tokyo, for her support, guidance and valuable suggestions for this research. It has truly been an honor to have the opportunity to work under her supervision.

I sincerely acknowledge Professor Junichi Koseki, Geotechnical engineering laboratory, The University of Tokyo, for his valuable comments and constructive criticism and suggestions for my research.

I am also grateful to Associate Professor Takashi Kiyota, Geodisaster mitigation engineering laboratory, Institute of Industrial Science, The University of Tokyo; Professor Taro Uchimura, Department of civil engineering, Saitama University, and Professor Tomoyoshi Nishimura, Department of civil engineering, Ashikaga Institute of Technology, for their encouragement and valuable suggestions for this study.

My special appreciation goes to the laboratory technician Mr. Takeshi Sato for his invaluable support all the time during experiments. His knowledge, experience and optimistic attitude always encouraged me.

I am also grateful to Dr. Yukika Miyashita, Public Works Research Institute, and laboratory technician at the time that I started my research. She was always of essential help teaching me the test procedures. Her comments and suggestions were valuable for this study.

My sincere appreciation is forwarded to Dr. Masahide Otsubo, Reseach Associate, Kuwano laboratory, Institute of Industrial Science, The University of Tokyo, for his valuable comments on my thesis.

My gratitude also goes to all my fellow students in Kuwano, Koseki and Kiyota laboratories, whose help was valuable to me.

At last but not least, I would like to thank my family and friends for their support and motivation during these three years in Japan. I specially dedicate this research to my nephew Simón, who was born at the same time as the writing of this dissertation. I hope he has a prosperous future and a life full of joy.

## Table of Contents

Abstract .....	I
Acknowledgement.....	III
Table of Contents .....	V
List of figures .....	IX
List of Tables.....	XXIII
Chapter 1. Introduction.....	1
1.1. General .....	1
1.2. Literature review .....	2
1.2.1. Case studies.....	2
1.2.2. Numerical analysis .....	3
1.2.3. Experimental studies.....	4
1.3. Objectives .....	8
1.4. Scope.....	9
1.5. Thesis organization .....	10
1.6. References .....	10
Chapter 2. Basic theories .....	15
2.1. General concepts in soil mechanics.....	15
2.2. Internal stability of granular materials .....	17
2.2.1. Kenney and Lau criterion .....	18
2.2.2. Other criteria .....	20
2.3. Hydraulic soil properties.....	22
2.3.1. Darcy's Law.....	22
2.3.2. Hydraulic gradient .....	23
2.3.3. Coefficient of permeability.....	24

2.3.4.	Pore volume of water passed .....	24
2.4.	Hollow cylindrical torsional shear test.....	25
2.4.1.	Formulation of stresses .....	25
2.4.2.	Formulation of strains.....	30
2.4.3.	Shear modulus G.....	31
2.5.	Additional considerations about void ratio .....	32
2.5.1.	Void ratio function $f(e)$ .....	32
2.5.2.	Intergranular void ratio and density .....	32
2.6.	Strength properties.....	33
2.6.1.	Critical state .....	34
2.7.	References .....	34
Chapter 3.	Material, apparatus and testing procedure.....	37
3.1.	Test material .....	37
3.1.1.	Silica sand No. 5 .....	37
3.1.2.	DL Clay .....	38
3.1.3.	Mixed Silica Sand and DL Clay.....	39
3.2.	One-dimensional column permeability test .....	44
3.2.1.	Test procedure.....	44
3.2.1.	Apparatus.....	45
3.3.	Hollow cylindrical torsional shear test.....	47
3.3.1.	Apparatus.....	49
3.3.2.	Experiment setup.....	64
3.3.3.	Test procedure.....	68
3.4.	References .....	72
Chapter 4.	Evaluation of suffusion by one dimensional column permeability test.....	73
4.1.	General.....	73
4.2.	Detached particles eroded.....	74
4.3.	Turbidity.....	82
4.3.1.	Calibration of turbidity.....	82
4.3.2.	Results.....	83
4.4.	Permeability .....	86

4.5.	Global void ratio .....	90
4.6.	Intergranular void ratio .....	92
4.7.	Relative density.....	94
4.8.	Intergranular relative density .....	97
4.9.	Grain size distribution.....	99
4.10.	Method of describing the shape of the PSD curve .....	104
4.11.	Analysis and conclusions.....	106
4.11.1.	Effects of the density.....	106
4.11.2.	Effects of the hydraulic gradient .....	108
4.11.3.	Effects of the initial fines content .....	108
4.11.4.	Grain size distribution .....	109
4.12.	References.....	110
Chapter 5.	Evaluation of the mechanical properties by hollow cylindrical torsional shear test	111
5.1.	General .....	111
5.2.	Eroded soil and turbidity .....	112
5.2.1.	Specimens confined at $\sigma_z = \sigma_r = \sigma_\theta = 60kPa$ .....	112
5.2.2.	Specimens confined at $\sigma_z = \sigma_r = \sigma_\theta = 150kPa$ .....	118
5.2.3.	Analysis.....	122
5.3.	Volumetric strain .....	123
5.3.1.	Specimens confined at $\sigma_z = \sigma_r = \sigma_\theta = 60kPa$ .....	123
5.3.2.	Specimens confined at $\sigma_z = \sigma_r = \sigma_\theta = 150kPa$ .....	125
5.3.3.	Analysis.....	126
5.4.	Global void ratio .....	127
5.4.1.	Specimens confined at $\sigma_z = \sigma_r = \sigma_\theta = 60kPa$ .....	127
5.4.2.	Specimens confined at $\sigma_z = \sigma_r = \sigma_\theta = 150kPa$ .....	129
5.4.3.	Analysis.....	130
5.5.	Intergranular void ratio .....	131
5.5.1.	Specimens confined at $\sigma_z = \sigma_r = \sigma_\theta = 60kPa$ .....	131
5.5.2.	Specimens confined at $\sigma_z = \sigma_r = \sigma_\theta = 150kPa$ .....	133
5.5.3.	Analysis.....	134
5.6.	Relative Density .....	135

5.6.1.	Specimens confined at $\sigma_z = \sigma_r = \sigma_\theta = 60kPa$ .....	135
5.6.2.	Specimens confined at $\sigma_z = \sigma_r = \sigma_\theta = 150kPa$ .....	136
5.6.3.	Analysis .....	137
5.7.	Intergranular Relative Density .....	138
5.7.1.	Specimens confined at $\sigma_z = \sigma_r = \sigma_\theta = 60kPa$ .....	138
5.7.2.	Specimens confined at $\sigma_z = \sigma_r = \sigma_\theta = 150kPa$ .....	140
5.7.3.	Analysis .....	141
5.8.	Shear strength.....	141
5.8.1.	Specimens confined at $\sigma_z = \sigma_r = \sigma_\theta = 60kPa$ .....	141
5.8.2.	Specimens confined at $\sigma_z = \sigma_r = \sigma_\theta = 150kPa$ .....	143
5.8.3.	Non-eroded specimens with lower density .....	144
5.8.4.	Analysis .....	148
5.9.	Small strain Shear Modulus .....	154
5.9.1.	Specimens confined at $\sigma_z = \sigma_r = \sigma_\theta = 60kPa$ .....	154
5.9.2.	Specimens confined at $\sigma_z = \sigma_r = \sigma_\theta = 150kPa$ .....	162
5.9.3.	Analysis .....	165
5.10.	Strength parameters .....	173
5.11.	Image analysis .....	179
5.11.1.	Specimens confined at $\sigma_z = \sigma_r = \sigma_\theta = 60kPa$ .....	184
5.11.2.	Specimens confined at $\sigma_z = \sigma_r = \sigma_\theta = 150kPa$ .....	186
5.11.3.	Void ratio variation at various heights in the specimen .....	187
5.12.	Analysis and conclusions .....	192
5.12.1.	Effects of the torsional shear in the degree of erosion .....	192
5.12.2.	Effects of the density and degree of erosion.....	195
5.12.3.	Effects of the confining pressure .....	199
5.13.	References.....	200
Chapter 6.	Conclusions and Recommendations .....	203
6.1.	Conclusions .....	203
6.1.1.	One-dimensional column permeability test .....	203
6.1.2.	Hollow cylindrical torsional shear test.....	204
6.2.	Recommendations for future research .....	206

## List of figures

Figure 1-1 Schematic illustration of two types of internal erosion: Piping (left) and suffusion (right) .....	2
Figure 1-2 Soil pipe in the head of a landslide scar at Arthur's Pass National Park (Pierson, 1983) .....	3
Figure 1-3 Packing of an internally unstable soil (Mojtaba, 2013) .....	4
Figure 1-4 Schematic illustration of seepage test (Kenney and Lau, 1985) .....	5
Figure 1-5 Experimental setup for seepage tests (Sterpi, 2003) .....	6
Figure 1-6 Stress-controlled erosion apparatus (Chang and Zhang, 2011) .....	7
Figure 2-1 Three phases of the soil element .....	15
Figure 2-2 Schematic representation of pores and constrictions .....	17
Figure 2-3 Schematic illustration of an internally unstable soil .....	18
Figure 2-4 Schematic internal stability criteria by Kenney and Lau (1985) .....	19
Figure 2-5 Internal stability criteria in H vs. F space by Kenney and Lau (1985) .....	20
Figure 2-6 Schematic internal stability criteria by Kezdi (1979) .....	21
Figure 2-7 Internal stability criteria in H vs. F space by Kezdi (1979) .....	22
Figure 2-8 Stress and strains in a soil element of a hollow cylindrical specimen .....	25
Figure 2-9 Radial and circumferential strains .....	30
Figure 2-10 Element deformation by a shear force F .....	32
Figure 2-11 Phase diagram of intergranular void ratio .....	33

Figure 3-1 Photograph and particle size distribution of Silica sand No. 5.....	38
Figure 3-2 Photograph and particle size distribution of DL Clay .....	39
Figure 3-3 Schematic illustration of a dense soil (left) and loose soil (right) .....	40
Figure 3-4 Photograph and particle size distribution of mixed Silica sand (65%) and DL Clay (35%) .....	41
Figure 3-5 Photograph and particle size distribution of mixed Silica sand (80%) and DL Clay (20%) .....	42
Figure 3-6 Comparison of grain size distribution based on Silica sand No. 5 (SS) and DL Clay (DLC).....	42
Figure 3-7 H vs. F curves for mixed soils .....	43
Figure 3-8 Variation of global void ratio with mass fraction of detached particles .....	43
Figure 3-9 Arrangement of permeability apparatus.....	44
Figure 3-10 Schematic permeability test arrangement.....	45
Figure 3-11 Soil chamber with holes on the bottom plate .....	46
Figure 3-12 Turbidimeter HACH 2100Q and samples used for calibration .....	47
Figure 3-13 Schematic operation of the turbidimeter (HACH company, 2013) .....	47
Figure 3-14 Hollow cylindrical torsional shear test apparatus .....	48
Figure 3-15 Transducers in the torsional apparatus.....	49
Figure 3-16 Representative dimensions of the specimen .....	50
Figure 3-17 Pedestals. (a) For non-eroded tests (b) For eroded tests.....	50
Figure 3-18 Axial and torsional loading systems .....	51
Figure 3-19 Load cell .....	52
Figure 3-20 Axial load calibration .....	52
Figure 3-21 Torsional load calibration .....	53



---

---

Figure 3-22 High Capacity Differential Pressure Transducer HCDPT.....	53
Figure 3-23 HCDPT calibration.....	54
Figure 3-24 Burettes and Low Capacity Differential Pressure Transducer LCDPT .....	54
Figure 3-25 LCDPT calibration.....	55
Figure 3-26 Linear Variable Differential Transducer (LVDT).....	55
Figure 3-27 Calibration of LVDT .....	56
Figure 3-28 Potentiometers. (a) Large (POT1) (b) Small (POT2) .....	56
Figure 3-29 Calibration of large potentiometer POT1.....	57
Figure 3-30 Calibration of small potentiometer POT2 .....	57
Figure 3-31 Gap sensor .....	58
Figure 3-32 Calibration of gap sensor 1.....	58
Figure 3-33 Calibration of gap sensor 2.....	59
Figure 3-34 (a) Clip gauge (b) Clip gauges attached to a specimen.....	59
Figure 3-35 Calibration of clip gauge 1 .....	60
Figure 3-36 Calibration of clip gauge 2 .....	60
Figure 3-37 Calibration of clip gauge 3 .....	61
Figure 3-38 Load cells and water tanks .....	61
Figure 3-39 Calibration of load cell for upper tank .....	62
Figure 3-40 Calibration of load cell for lower tank.....	62
Figure 3-41 Amplifiers.....	63
Figure 3-42 Computer.....	63
Figure 3-43 Inner membrane and base pedestal .....	64
Figure 3-44 Outer membrane and outer mold.....	64

---

---

Figure 3-45 Gauze and inner mold .....	65
Figure 3-46 Specimen preparation .....	65
Figure 3-47 Placement of the top cap and removal of the mold .....	66
Figure 3-48 Cap for the inner hollow and diameter measurement .....	66
Figure 3-49 Placement of the load cell cap and clip gauges.....	67
Figure 3-50 Placement of the cell .....	67
Figure 3-51 Connection to the loading system.....	68
Figure 3-52 Representative results during Small Torsional Cyclic Loadings.....	69
Figure 3-53 Schematic STCL application during monotonic torsional shearing .....	70
Figure 3-54 Non-eroded test procedure.....	70
Figure 3-55 Process for erosion in experiments.....	71
Figure 3-56 Schematic illustration of application of erosion during torsional shearing .....	72
Figure 4-1 Volume of soil drained from dense specimens .....	75
Figure 4-2 Schematic volume distribution in dense specimens. (left) Before (right) After erosion .....	76
Figure 4-3 Volume of soil drained from loose specimens with 20% of initial content of detached particles.....	77
Figure 4-4 Volume soil drained from loose specimens with 35% of initial content of detached particles.....	77
Figure 4-5 Specimens after erosion: Dense specimen (left) Loose specimen (right) .....	78
Figure 4-6 Schematic volume distribution in Loose specimens. (left) Before erosion (right) After erosion .....	79
Figure 4-7 Comparison of the volume of soil eroded in the loose specimens .....	80
Figure 4-8 Total soil drained vs. Hydraulic gradient .....	81

---

---

Figure 4-9 Schematic intergranular space .....	82
Figure 4-10 Result of calibration for quantifying turbidity.....	82
Figure 4-11 Samples of water collected after seepage .....	83
Figure 4-12 Turbidity in dense specimens.....	84
Figure 4-13 Turbidity in loose specimens with 20% of initial content of detached particles	84
Figure 4-14 Turbidity in loose specimens with 35% of initial content of detached particles	85
Figure 4-15 Comparison of the turbidity in the loose specimens .....	86
Figure 4-16 Permeability in dense specimens.....	87
Figure 4-17 Permeability in loose specimens with 20% of initial content of detached particles .....	88
Figure 4-18 Permeability in loose specimens with 35% of initial content of detached particles .....	88
Figure 4-19 Comparison of the permeability in the loose specimens.....	89
Figure 4-20 Global void ratio in dense specimens.....	90
Figure 4-21 Global void ratio in loose specimens with 20% of initial content of detached particles .....	90
Figure 4-22 Global void ratio in loose specimens with 35% of initial content of detached particles .....	91
Figure 4-23 Comparison of the global void ratio in the loose specimens.....	91
Figure 4-24 Intergranular void ratio in dense specimens.....	92
Figure 4-25 Schematic intergranular void ratio before erosion (left) and after erosion (right) .....	92
Figure 4-26 Intergranular void ratio in loose specimens with 20% of initial content of detached particles .....	93

---

---

Figure 4-27 Intergranular void ratio in loose specimens with 35% of initial content of detached particles.....	93
Figure 4-28 Comparison of the Intergranular void ratio in the loose specimens.....	94
Figure 4-29 Relative density in dense specimens.....	95
Figure 4-30 Relative density in loose specimens with 20% of initial content of detached particles.....	95
Figure 4-31 Relative density in loose specimens with 35% of initial content of detached particles.....	96
Figure 4-32 Comparison of the Intergranular void ratio in the loose specimens.....	96
Figure 4-33 Intergranular relative density in dense specimens .....	97
Figure 4-34 Intergranular relative density in loose specimens with 20% of initial fines.....	97
Figure 4-35 Intergranular relative density in loose specimens with 35% of initial content of detached particles.....	98
Figure 4-36 Comparison of the Intergranular void ratio in the loose specimens.....	98
Figure 4-37 Grain size distribution of dense specimens.....	99
Figure 4-38 Fraction flushed in dense specimens .....	100
Figure 4-39 Grain size distribution of loose specimens with initial fines content of 20% ..	101
Figure 4-40 Fraction flushed in dense specimens with initial fines content of 20% .....	102
Figure 4-41 Grain size distribution of loose specimens with initial fines content of 35% ..	102
Figure 4-42 Fraction flushed in dense specimens with initial fines content of 35% .....	103
Figure 4-43 H vs. F curves for the dense specimens.....	104
Figure 4-44 H vs. F curves for the loose specimens with 20% of initial fines .....	105
Figure 4-45 H vs. F curves for the loose specimens with 35% of initial fines .....	105
Figure 4-46 Summary of results.....	108

---

---

Figure 4-47 Fraction flushed vs. hydraulic gradient .....	110
Figure 5-1 Eroded soil and turbidity. Dense eroded before shearing D-EbSH-60.....	113
Figure 5-2 Schematic erosion procedure during torsional shearing .....	114
Figure 5-3 Eroded soil and turbidity. D-Eb&dSH-60 .....	115
Figure 5-4 Eroded soil and turbidity. Medium eroded before shearing M-EbSH-60 .....	115
Figure 5-5 Eroded soil and turbidity. Medium eroded before and during shearing M-Eb&dSH-60 .....	116
Figure 5-6 Eroded soil and turbidity. Loose eroded before shearing L-EbSH-60 .....	117
Figure 5-7 Eroded soil and turbidity. Loose eroded before and during shearing L-Eb&dSH-60 .....	117
Figure 5-8 Eroded soil and turbidity. Dense eroded before shearing D-EbSH-150.....	119
Figure 5-9 Eroded soil and turbidity. Dense eroded before and during shearing D-Eb&dSH-150 .....	119
Figure 5-10 Eroded soil and turbidity. Loose eroded before shearing L-EbSH-150 .....	120
Figure 5-11 Eroded soil and turbidity. Loose eroded before and during shearing L-Eb&dSH-150 .....	120
Figure 5-12 Final amount of eroded soil in all the experiments .....	121
Figure 5-13 Turbidity vs. increment of eroded soil .....	122
Figure 5-14 Increment of eroded soil with varying relative density and confining pressure .....	123
Figure 5-15 Volumetric strain Dense $\sigma=60$ kPa .....	124
Figure 5-16 Volumetric strain Medium $\sigma=60$ kPa .....	124
Figure 5-17 Volumetric strain Loose $\sigma=60$ kPa.....	125
Figure 5-18 Volumetric strain Dense $\sigma=150$ kPa.....	125

---

---

Figure 5-19 Volumetric strain Loose $\sigma=150$ kPa.....	126
Figure 5-20 Comparison of volumetric strain for all the specimens with maximum erosion .....	127
Figure 5-21 Global void ratio Dense $\sigma=60$ kPa .....	128
Figure 5-22 Global void ratio Medium $\sigma=60$ kPa.....	128
Figure 5-23 Global void ratio Loose $\sigma=60$ kPa .....	129
Figure 5-24 Global void ratio Dense $\sigma=150$ kPa .....	129
Figure 5-25 Global void ratio Loose $\sigma=150$ kPa.....	130
Figure 5-26 Comparison of the global void ratio for all the specimens with maximum erosion .....	130
Figure 5-27 Intergranular void ratio Dense $\sigma=60$ kPa .....	131
Figure 5-28 Intergranular void ratio Medium $\sigma=60$ kPa.....	132
Figure 5-29 Intergranular void ratio Loose $\sigma=60$ kPa .....	132
Figure 5-30 Intergranular void ratio Dense $\sigma=150$ kPa .....	133
Figure 5-31 Intergranular void ratio Loose $\sigma=150$ kPa .....	134
Figure 5-32 Comparison of the Intergranular void ratio for all the specimens max erosion .....	134
Figure 5-33 Relative density Dense $\sigma=60$ kPa .....	135
Figure 5-34 Relative density Medium $\sigma=60$ kPa.....	135
Figure 5-35 Relative density Loose $\sigma=60$ kPa .....	136
Figure 5-36 Relative density Dense $\sigma=150$ kPa .....	136
Figure 5-37 Relative density Loose $\sigma=150$ kPa.....	137
Figure 5-38 Comparison of the relative density for all the specimens with maximum erosion .....	137

Figure 5-39 Intergranular Relative density Dense $\sigma=60$ kPa.....	138
Figure 5-40 Intergranular Relative density Medium $\sigma=60$ kPa .....	139
Figure 5-41 Intergranular Relative density Loose $\sigma=60$ kPa .....	139
Figure 5-42 Intergranular Relative density Dense $\sigma=150$ kPa.....	140
Figure 5-43 Intergranular Relative density Loose $\sigma=150$ kPa .....	140
Figure 5-44 Comparison of the intergranular relative density for all the specimens with maximum erosion .....	141
Figure 5-45 Stress-strain relationship for dense specimens confined at 60 kPa .....	142
Figure 5-46 Stress-strain relationship for medium-dense specimens confined at 60 kPa..	142
Figure 5-47 Stress-strain relationship for loose specimens confined at 60 kPa .....	143
Figure 5-48 Stress-strain relationship for dense specimens confined at 150 kPa .....	143
Figure 5-49 Stress-strain relationship for loose specimens confined at 150 kPa .....	144
Figure 5-50 Relative density variation of the dense specimens.....	145
Figure 5-51 Comparison of the stress-strain relationship for Dense specimens confined at 60 kPa.....	145
Figure 5-52 Detail of $\tau_{peak}$ for dense specimens confined at 60 kPa.....	146
Figure 5-53 Relative density variation of the loose specimens.....	147
Figure 5-54 Comparison of the stress-strain relationship for Loose specimens confined at 60 kPa.....	147
Figure 5-55 Detail of $\tau_{peak}$ for loose specimens confined at 60 kPa.....	148
Figure 5-56 Comparison of the shear stress strain curves of all the specimens .....	149
Figure 5-57 $\tau_{peak}$ variation for the specimens confined at 60 kPa .....	150
Figure 5-58 $\tau_{peak}$ variation for the specimens confined at 150 kPa .....	151
Figure 5-59 $G_{50}$ variation for the specimens confined at 60 kPa .....	152

Figure 5-60 $G_{50}$ variation for the specimens confined at 150 kPa .....	152
Figure 5-61 Shear stress transmission .....	154
Figure 5-62 $G$ variation of loose specimens confined at 60 kPa.....	156
Figure 5-63 $G/f(e)$ variation of Loose specimens confined at 60 kPa.....	157
Figure 5-64 $G/f(e_s)$ variation of loose specimens confined at 60 kPa .....	158
Figure 5-65 $G$ variation of dense specimens confined at 60 kPa.....	159
Figure 5-66 $G/f(e)$ variation of dense specimens confined at 60 kPa .....	159
Figure 5-67 $G/f(e_s)$ variation of dense specimens confined at 60 kPa .....	160
Figure 5-68 $G$ variation of medium-dense specimens confined at 60 kPa .....	160
Figure 5-69 $G/f(e)$ variation of medium-dense specimens confined at 60 kPa.....	161
Figure 5-70 $G/f(e_s)$ variation of medium-dense specimens confined at 60 kPa.....	161
Figure 5-71 $G$ variation of dense specimens confined at 150 kPa.....	162
Figure 5-72 $G/f(e)$ variation of dense specimens confined at 150 kPa .....	163
Figure 5-73 $G/f(e_s)$ variation of dense specimens confined at 150 kPa .....	163
Figure 5-74 $G$ variation of loose specimens confined at 150 kPa.....	164
Figure 5-75 $G/f(e)$ variation of loose specimens confined at 150 kPa .....	164
Figure 5-76 $G/f(e_s)$ variation of loose specimens confined at 150 kPa .....	165
Figure 5-77 Comparison of $G/f(e_s)$ in dense specimens .....	166
Figure 5-78 Comparison of $G/f(e_s)$ in loose specimens .....	167
Figure 5-79 Variation of $G$ at different confining pressures, in specimens non-eroded.....	167
Figure 5-80 Variation of $G$ at different confining pressures, in specimens eroded before shearing.....	168
Figure 5-81 Variation of $G$ at different confining pressures, in specimens eroded before and during shearing .....	168



---

---

Figure 5-82 Variation of $m$ for loose and dense specimens.....	169
Figure 5-83 Average $m$ for loose and dense specimens.....	170
Figure 5-84 $G/f(e_s)$ before shearing of specimens confined at 60 kPa.....	171
Figure 5-85 $G/f(e_s)$ before shearing of specimens confined at 150 kPa.....	171
Figure 5-86 Estimation of the amount of detached particles acting on the structure .....	172
Figure 5-87 Influence of the detached particles on the structure .....	172
Figure 5-88 Peak strength and critical states for dense specimens non-eroded.....	173
Figure 5-89 Peak strength and critical states for dense specimens eroded before shearing .....	174
Figure 5-90 Peak strength and critical states for dense specimens eroded before and during shearing .....	174
Figure 5-91 Peak strength and critical states for loose specimens non-eroded.....	175
Figure 5-92 Peak strength and critical states for loose specimens eroded before shearing .....	175
Figure 5-93 Peak strength and critical states for loose specimens eroded before and during shearing .....	176
Figure 5-94 Variation of the peak and critical state friction angle.....	177
Figure 5-95 Critical state lines for dense and loose specimens .....	178
Figure 5-96 Comparison of the peak shear stresses and the critical state line.....	179
Figure 5-97 Location of the images taken in the specimen .....	179
Figure 5-98 Samples for image analysis.....	180
Figure 5-99 Digital microscope .....	180
Figure 5-100 Microscope images.....	180
Figure 5-101 Microscope images of a non-eroded soil (left) and eroded soil (right). .....	181

---

---

Figure 5-102 ImageJ software.....	181
Figure 5-103 Image analysis of a non-eroded sample.....	182
Figure 5-104 Image analysis of an eroded sample .....	183
Figure 5-105 Microscope images of soils with different fines content .....	183
Figure 5-106 Calibration for image analysis .....	184
Figure 5-107 Percentage of eroded fines for the dense specimens confined at 60 kPa.....	185
Figure 5-108 Percentage of eroded fines for the medium-dense specimens confined at 60 kPa.....	185
Figure 5-109 Percentage of eroded fines for the loose specimens confined at 60 kPa .....	186
Figure 5-110 Percentage of eroded fines for the dense specimens confined at 150 kPa...	186
Figure 5-111 Percentage of eroded fines for the loose specimens confined at 150 kPa ....	187
Figure 5-112 Position of the clip gauges.....	188
Figure 5-113 Void ratio variation at various heights .....	188
Figure 5-114 Flow of particles eroded for the dense specimens confined at 60 kPa .....	189
Figure 5-115 Flow of particles eroded for the medium dense specimens confined at 60 kPa .....	190
Figure 5-116 Flow of particles eroded for the loose specimens confined at 60 kPa .....	190
Figure 5-117 Flow of particles eroded for the dense specimens confined at 150 kPa .....	191
Figure 5-118 Flow of particles eroded for the loose specimens confined at 150 kPa .....	191
Figure 5-119 Turbidity and eroded soil of L-Eb&dSH-60 (same as Figure 5-7) .....	192
Figure 5-120 Variation of $\varepsilon_{vol}$ , $e$ and $e_s$ of L-Eb&dSH-60 .....	193
Figure 5-121 Variation of $\varepsilon_{vol}$ , $e$ and $e_s$ of L-Eb&dSH-60 .....	194
Figure 5-122 Variation of $D_r$ and $D_{rs}$ of L-Eb&dSH-60 .....	194
Figure 5-123 Arrangement of particles before and after torsional shearing .....	194

---

---

Figure 5-124 Arrangement of particles before and after erosion .....	195
Figure 5-125 Variation of peak shear stress .....	196
Figure 5-126 Variation of shear modulus .....	196
Figure 5-127 Average void ratio .....	197
Figure 5-128 Average intergranular void ratio .....	198
Figure 5-129 Average relative density .....	198
Figure 5-130 Average intergranular relative density.....	199
Figure 5-131 Transmission of stresses. Before shearing (left) During torsional shearing (right) .....	200



## List of Tables

Table 2-1 Expressions for basic soil parameters based on weight and volume.....	16
Table 2-2 Relationships among unit weight, void ratio and water content.....	17
Table 3-1 Properties of Silica sand No. 5 .....	37
Table 3-2 Properties of DL Clay.....	38
Table 3-3 Determination of soil proportions according to Kenney and Lau (1985).....	40
Table 3-4 Percentages of mixed Silica sand and DL Clay .....	41
Table 4-1 Soil description for to the relative density (Lambe and Whitman, 1979) .....	73
Table 4-2 Properties of the permeability tests.....	74
Table 4-3 Percentage of soil eroded.....	79
Table 4-4 Classification of soils permeability .....	89
Table 4-5 Fraction flushed in the dense specimens .....	101
Table 4-6 Fraction flushed in the loose specimens .....	103
Table 4-7 Summary of results for permeameter test.....	107
Table 5-1 Torsional tests conditions.....	112
Table 5-2 Eroded soil in the tests confined at 60kPa .....	116
Table 5-3 Eroded soil in the tests confined at 150kPa .....	121
Table 5-4 Classification of the specimens tested, according to the role of fines.....	153
Table 5-5 Measurement of G by STCL during the tests .....	155
Table 5-6 Summary of strength parameters .....	177



# Chapter 1. Introduction

## 1.1. General

Internal erosion is defined as the transportation of finer soil particles from the main structure inside the ground, due to the mechanical action of seepage flow. The result of internal erosion can be observed in the field as chains of macropores parallel to the ground surface. The transportation of fines affects various characteristics of the soil including hydraulic conductivity and mechanical behavior (Schuler 1995).

The causes of internal erosion can be explained by four mechanisms: Leak erosion, backward erosion and piping, soil contact erosion, and suffusion (Fell and Fry, 2007; Bonelli, 2012). This research focuses particularly on suffusion, in which the fines are gradually transported through the voids between the matrix of coarser-grains (Figure 1-1).

It is the grain size distribution that governs the growth of suffusion in the ground influenced by the hydraulic conditions. (Salehi and Witt, 2011). Consequently, the resistance of a soil against suffusion depends on a geometric criterion associated with the soil skeleton and the constrictions to retain the fines inside the pores.

The phenomenon of internal erosion causes failure of hydraulic structures including landslides, collapse of dams and levees, and other ground disasters (Fry et al., 1997; Foster et al., 2000). Specifically, suffusion is related to some dam failures in the past (Fell et al. 2003; Zhang and Chen 2006; Xu and Zhang 2009; Zhang et al. 2009). The stability of slopes is also affected by the action of internal erosion, e.g. the heavy rainfalls triggered various and large landslides in Izu island and Hiroshima, Japan.

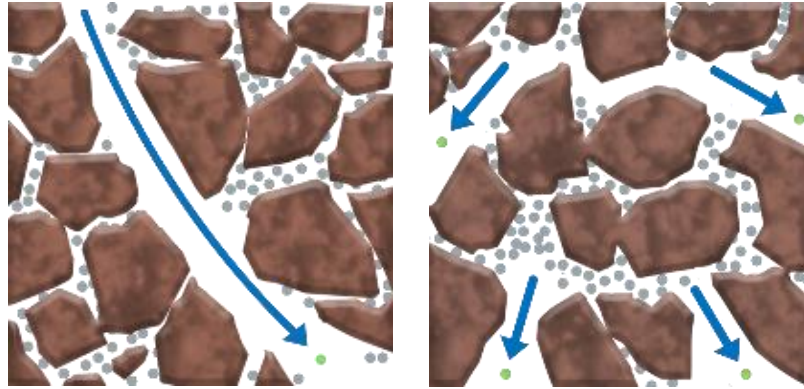


Figure 1-1 Schematic illustration of two types of internal erosion: Piping (left) and suffusion (right)

## 1.2. Literature review

### 1.2.1. Case studies

The most probable cause of failure in dams and leveed is the action of internal erosion and piping. Suffusion, which is a type of internal erosion, can be developed due to piping, and it may cause the failure. Internal erosion can be easily observed in field, but it is difficult to distinguish specifically the action of suffusion, as just some of the fines are transported from their original location. Besides, the evidence of the factor which triggered the disaster disappears after the embankment failure.

Internal erosion developed as piping below overtopping is a main cause of dam failures (Foster et al, 2000). Generally, the failures due to piping have been reported in homogeneous earthfill dams with lack of seepage control. “Dams with poor control of seepage and pore pressures in the embankment and foundation have generally experienced more problems associated with piping and slope stability compared with other dam types (...) Dams with downstream rockfill zones have a low frequency of failure by all piping modes of failure but a high proportion of piping accidents, suggesting that piping is less likely to progress to breaching in rockfill dams than in dam types with downstream zones of earthfill.” (Foster et al, 2000).

Other reports point soil erosion as the main factor for landslide initiation, gully erosion failure, and stream bank failures (Faulkner, 2006; Uchida et al, 2001; Wilson et al, 2011).



Pierson (1983) investigated specifically the role of soil pipes in slope stability through observation reports (Figure 1-2) and experimental results, concluding that piping is produced by water seepage and thus high pore pressures may be the key factor: “Interconnected networks of soil pipes in hillslope soils can rapidly transmit water and speed drainage from hillslopes during rainstorms (...) Hydrostatic head from water standing in the pipe can produce high pore pressures in the soil around the pipe, even in excess of those generated by total saturation of the soil matrix” (Pierson, 1983).

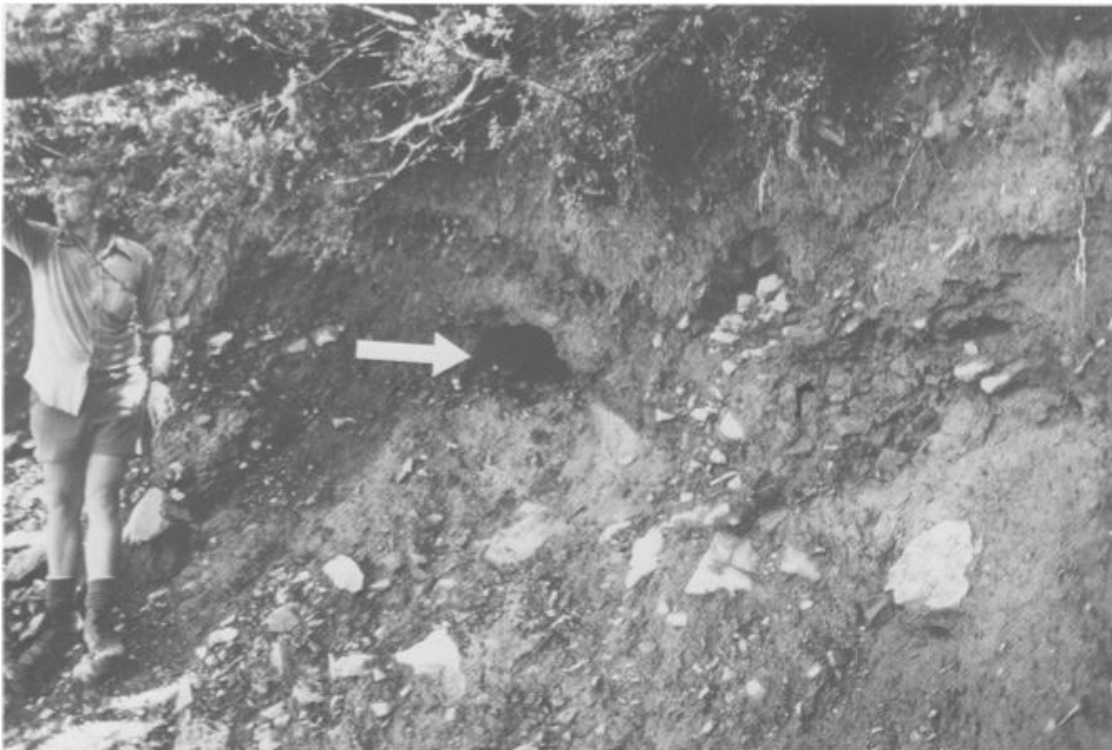


Figure 1-2 Soil pipe in the head of a landslide scar at Arthur’s Pass National Park (Pierson, 1983)

#### *1.2.2. Numerical analysis*

Numerical models simulating suffusion has been performed by many researchers. Stress transmission analysis using Discrete Element Method (DEM) (Figure 1-3), demonstrates suffusion in an internally unstable soil where the coarse-grain matrix transfers stresses, while

loose particles move freely between the pores of the primary fabric (Mojtaba, 2013), confirming the criteria of Kenney & Lau (1985) which will be explained in detail in Chapter 2 .

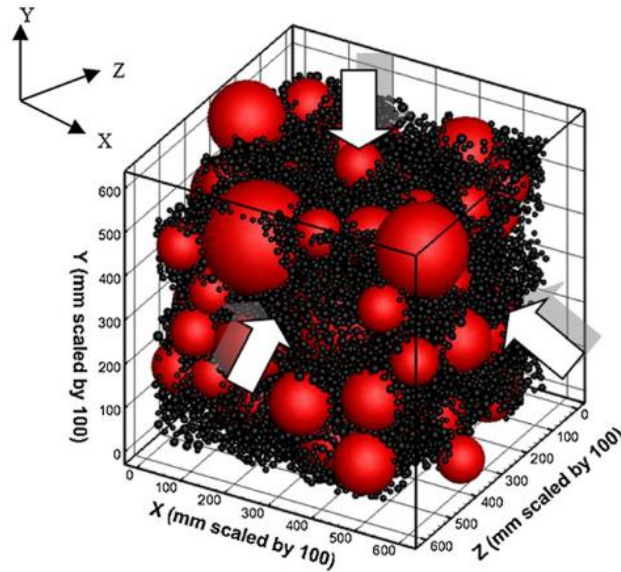


Figure 1-3 Packing of an internally unstable soil (Mojtaba, 2013)

3D spherical discrete elements considering interaction between fluid and solid particles are used to investigate the effects of grain size distribution, constriction sizes and the velocity of particles transported. The study of the variation in void ratios and contacts between particles shows changes in the behavior of eroded soils (Aboul et al, 2016). Using finite difference method models enables to prove that the hydraulic characteristics of internally unstable soils are affected by suffusion (Ahmed, 2016).

Nevertheless, numerical models using spherical particles simplify the actual particle shape and surface rugosity, underestimating the resistance against flow of finer particles.

### *1.2.3. Experimental studies*

Various experimental studies have been performed applying a water flow through a soil specimen, measuring the amount of particles transported. These procedures have enabled evaluation of different characteristics of the soil, e.g. geometrical characteristics, hydraulic properties, and mechanical properties.

a. Geometrical characteristics:

Soils with potential of being affected by suffusion are considered as internally unstable. Most of the experimental research about suffusion and erosion of fines is based on the design of filters for dams. Kenney and Lau (1985) performed a series of seepage tests using various types of soils to classify their grain size distribution into stable or unstable grain size distributions (Figure 1-4). Based on the results, Kenney determined criteria to assess the resistance of the fine particles to be transported from their original place between the pores of coarser grains.

Many researchers (Sherard et al, 1984; Ke and Takahashi, 2012) studied the behavior of soils subjected to a water flow using various grain size distribution. Soils collected at different locations in the samples were compared to investigate the performance of the filters.

Experiments with upward seepage flow with varying hydraulic gradient aided to understand the susceptibility to erosion based on the grain size distribution (Skempton and Brogan, 1994; Sterpi, 2003; Ke and Takahashi, 2012).

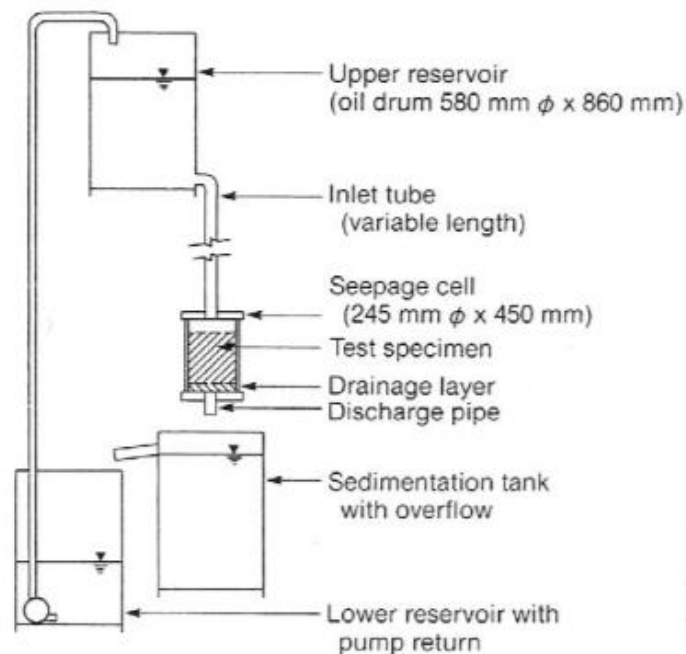


Figure 1-4 Schematic illustration of seepage test (Kenney and Lau, 1985)

b. Hydraulic properties:

One-dimensional tests also have been carried out to investigate the effects of seepage on the hydraulic characteristics of a soil such as critical hydraulic gradients. Some researchers have investigated the behavior of particles transportation in soils with open cracks by means of the Hole Erosion Test (Wan and Fell, 2002; Benahmed and Bonelli, 2012).

The critical hydraulic gradients were evaluated under various stress states and stress paths using stress controlled erosion tests (Chang and Zhang, 2013). Sterpi (2003) conducted experiments on reconstituted samples of well graded sand and gravel by evaluating the effect of the hydraulic gradient before reaching critical conditions. The amount of particles eroded was measured after sedimentation (Figure 1-5). Local volume reductions and variations of the mechanical characteristics were found as consequence of the fine particles erosion.

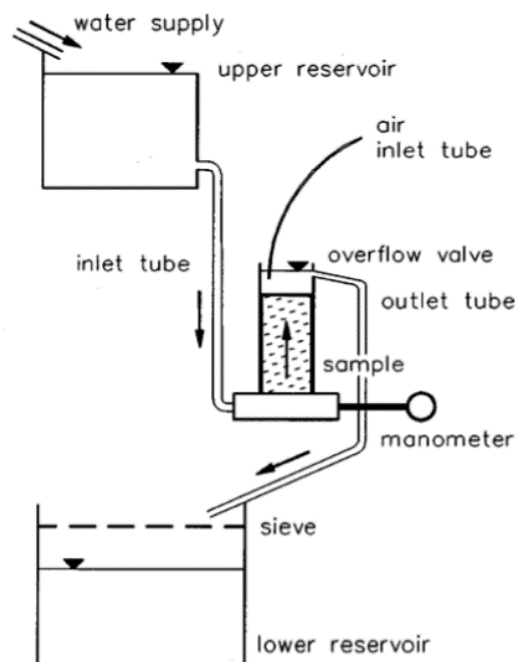


Figure 1-5 Experimental setup for seepage tests (Sterpi, 2003)

c. Mechanical properties:

One-dimensional seepage tests are also used to evaluate the mechanical properties of soils affected by the action of suffusion. Ke and Takahashi (2012) studied the effect of the fines content, density and hydraulic gradient on soils eroded by a seepage flow by measuring cone penetration resistance. They concluded that the internal erosion reduces the cone tip resistance compared with uneroded soils.

In addition to the unconfined seepage analysis, Chang and Zhang (2011) evaluated the effect of internal erosion on the drained shear strength of the soil under various stress states. The testing apparatus consists of a triaxial machine with soil and water collection systems (Figure 1-6). The results show that the changes in the permeability and deformation resulted in an increase in the deviatoric stress, and changes in the shear strength depending on the stress states.

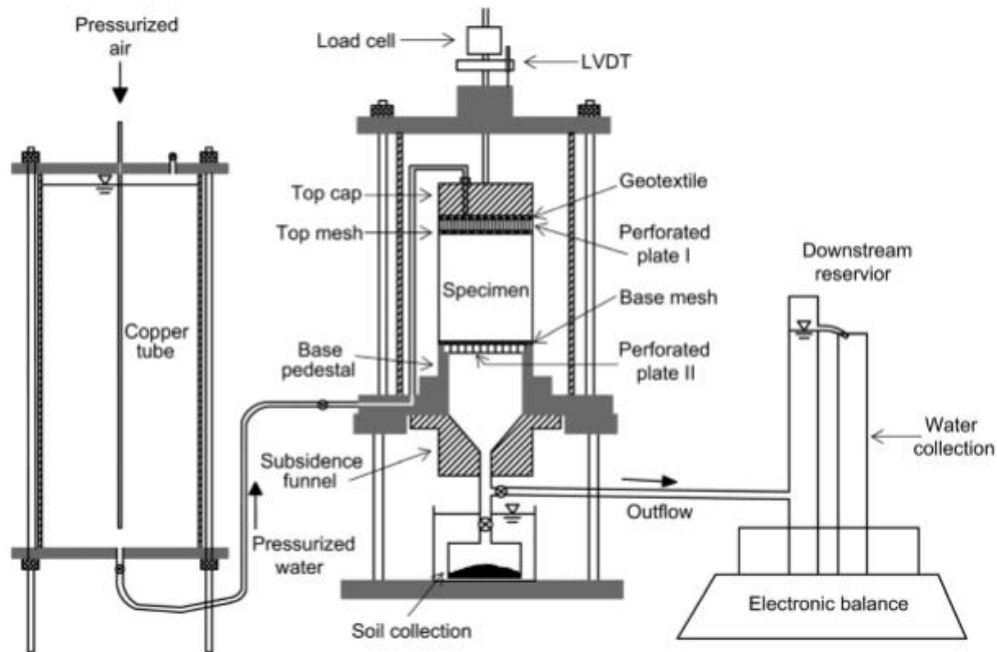


Figure 1-6 Stress-controlled erosion apparatus (Chang and Zhang, 2011)

Xiao and Shwiyhat (2012) used a modified triaxial apparatus which allows the gathering of eroded particles, which are removed out from the specimen by the action of seepage,

in consolidated undrained (CU) tests performed to gap-graded soils. The effects of erosion by suffusion on the permeability, volume change, and compressive strength were measured. The results show that the compressive strength is larger after erosion.

Sato and Kuwano (2014) evaluated the soil characteristics of an unstable soil (Young's modulus, Poisson's ratio, deformation and dilatancy) using a modified triaxial apparatus with a bottom plate with holes. The results of experiments under drained conditions suggest that even a small degree of erosion can cause a reduction in the soil stiffness.

### 1.3. Objectives

The mechanism of internal erosion was studied using numerical simulations or laboratory experiments based on one-dimensional seepage and modified triaxial tests. The previous investigations focused on the effects of internal erosion under controlled stress conditions with increasing deviatoric stress on triaxial tests. Thus, the main objective of this research is to evaluate the mechanical properties of a soil subjected to suffusion under constant normal stresses with torsional shear force. To achieve this objective, the following aims must be taken into account:

- Suffusion is a complex process to be modelled as just the fines migrate while the coarser-grain matrix remains unmoved. Hence, a primary objective of this research is to obtain soils affected by suffusion.
- The effect of density, initial fines content and hydraulic gradient on the hydraulic properties of an internally unstable soil was investigated.
- In the suffusion process, the water drained out from the ground contains fine particles detached from the main soil structure. The amount of these fines can be estimated by measuring the turbidity of the water. Therefore, an objective of this research is to evaluate how turbidity can be related to the degree of erosion.

- In an internally stable soil the finer grains are confined between larger particles; by the action of suffusion these fines move between adjacent pores through constrictions. However, after a determined volume of water had passed through the soil, the potentially movable particles left the soil matrix or were piled in new pores clogging the constrictions. A small shear strain applied to the soil will create new constrictions and move the fines trapped in the pores. Therefore, this research evaluates how the shear strain affects the degree of erosion.
- Finally, this research aims to evaluate the influence of the relative density, degree of erosion and confining pressure on the mechanical properties of a soil including small strain stiffness and shear strength.

#### 1.4. Scope

The present research evaluates the properties of a soil affected by suffusion. Therefore, two kinds of experiments were performed:

- a. One-dimensional column permeability test: Soils considered as internally unstable are placed in an acrylic chamber with a bottom plate with holes. Pressurized water is applied from the top part of the chamber to generate suffusion and move some of the fines, allowing them to evacuate from the bottom plate. Soils with different initial fines content and relative densities are tested under seepage with various hydraulic gradient. The changes in permeability, amount of drained particles, turbidity, and grain size distribution are studied, among others.
- b. Hollow cylindrical torsional shear test: Torsional shear tests are conducted to evaluate the mechanical characteristics of soil specimens before and after suffusion, with densities ranging from loose to dense specimens, at different confining pressures. The shear modulus is calculated under low-amplitude torsional cyclic loadings in various stages during the test. The turbidity and amount of drained particles are also measured at various erosion stages along the experiments. Finally, the influence of erosion on the shear strength is evaluated by shearing the specimens.

### 1.5. Thesis organization

This thesis consists of 6 chapters. The outline of each chapter is summarized below.

- Chapter 1 Introduction: The general introduction to the issues studied can be found in this chapter. The previous research related to internal erosion is also mentioned to highlight the purpose and objectives of the present study.
- Chapter 2 Basic theories: A general description of the basic soil mechanics is included considering the hydraulic properties of a soil as well as the mechanical characteristics.
- Chapter 3 Material, apparatus and testing procedure: The characteristics of the soil studied and the apparatuses used in the experiments are described in detail. The procedure of each type of test is also included.
- Chapter 4 Evaluation of suffusion by one-dimensional column permeability test: The results of the permeability tests are presented and analyzed. The variation of the hydraulic characteristics due to induced suffusion incited by a seepage flow are discussed.
- Chapter 5 Evaluation of the mechanical properties of soils by hollow cylindrical torsional shear test: The results and analyses of the torsional shear tests are presented. The influence of suffusion on the mechanical properties of soils is discussed in detail.
- Chapter 6 Summaries, conclusions and recommendations: The summary of the findings in this study is presented as well as conclusions and recommendations for future works.

### 1.6. References

Aboul Hosn R. & L. Sibille, N. Benahmed, B. Chareyre. (2016). A discrete numerical description of the mechanical response of soils subjected to degradation by suffusion. Scour and erosion – Harris, Whitehouse & Moxon (Eds), 397 – 405.



Ahmed, B. (2016). Modeling of particles migration in porous media: Application to soil suffusion. Scour and erosion – Harris, Whitehouse & Moxon (Eds), 407 – 414.

Benahmed N., & Bonelli S. (2012). Investigating concentrated leak erosion behavior of cohesive soils by performing Hole Erosion Test. *European Journal of Environmental and Civil Engineering*, 16(1), 43 – 58.

Bonelli, S. (Ed.). (2012). *Erosion of geomaterials*. ISTE Ltd and John & Sons, Inc.

Chang, D.S. and Zhang, L.M. (2011). A Stress-controlled Erosion Apparatus for Studying Internal Erosion in Soils. *Geotechnical Testing Journal*, Vol. 34, No. 6 Paper ID GTJ103889, 579 – 589.

Chang, D.S., and Zhang, L.M. (2013). Critical Hydraulic Gradients of Internal Erosion under Complex Stress States. *Journal of geotechnical and geoenvironmental engineering*. ASCE 139(9), 1454 – 1467.

Faulkner, H. (2006). Piping hazard on collapsible and dispersive soils in Europe. *Soil Erosion in Europe*, 537 – 562.

Fell, R., Wan, C. F., Cyganiewicz, J., and Foster, M. (2003). Time for Development of Internal Erosion and Piping in Embankment Dams. *J. Geotech. Geoenviron. Eng.*, Vol. 129, No. 4, 307 – 314.

Fell, R. and Fry, J. J. (2007). *The State of the Art of Assessing the Likelihood of Internal Erosion of Embankment Dams, Water Retaining Structures and Their Foundations*. Internal Erosion of Dams and Their Foundations (Taylor & Francis, London), 1 – 23.

Foster, M., Fell, R., Spannagle, M. (2000b). The statistics of embankment dam failures and accidents. *Canadian Geotech. J.* 37(5), 1000 – 1024.

Fry, J.J., Degoutte, G., & Goubet, A. (1997). L'érosion interne: typologie, détection et réparation. *Can. Geotech. J.* Volume 37, 1000 – 1024.

Ke, L. and Takahashi, A. 2012. Strength reduction of cohesionless soil due to internal erosion induced by one-dimensional upward seepage flow. *Soils and foundations*. The Japanese Geotechnical Society. 2012;52(4), 698 – 711.

Kenney, T.C. and Lau, D. (1985). Internal stability of granular filters. *Canadian Geotechnical Journal*, 22, 215 – 225.

Li, M. (2016). Critical hydraulic gradients for internally unstable cohesionless soils. *GeoVancouver 2016*.

Mojtaba Farahnak Lanroudi, A. S., Piltan Tabatabaie Shourijeh, R. S. (2013). Stress transmission in internally unstable gap-graded soils using discrete element modelling Powder technology. Volume 247, 161 – 171.

Pierson, T. C. (1983). Soil pipes and slope stability. *Qtly. J. Eng.Geol. and Hydrogeol.* 16(1), 1 – 11.

Salehi Sadaghiani, M. R. and Witt, K. J. (2011) Variability of the grain size distribution of a soil related to suffusion. *ISGSR 2011 - Vogt, Schuppener, Straub & Bräu (eds)*, 239 – 248.

Sato, M. and Kuwano, R. (2014). Effects of internal erosion on mechanical properties evaluated by triaxial compression tests. *Japanese Geotechnical Society Special Publication. The 15th Asian Regional Conference on Soil Mechanics and Geotechnical Engineering*, 1056 – 1059.

Schuler, U., 1995, “How to Deal with the Problem of Suffusion,” *Research and Development in the Field of Dams*, Switzerland National Committee on Large Dams, Crans-Montana, Switzerland, 145 – 159.

Sherard, J.L., Dunnigan, L.P., and Talbot, J.R. (1984). Basic properties of sand and gravel filters. *Journal of Geotechnical Engineering, ASCE*, 110(6), 684 – 700.

Skempton, A. W., and Brogan, J. M. (1994). Experiments on piping in sandy gravels. *Geotechnique*, 44(3), 449 – 460.

Sterpi, D. (2003) Effects of the erosion and transport of fine particles due to seepage flow. *International journal of geomechanics*. ASCE, 111 – 122.

Uchida, T., K. Kosugi, and T. Mizuyama. (2001). Effects of pipeflow on hydrological process and its relation to landslide: A review of pipeflow studies in forested headwater catchments. *Hydrol. Proc.* 15(11), 2151 – 2174.

Wan C.F., Fell R. (2002). Investigation of internal erosion and piping of soils in embankment dams by the slot erosion test and the hole erosion test. UNICIV Report, no. R-412, July 2002.

Wilson, G. V., R. K. Periketi, G. A. Fox, S. Dabney, F. D. Shields, and R. F. Cullum. (2007). Soil properties controlling seepage erosion contributions to streambank failure. *Earth Surface Proc. and Landforms* 32(3), 447 – 459.

Xiao, M. and Shwiyhat (2012). Experimental Investigation of the Effects of Suffusion on Physical and Geomechanic Characteristics of Sandy Soils. *Geotechnical Testing Journal*, Vol. 35, No. 6, ASTM, 890 – 900.

Zhang, L. M. and Chen, Q., 2006, “Seepage Failure Mechanism of the Gouhou Rockfill Dam during Reservoir Water Infiltration,” *Soils and Foundations*, Vol. 46, No. 5, 557 – 568.



## Chapter 2. Basic theories

The main theories and concepts used in this research are summarized below. Firstly, the general concepts in soil mechanics are presented, which are essential in all the calculations and descriptions of the specimens studied. Moreover, this chapter includes the criteria commonly used to assess the internal stability of granular materials and the concepts used to evaluate the hydraulic and mechanical properties of soil.

### 2.1. General concepts in soil mechanics

The soil is defined as a heterogeneous system consisting of three phases: solid, liquid and gas (Figure 2-1). The solid phase consists of mineral particles of soil; the liquid phase is commonly constituted by water (although there can be other liquids in some soils); and the gas phase is made of air, even though other gases as sulphurous vapors and carbonic anhydride can be present. Some soils can also contain organic material such as partially decomposed plant residues. In addition, the viscous layer of adsorbed water has properties between solid and liquid phase, but usually assumed to be liquid (Juárez and Rico, 2005). The phases of the soil can be expressed in terms of volume and weight; the basic expressions are compiled in the Table 2-1.

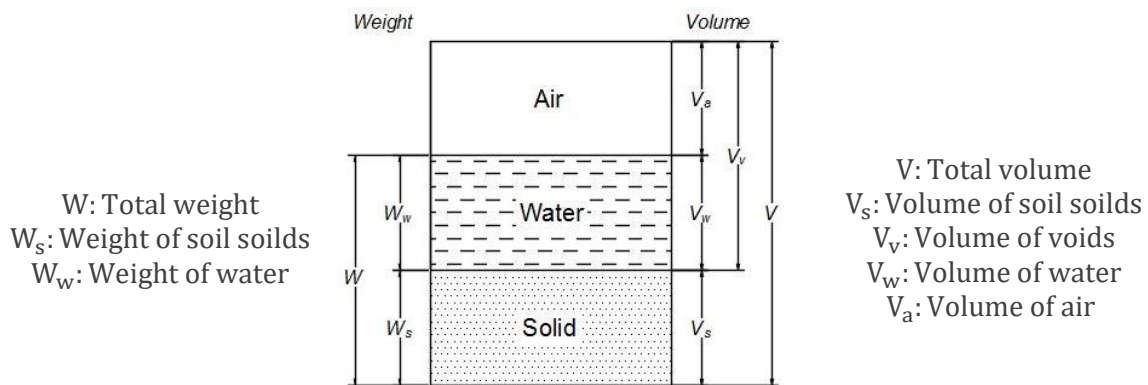


Figure 2-1 Three phases of the soil element

Table 2-1 Expressions for basic soil parameters based on weight and volume

Total volume ( $V$ )	$v = v_s + v_v = v_s + v_w + v_a$	(2-1)
Total weight ( $W$ )	$W = W_s + W_w$	(2-2)
Void ratio ( $e$ )	$e = \frac{v_v}{v_s}$	(2-3)
Porosity ( $n$ )	$n = \frac{v_v}{v}$	(2-4)
Degree of saturation ( $S_r$ )	$S_r = \frac{v_w}{v_v}$	(2-5)
Water content ( $w$ )	$w = \frac{W_w}{W_s}$	(2-6)
Unit weight ( $\gamma$ )	$\gamma = \frac{W}{v}$	(2-7)
Dry unit weight ( $\gamma_d$ )	$\gamma_d = \frac{W_s}{v}$	(2-8)

Furthermore, considering the solids volume as one, there can be obtained some relationships among unit weight, void ratio, and water content. The consequent relationships are summarized in Table 2-2.

Table 2-2 Relationships among unit weight, void ratio and water content

Specific gravity ( $G_s$ )	$G_s = \frac{W_s}{\gamma_w}$	(2-9)
Dry unit weight ( $\gamma_d$ )	$\gamma_d = \frac{G_s \gamma_w}{1 + e}$	(2-10)
Saturated unit weight ( $\gamma_{sat}$ )	$\gamma_{sat} = \frac{(G_s + e) \gamma_w}{1 + e}$	(2-11)
Relative density ( $D_r$ )	$D_r = \frac{e_{max} - e}{e_{max} - e_{min}}$	(2-12)

Where,  $e_{max}$ : Void ratio at the loosest state  
 $e_{min}$ : Void ratio at the densest state

## 2.2. Internal stability of granular materials

The process of suffusion is often related to soils that are internally unstable. In such kind of soils, the fine particles can be freely transported between the pores made by the coarser grains. The pores refer to the intergranular space made by the coarse particles, in an arrangement of 4 spherical particles representing the primary fabric, there is one pore with a 3D shape (Figure 2-2 (a)); the constrictions are the opening windows connecting two pores, in the arrangement of 4 spheres there are 4 constrictions which have 2 dimensions (Figure 2-2 (b)).

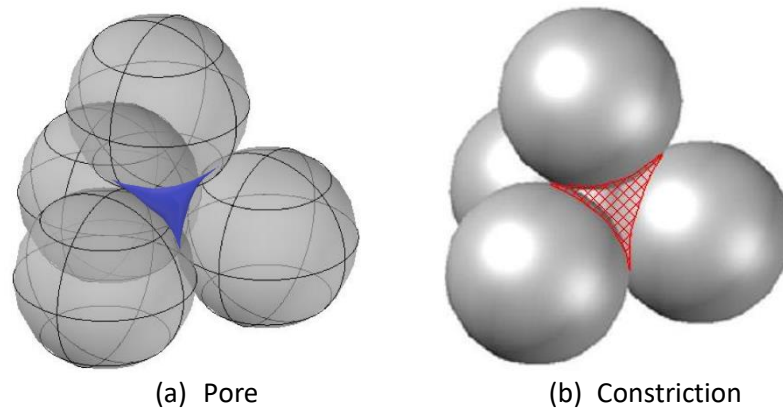


Figure 2-2 Schematic representation of pores and constrictions

Some researchers have developed criteria to determine the susceptibility of a soil to be internally unstable as below.

### 2.2.1. Kenney and Lau criterion

A commonly used criterion is developed by Kenney and Lau (1985). They performed a series of seepage tests using a variety of granular samples, and defined the internal stability of a soil as: “the ability of a granular material to prevent loss of its own small particles due to disturbing agents such as seepage and vibration”. The following conditions are needed for small particles to move between the pore spaces in a loose fabric:

- There is a primary fabric which transfers stresses, and its particles are immovable (Figure 2-3).
- There must be loose or detached particles within the intergranular voids and are movable among the pores.
- The constrictions made by the primary fabric are larger than some of the loose particles.

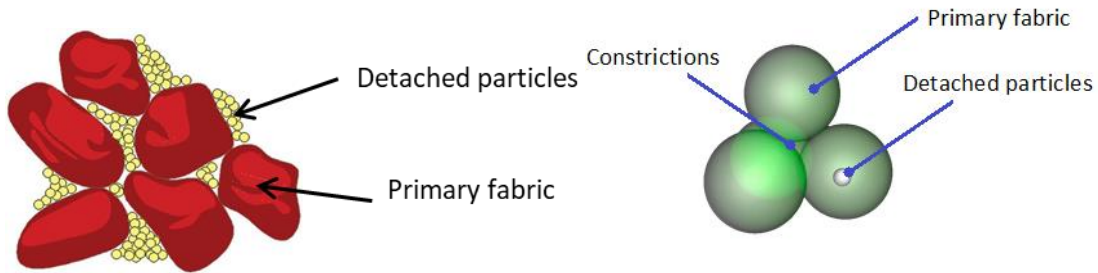


Figure 2-3 Schematic illustration of an internally unstable soil

The amount of detached particles that can be in the voids between the coarser particles is determined by:

$$f_p + f_1 = 1 \quad (2-13)$$

$$f_p \geq \frac{1}{1 + e_p(1 - n_1)} \quad (2-14)$$



where:

$f_p$ : Fraction of the primary fabric in the total mass

$f_1$ : Fraction of the detached particles

$e_p$ : Void ratio of the primary fabric

$n_1$ : Average porosity between the primary fabric and detached particles

In order to determine if a soil satisfies the condition of internally stable or internally unstable, a H:F curve can be used. Where F is the mass fraction smaller than the particle diameter (D), and H is the mass fraction between D and 4D. The assumption of the threshold of 4D is given by Kenney et al (1985), where it was found that the size of most of the constrictions is approximately  $\frac{1}{4}$  of the fine particles (Figure 2-4). Then, a particle with size D can pass in the constrictions of particles with diameter 4D, and therefore this measure represents the amount of particles that form constrictions small enough to retain the particles of size D.

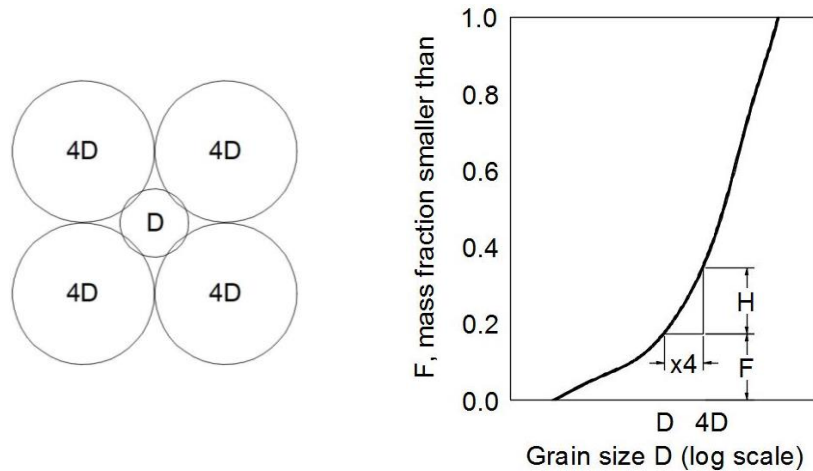


Figure 2-4 Schematic internal stability criteria by Kenney and Lau (1985)

A boundary curve  $H=1.3F$  established according to Loebotsjkov (1969) was initially adopted by Kenney and Lau (1985), but later modified to  $H=F$  in subsequent investigations (Kenney and Lau, 1986). In addition, threshold values of  $F=0.2$  for widely-graded primary fabrics (WG) and  $F=0.3$  for narrowly-graded primary fabrics (NG) are considered. Then, the materials with shape curves that lie in the zone below the limiting grain size distribution curve and with F lower than the limit set for WG or NG depending on each case, are considered as unstable

(Figure 2-5). However, Kenney and Lau still recommended to reduce the inclination of the boundary to  $H=0.9F$ , based on the envelope of all the laboratory experiments performed.

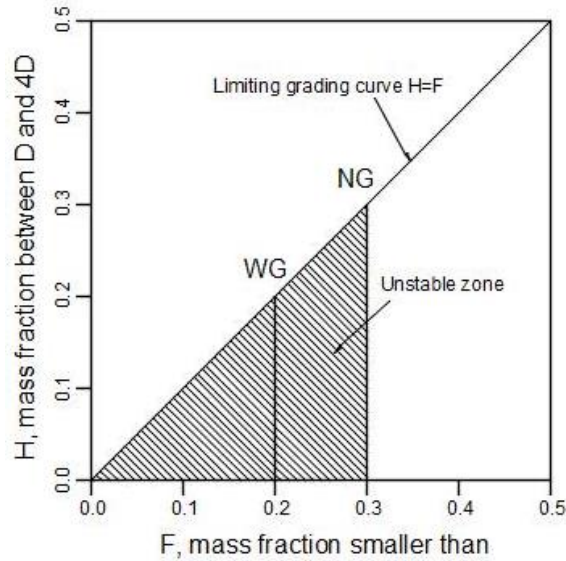


Figure 2-5 Internal stability criteria in H vs. F space by Kenney and Lau (1985)

#### 2.2.2. Other criteria

Many researchers have proposed criteria to define whether a granular material can be considered as unstable or not. Skempton and Brogan (1994) suggest that if a soil contains around 35% of fines, the fine particles can be freely transported through the Intergranular spaces of the coarse particles. Such a soil can be considered as internally unstable and sensitive to suffusion.

A classical criterion for filter design is proposed by Terzaghi (1939) based on laboratory experiments (2-15). Fannin (2008) describes Terzaghi's expression as  $1/5$  of the diameter of the largest grain in the fines can be contained by a pore of the coarse grain fraction, but as a factor of safety it is considered that the larger material should be 4 times the smaller material, instead of 5.

$$D_{15} \leq 4D_{85} \quad (2-15)$$

where,

$D_{15}$ : Particle diameter with 15% passing in the filter

$D_{85}$ : Particle diameter with 85% passing in the filter

Kezdi (1979) also carried out seepage tests using filter materials; their results support the Terzaghi's filter criterion, in which the relationship between  $D_{15}$  and  $d_{85}$  is limited by 4 (Figure 2-6). This finding was posteriorly supported by Kenney's investigations using analytical models considering spherical particles.

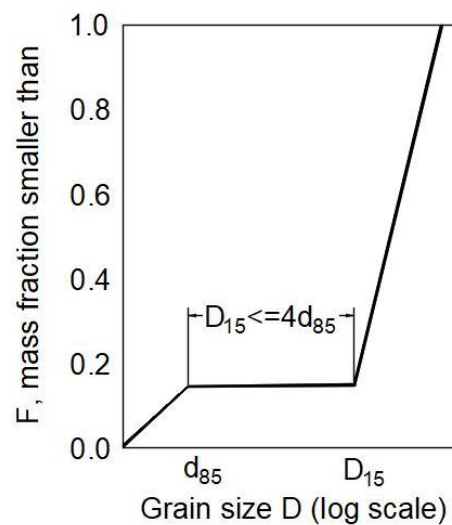


Figure 2-6 Schematic internal stability criteria by Kezdi (1979)

Chapuis (1992) demonstrated that Kezdi criterion considers that a material is unstable if  $H$  is lower than 0.15 in the  $H$  vs.  $F$  space (Figure 2-7). Fannin and Moffat (2006) found the threshold of  $D_{15}/d_{85} \leq 5$  based on their experimental seepage tests. Similarly, Bertram (1940) found the relation of  $D_{15}/d_{85} \leq 6$ , although these criteria are conservative due to the high hydraulic gradients applied in the experiments.

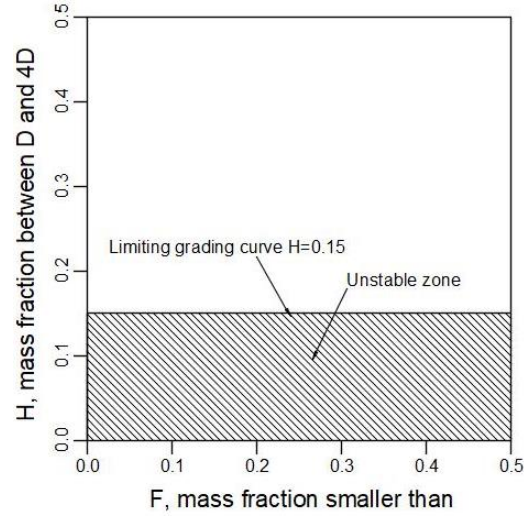


Figure 2-7 Internal stability criteria in H vs. F space by Kezdi (1979)

### 2.3. Hydraulic soil properties

One-dimensional column permeability tests are included in this study. Some of the basic theories about the hydraulic properties of soils are described below.

#### 2.3.1. Darcy's Law

The water flow in porous media is governed by a law established by Darcy (1856) by means of experimental studies in soils subjected to a seepage flow. Darcy found that if the water flows at small velocities, the total discharge is determined by equation (2-16) for the one-dimensional case.

$$Q = \frac{\delta V}{\delta t} = k \cdot i \cdot A \quad (2-16)$$

Where,

$Q$ : Discharge [ $\text{length}^3/\text{time}$ ]

$\delta V$ : Volume of water variation per unit time [ $\text{length}^3$ ]

$\delta t$ : Unit time [time]

$k$ : Coefficient of permeability [ $\text{length}/\text{time}$ ]

$i$ : Hydraulic gradient [dimensionless]

$A$ : Cross section of the soil normal to the direction of flow [ $\text{length}^2$ ]

Considering the continuity equation (2-17), the total discharge can be expressed as (2-18), which is known as the Darcy's Law.

$$Q = v \cdot A \quad (2-17)$$

Where,

$Q$ : Discharge [length<sup>3</sup>/time]

$v$ : Velocity [length/time]

$A$ : Cross section [length<sup>2</sup>]

$$v = k \cdot i \quad (2-18)$$

### 2.3.2. Hydraulic gradient

The water flows into a porous medium is described with the filtration lines, where a drop of water flows through a permeable material. Despite the erratic movement of the water into the soil, the filtration lines are defined as straight and parallel to the flow direction. The water always flows from a point with larger hydraulic head to one with lower hydraulic head. The concept of hydraulic head is defined as (2-19)

$$h_a = z_a + \frac{u_a}{\gamma_w} + \frac{v^2}{2g} \quad (2-19)$$

Where,

$h_a$ : Total hydraulic head at point a [length]

$z_a$ : Elevation at point a [length]

$u_a$ : Pressure at point a [force/length<sup>2</sup>]

$\gamma_w$ : Unit weight of water [Force/length<sup>3</sup>]

$v$ : Velocity [length /time]

$g$ : Gravitational acceleration [length/time<sup>2</sup>]

The difference in hydraulic head  $\Delta h$  between point a and point b is given by (2-20). Relating this concept to the filtration lines, the hydraulic gradient  $i$  can be expressed by (2-21) considering the flow direction as positive.

$$\Delta h = h_a - h_b \quad (2-20)$$

$$i = \frac{\Delta h}{L} \quad (2-21)$$

Where,

$\Delta h$ : Difference between two hydraulic heads [length]

$i$ : Hydraulic gradient [dimensionless]

### 2.3.3. Coefficient of permeability

The analysis for the experiments in this study was made following the expressions for a falling head permeability test as below:

$$\begin{aligned} q &= -a \frac{\Delta h}{\Delta t} \\ k \frac{h}{L} A &= -a \frac{\Delta h}{\Delta t} \\ - \int_{h_i}^h \frac{1}{h} dh &= \frac{Ak}{aL} \int_{t_i}^t dt \\ \ln \left( \frac{h_i}{h} \right) &= \frac{Ak}{aL} (t - t_i) \end{aligned} \quad (2-22)$$

Where,

$k$ : Coefficient of permeability [length /time]

$A$ : Cross section of the sample [length<sup>2</sup>]

$a$ : Cross section of the water tank [length<sup>2</sup>]

$L$ : Height of the sample [length]

### 2.3.4. Pore volume of water passed

The pore volume index ( $PV$ ) is used for measuring the amount of water applied during the permeability tests, in relation to its void ratio, given by:

$$PV = \frac{\text{Volume of water passed in } \Delta t}{\text{Volume of voids}} \quad (2-23)$$

## 2.4. Hollow cylindrical torsional shear test

### 2.4.1. Formulation of stresses

The hollow cylinder specimen in torsional shear apparatus has four degrees of freedom from the point of view of loads/pressures: axial load ( $F_z$ ), torque ( $T$ ), inner cell pressure ( $P_i$ ) and outer cell pressure ( $P_o$ ). These induce four stresses: radial stress  $\sigma_r$ , circumferential stress  $\sigma_\theta$ , axial stress  $\sigma_z$  and shear stress  $\tau_{z\theta}$ .

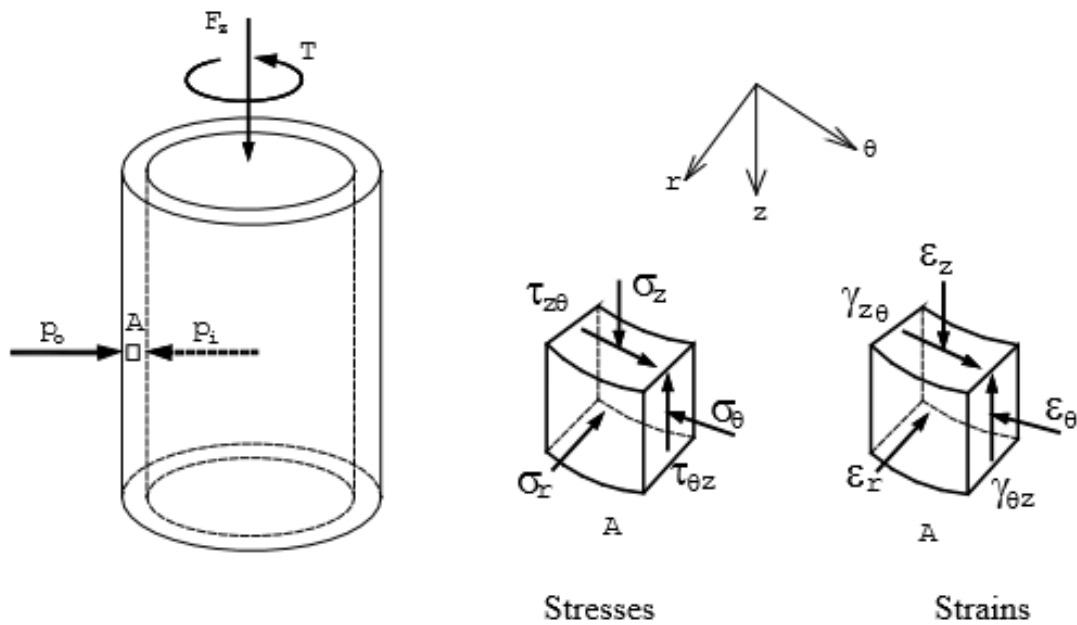


Figure 2-8 Stress and strains in a soil element of a hollow cylindrical specimen

#### a. Axial stress $\sigma_z$ :

The vertical stress considered as an average of the stress at the middle height of the specimen is given by:

$$\bar{\sigma}_z = \frac{LC}{A} + \sigma_h + \sigma_g + \sigma_{mem} \quad (2-24)$$

Where,

$LC$ : Axial load detected by the inner load cell

$A$ : Cross-sectional area of the specimen,  $A = \pi(r_o^2 - r_i^2)$

$r_o$ : Outer radius

$r_i$ : Inner radius

$\sigma_h$ : Horizontal stress,  $\sigma_h = \sigma_r = \sigma_\theta$  (in this study)

$\sigma_g$ : Vertical stress of the specimen due to its self-weight at the middle height,  $\sigma_g = \gamma' H/2$

$H$ : Height of the specimen

$\gamma'$ : Unit weight of soil in water ( $\text{N/cm}^3$ ),  $\gamma' = (G_s - 1)/(1 + e) \cdot \rho_w \cdot g$

$G_s$ : Specific gravity

$e$ : Void ratio

$g$ : Gravitational acceleration ( $9.80665 \text{ m/s}^2$ )

$\rho_w$ : Density of water ( $1\text{g/cm}^3$ )

$\sigma_{mem}$ : Correction for membrane stress, (Tatsuoka et al., 1986)

If  $\varepsilon_z > 0$ ,  $\sigma_{mem} = 0$

$\varepsilon_z < 0$ ,  $\sigma_{mem} = -\frac{3}{8} \varepsilon_z \cdot t_{mem} \cdot \frac{E_{mem}}{(r_o - r_i)}$

$\varepsilon_z$ : Axial strain

$t_{mem}$ : Thickness of the membrane (0.03cm for this study)

$E_{mem}$ : Young's modulus of the membrane (1492.11kPa for this study)

#### b. Radial and circumferential stress $\sigma_r$ and $\sigma_\theta$ :

Considering the hollow cylinder specimen as a uniform material subjected to uniform inner pressure ( $p_i$ ) and outer pressure ( $p_o$ ), the stress distribution is assumed to be symmetrical with respect to the vertical axis ( $z$ ) of the hollow cylinder. The stress components do not depend on radial angle ( $\theta$ ), and are a function of radius ( $r$ ) only (Timoshenko and Goodier, 1970). As a result, shear stress ( $\tau_{r\theta}$ ) equals 0. The equation (2-25) shows the equation of equilibrium in the radial direction.

$$\frac{\delta \sigma_r}{\delta r} + \frac{\sigma_r - \sigma_\theta}{r} + \omega = 0 \quad (2-25)$$

Where,

$\omega$ : Body force. When  $\omega$  equals 0, the following expressions are obtained:



$$\sigma_r = \frac{B}{r^2} + 2C \quad (2-26)$$

$$\sigma_\theta = -\frac{B}{r^2} + 2C \quad (2-27)$$

where B and C are constants. Then, the following expressions are obtained:

$$\sigma_r = \frac{p_0 r_0^2 - p_i r_i^2}{r_0^2 - r_i^2} - \frac{r_i^2 r_0^2 (p_0 - p_i)}{r_0^2 - r_i^2} \cdot \frac{1}{r^2} \quad (2-28)$$

$$\sigma_\theta = \frac{p_0 r_0^2 - p_i r_i^2}{r_0^2 - r_i^2} + \frac{r_i^2 r_0^2 (p_0 - p_i)}{r_0^2 - r_i^2} \cdot \frac{1}{r^2} \quad (2-29)$$

where,

$r_i$ : Inner ratio of the specimen

$r_0$ : Outer ratio of the specimen

Considering the average of the stress components without weighting, the expressions turn as:

$$\overline{\sigma_r} = \frac{p_0 r_0 + p_i r_i}{r_0 + r_i} \quad (2-30)$$

$$\overline{\sigma_\theta} = \frac{p_0 r_0 - p_i r_i}{r_0 - r_i} \quad (2-31)$$

Considering the average of the stress components with weighting, the expressions are:

$$\overline{\sigma_r} = \frac{p_0 r_0^2 - p_i r_i^2}{r_0^2 - r_i^2} - \frac{2 R_i^2 R_0^2 (p_0 - p_i)}{(r_0^2 - r_i^2)^2} \ln \left( \frac{r_0}{r_i} \right) \quad (2-32)$$

$$\overline{\sigma_\theta} = \frac{p_0 r_0^2 - p_i r_i^2}{r_0^2 - r_i^2} + \frac{2 r_i^2 r_0^2 (p_0 - p_i)}{(r_0^2 - r_i^2)^2} \ln \left( \frac{r_0}{r_i} \right) \quad (2-33)$$

In this research, the inner and outer cell pressures are equal ( $p_i = p_0$ ), then:

$$\overline{\sigma_r} = \overline{\sigma_\theta} = p_0 \quad (2-34)$$

c. Shear stress  $\tau_{z\theta}$ :

A shear stress  $\tau_{z\theta}$  acting on a soil element with area  $dA = r d\theta dr$ , is expressed by:

$$dT = \tau_{z\theta} r^2 d\theta dr \quad (2-35)$$

$$T = \int_{R_i}^{R_0} \int_0^{2\pi} \tau_{z\theta} r^2 d\theta dr \quad (2-36)$$

$$T = 2\pi \int_{R_i}^{R_0} \tau_{z\theta} r^2 dr \quad (2-37)$$

In a perfectly plastic material, the expression is as follows:

$$T = 2\pi \tau_{z\theta} \int_{R_i}^{R_0} r^2 dr \quad (2-38)$$

$$T = \frac{2}{3} \pi \tau_{z\theta} (r_0^3 - r_i^3) \quad (2-39)$$

$$T = \frac{3T}{2\pi(r_0^3 - r_i^3)} \quad (2-40)$$

Considering the material as linear elastic, the shear stress distribution is linear in the radial direction. Then, defining  $\tau_{max}$  as the shear stress at  $r = r_0$ , the shear stress at any distance is:

$$\tau_{z\theta} = \frac{\tau_{max}}{r_o} r \quad (2-41)$$

Then the average shear stress  $\overline{\tau_{z\theta}}$  can be expressed as:

$$\overline{\tau_{z\theta}} \int_{R_i}^{R_o} r^2 dr = \int_{R_i}^{R_o} \frac{\tau_{max}}{r_o} r^3 dr \quad (2-42)$$

$$\overline{\tau_{z\theta}} = \frac{3}{4} \frac{\tau_{max}}{r_o} \left( \frac{r_o^4 - r_i^4}{r_o^3 - r_i^3} \right) \quad (2-43)$$

Considering the equivalent shear stress that gives the same shear force as the linearly distributed shear, the average shear stress  $\overline{\tau_{z\theta}^*}$  is:

$$\overline{\tau_{z\theta}^*} = \frac{1}{2} \frac{\tau_{max}}{R_o} (r_o + r_i) \quad (2-44)$$

Comparing the expressions (2-41) and (2-39):

$$\overline{\tau_{z\theta}^*} = \frac{T}{\pi(r_o - r_i)(r_o^2 + r_i^2)} \quad (2-45)$$

Considering the shear stress as an average of equations (2-40) and (2-45):

$$\overline{\tau_{z\theta}} = \frac{1}{2} \left[ \frac{3T}{2\pi(r_o^3 - r_i^3)} + \frac{T}{\pi(r_o - r_i)(r_o^2 + r_i^2)} \right] \quad (2-46)$$

$$T = T_{LC} + T_{mem} \quad (2-47)$$

$$T_{mem} = -2 \cdot \frac{\pi}{3} \cdot t_{mem} \cdot \frac{E_{mem}}{H} \cdot a \cdot (r_o^3 + r_i^3) \quad (2-48)$$

where,

$T_{LC}$ : Torque detected by the inner load cell

$a$ : Angle of rotation detected from potentiometers

$t_{mem}$ : Thickness of the membrane (0.03cm for this study)

$E_{mem}$ : Young's modulus of the membrane (1492.11kPa for this study)

d. Principal stresses:

The three principal stresses are given by:

$$\sigma_1 = \frac{\sigma_z + \sigma_\theta}{2} + \sqrt{\frac{(\sigma_z - \sigma_\theta)^2}{2} + \tau_{z\theta}^2} \quad (2-49)$$

$$\sigma_2 = \sigma_r \quad (2-50)$$

$$\sigma_3 = \frac{\sigma_z + \sigma_\theta}{2} - \sqrt{\frac{(\sigma_z - \sigma_\theta)^2}{2} + \tau_{z\theta}^2} \quad (2-51)$$

#### 2.4.2. Formulation of strains

The corresponding strains: radial strain  $\varepsilon_r$ , circumferential strain  $\varepsilon_\theta$  (Figure 2-9), vertical strain  $\varepsilon_z$ , shear strain  $\gamma_{z\theta}$ , and volumetric strain  $\varepsilon_{vol}$  are given by:

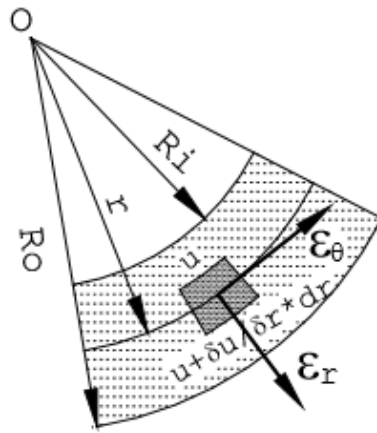


Figure 2-9 Radial and circumferential strains

$$\bar{\varepsilon}_r = -\frac{u_o - u_i}{R_o - R_i} \quad (2-52)$$

$$\bar{\varepsilon}_\theta = -\frac{u_o + u_i}{R_o + R_i} \quad (2-53)$$

$$\bar{\varepsilon}_z = -\frac{\Delta H}{H} \quad (2-54)$$

$$\bar{\gamma}_{z\theta} = \frac{(R_o + R_i)}{2} \cdot \frac{\Delta\theta}{H} \quad (2-55)$$

$$\varepsilon_{vol} = \varepsilon_z + \varepsilon_r + \varepsilon_\theta \quad (2-56)$$

where,

$u_i$ : Displacement in the radial direction at inner radio

$u_o$ : Displacement in the radial direction at outer radio

$R_i$ : Distance from the center of the specimen to the inner radio

$R_o$ : Distance from the center of the specimen to the outer radio

$H$ : Height of the specimen

$\Delta H$ : Height variation

$\Delta\theta$ : Rotation angle

#### 2.4.3. Shear modulus $G$

The Shear modulus ( $G$ ) describes the deformation characteristics of the material to a shear force (Figure 2-10).  $G$  is defined as the ratio of the shear stress to the shear strain (2-57). In this study, the shear modulus is measured by the application of small torsional cyclic loadings. It was calculated in various stages during the tests by 11 cycles of small strain amplitude ( $\gamma_{z\theta} < 0.001\%$ ).

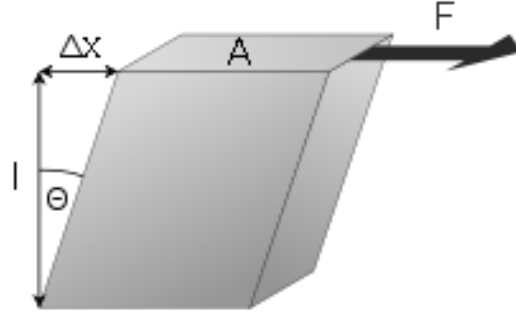


Figure 2-10 Element deformation by a shear force  $F$

$$G = \frac{\tau_{z\theta}}{\gamma_{z\theta}} \quad (2-57)$$

### 2.5. Additional considerations about void ratio

In addition to the basic theories in soil mechanics previously mentioned, some other theories related to the effects of the void ratio, such as the void ratio function and intergranular void ratio and density are considered in this research and introduced below.

#### 2.5.1. Void ratio function $f(e)$

The density varies in the different specimens studied in this research. To isolate the effects of density from the results, a void ratio function  $f(e)$  is used. Although various researchers have suggested void ratio functions to minimize the effects of density, the expression proposed by Hardin and Richart (1963) for a granular geomaterial is widely used than others.

$$f(e) = \frac{(2.17 - e)^2}{1 + e} \quad (2-58)$$

#### 2.5.2. Intergranular void ratio and density

A silty sand is studied in this research. The microstructure of this kind of soil is complex, but can be simplified considering just two submatrices of coarser grains (primary fabric) and finer grains (loose particles). In a material susceptible to suffusion the fines are small enough to

move between the pores of the coarser grains, and then it is possible that the finer grains do not transfer stresses (Thevanayagam, 1998). If the fines do not participate in transferring the forces, the intergranular void ratio  $e_s$  should be considered (2-59); it is defined as the void ratio of the original coarser-grains matrix structure by assuming the fine particles as if they were void space (Mitchell, 1976) (Figure 2-11). Consequently, the intergranular relative density  $D_{rs}$  is expressed by (2-60) (Thevanayagam, 1998).

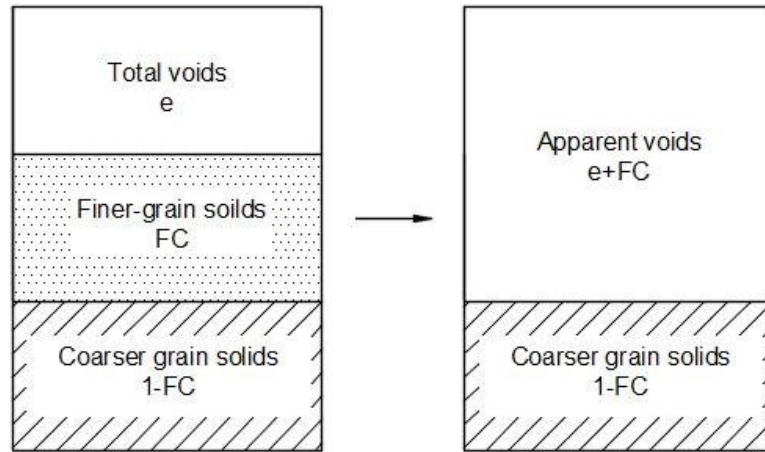


Figure 2-11 Phase diagram of intergranular void ratio

$$e_s = \frac{e + FC/100}{1 - FC/100} \quad (2-59)$$

$$D_{rs} = \frac{e_{max,HS} - e_s}{e_{max,HS} - e_{min,HS}} \quad (2-60)$$

Where,

$e$ : Global void ratio

$FC$ : Fines content

$e_{max,HS}$ : Maximum void ratio of the host sand without any fines

$e_{min,HS}$ : Minimum void ratio of the host sand without any fines

## 2.6. Strength properties

The Mohr-Coulomb equation is the relationship for the characterization of the strength properties most widely used. It states that:

$$\tau_{ff} = c + \sigma_{ff} \tan \varphi \quad (2-61)$$

$$\tau_{ff} = c' + \sigma'_{ff} \tan \varphi' \quad (2-62)$$

where,

$\tau_{ff}$ : Shear stress at failure on the failure plane

$c$ : cohesion intercept

$\sigma_{ff}$ : Normal stress on the failure plane

$\varphi$ : Friction angle

The equation (2-61) refers to the total stress parameters, and the equation (2-62) for the effective stress parameters.

#### 2.6.1. Critical state

For torsional shear tests, the critical state strength can be expressed as:

$$\tau_{CS} = Mp'_{CS} \quad (2-63)$$

where,

$\tau_{CS}$ : Shear stress at critical state

$p'_{CS}$ : Mean effective stress at critical state

$M$ : Critical state stress ratio

## 2.7. References

Bertram, G. E. (1940). An experimental investigation of protective filters. Soil mechanics series No. 7. Cambridge MA: Graduate school of engineering, Harvard University.

Braja M. Das. (1983). Principles of geotechnical engineering. Thomson.

Chapuis, R. P. (1992). Similarity of internal stability criteria for granular soils. Canadian Geotechnical Journal, 29(4), 711 – 713.



Darcy, H. (1856). Les Fontaines Publiques de la Ville de Dijon (The public fountains of the city of Dijon. Dalmont, Paris.

Fannin, R. J. and Moffat, R. A. (2006) Observations on internal stability of cohesionless soils. *Geotechnique*, 56(7).

Fannin, R. J. (2008). Karl Terzaghi: From theory to practice in geotechnical filter design. *Journal of Geotechnical and Geoenvironmental Engineering*, ASCE, 134(3), 267 – 276.

Hardin, B. O., and Richart, F. E. J. (1963). Elastic wave velocities in granular soils. *J. Soils Mechanics and Foundation, Div.*, 89(1), 33 – 65.

Juárez Badillo, E. and Rico Rodríguez, A. (1974). *Mecánica de suelos Tomo 1 Fundamentos de la mecánica de suelos*. Limusa.

Kenney, T. C., Chahal, R., Chiu, E., Ofoegbu, G. I., Omange, G. N., and Ume, C. A. (1985) Controlling constriction sizes of granular filters. *Canadian Geotechnical Journal*, 22(1), 32 – 43.

Kenney, T.C. and Lau, D. (1985). Internal stability of granular filters. *Canadian Geotechnical Journal*, 22, 215 – 225. *Can. Geotech. J.* 45, 1303 – 1309.

Kenney, T.C. and Lau, D. (1986). Internal stability of granular filters: Reply. *Canadian Geotechnical Journal*, 23(3), 420 -423.

Kezdi, A. (1979). *Soil physics: Selected topics*.

Li, M. and Fannin R. J. (2008). Comparison of tow criteria for internal stability of granular soil.

Loebotsjkov, E.A. (1969). The calculation of suffusion properties of noncohesive soils when using the non-suffosion analog. *International Conference on Hydraulic Research*, Brno, Czechoslovakia. Publication of the Technical University of Brno, Svazek B-5, 135-148.

Mitchell, J. K. and Soga, K. (1976). *Fundamentals of soil behavior*, Wiley, New York.

Skempton, A. W. and Brogan, J. M. (1994). Experiments on piping in sandy gravels. *Geotechnique*, 44, No. 3, 449 – 460.

Taylor, H. F., and O'sullivan, C. (2016). Interpreting filtration-based suffusion criteria using micro-computed tomography and laboratory filter tests. *Scour and Erosion – Harris, Whitehouse & Moxon (Eds). 2016 Taylor & Francis Group, London, ISBN 978-1-138-02979-8*, 515 – 521.

Tatsuoka, F., Sakamoto, M., Kawamura, T. and Fukushima, S. (1986). Strength and deformation characteristics of sand in plane strain compression at extremely low pressures. *Soils and foundations* 26, No. 1, 65 – 84.

Terzaghi, K. (1939) Soil mechanics: A new chapter in engineering science. *Journal of the Institution of Civil Engineers*, 12: 106 – 141.

Thevanayagam, S. (1998). *Journal of geotechnical and geoenvironmental engineering*, 124(6), 479 – 491.

Timoshenko, S. and Goodier, J. N. (1970). *Theory of elasticity*.

## Chapter 3. Material, apparatus and testing procedure

In this chapter, materials used for the experimental tests are introduced, as well as the apparatuses and the procedure of the experiments.

Two kinds of experiments are performed in this research: one-dimensional column permeability tests used for obtaining the hydraulic and erosion properties of the tested soils, and hollow cylindrical torsional shear tests used to obtain mechanical properties of the soils. The details about the apparatuses and complementary devices are described below.

### 3.1. Test material

#### 3.1.1. Silica sand No. 5

Silica sand is produced by the degradation of quartz. The quartz crystals are broken into small particles and named as Silica sand. Silica sand No. 5 is used in this research, and the physical properties are shown in Table 3-1. Additionally, images of the grains, and particle size distribution are illustrated in Figure 3-1.

Table 3-1 Properties of Silica sand No. 5	
Property	Value
Specific gravity $G_s$	2.65
Mean particle diameter $D_{50}$	0.55 mm
Maximum void ratio $e_{max}$	1.02
Minimum void ratio $e_{min}$	0.67

### 3.1.2. DL Clay

DL clay is a non-plastic silt that looks yellowish brown. This fine material is used in this research as loose or detached particles. Its properties are listed in Table 3-2. The image and particle size distribution are shown in Figure 3-2.

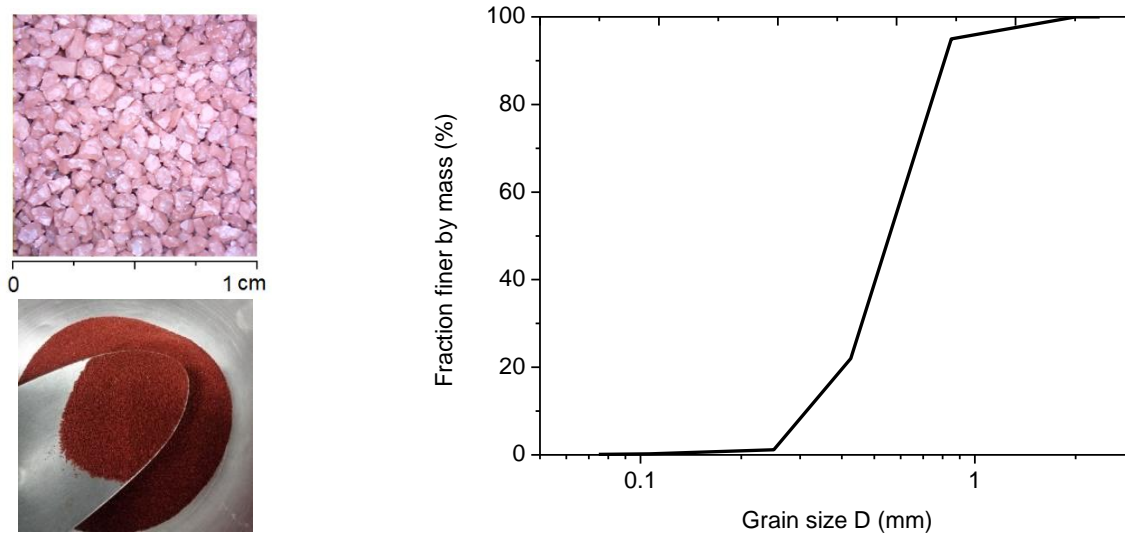


Figure 3-1 Photograph and particle size distribution of Silica sand No. 5

Table 3-2 Properties of DL Clay

Property	Value
Specific gravity $G_s$	2.665
Mean particle diameter $D_{50}$	23 $\mu\text{m}$
Maximum void ratio $e_{max}$	1.29
Minimum void ratio $e_{min}$	0.66

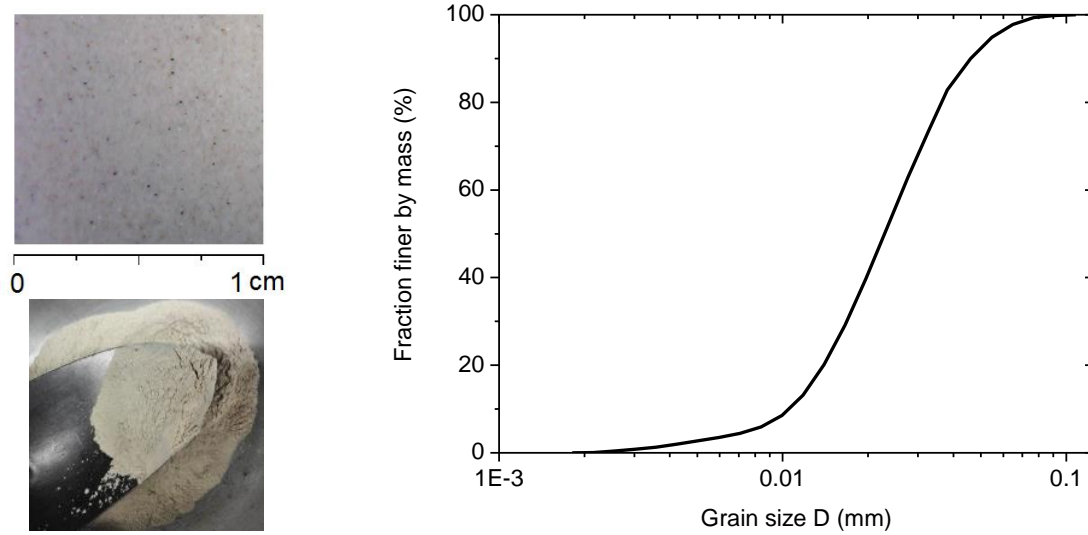


Figure 3-2 Photograph and particle size distribution of DL Clay

### 3.1.3. Mixed Silica Sand and DL Clay

In order to obtain an internally unstable soil as explained in Chapter 2 Basic theories, the two types of soil introduced above are mixed in different proportions following Kenney and Lau (1985) criterion for estimating the percentages of primary fabric and detached particles.

Silica sand is used as a primary fabric ( $f_p$ ), and its grains transmit stresses and remain in the soil matrix after erosion. DL Clay is considered as the detached particles ( $f_1$ ) which are located within the intergranular spaces (pores) made by the primary fabric, and can move freely in the pores through the constrictions. Then the detached particles do not transfer stresses and can be moved easily by the water flow during erosion.

Equations (2-13) and (2-14) are the expressions suggested by Kenney and Lau (1985) for determining the proportion of the coarse and fine particles (by mass), considering the void ratio of the primary fabric ( $e_p$ ) and average porosity ( $n_1$ ). One objective of this research is assessing the behavior of erosion of a soil with various densities (and therefore void ratio and porosity), and then the proportions change with density (Table 3-3).

Table 3-3 Determination of soil proportions according to Kenney and Lau (1985)

Loose soil $D_r \approx 40\%$	Dense soil $D_r \approx 90\%$
$e_p = e_{max,p} = 1.02, n_1 = 0.475$	$e_p = e_{min,p} = 0.67, n_1 = 0.475$
$f_p \geq \frac{1}{1 + e_p(1 - n_1)}$	$f_p \geq \frac{1}{1 + e_p(1 - n_1)}$
$f_p \geq \frac{1}{1 + 1.02(1 - 0.475)} \geq \mathbf{0.35}$	$f_p \geq \frac{1}{1 + 0.67(1 - 0.475)} \geq \mathbf{0.74}$
$f_p + f_1 = 1$	$f_p + f_1 = 1$
$f_1 = \mathbf{0.65}$	$f_1 = \mathbf{0.26}$

As observed in Table 3-3, the fraction of detached particles is smaller for the dense soil. This is consequent with the fact that in a dense specimen coarse grains are closer to each other. Therefore, the pores are smaller and can contain less fines compared to a loose specimen (Figure 3-3).

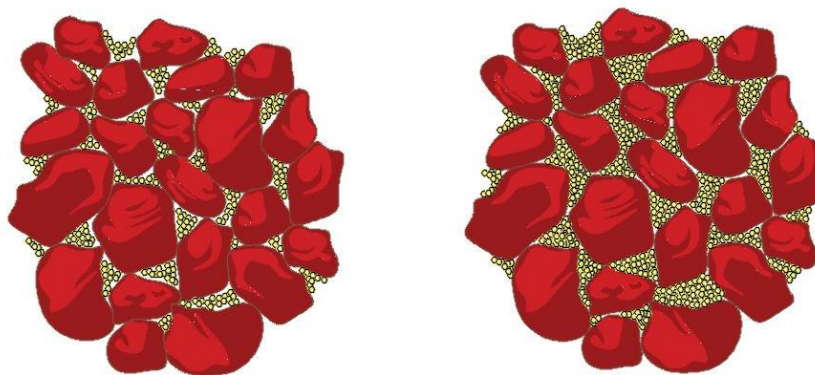


Figure 3-3 Schematic illustration of a dense soil (left) and loose soil (right)

In the dense specimen the size of the constrictions is smaller and hence it is more difficult for the fines to move by the action of seepage. For this reason, the amount of detached

particles in the dense specimens is reduced in order to facilitate the movement and avoid possible clogging of the constrictions.

The proportions of the fabrics used in this study are summarized in (Table 3-4). In addition, experiments in loose specimens with fewer fines were performed in order to compare the results between loose and dense specimens.

Table 3-4 Percentages of mixed Silica sand and DL Clay

Density	Primary fabric (Silica sand)	Detached particles (DL Clay)
Dense soil $D_r \approx 90\%$	80%	20%
Loose soil $D_r \approx 40\%$	65%	35%
Loose soil $D_r \approx 40\%$	80%	20%

The particle size distribution of the mixed soils are shown in Figure 3-4 and Figure 3-5. Figure 3-6 compares the particle size distribution of original and mixed soils.

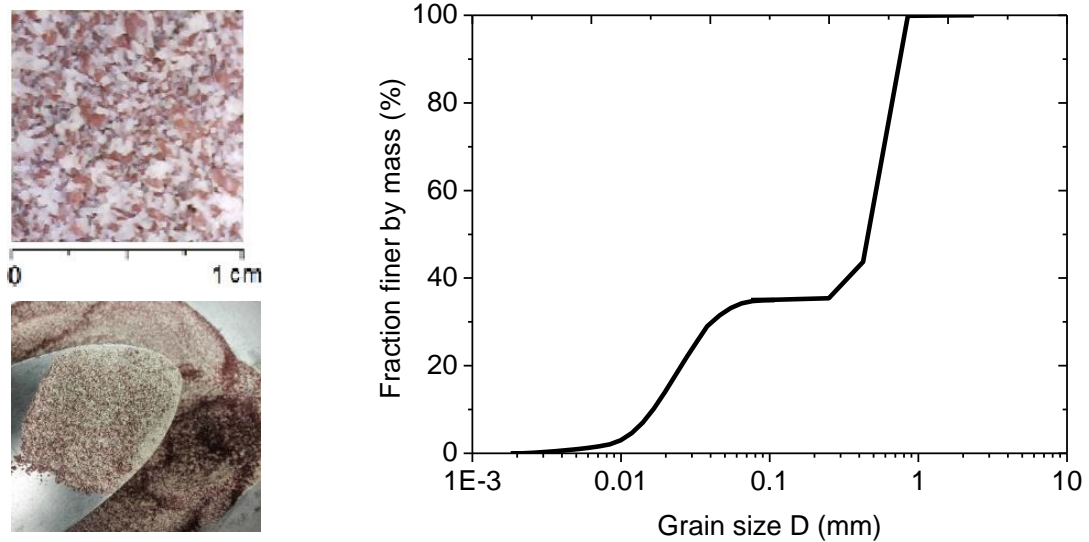


Figure 3-4 Photograph and particle size distribution of mixed Silica sand (65%) and DL Clay (35%)

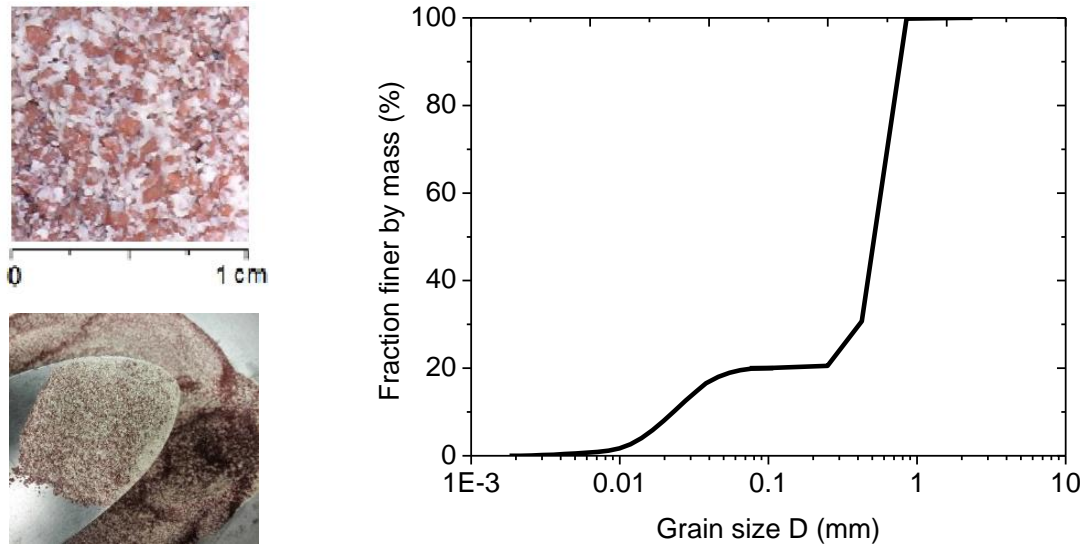


Figure 3-5 Photograph and particle size distribution of mixed Silica sand (80%) and DL Clay (20%)

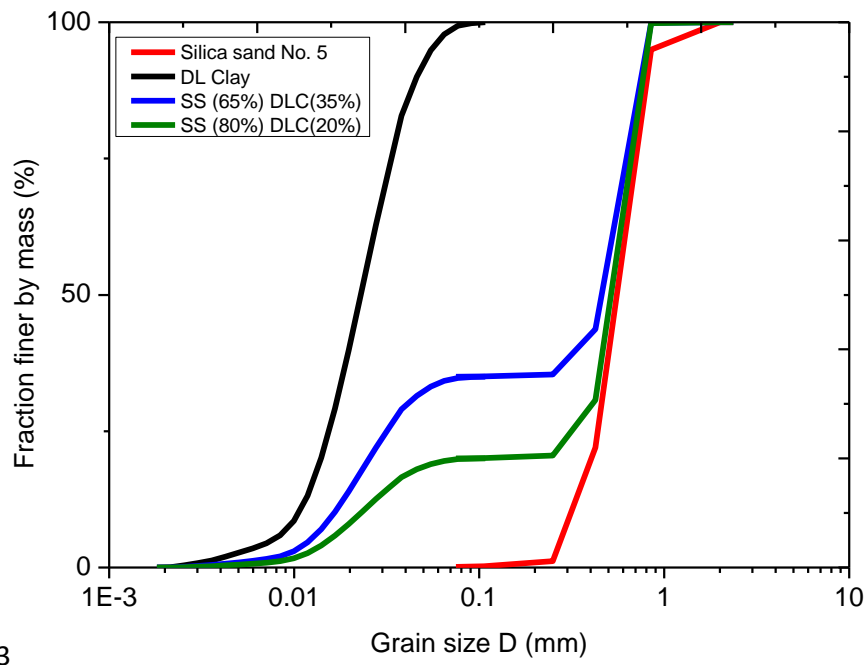


Figure 3-6 Comparison of grain size distribution based on Silica sand No. 5 (SS) and DL Clay (DLC)



Following the Kenney and Lau (1985) criterion, the mixtures with 35% and 20% of fines are both considered as internally unstable, as the curves  $H$  vs.  $F$  lie below the stable line and smaller than the limit for narrowly graded soils (NG) (Figure 3-7) where Silica sand is defined as a narrowly graded soil.

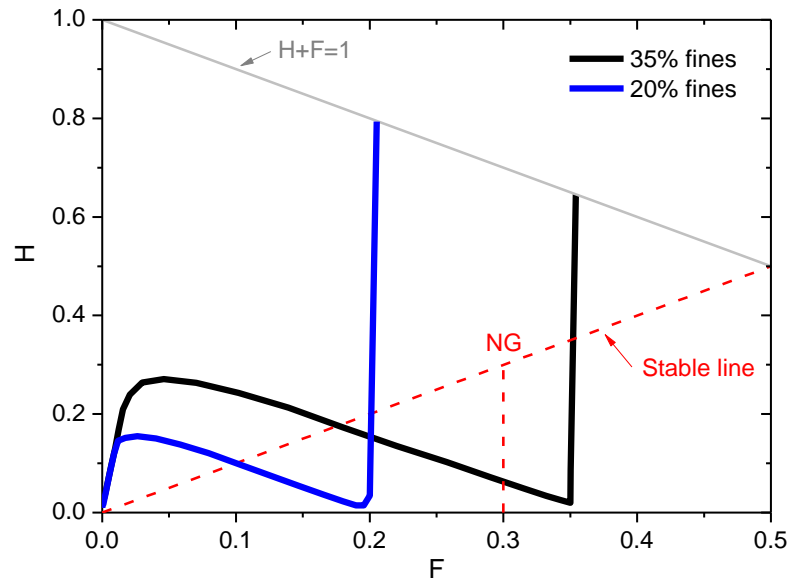


Figure 3-7  $H$  vs.  $F$  curves for mixed soils

The maximum and minimum global void ratios ( $e$ ) change with the variation in volume fraction of detached particles (DL Clay) (Figure 3-8).

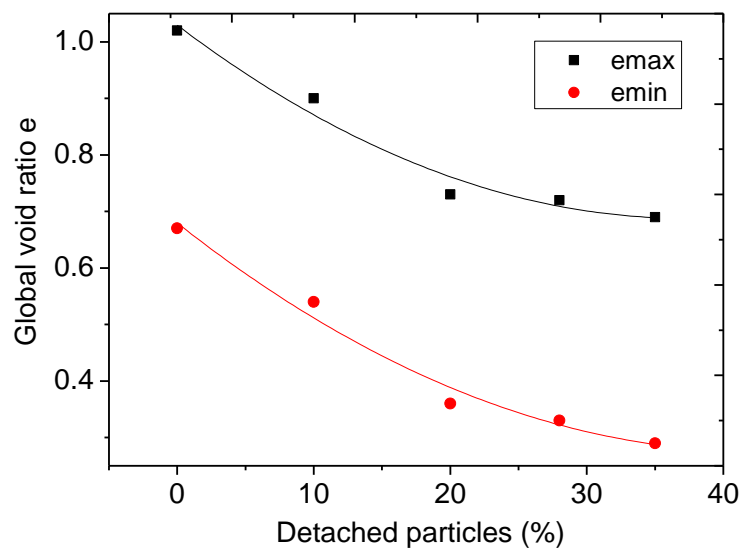


Figure 3-8 Variation of global void ratio with mass fraction of detached particles

### 3.2. One-dimensional column permeability test

Permeability tests are performed to understand the hydraulic characteristics of a soil subjected to erosion. The overall arrangement of the permeameter apparatus is shown in Figure 3-9.

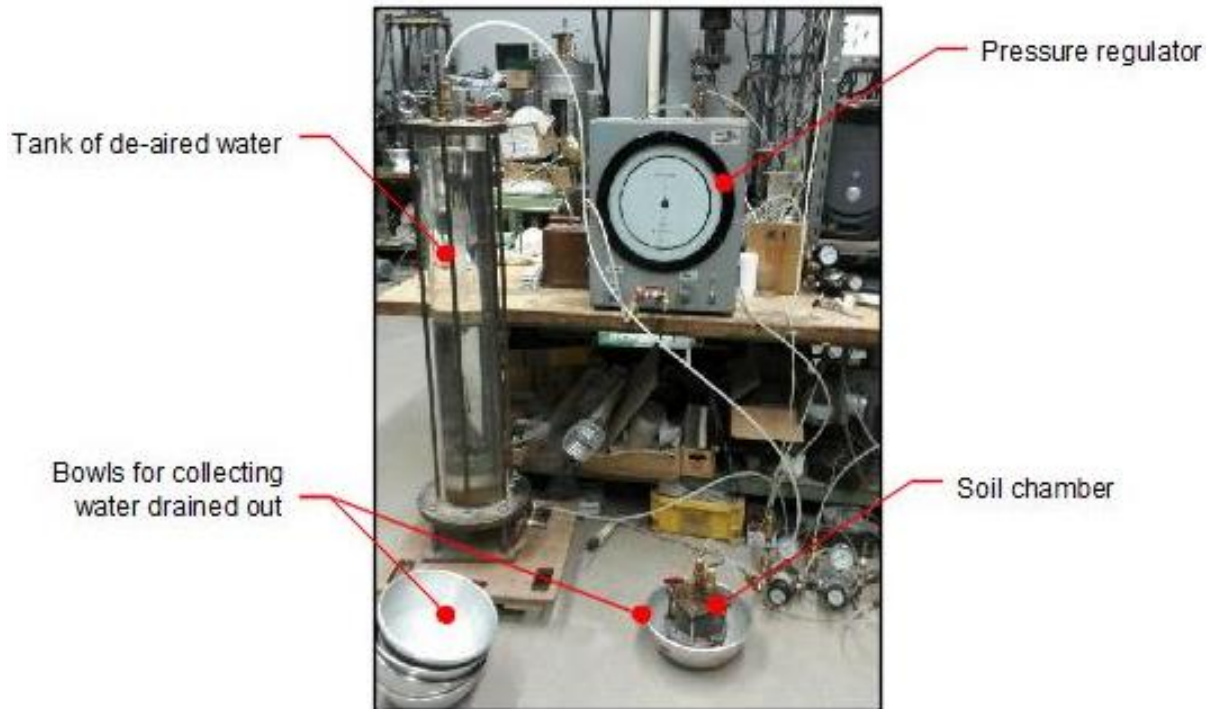


Figure 3-9 Arrangement of permeability apparatus

#### 5.1.1. Test procedure

De-aired water made from distilled water was applied under a prescribed pressure to the top part of a chamber that contains the soil specimen. The bottom plate of the chamber had holes of 5mm in diameter, and gauze was placed over the bottom plate. The purpose of using the open bottom plate was to induce the erosion of the specimen, allowing the fine particles to escape through the holes. The drained water was divided into every 400 cm<sup>3</sup>, and the turbidity of the drained water was measured using a turbidimeter. The collected water was dried in the oven to measure the weight of detached particles eroded from the specimen (Figure 3-10).

The tests were carried out for specimens with various relative densities values (4% to 90%) and two values of fines content (20% and 35%). The water pressure applied to the specimens was kept constant during each experiment. The hydraulic pressure was varied in the tests where the applied water pressure was varied from 25 to 80 kPa for the loose specimens, and from 110 to 220 kPa for the dense specimens.

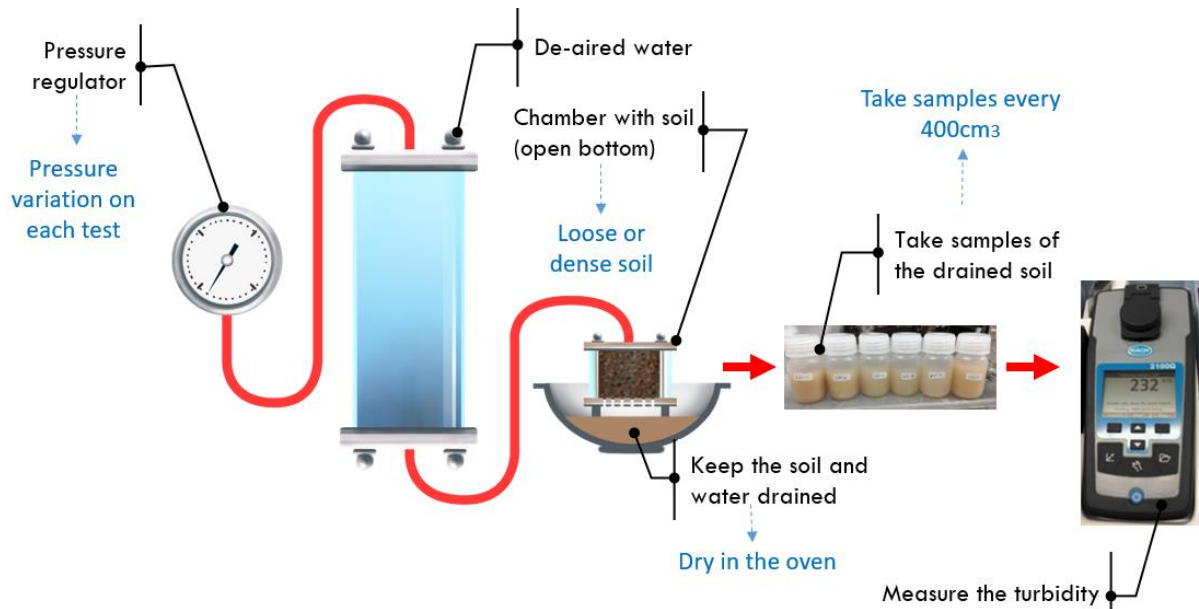


Figure 3-10 Schematic permeability test arrangement

### 3.2.1. Apparatus

#### a. Soil chamber:

A soil chamber with 81 mm in inner diameter and 67 mm in height was used. The thickness of transparent acrylic wall was 20 mm. As mentioned above, the bottom plate had 88 holes of 5 mm in diameter (Figure 3-11). Two layers of gauze with 1 mm of opening are placed over the bottom plate, so that the primary fabric remains in the specimen while the detached particles can escape from it. Additionally, a piece of sponge with 10 mm in thickness was placed over the top of the soil to distribute the water entering to the soil uniformly.



Figure 3-11 Soil chamber with holes on the bottom plate

b. Turbidimeter:

The turbidity refers to the cloudiness of a fluid caused by large numbers of individual particles that are generally invisible to the naked eye, similar to smoke in air. It is expressed in terms of Nephelometric Turbidity Units (NTU), which is calculated based on how much light is reflected for the amount of particles, but it depends on the color, reflectivity and shape.

The apparatus used to measure the turbidity is turbidimeter HACH 2100Q with range from 0 to 1000 NTU (Figure 3-12). The measurement system works as follows: a lamp emits light to a series of lenses to focus the light to the sample; the light reflection is perceived by various light detectors placed in different angles, and the final value displayed is the ratio measurement of all light detectors (HACH company, 2013) (Figure 3-13).



Figure 3-12 Turbidimeter HACH 2100Q and samples used for calibration

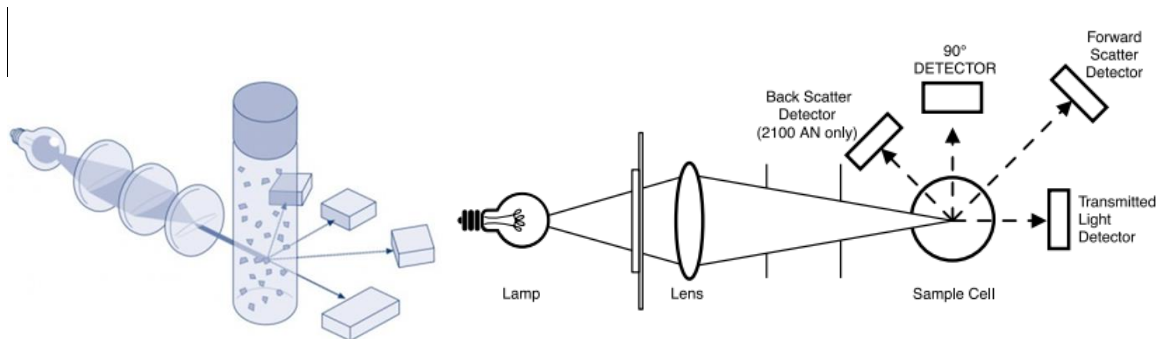


Figure 3-13 Schematic operation of the turbidimeter (HACH company, 2013)

### 3.3. Hollow cylindrical torsional shear test

The hollow cylindrical torsional shear apparatus (Figure 3-14) was used in this study to evaluate the mechanical properties of soil eroded by suffusion.

The tests aim to obtain the properties under varied degrees of erosion: non-eroded, eroded before torsional shearing, and eroded before and during torsional shearing; the variation in

sample density: dense, medium and loose; and the variation in confining stress:  $\sigma_z = \sigma_r = \sigma_\theta = 60\text{kPa}$  and  $\sigma_z = \sigma_r = \sigma_\theta = 150\text{kPa}$ .

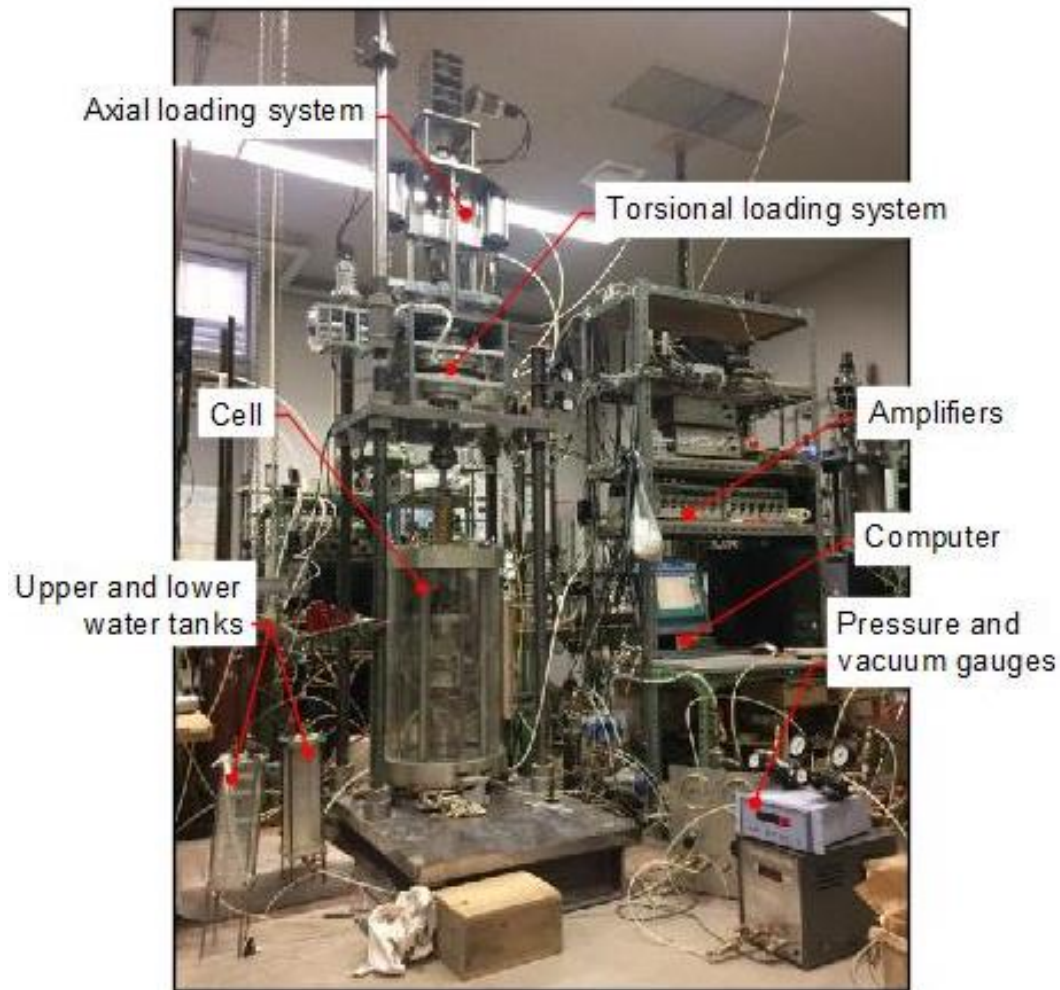


Figure 3-14 Hollow cylindrical torsional shear test apparatus

Transducers and devices used for the hollow cylindrical torsional shear apparatus are shown in Figure 3-15.



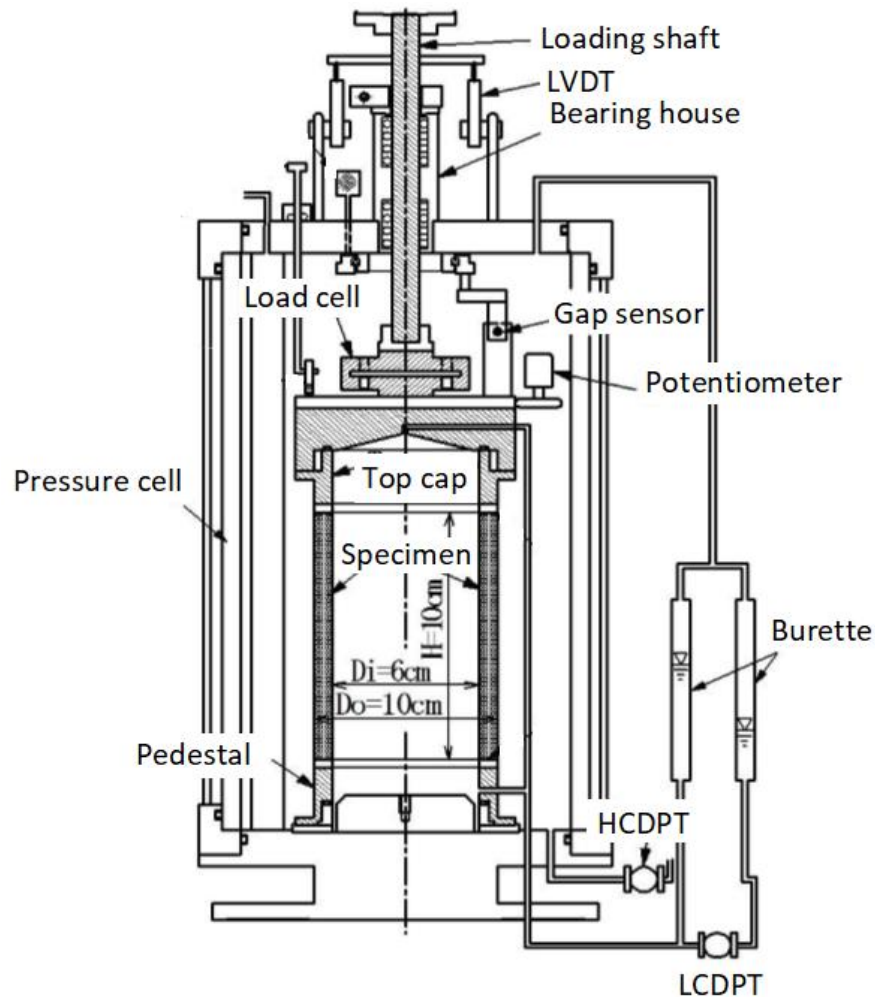


Figure 3-15 Transducers in the torsional apparatus

### 3.3.1. Apparatus

#### a. Specimen dimensions and pedestals

Two special modifications were made to the original apparatus: The reduction of specimen size and a modified pedestal for erosion. The size of the specimen was reduced to achieve the water propagation and erosion in a shorter time. The dimensions of the sample used were 100 mm in height, 100 mm in outer diameter, and 60 mm in inner diameter (Figure 3-16).

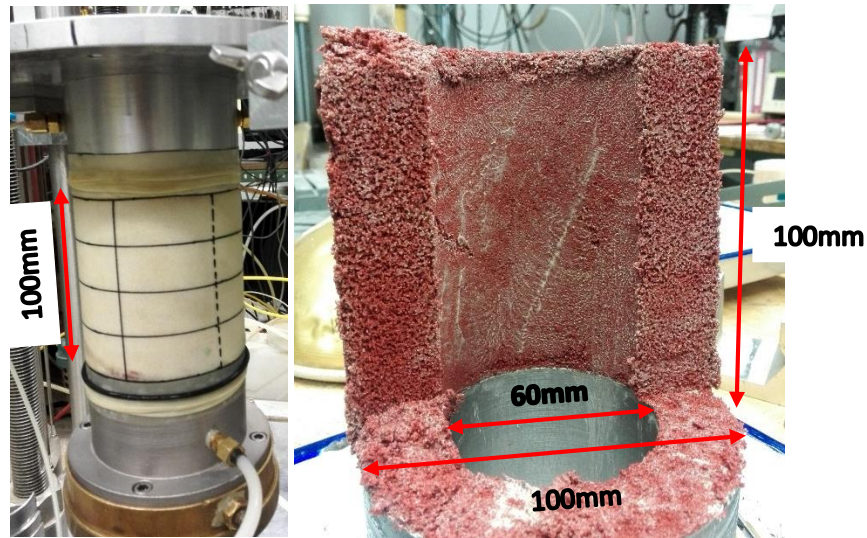


Figure 3-16 Representative dimensions of the specimen

Two types of pedestals were used: a standard pedestal with a porous metal which allows the drainage of water but not soil particles out of the specimen. Due to blades inserted normal to the pedestal frictional force was applied to the soil during the torsional shearing (Figure 3-17 (a)). This pedestal was used for the tests without erosion.

For the tests with erosion, a pedestal having 80 holes with 3mm in diameter was used. Additionally, two layers of gauze with an opening of 1mm were placed over the pedestal surface (Figure 3-17 (b)). This system allows the drainage of water and fine particles, but the coarse grains remain in the specimen.

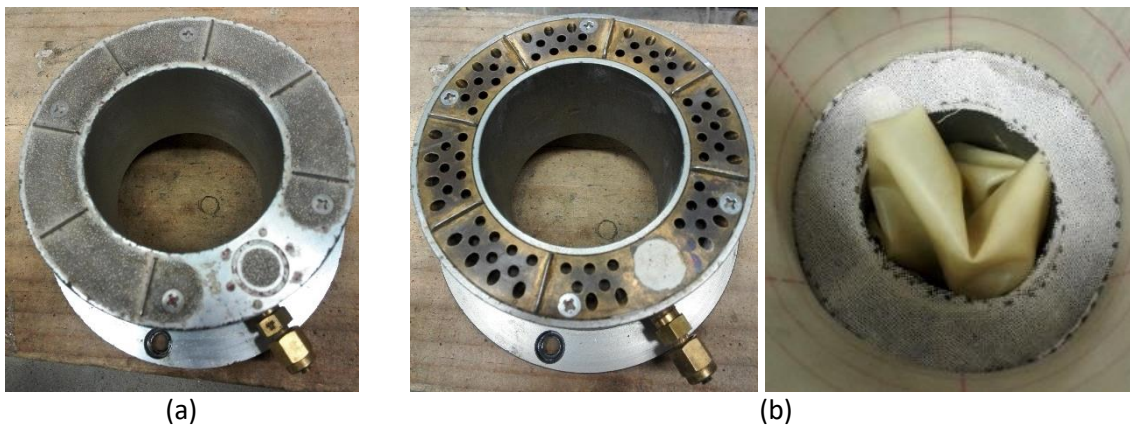


Figure 3-17 Pedestals. (a) For non-eroded tests (b) For eroded tests



### b. Loading systems

The axial loading system for the torsional shear apparatus consists of an AC servo-motor, a reduction gear system with two gears, electromagnetic clutches, brakes, and a ball screw with a pre-pressured nut. The lower gear rotates in the opposite direction from the upper gear.

In the torsional loading system, the torque is transmitted to the loading shaft through a metal band. Both axial and torsional loading systems are designed to have negligible backlashes (Figure 3-18).

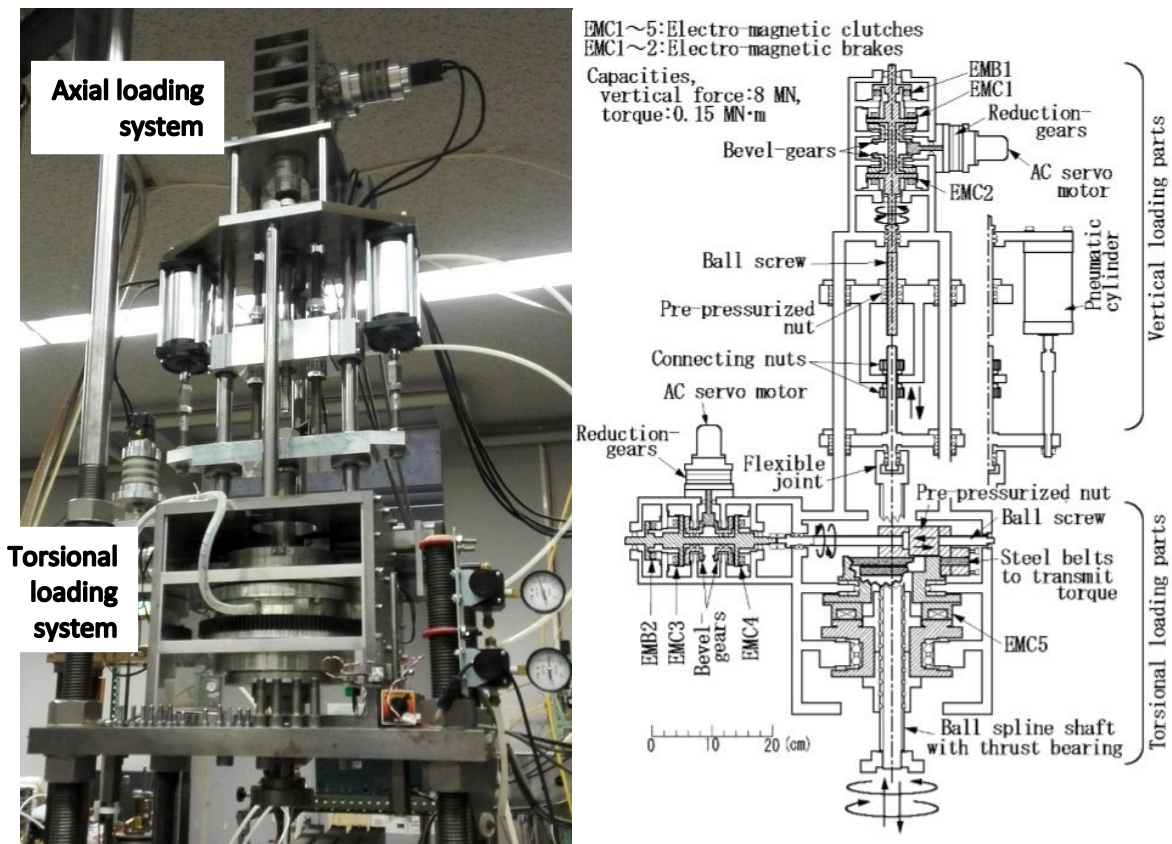


Figure 3-18 Axial and torsional loading systems

### c. Load cell

The two-component load cell (Figure 3-19) has a capacity of 1000 N in axial load and 300 kN.m in torsional load. The axial load and torque are applied simultaneously and

independently on the hollow cylindrical specimen via two servo-motors at constant strain rates. The result of calibration of axial and torsional load is shown in Figure 3-20 and Figure 3-21.

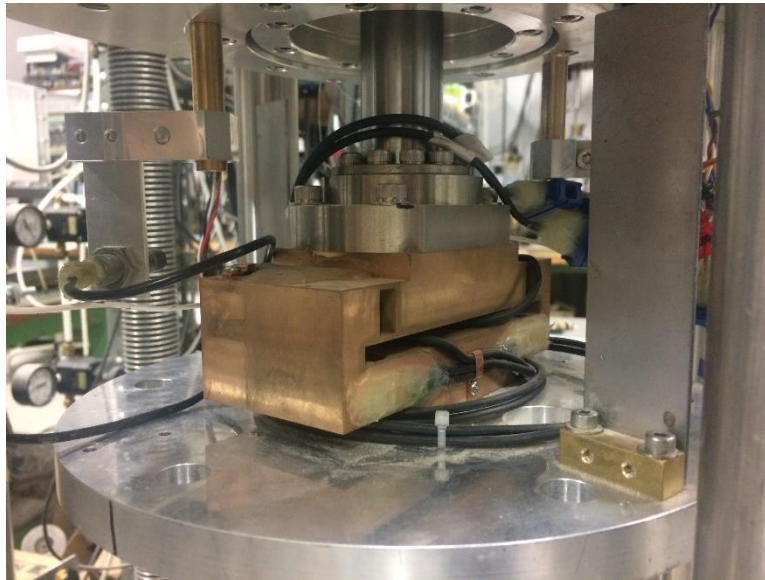


Figure 3-19 Load cell

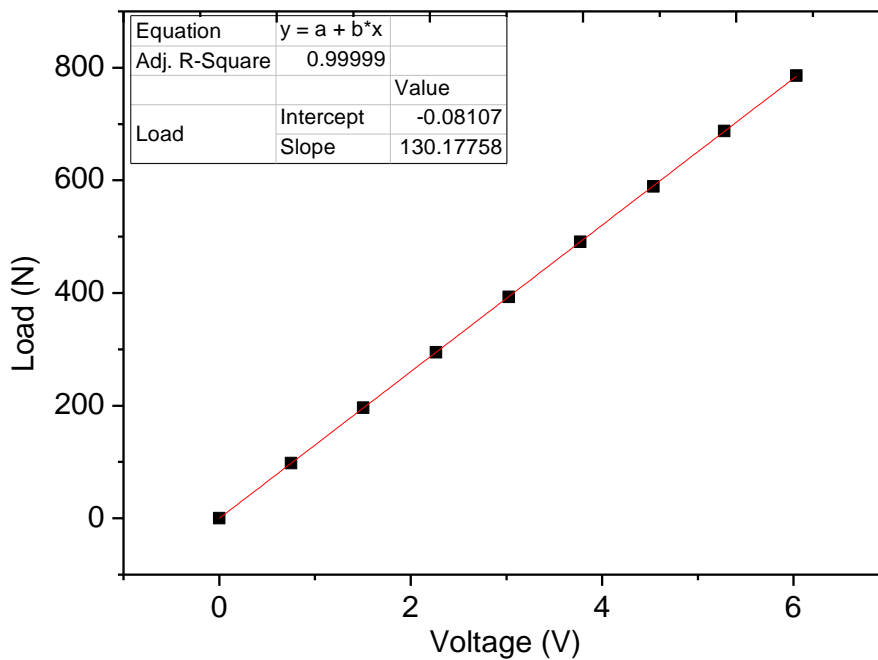


Figure 3-20 Axial load calibration

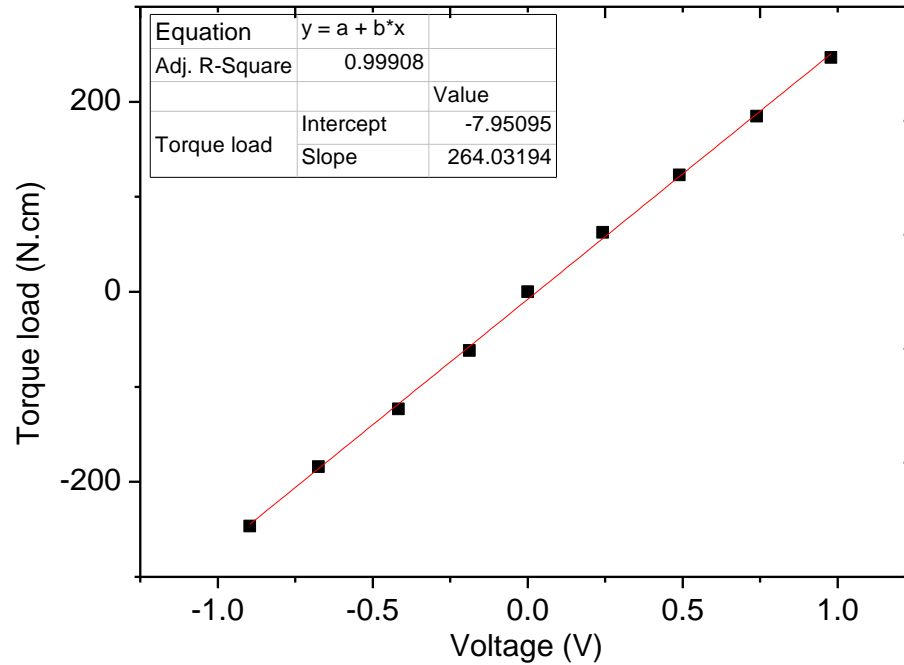


Figure 3-21 Torsional load calibration

d. High Capacity Differential Pressure Transducer (HCDPT)

The High Capacity Differential Pressure Transducer (HCDPT) (Figure 3-22) controls the cell pressure for confining stress. The result of calibration of HCDPT is shown in Figure 3-23.



Figure 3-22 High Capacity Differential Pressure Transducer HCDPT

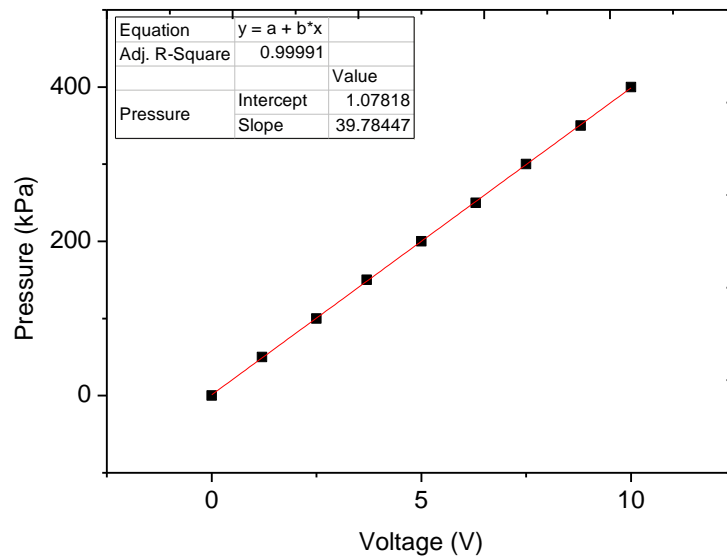


Figure 3-23 HCDPT calibration

e. Low Capacity Differential Pressure Transducer (LCDPT)

The Low Capacity Differential Pressure Transducer (LCDPT) (Figure 3-24) was used for measuring the change in the volume of the inner hollow. The system consists of two burettes with inner diameter of 21.7 mm, one of these was used to measure the volumetric changes ( $65 \text{ cm}^3$  of capacity), and the other was used as reference. The inner hollow was filled with de-aired water and was connected to the LCDPT to measure the change in volume of the inner hollow. At the same time, the cell pressure was connected to the LCDPT so that the same pressure was applied between the inner hollow and the outer part of the specimen. The result of calibration for the LCDPT is shown in Figure 3-25.

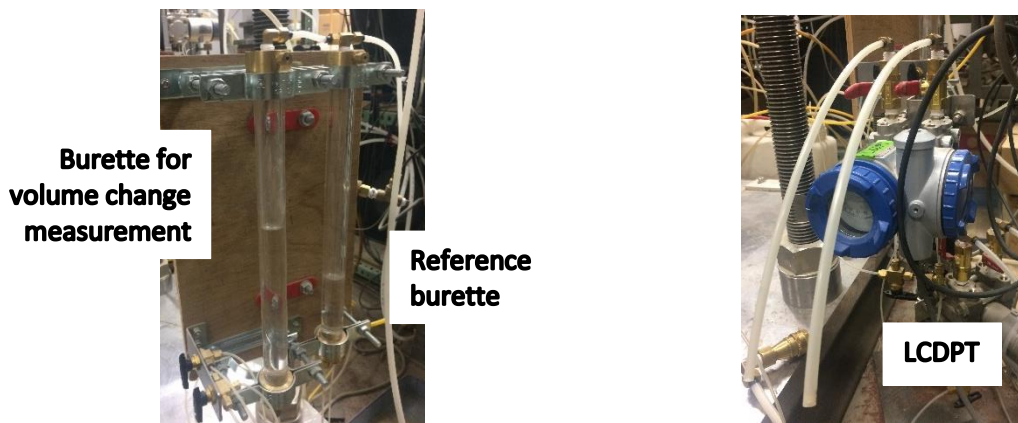


Figure 3-24 Burettes and Low Capacity Differential Pressure Transducer LCDPT

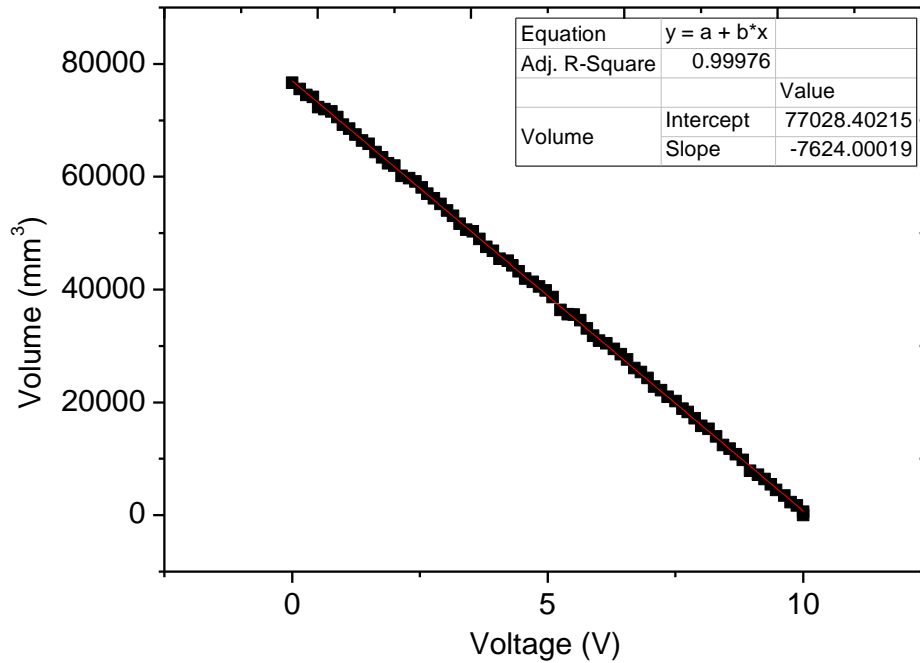


Figure 3-25 LCDPT calibration

f. Linear Variable Differential Transducer (LVDT)

The Linear Variable Differential Transducer (LVDT) (Figure 3-26) was used to measure the axial displacement externally. It consists of a piston which is in contact with a horizontal plate. The result of calibration of the LVDT is illustrated in Figure 3-27.



Figure 3-26 Linear Variable Differential Transducer (LVDT)

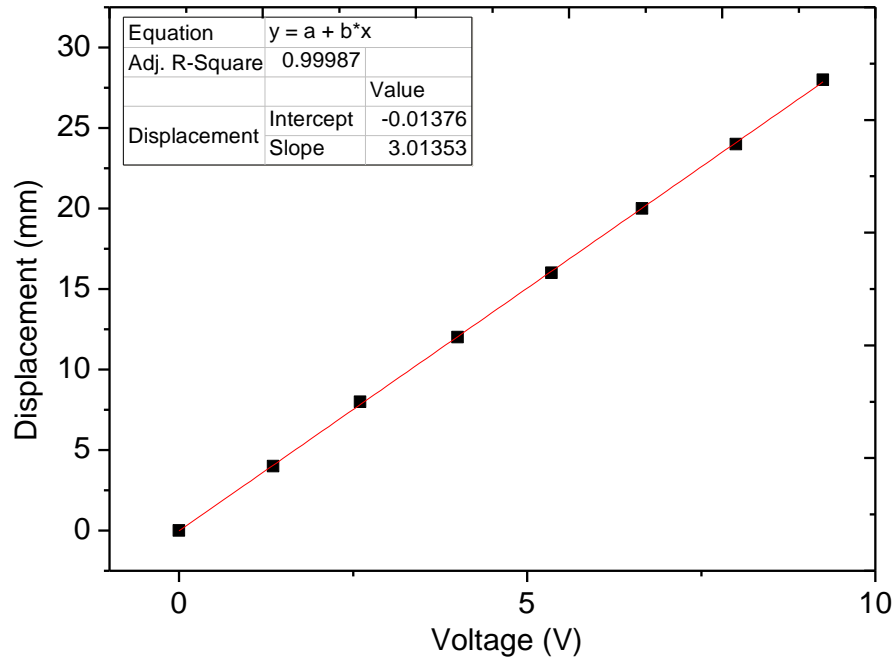
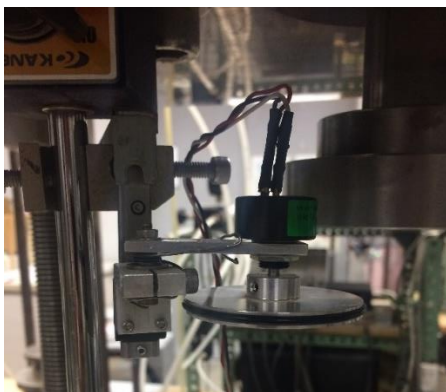


Figure 3-27 Calibration of LVDT

#### g. Potentiometers

Two potentiometers were used to measure the rotation of the top cap, and therefore used to estimate the shear strain level during torsional shearing. A large potentiometer (Figure 3-28 (a)) (POT1) with 50 mm of diameter was attached to the loading shaft outside the cell. A small potentiometer (Figure 3-28 (b)) with 30 mm of diameter (POT2) was attached to the top cap inside the cell. The result of calibration for the large and small potentiometers is shown in Figure 3-29 and Figure 3-30.



(a)



(b)

Figure 3-28 Potentiometers. (a) Large (POT1) (b) Small (POT2)



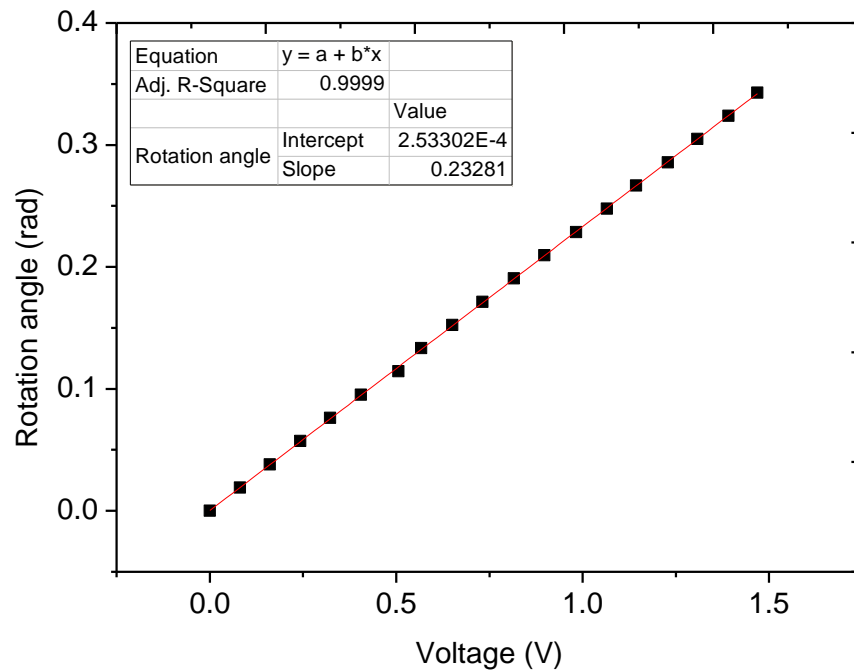


Figure 3-29 Calibration of large potentiometer POT1

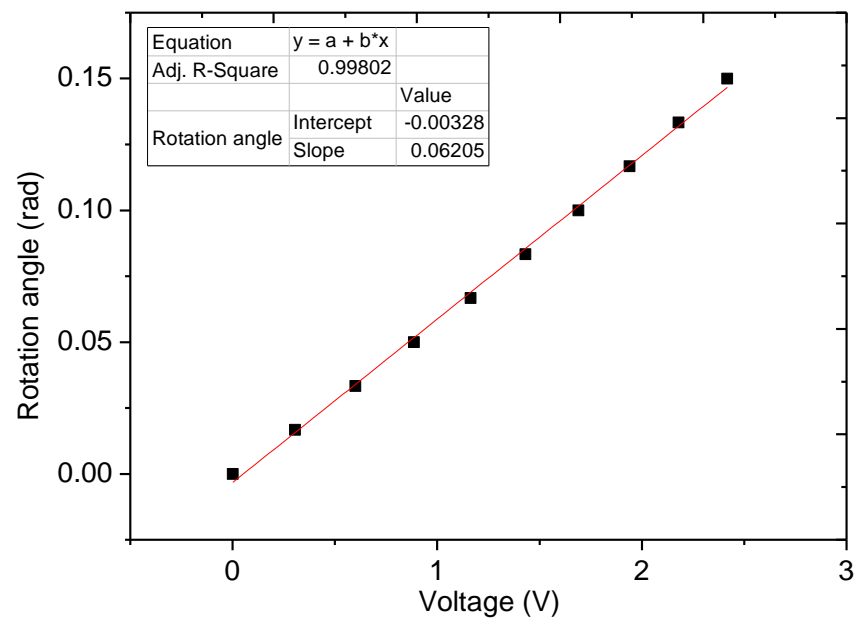


Figure 3-30 Calibration of small potentiometer POT2

#### h. Gap sensors

Two gap sensors were used to measure small torsional displacement, and hence used to estimate the shear strain level during the small torsional cyclic loadings. They were fixed to

the upper part of the cell and can be rotated by a knob from the outside of the cell. The rotation was estimated by the breach between the gap sensor and vertical plates attached to the top cap (Figure 3-31). The result of calibration for the two gap sensors is shown in Figure 3-32 and Figure 3-33.



Figure 3-31 Gap sensor

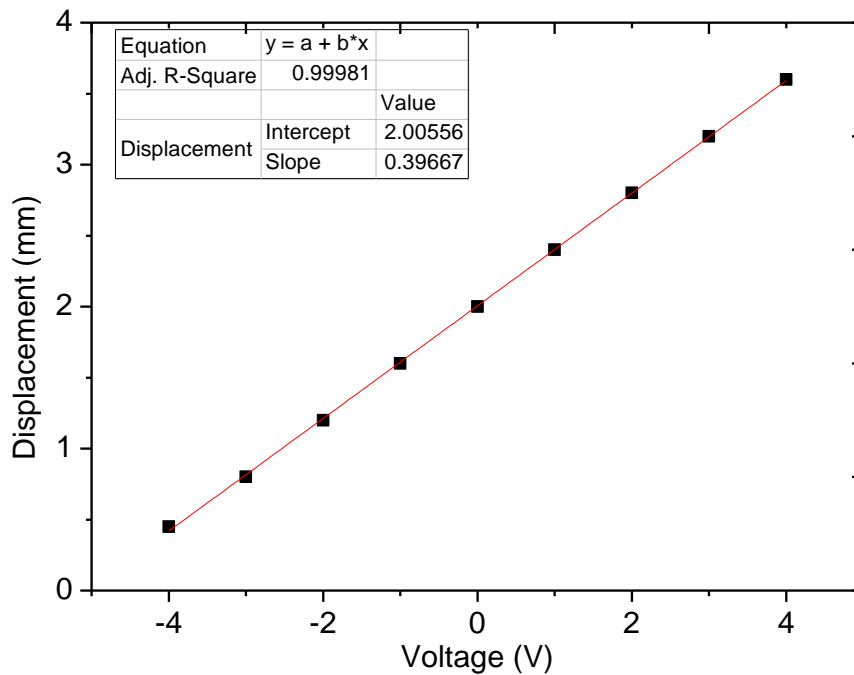


Figure 3-32 Calibration of gap sensor 1



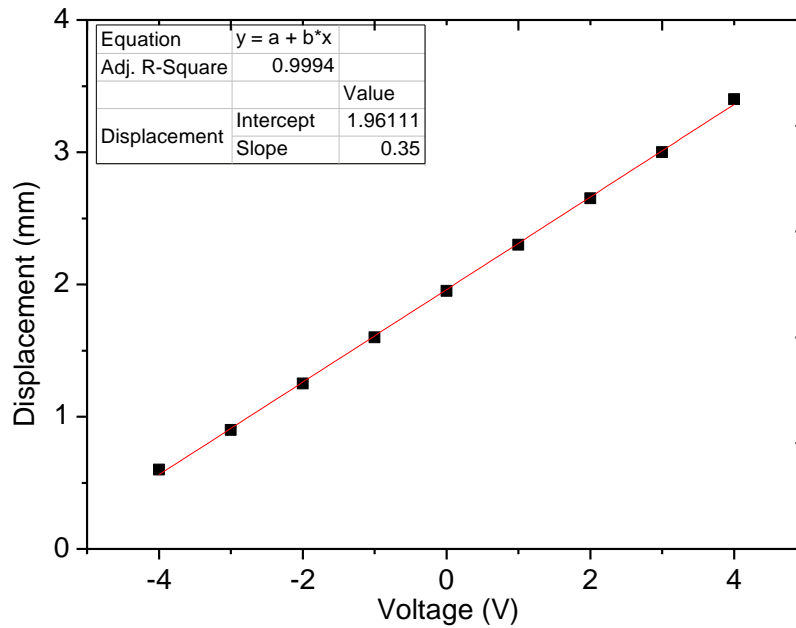
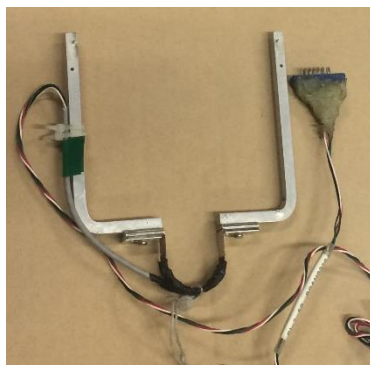


Figure 3-33 Calibration of gap sensor 2

i. Clip gauges

The clip gauges (Figure 3-34 (a)) were used to measure the small deformation of the specimen in the radial direction. The positions of the clip gauges were fixed using a thread hung from the top cap, and attached to the specimen through metal cubes glued to the outer membrane. Three clip gauges recorded the radial deformation at the top, middle and bottom part of the specimen (Figure 3-34 (a)). The result of calibration for the clip gauges is shown in Figure 3-35, Figure 3-36 and Figure 3-37.



(a)



(b)

Figure 3-34 (a) Clip gauge (b) Clip gauges attached to a specimen

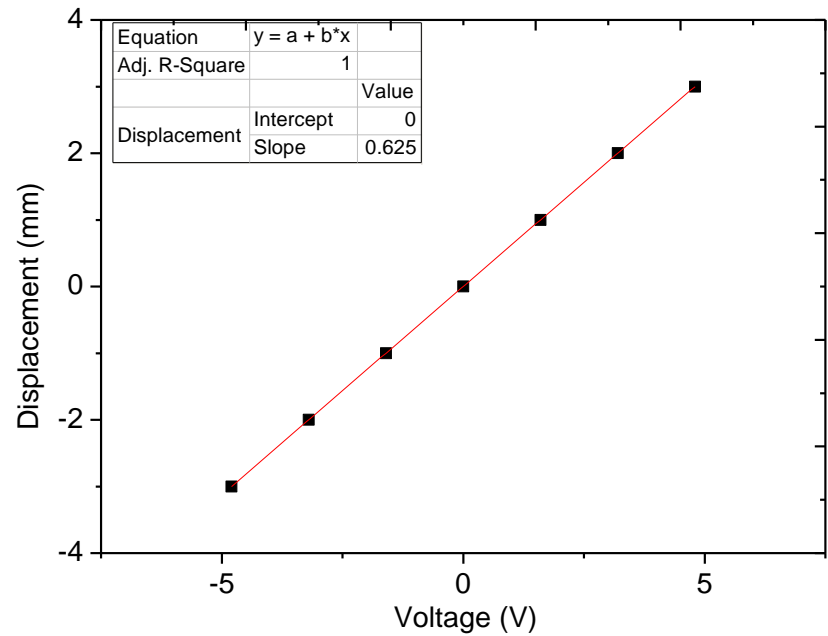


Figure 3-35 Calibration of clip gauge 1

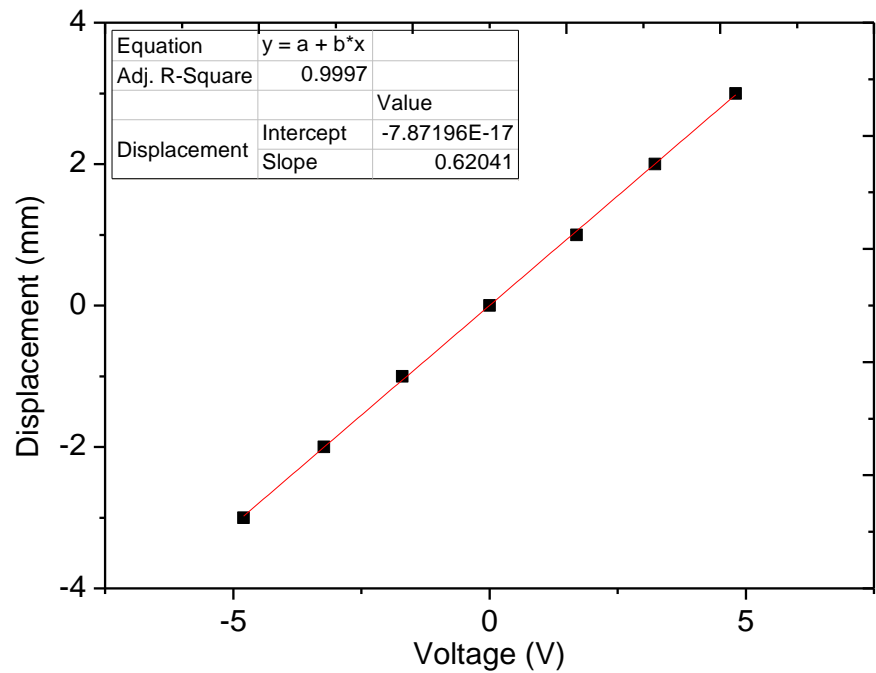


Figure 3-36 Calibration of clip gauge 2

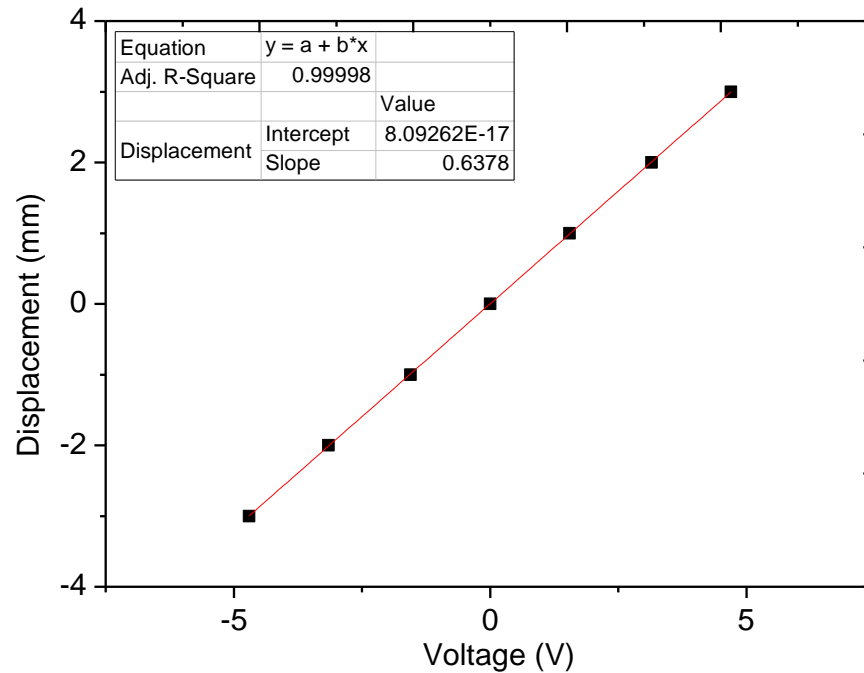


Figure 3-37 Calibration of clip gauge 3

j. Water tanks load cells

Two tanks were connected to the specimen. From the upper tank the water to the top part of the specimen was applied, and the lower tank collected the water drained from the specimen (Figure 3-38). The change in weight of the tanks was measured using two load cells. The result of calibration of the load cells is illustrated in Figure 3-39 and Figure 3-40.

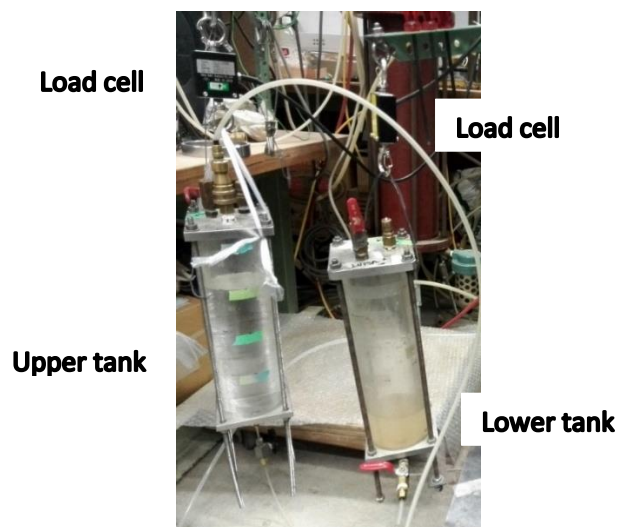


Figure 3-38 Load cells and water tanks

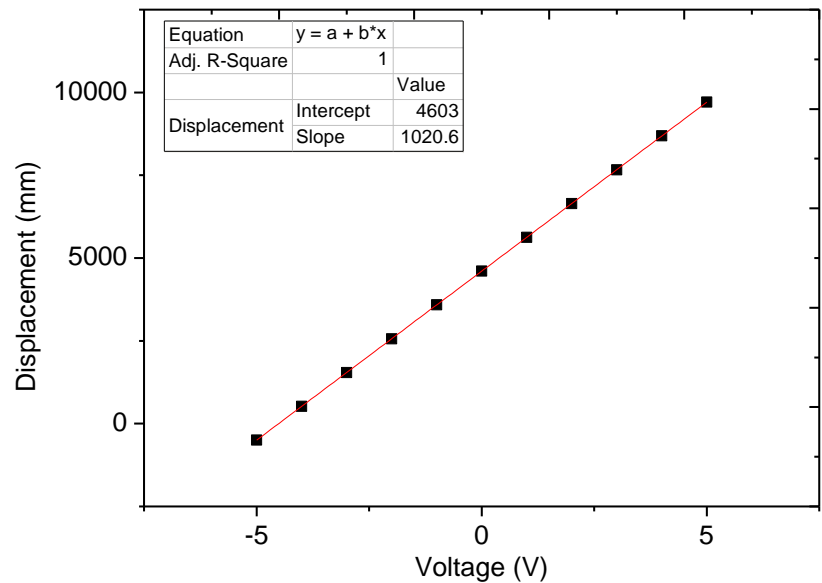


Figure 3-39 Calibration of load cell for upper tank

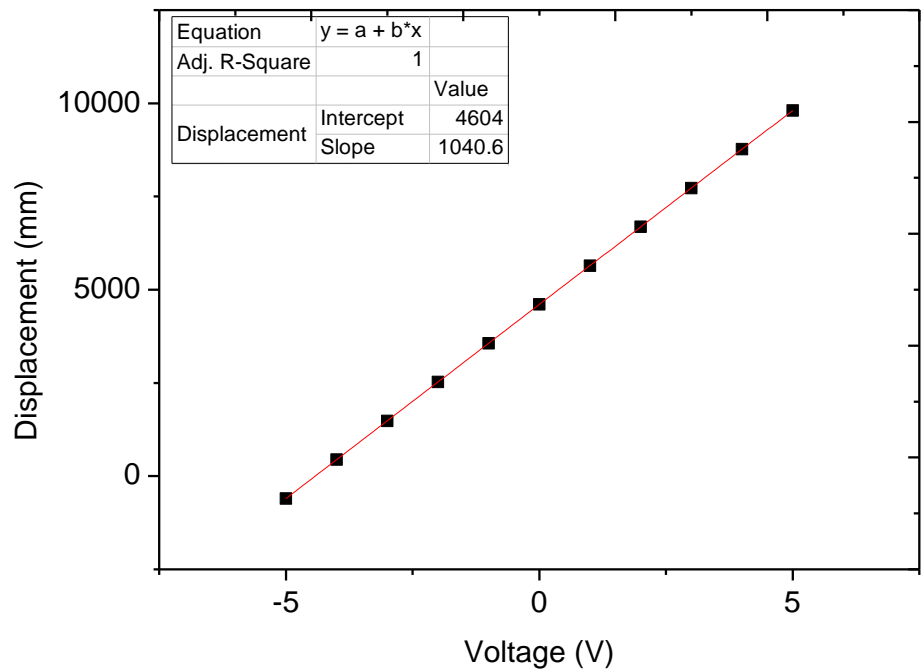


Figure 3-40 Calibration of load cell for lower tank

### k. Amplifiers

Ten amplifiers were used in the experiments (Figure 3-41). These electronic devices increase the voltage of the signals send by all the transducers. The amplifiers show the voltage generated by: axial load cell, torsional load cell, potentiometer 1, potentiometer 2, LVDT, lower tank, upper tank, clip gauge 1, clip gauge 2 and clip gauge 3.



Figure 3-41 Amplifiers

### l. Data acquisition system

The analogue values generated from the amplifiers is sent to the A/D (analog to digital) converter, and then to the computer (Figure 3-42). A servo-control system of the apparatus was operated using a program called DigitShowBasic installed in the computer. The program enables application of desired controls including sampling time, confining pressure, vertical and torsional loads.

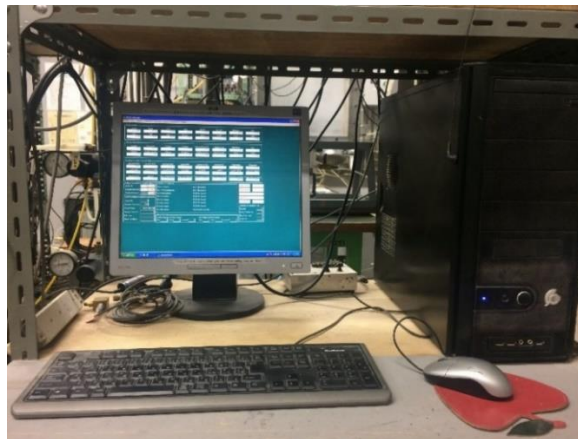


Figure 3-42 Computer

### 3.3.2. Experiment setup

The inner membrane (60 mm in diameter; 0.3 mm in thickness) was placed with application of vacuum grease in an inner ring, and then inserted to the pedestal. The pedestal attached to the base was fixed with four bolts (Figure 3-43).



Figure 3-43 Inner membrane and base pedestal

Grid lines were drawn on the outer membrane to measure the deformation of soils; they also indicate the location of the clip gauges. The membrane was attached to the pedestal with white grease and rubber bands. An O-ring was placed over the membrane to seal the gap fully and apply the vacuum pressure. The outer mold was placed and the membrane was folded at the upper part (Figure 3-44). Vacuum was applied to the gap between the outer mold and the outer membrane to fix the position of membrane.



Figure 3-44 Outer membrane and outer mold

For the test cases with erosion, a pedestal with holes on its surface was used. A piece of gauze with the shape (cross-section) of the specimen section was placed above the pedestal. Then the inner mold was placed (Figure 3-45).

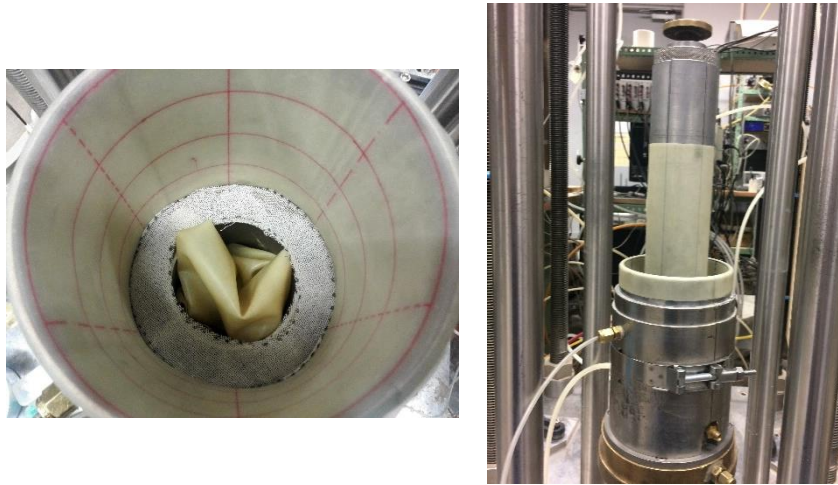


Figure 3-45 Gauze and inner mold

The specimen was prepared by dividing into 12 layers with tamping to achieve the relative density desired. A mold extension was used to compact the upper layers uniformly. The surplus soil was kept in a carton collector after leveling the top part (Figure 3-46).



Figure 3-46 Specimen preparation

The top cap was placed on the top of the specimen through a cantilever hand and counter balance, keeping it normal to the sample surface by adjusting the steel cables. Two clamps



help to locate the top cap just touching the upper part of the specimen but not resting on it. Afterwards, the outer membrane was attached to the top cap and a vacuum pressure of 30 kPa was applied inside the specimen. Then the outer and inner molds were removed (Figure 3-47).

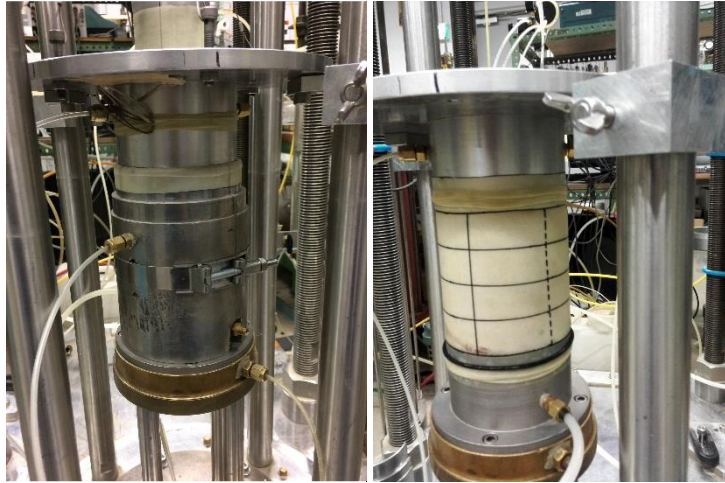


Figure 3-47 Placement of the top cap and removal of the mold

The inner hollow was sealed with a cap that has a pipe opened to let out the air during the posterior filling with water. The outer diameter and height of the sample were measured at several locations (Figure 3-48).



Figure 3-48 Cap for the inner hollow and diameter measurement



The cap for load cell was positioned over the specimen using a pulley and fixed to the poles with four bolts, and to the top cap with six bolts. The clip gauges were attached to the specimen at three different heights (Figure 3-49).



Figure 3-49 Placement of the load cell cap and clip gauges

The small potentiometer POT2 was fixed to one of poles, with the rubber touching the top cap. All the transducers were connected (clip gauges, small potentiometer, vertical and torsional load cells, and gap sensors) and set to zero in the amplifiers and controlling software. Then, the cell was carefully placed using the crane (Figure 3-50).



Figure 3-50 Placement of the cell

The inner hollow was filled with de-aired water applied from bottom to top with 5 kPa of pressure. The burettes of the LCDPT were filled with water till a middle height, and the air inside the system was released. Then, the LCDPT was connected to the inner hollow.

The cell pressure was increased gradually up to 30 kPa while the negative pressure inside the specimen was reduced simultaneously so that the effective stress to the specimen was kept constant (30 kPa).

Afterwards, the effective stress was controlled using the computer, and the pressure applied from the regulator was released. The system was connected to the loading system (Figure 3-51). Finally, the large potentiometer and LVDT were placed, and the test was started and controlled from the computer.

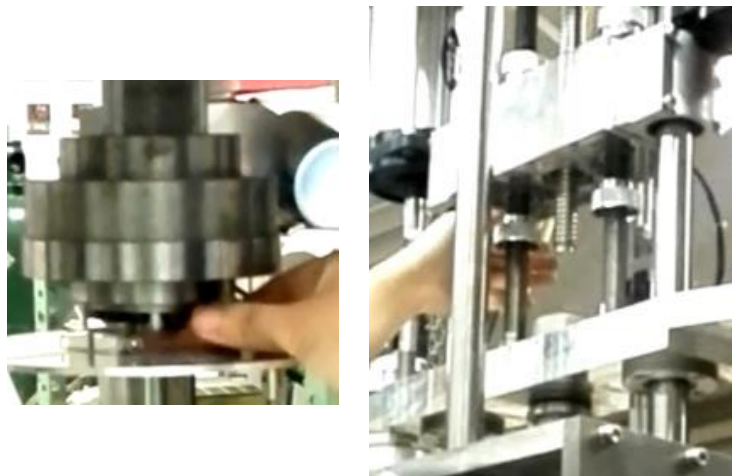


Figure 3-51 Connection to the loading system

### *3.3.3. Test procedure*

Three types of experimental procedures were used for the drained torsional tests: without erosion (using the pedestal with porous metal), with erosion before shearing, and with erosion before and during shearing (using the pedestal with holes), on the specimens with various density values and confined stress levels.

a. Non-eroded test

1. After the setup process, the confining pressure was increased to a certain value (60 kPa or 150 kPa depending on the test cases).
2. After isotropic consolidation for around 12 hours, the first small torsional cycling loading (STCL) was applied in dry state. As mentioned before, the strain values during STCL were measured by the gap sensors; the shear modulus was calculated using the stress-strain responses. A typical result of relationship between  $\tau_{z\theta}$  and  $\gamma_{z\theta}$  during the STCL is illustrated in Figure 3-52. During this step the sampling time was set to 0.2 s to record a large number of data points during 11 cycles of small-strain loading ( $\gamma_{z\theta} < 0.001\%$ ).

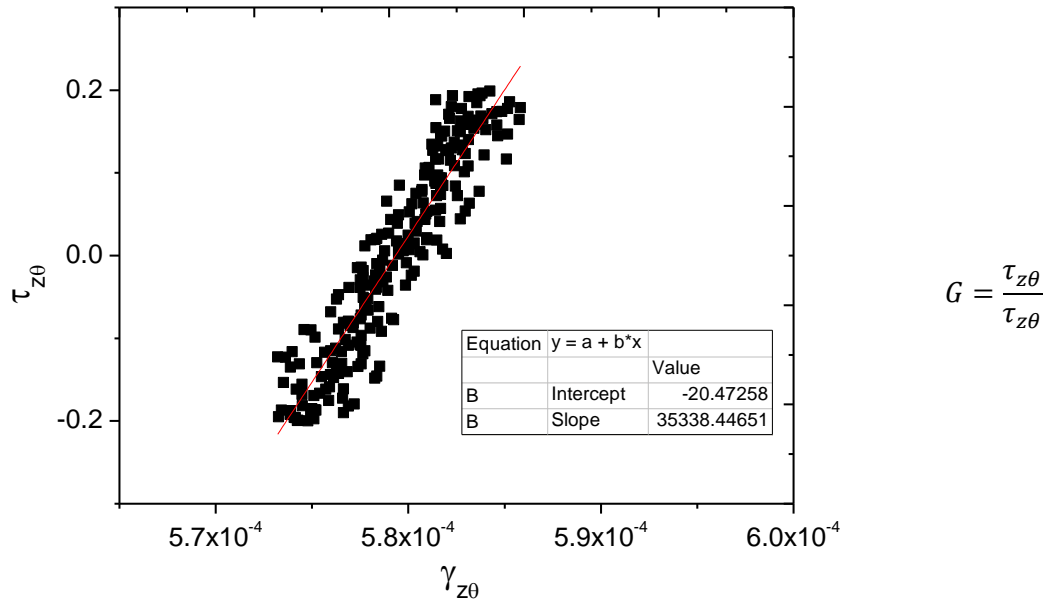


Figure 3-52 Representative results during Small Torsional Cyclic Loadings

3. The specimen was saturated applying water from bottom to top at a low rate.
4. Again, a STCL was applied to the saturated specimen.
5. The drained torsional shearing was applied. Shear strain was applied at a rate of  $\gamma_{z\theta} = 0.1\%/min$  until the shear stress reached 10 kPa.
6. A STCL was applied to the specimen at  $\tau_{z\theta} = 10kPa$ .
7. Steps 5 and 6 were repeated at higher shear stress levels (20, 30, and 40 kPa) (Figure 3-53).

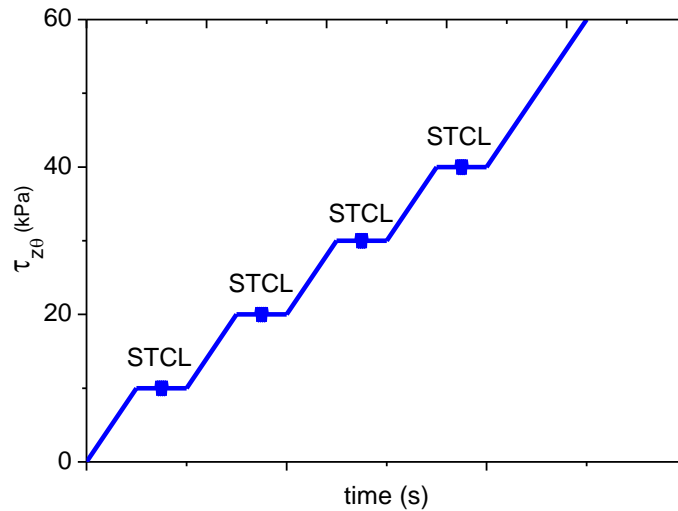


Figure 3-53 Schematic STCL application during monotonic torsional shearing

8. Finally the specimen was sheared till the shear strain reached  $\gamma_{z\theta} = 20\%$ .

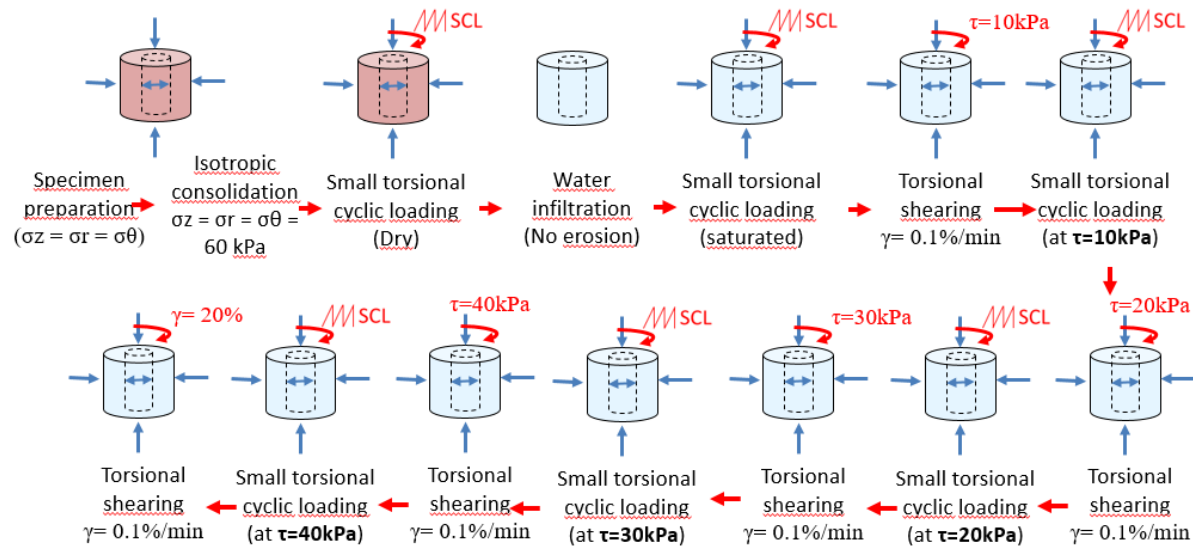


Figure 3-54 Non-eroded test procedure

#### b. Test eroded before shearing

The procedure for a non-eroded test was schematically represented in Figure 3-54. In the tests with erosion the base pedestal with holes on its surface (Figure 3 17) was used. Steps

1 and 2 above were also used for the non-eroded test, and then the erosion process was carried out as below:

1. For the erosion of the specimen, water was applied from the upper tank at 45 kPa of pressure. The water flowed from top to bottom and the drained water and detached particles eroded were kept in the lower tank (Figure 3-55).

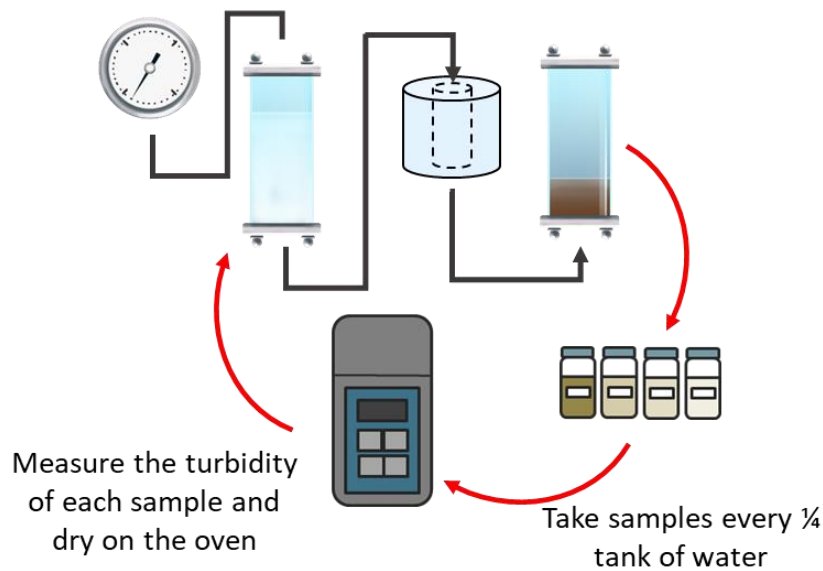


Figure 3-55 Process for erosion in experiments

2. The capacity of the tanks was 1.5 l. When every quarter of tank (375 ml) passed from the upper tank to the lower tank, the inflow was stopped and the water in the lower tank was taken out. The turbidity was measured and the water with fines was dried in the oven to measure the weight of fines eroded.
3. When another 375 ml of water passed through the specimen, step 2 was repeated until the value of the turbidity decreased below 100 NTU. The time spent for this process varied with each test case depending on the density of the specimen. Typically, a time between 5 and 9 hours was spent for the application of 3 to 5 tanks of water.
4. Then the drained torsional shearing test was started following the same procedure as described in step 4 to step 8 for the non-eroded test.

c. Test eroded before and during shearing

The same procedure as step 1 and step 2 for the non-eroded test was followed, as well as step 1 to step 3 for the test eroded before shearing. Only the procedure during shearing was different as below:

1. The erosion process shown in Figure 3-55 was used during shearing at different shear stress levels (10, 20, 30 and 40 kPa).
2. The STCL was applied before and after each erosion process (Figure 3-56).
3. Finally, the specimen was sheared till the shear strain reached  $\gamma_{z\theta} = 20\%$ .

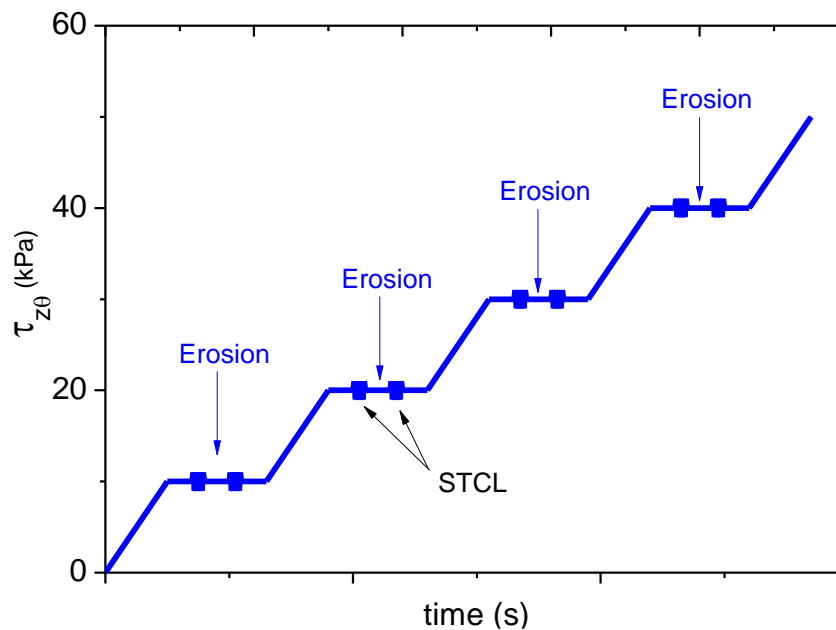


Figure 3-56 Schematic illustration of application of erosion during torsional shearing

### 3.4. References

Hach company. (2013). 2100 Series Laboratory Turbidimeters. LIT2498 Rev 4.

Kenney, T.C. and Lau, D. (1985). Internal stability of granular filters. Canadian Geotechnical Journal, 22, 215 – 225. Can. Geotech. J. 45, 1303 – 1309.

## Chapter 4. Evaluation of suffusion by one dimensional column permeability test

### 4.1. General

The one-dimensional column permeability test enables evaluation of the hydraulic characteristics of an internally unstable soil, and its behavior under the action of suffusion. The experiments performed aim to evaluate the effect of a water flow on the soil considering the variation in the relative density, initial fines content and hydraulic gradient as detailed below:

- Relative density: Loose ( $41\% \leq D_r \leq 50\%$ ) and very dense ( $88\% \leq D_r \leq 90\%$ ) specimens (Table 4-1)
- Initial fines content: Detached particles content of 20% and 35%.
- Hydraulic gradient: For the loose specimens the detached particles are easily removed from the specimen, and therefore the hydraulic gradients are low (25 to 80). In the dense specimens a higher hydraulic gradient is required to erode the fines (110 to 220).

Table 4-1 Soil description for to the relative density (Lambe and Whitman, 1979)

$D_r$ (%)	Description
0 – 15	Very loose
15 – 50	Loose
50 – 70	Moderately dense
70 – 85	Dense
85 - 100	Very dense

A total of 10 tests were carried out. The specifications for the permeability tests are listed in Table 4-2. The results and analysis of these tests are explained below.

Table 4-2 Properties of the permeability tests

Density	% Primary fabric (Silica sand No. 5)	% Detached particles (DL Clay)	$\rho_d$ ( $g/cm^3$ )	$D_r$ (%)	Hydraulic gradient $i$	ID
Loose	65	35	1.58	50	25	L25-35%
			1.55	50	50	L50-35%
			1.56	53	80	L80-35%
Loose	80	20	1.50	41	25	L25-20%
			1.50	42	50	L50-20%
			1.52	46	80	L80-20%
Dense	80	20	1.85	88	110	D110-20%
			1.85	89	150	D150-20%
			1.85	88	190	D190-20%
			1.85	90	220	D220-20%

#### 4.2. Detached particles eroded

Figure 4-1 illustrates the relationship between the amount soil drained and the volume of water passed (expressed in pore volume) for the dense specimens. Around 2% of soil is drained (the initial detached particles content is 20%), and then 18% of fine particles remain inside the specimen. Since the volume of specimen is constant due to the rigid chamber, the



volume of the 2% of drained particles is replaced with water (since it is saturated) (Figure 4-2).

Since the initial relative density of the specimens was around 90%, the particles that are part of the primary fabric were assumed to carry stronger contact forces and closer to each other. A small size of constrictions that restricts the movement of detached particles resulted in a small volume of eroded particles.

Referring to Figure 4-1, the slopes of the eroded particles are steeper in the beginning of the test and turns flatter at a larger volume of water. This means that a larger amount of fines left the matrix with the action of the seepage at the beginning of the tests. Although most of the initial fines remained in the specimen, the rate of erosion decreased drastically mainly because of the clogging of the bottom opening and the obstruction of the constrictions in the primary fabric.

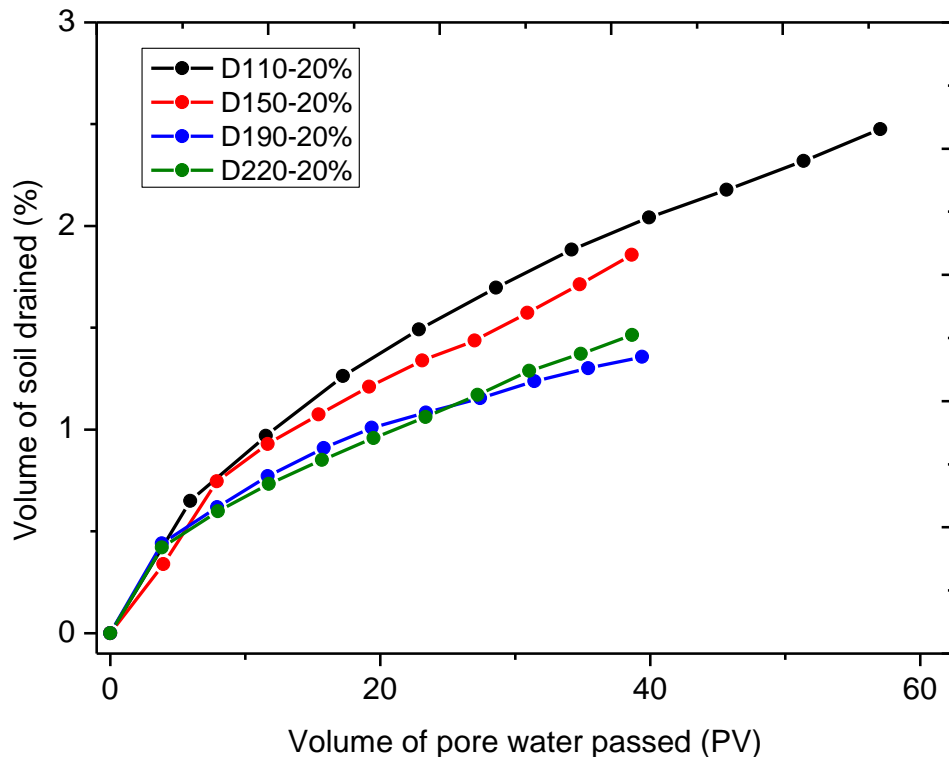


Figure 4-1 Volume of soil drained from dense specimens

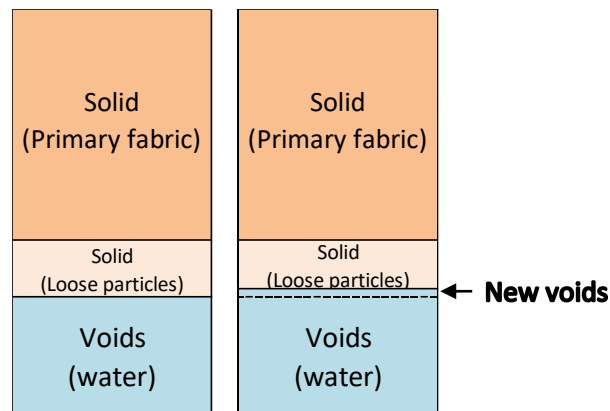


Figure 4-2 Schematic volume distribution in dense specimens. (left) Before (right) After erosion

Additionally, the effect of the hydraulic gradient on the degree of erosion can be appreciated in Figure 4-1. Initially, it was expected that the amount of drained particles increases with the rise of hydraulic gradient; however, the maximum degree of erosion was achieved with the lowest hydraulic gradient examined (D110-20%), and the amount of particles drained were lowered with higher hydraulic gradients (up to  $i = 220$ ). It should be noted that the erosion did not occur with a hydraulic gradient below 110.

A possible explanation to this behavior is that with small hydraulic gradients (below 110) the water flow force is not enough to move the fines, and with very high hydraulic gradients the particles are moved so aggressively that clog the constrictions immediately. Nevertheless, a middle hydraulic gradient moves the particles gently enough to displace them through constrictions without clogging.

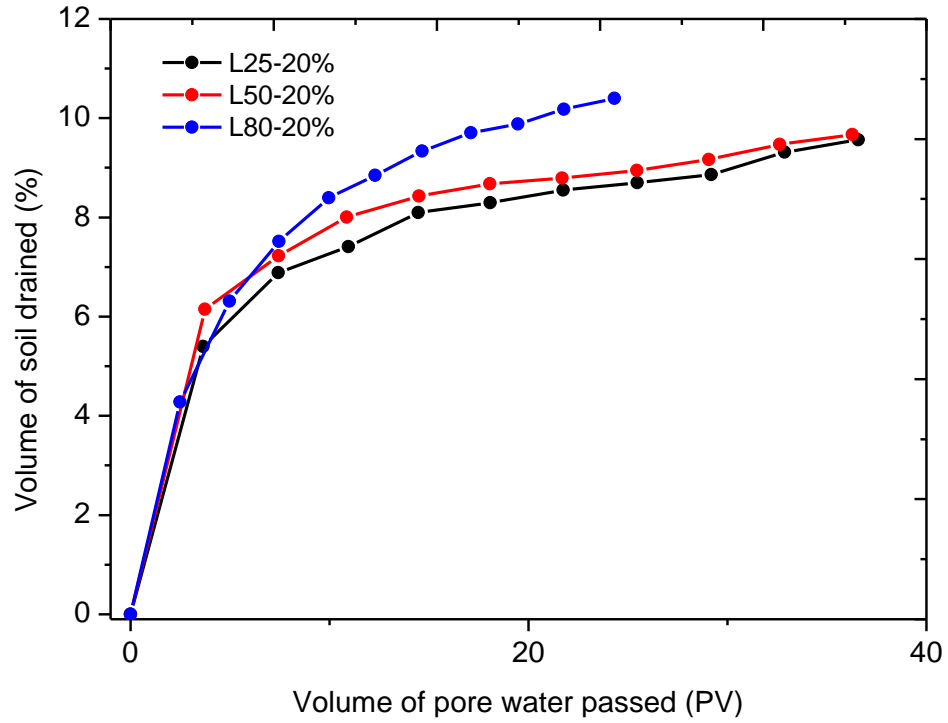


Figure 4-3 Volume of soil drained from loose specimens with 20% of initial content of detached particles

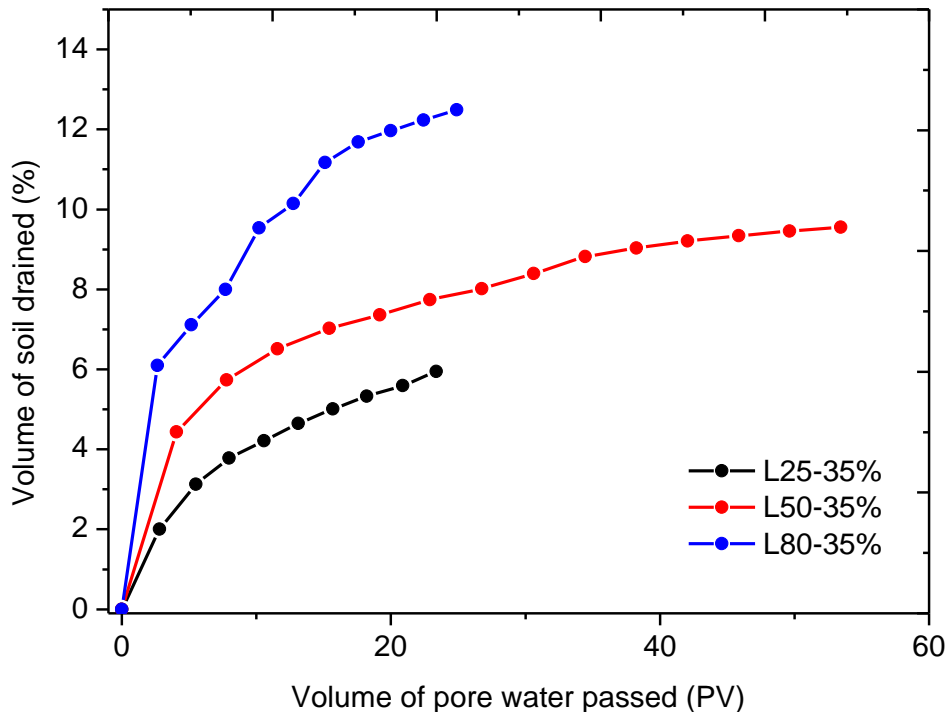


Figure 4-4 Volume soil drained from loose specimens with 35% of initial content of detached particles

Figure 4-3 and Figure 4-4 show the amount of drained soil from the loose specimens. The maximum amount of soil eroded is around 10% and 12% for the specimens with initial fines content of 20% and 35%, respectively.

Figure 4-5 shows two specimens after finishing the test. As it can be observed, the amount of fines (white particles) is lower in the loose specimen, compared to the dense one.



Figure 4-5 Specimens after erosion: Dense specimen (left) Loose specimen (right)

The percentage of eroded soil for the loose samples is greater than that for the dense specimens due to the larger size of constrictions in a loose specimen, which results in a greater final volume of voids (Figure 4-6). Although a greater percentage of eroded particles is observed in the specimens with higher initial fines content, a lower degree of erosion, 34% and 50% of the total fines, is moved out from specimens with initial fines content of 35% and 20%, respectively (Table 4-3).

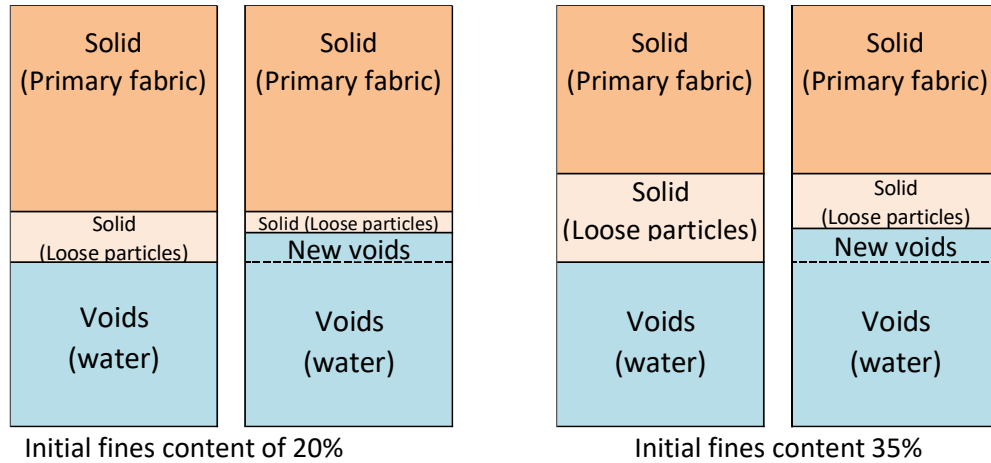


Figure 4-6 Schematic volume distribution in Loose specimens. (left) Before erosion  
(right) After erosion

Table 4-3 Percentage of soil eroded

% Primary fabric (Silica sand No. 5)	% Detached particles (DL Clay)	Maximum volume eroded / the total soil (%)	Maximum volume eroded / the fines fraction (%)
65	35	12	34
80	20	10	50

In these specimens, erosion is achieved at lower hydraulic gradients (from 25 to 80); however, compared to the dense specimens, an opposite behavior is observed: The higher the gradient becomes, the greater the erosion takes place. Since the size of the constrictions is greater the fines can move between pores easier without clogging, and this action is enhanced with a greater force of water.

It is also noted that the trend in the specimen with initial fines content of 20% (Figure 4-3) is more consistent than that with initial fines content of 35% (Figure 4-4) in which there is a considerable difference in the results at different hydraulic gradients. This behavior shows that the fines content influences the size of the pores and constrictions: A greater amount of fines located in the intergranular space makes greater constrictions and hence the influence of the hydraulic gradient is more noticeable.

Figure 4-7 compares the loose tests, which have similar density and hydraulic gradient applied, but different fines content.

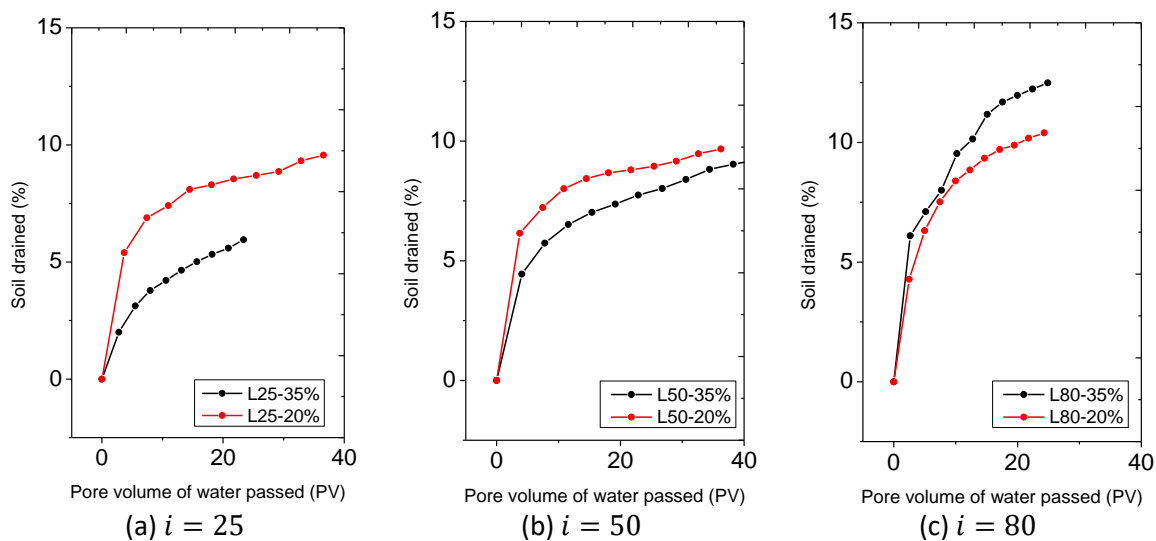


Figure 4-7 Comparison of the volume of soil eroded in the loose specimens

Referring to Figures 4-7(a) and 4-7(b) (hydraulic gradient of 25 and 50), the specimens with 20% of initial fines content exhibit a greater erosion than the specimens with 35%, whilst the opposite trend is observed in Figures 4-7(c) for a higher hydraulic gradient of 80.

There is a threshold value of the hydraulic gradient at which the trend of erosion degree differs. When the force of the seepage is low, the particles can be moved easily if there is less initial amount of fines (because there is more separation between the fabric particles

and therefore weaker contact force. In contrast, at higher hydraulic gradients, the degree of erosion is governed by the force of water but not by the connectivity between particles.

This trend is also observed in Figure 4-8. Each data point represents the maximum percentage of soil eroded in each test case. The blue and red lines are the results of the loose tests; the specimens with larger initial fines content gives a steeper curve, while the specimens with less fines show a flatter curve. Then, the initial fines content influences the response in terms of erosion. It is also noted that in the dense specimens, even though very high gradients were applied, the degree of erosion is low and decreasing with the rise of hydraulic gradient (Black curve).

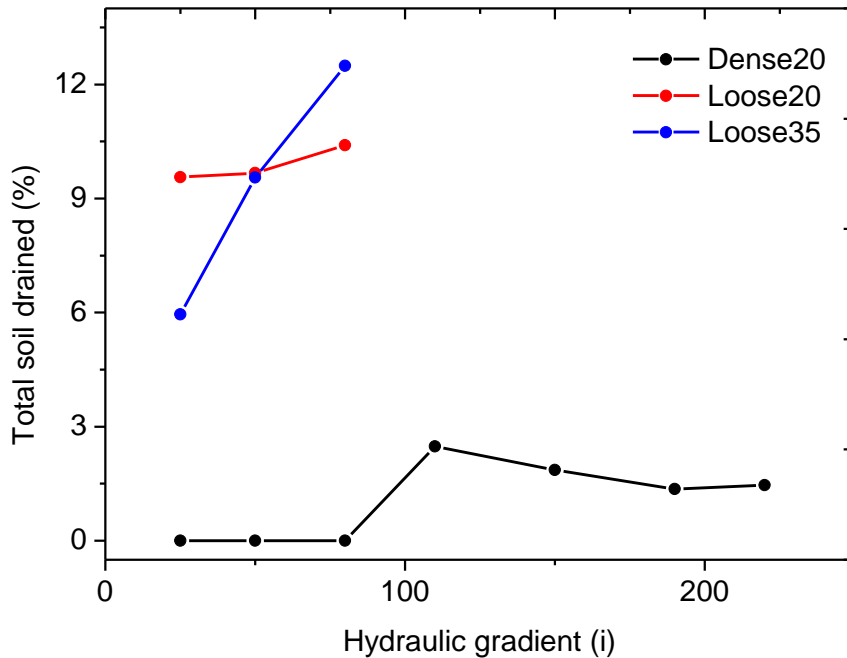


Figure 4-8 Total soil drained vs. Hydraulic gradient

The difference in the degree of suffusion (eroded particles) can be attributed to the intergranular space. In the loose specimens the Intergranular void space is larger, and the fines can move easily through constrictions, while in dense specimens most of the fines are confined in the Intergranular void space (Figure 4-9).

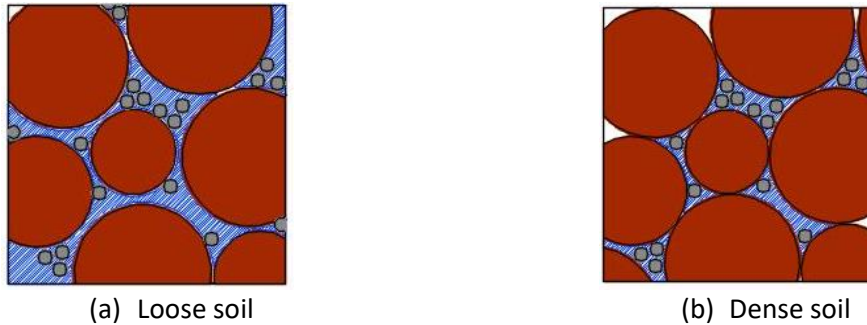


Figure 4-9 Schematic intergranular space

### 4.3. Turbidity

#### 4.3.1. Calibration of turbidity

As mentioned in Chapter 3, the turbidity refers to the cloudiness of a fluid caused by large numbers of individual particles that are generally indistinguishable to the naked eye. The turbidity value is directly proportional to the amount of soil particles in the water drained from the specimen. Figure 4-10 shows the calibration of the turbidity index against soil/water drained from the specimen, and it enables estimation of the amount of fines eroded.

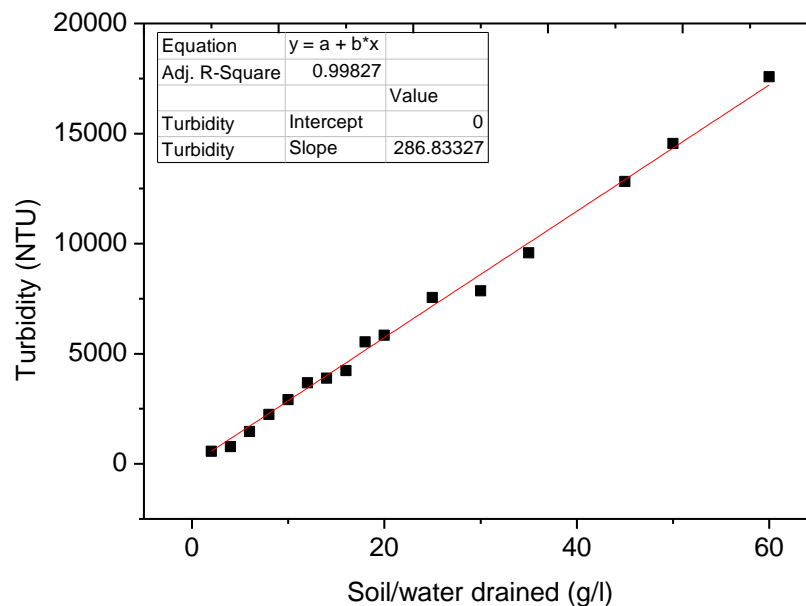


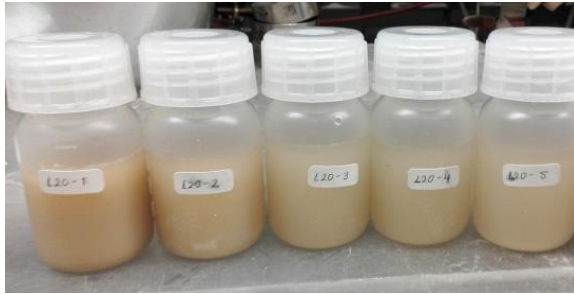
Figure 4-10 Result of calibration for quantifying turbidity



#### 4.3.2. Results

As explained in Section 4.2, the amount of particles eroded at the beginning of each experiment is larger than the particles eroded during the latter cycles of water applied. Consequently, the turbidity of the water is greater at the start of the seepage and decreases continuously throughout the test.

Figure 4-11 illustrates samples of water collected after seepage, and the variation of turbidity during the test. Each sample is collected every 400 ml of water passed; the first bottle (left side) in Figure 4-11(a) is the sample of the first 400 ml, and the color becomes weaker for the bottles situated to the right side. This represents the decrease in the fines concentration in the water. For the dense specimen (Figure 4-11(b)), the color becomes almost clear (low turbidity).



(a) loose specimen test



(b) dense specimen test

Figure 4-11 Samples of water collected after seepage

The turbidity values are significantly higher at the first amounts of water passed, and then decrease substantially until a steady trend is attained (Figure 4-12), which is consistent with the results obtained for the amount of drained soil (Figure 4-1).

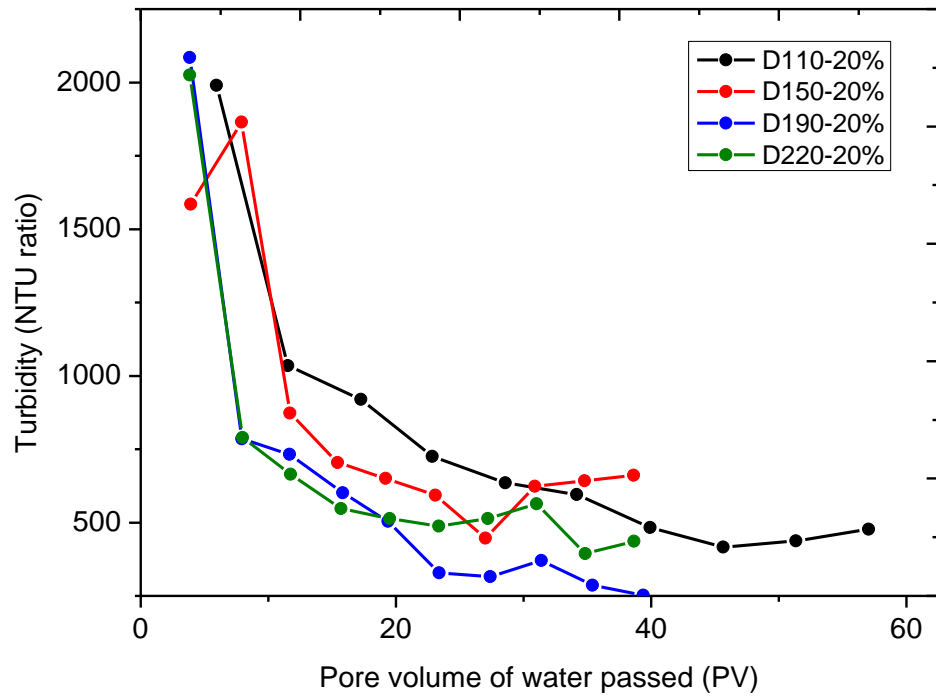


Figure 4-12 Turbidity in dense specimens

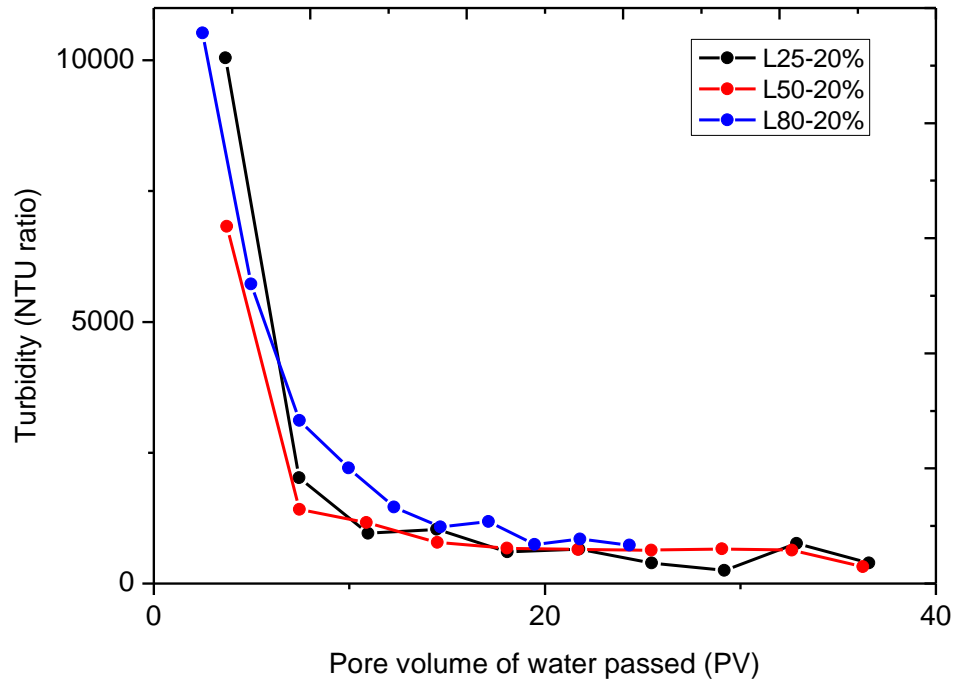


Figure 4-13 Turbidity in loose specimens with 20% of initial content of detached particles

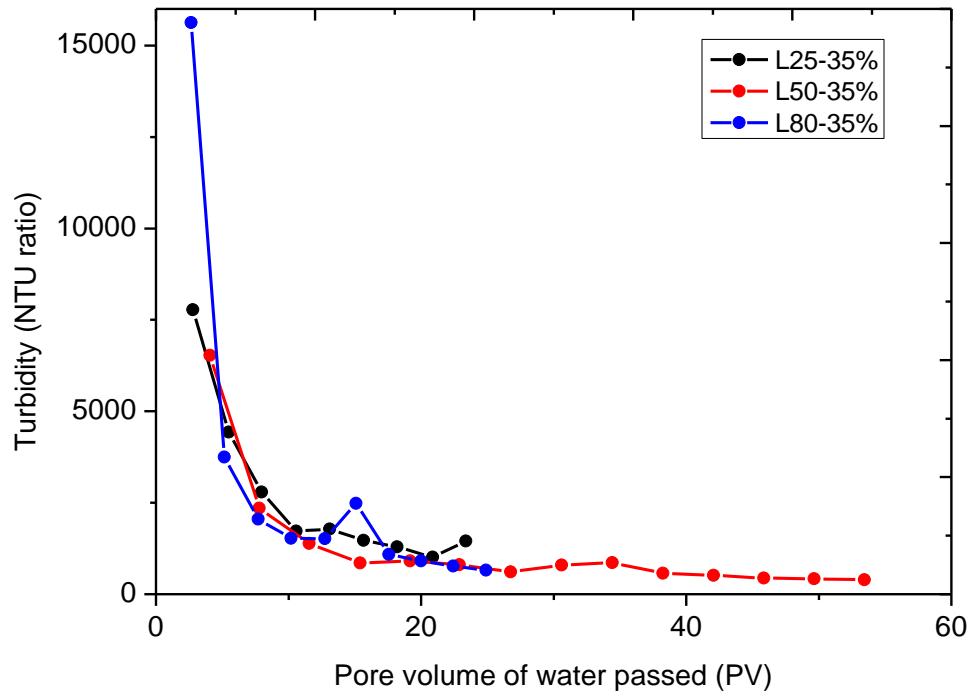


Figure 4-14 Turbidity in loose specimens with 35% of initial content of detached particles

For the loose specimens (Figure 4-13 and Figure 4-14) the same trend is observed, although the maximum values of turbidity in the loose specimens are larger (10000 NTU, 15000 NTU) compared to the values in the dense station (2000 NTU).

Figure 4-15 compares the turbidity values observed for the loose specimens. The initial fines content affects the turbidity value insignificantly, since the trend in the curves is similar. On the other hand, a high hydraulic gradient increases the turbidity value (Figure 4-15(c)), indicating a larger amount of fines eroded as concluded in the previous subsection.

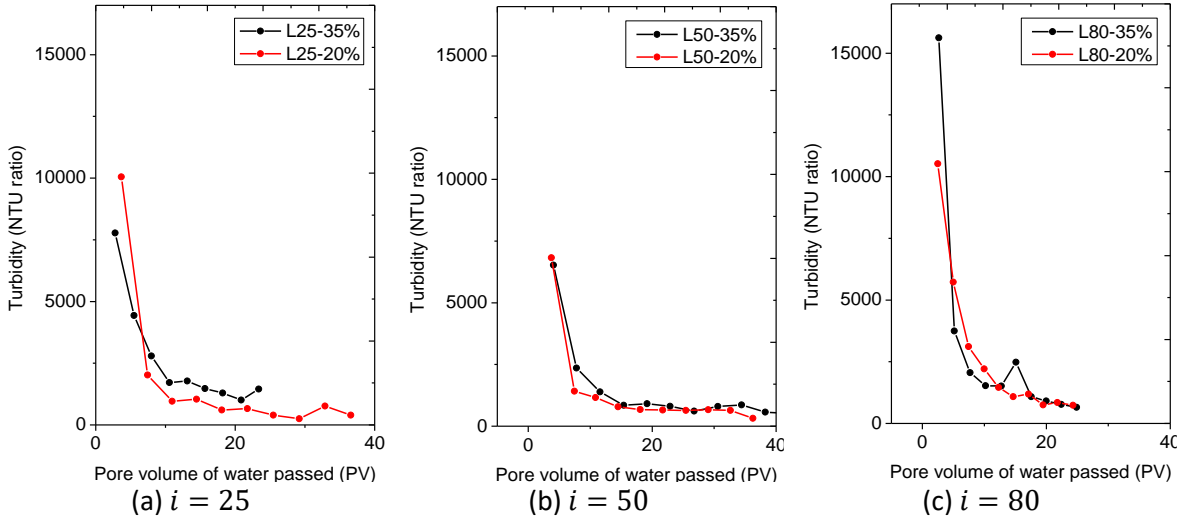


Figure 4-15 Comparison of the turbidity in the loose specimens

#### 4.4. Permeability

Since some of the particles have been moved out from the specimen, a change in the permeability value by the action of seepage is expected. Figure 4-16 shows the variation in the permeability during the experiment.

The curves reach a steady state after the first infiltration, which suggests that certain water paths are made after the movement of particles.

Particularly the curves in dense specimens (Figure 4-16) show higher permeability values in the specimen eroded at a low hydraulic gradient ( $i = 110$ , black curve), and lower permeability values in the specimen eroded at a high hydraulic gradient ( $i = 220$ , green curve). These results are consistent with the behavior observed for the eroded particles (Section 4.2): “with very high hydraulic gradients the particles are moved so aggressively that clog the constrictions immediately. Nevertheless, a middle hydraulic gradient moves the particles gently enough to displace them between constrictions without clogging”.

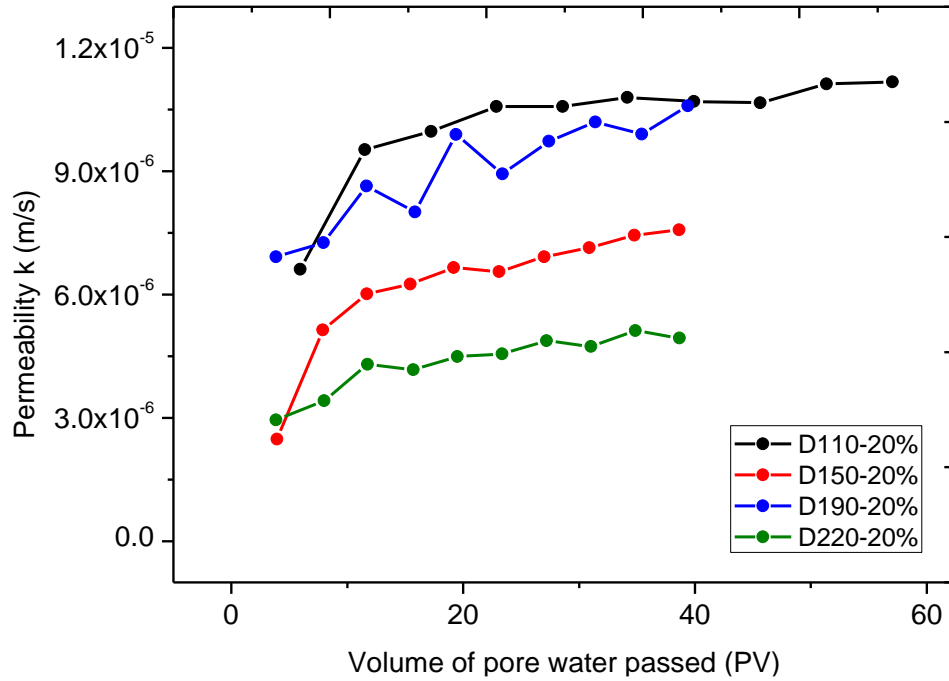


Figure 4-16 Permeability in dense specimens

In the loose specimens with initial fines content of 20% the variation of permeability is insignificant despite the variation in hydraulic gradients, due to the similarity in the amount of particles displaced out (Figure 4-17). The specimens with initial fines content of 35% show permeability directly proportional to the hydraulic gradient (Figure 4-18).

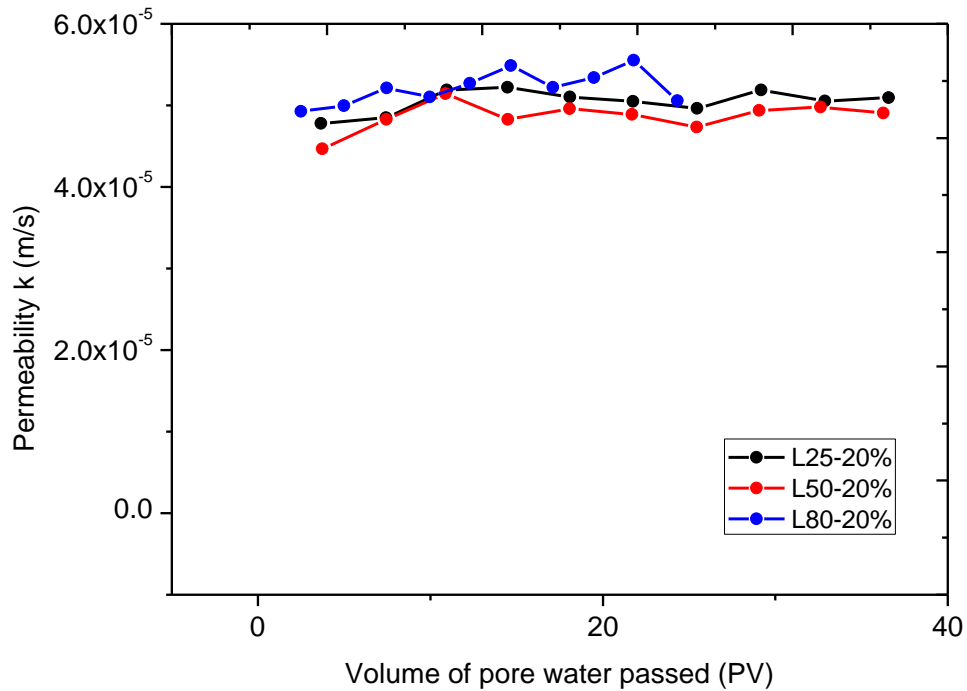


Figure 4-17 Permeability in loose specimens with 20% of initial content of detached particles

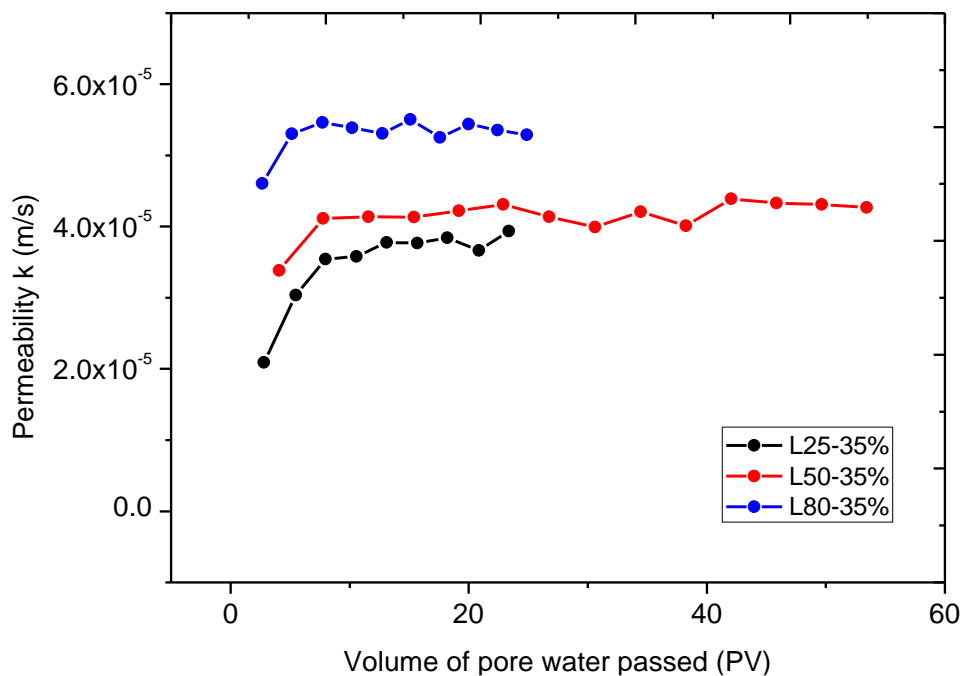


Figure 4-18 Permeability in loose specimens with 35% of initial content of detached particles

The water flows more easily when the soil has lower fines content, compared to a soil with the same density and hydraulic gradient applied (Figure 4-19).

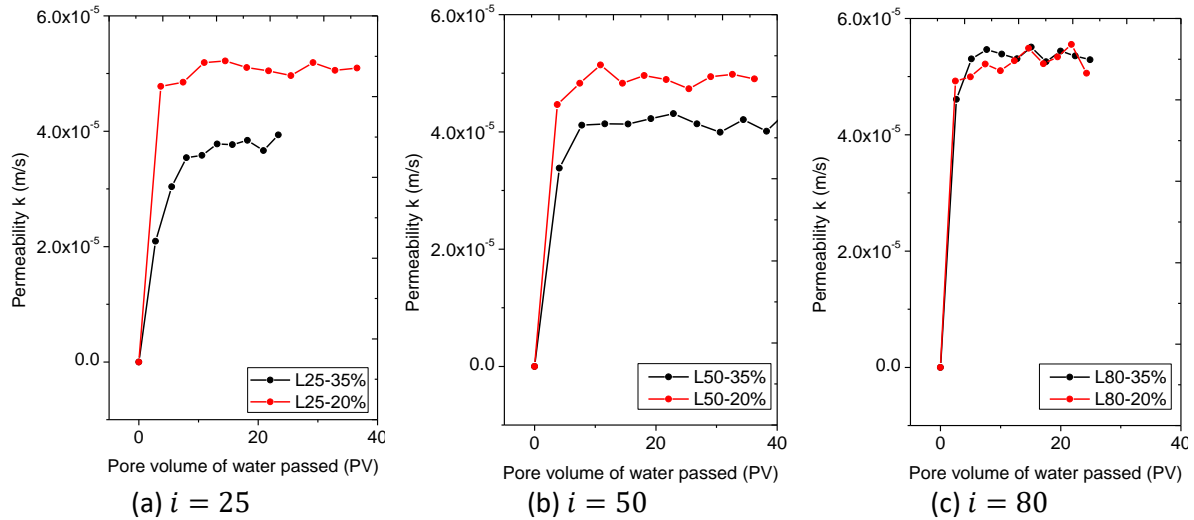


Figure 4-19 Comparison of the permeability in the loose specimens

The average coefficient of permeability for the dense specimens can be classified as weak in permeability character and small in permeability, which is typical for silts (Table 4-4 blue line). The loose specimens show typical characteristics for sands that have good flow water (Table 4-4 red line). The original soil studied (before erosion) is classified as a silty sand; in dense specimens, the permeability behavior is closely related to silt since the degree of erosion obtained is low.

Table 4-4 Classification of soils permeability

Character of permeability (Pazdro and Kozerski, 1990)	Very Good			Good	Aver	Weak	Semi-permeable			Impermeable				
Classification of permeability (Terzaghi and Peck, 1967)	Large			Average			Small			Very small		Practically impermeable		
Characteristic of flow water (Head, 1985)	Good						Weak			Practically impermeable				
Soil	Stones and gravel		Sands			Silts					High plastic clays		Hard clays	
Coefficient of permeability k(m/s)	10 <sup>-1</sup>	10 <sup>-2</sup>	10 <sup>-3</sup>	10 <sup>-4</sup>	10 <sup>-5</sup>	10 <sup>-6</sup>	10 <sup>-7</sup>	10 <sup>-8</sup>	10 <sup>-9</sup>	10 <sup>-10</sup>	10 <sup>-11</sup>	10 <sup>-12</sup>		

#### 4.5. Global void ratio

Figure 4-20 shows the variation of void ratio in the dense specimens. The trend in the specimen eroded with  $i = 110$  differs from the others, resulting from the higher amount of particles displaced out in this test. Figure 4-21 and Figure 4-22 show the results for the loose specimens which have the same trend explained in the previous subsections.

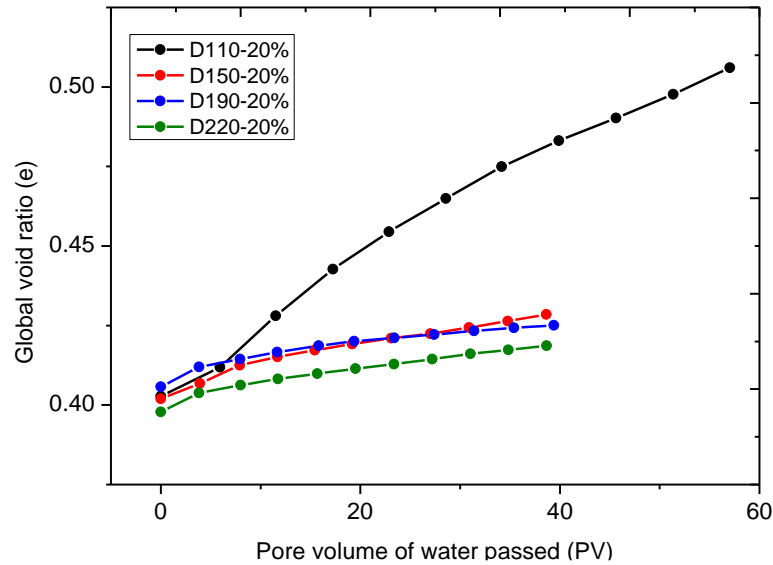


Figure 4-20 Global void ratio in dense specimens

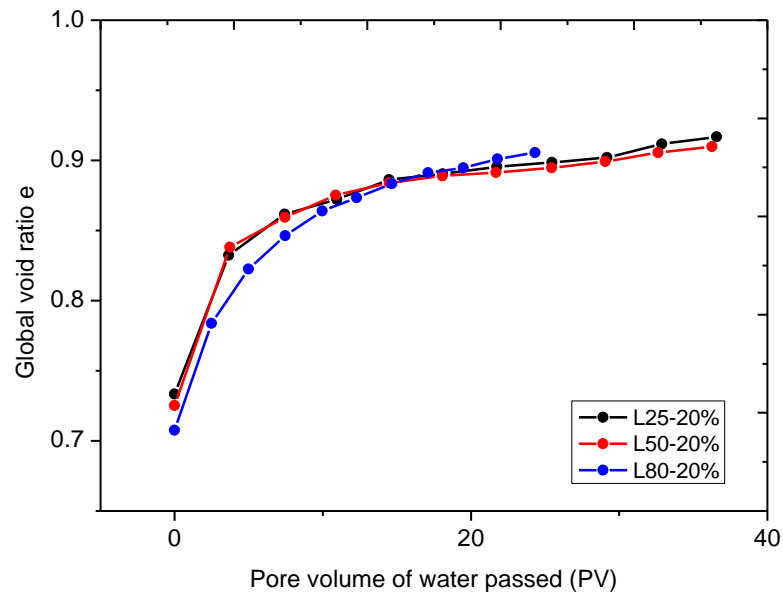


Figure 4-21 Global void ratio in loose specimens with 20% of initial content of detached particles



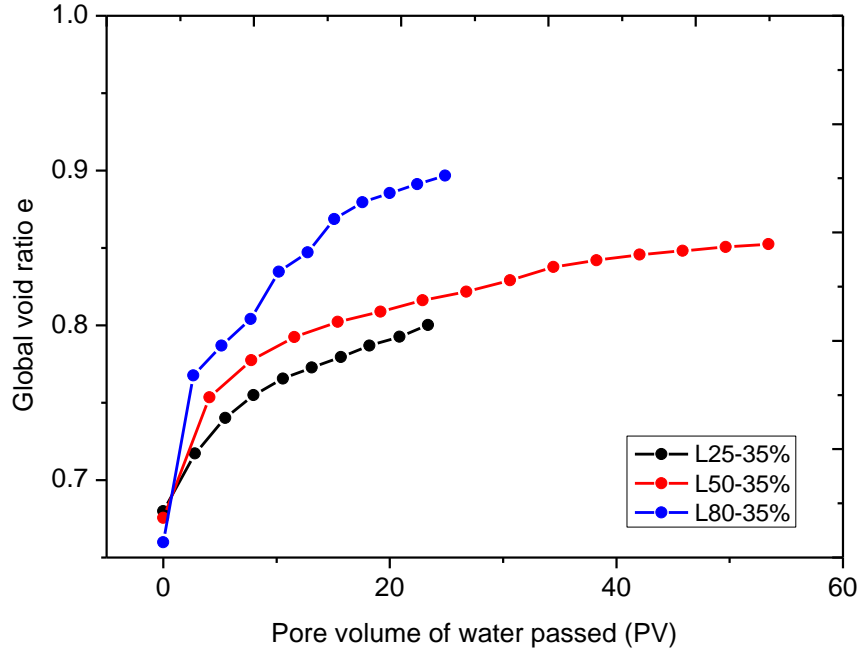


Figure 4-22 Global void ratio in loose specimens with 35% of initial content of detached particles

Although the initial global void ratio is larger in the specimen with fewer fines, it increased considerably more compared with the specimens with more initial fines. However, the initial fines content affects the global void ratio insignificantly, when the hydraulic gradients are higher (Figure 4-23)

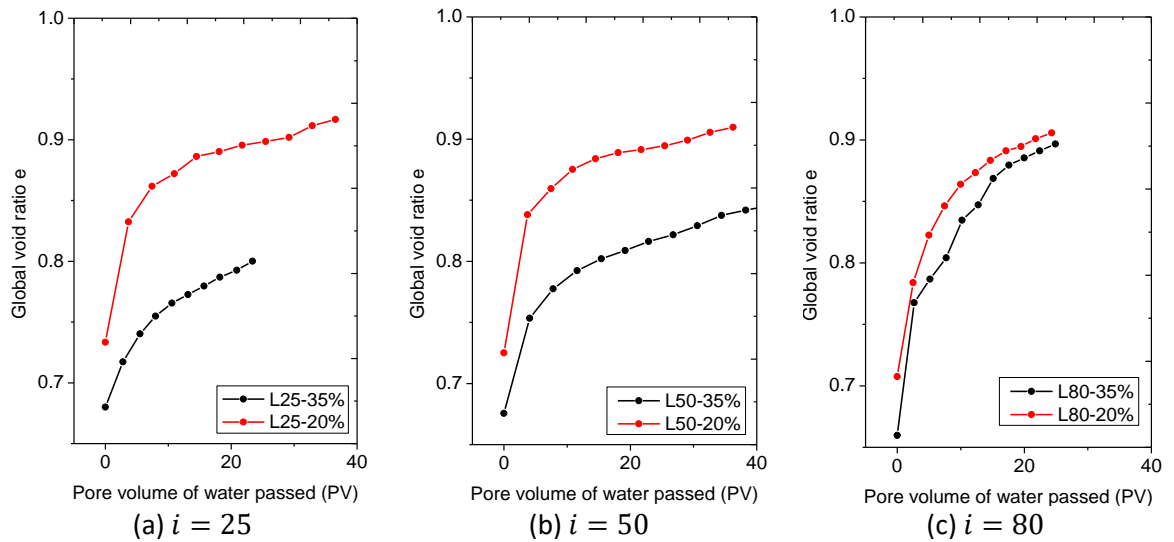


Figure 4-23 Comparison of the global void ratio in the loose specimens

#### 4.6. Intergranular void ratio

The intergranular void ratio is defined as the void ratio of the original coarser-grains matrix structure assuming the fine particles as if they were void space (Mitchell, 1976) (see 2.5.2 Intergranular void ratio and density, equation (2-59)). Contrary to the global void ratio ( $e$ ), the intergranular void ratio ( $e_s$ ) decreases along the erosion process (Figure 4-24). This response can be attributed to the movement of the primary fabric particles.

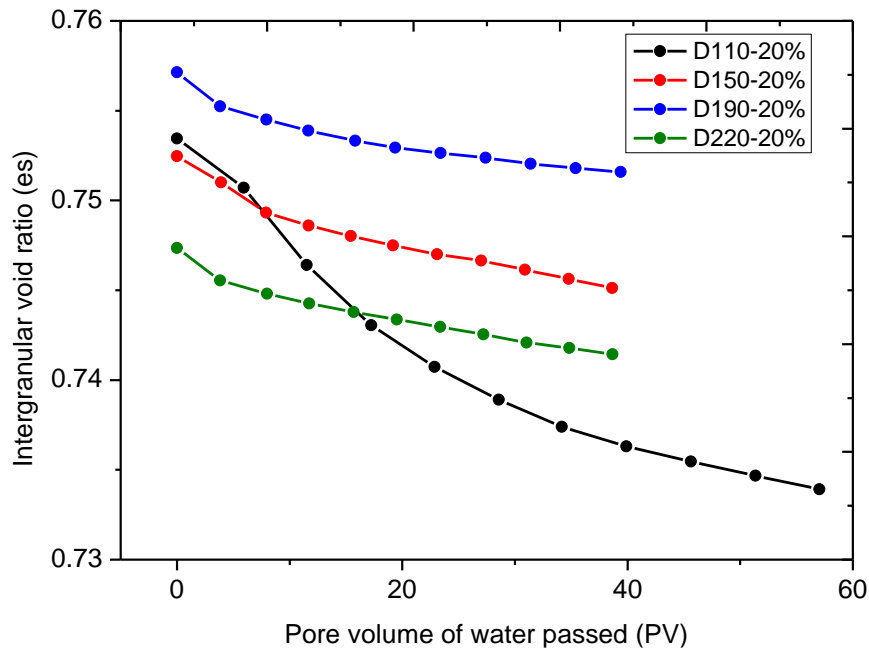


Figure 4-24 Intergranular void ratio in dense specimens

Although the coarser particles do not move out from the soil matrix, the suffusion moves away the fines inside its pores, reducing the intergranular void ratio (Figure 4-25).

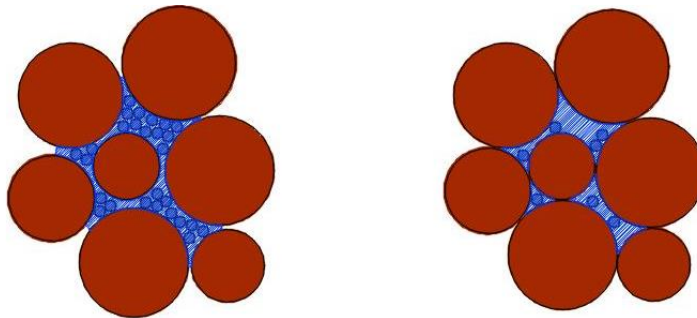


Figure 4-25 Schematic intergranular void ratio before erosion (left) and after erosion (right)

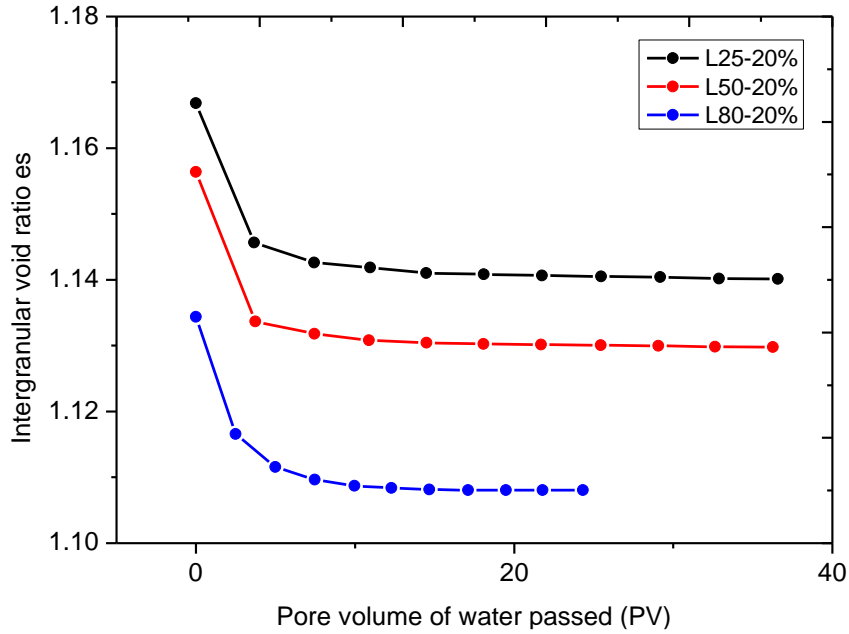


Figure 4-26 Intergranular void ratio in loose specimens with 20% of initial content of detached particles

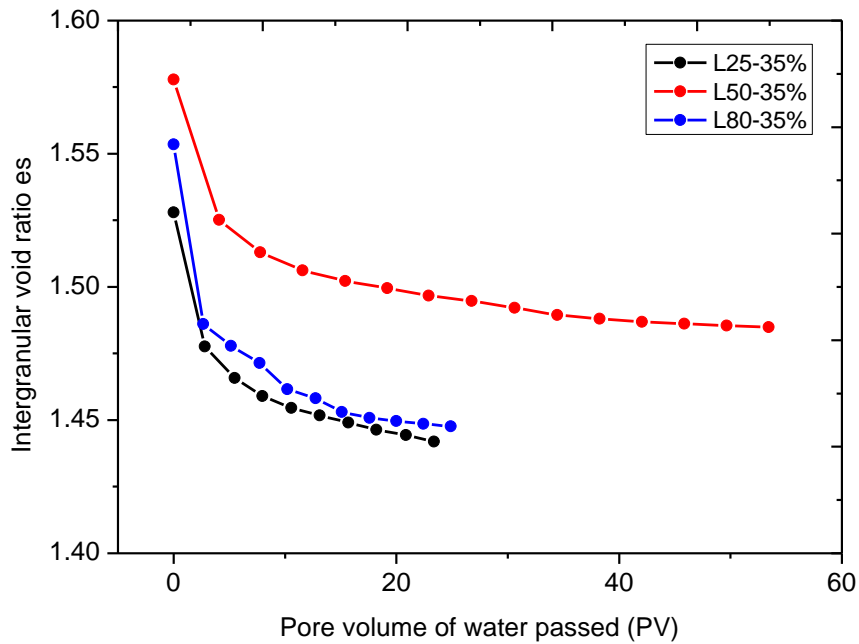


Figure 4-27 Intergranular void ratio in loose specimens with 35% of initial content of detached particles

Similarly, the loose specimens exhibit a decrease in  $e_s$  at the initial stages of suffusion, reaching a stable trend later despite the continuous flow of water (Figure 4-26 and Figure 4-27).

Figure 4-28 shows that despite the increased hydraulic gradient a significant difference in  $e_s$  is not observed. Nevertheless, there is a considerable effect of the initial content of fines on  $e_s$  where the percentage of primary fabric is also different (80% and 65%).

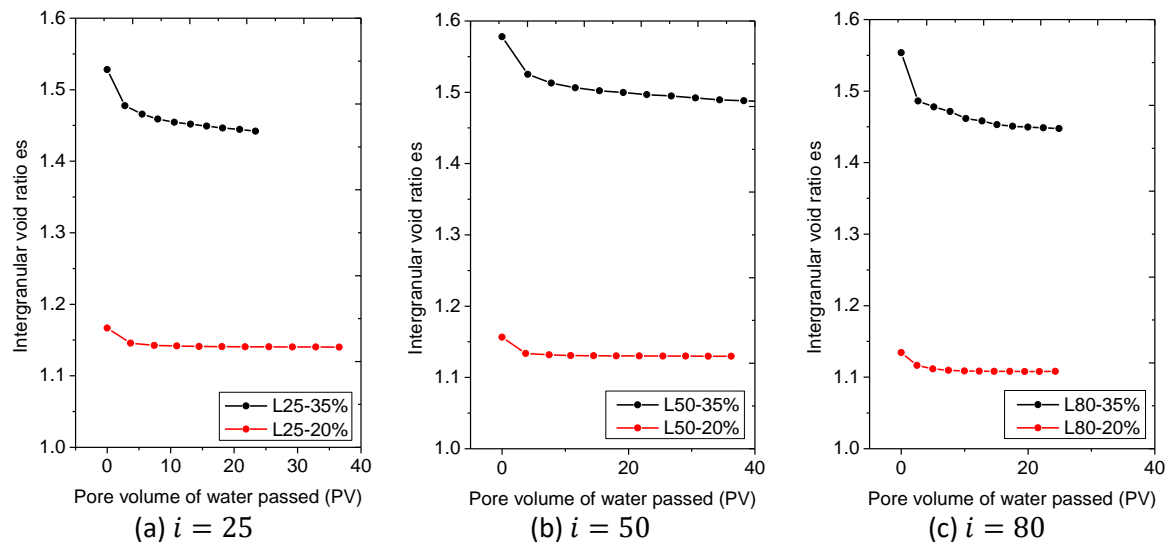


Figure 4-28 Comparison of the Intergranular void ratio in the loose specimens

#### 4.7. Relative density

Similar to the results discussed previously, the relative density also exhibits a more drastic change in the initiation of the seepage to finally reach a consistent curve (Figure 4-29, Figure 4-30, Figure 4-31, Figure 4-32). Although  $e_{max}$  and  $e_{min}$  change with the degree of suffusion, for the calculation of the relative density are assumed to be the same with a non-eroded soil.

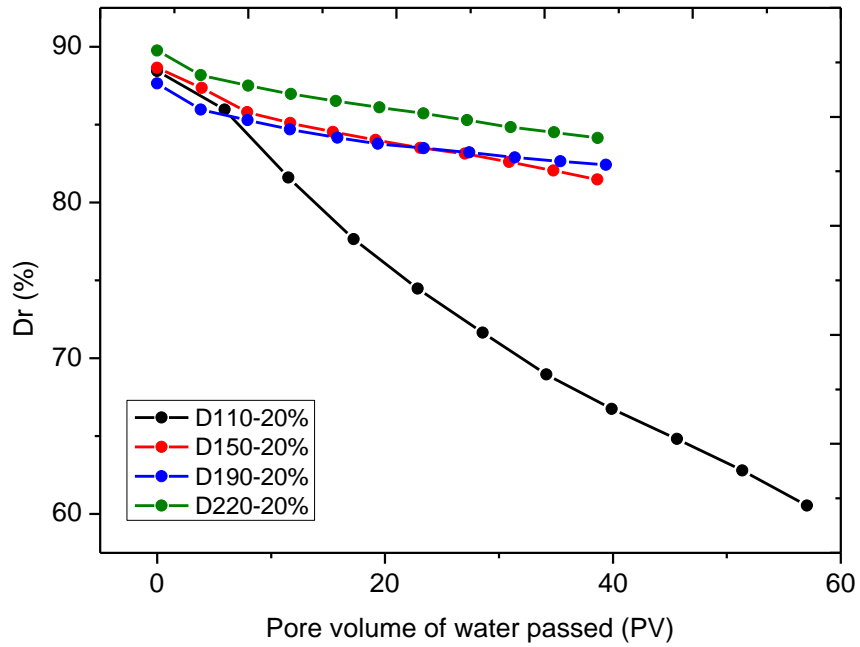


Figure 4-29 Relative density in dense specimens

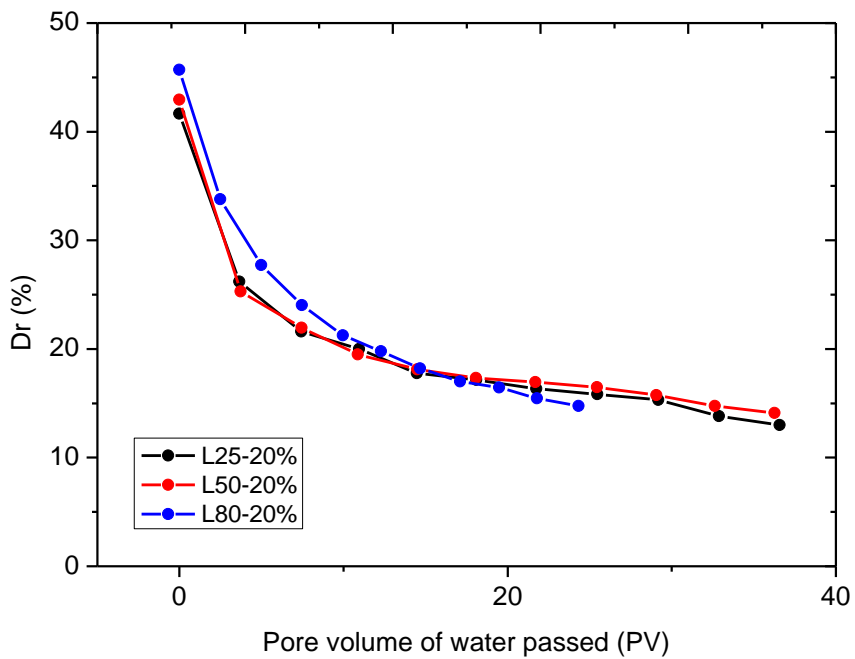


Figure 4-30 Relative density in loose specimens with 20% of initial content of detached particles

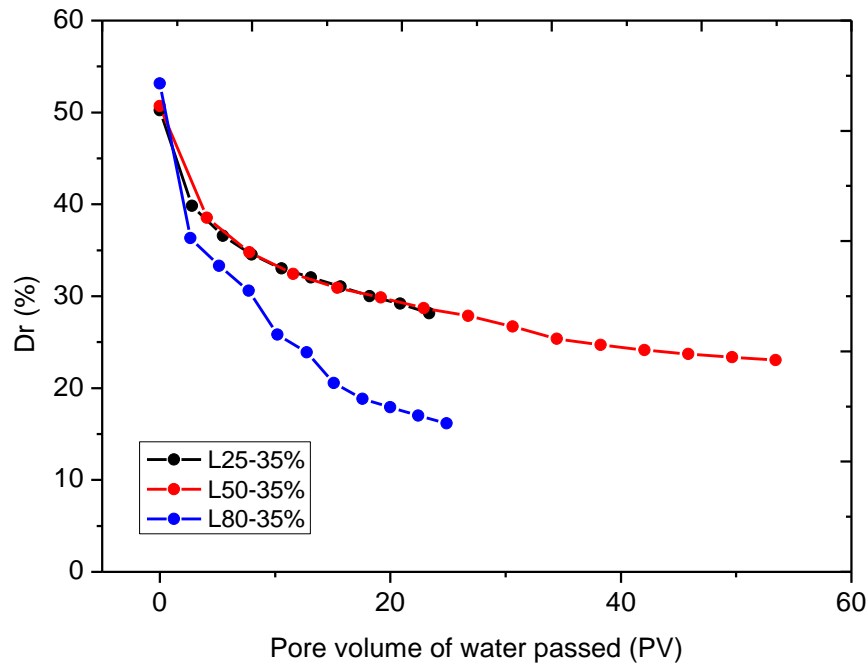


Figure 4-31 Relative density in loose specimens with 35% of initial content of detached particles

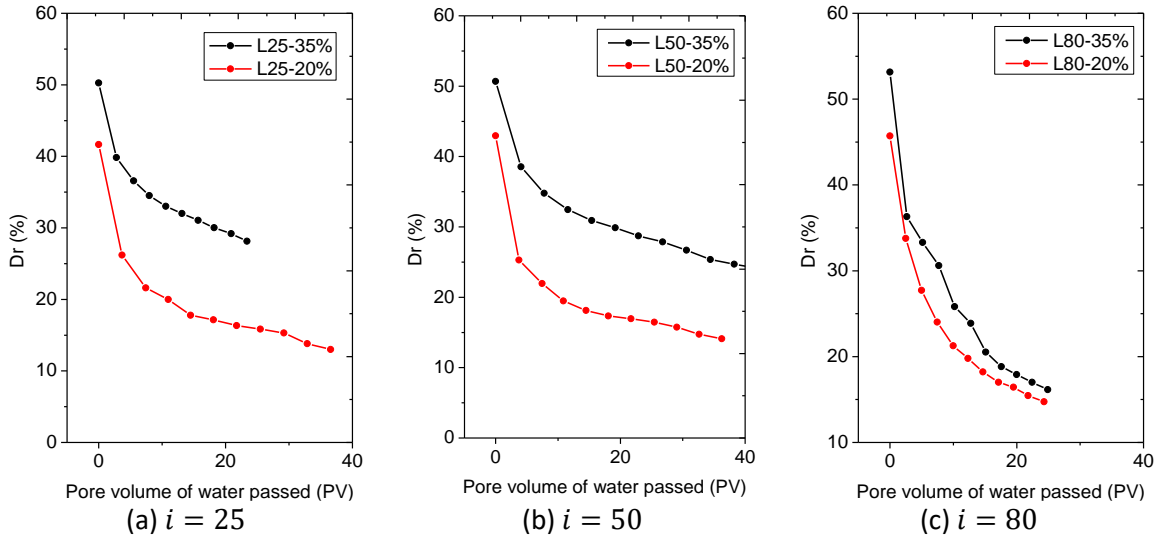


Figure 4-32 Comparison of the Intergranular void ratio in the loose specimens

#### 4.8. Intergranular relative density

Contrary to the variation of relative density ( $D_r$ ), the intergranular relative density ( $D_{rs}$ ) increases along with the erosion process (Figure 4-33 to Figure 4-36). These results are related to the variation of intergranular relative density ( $e_s$ ) discussed above.

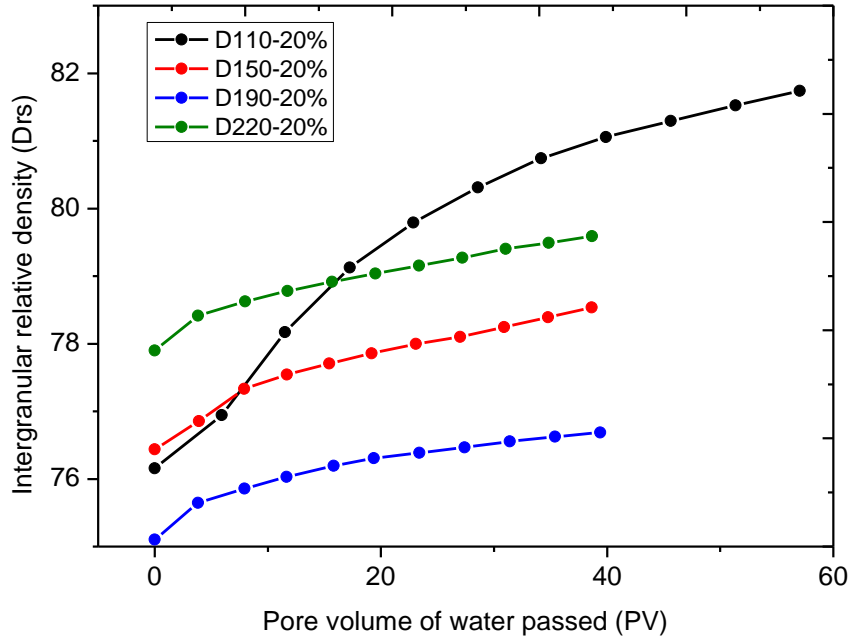


Figure 4-33 Intergranular relative density in dense specimens

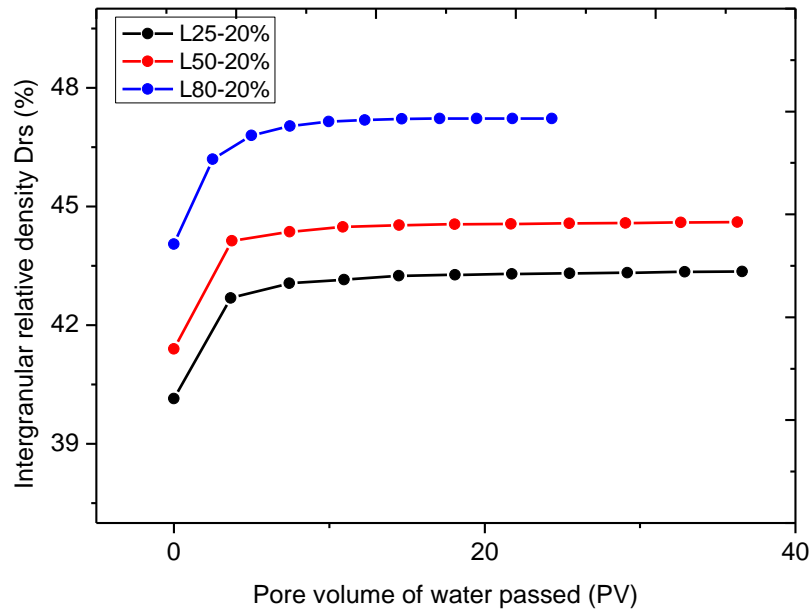


Figure 4-34 Intergranular relative density in loose specimens with 20% of initial fines

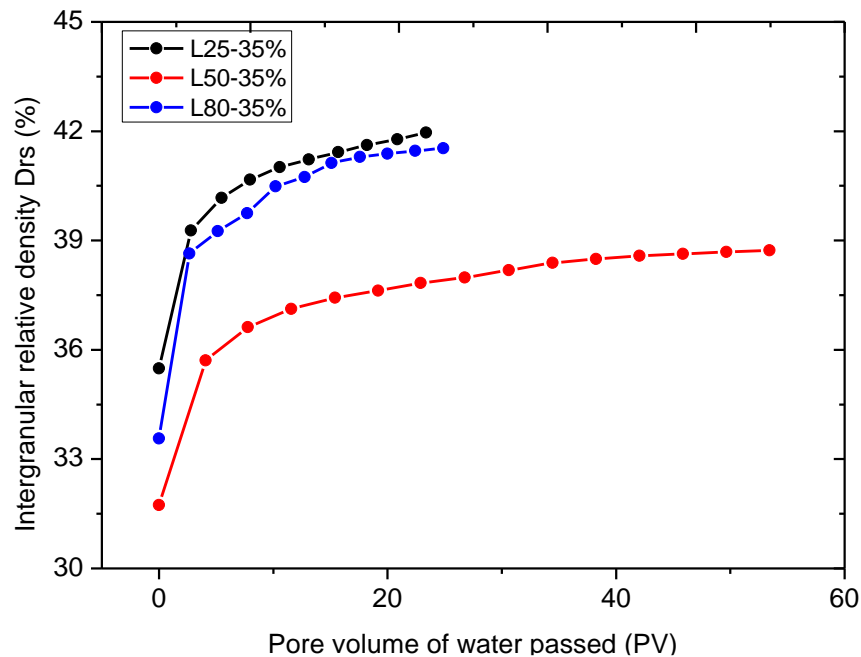


Figure 4-35 Intergranular relative density in loose specimens with 35% of initial content of detached particles

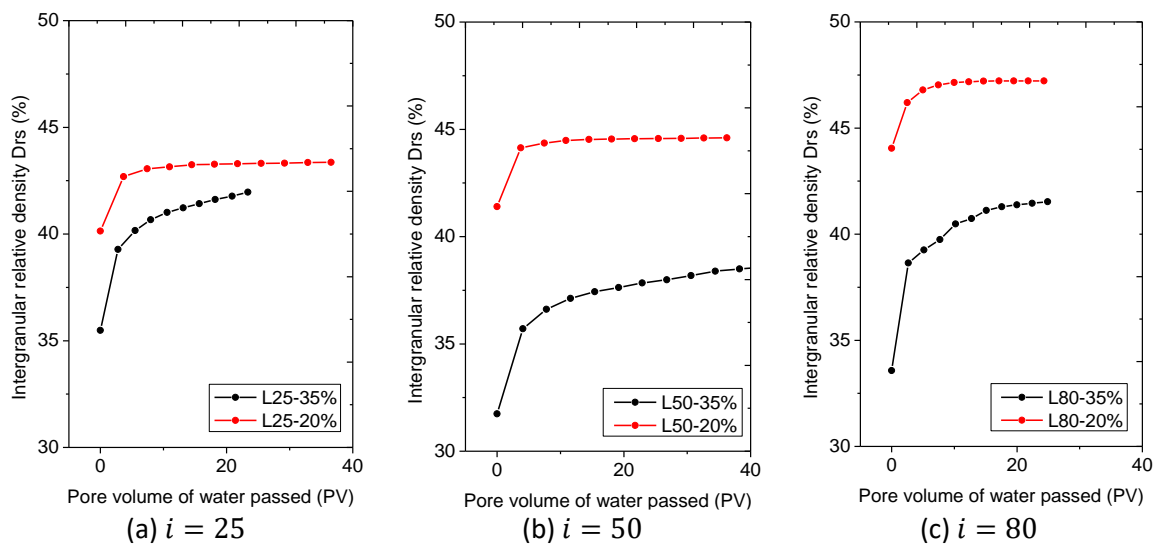


Figure 4-36 Comparison of the Intergranular void ratio in the loose specimens



#### 4.9. Grain size distribution

The grain size distribution of the soils was recorded before and after each test. Figure 4-37 shows the initial curve (before the tests) and the final curves after erosion. It can be appreciated that the mass in diameters smaller than 0.1 mm have decreased due to erosion.

In order to estimate the percentage of loss, Kenney and Lau (1985) suggested a method of stretching the initial grain size distribution curve: “The cumulative mass grain size distribution for the two samples (before and after water seepage) must be identical in the range of particles sizes where no losses have occurred but must differ in the range of sizes where losses have occurred (...) The vertical scale of the initial curve is extended (stretched) downwards until curve it became coincident with the eroded soil curve in the coarse range of particles.” (Kenney and Lau, 1985).

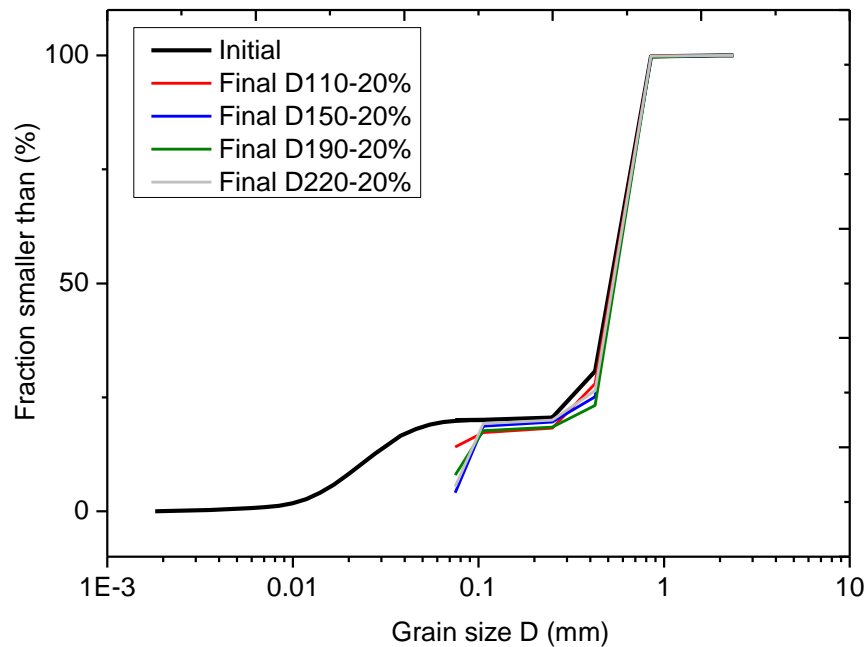


Figure 4-37 Grain size distribution of dense specimens

Following this procedure, it is possible to estimate the fraction flushed as well as the maximum size particle eroded. Figure 4-38 shows as an example the stretched curve for the specimen D110-20%; for this specimen (and for all the tests performed) the maximum size particle eroded is around 0.106 mm, which means that only the detached particles fraction was eroded and not the primary fabric. It was necessary for the initial curve to extend the vertical scale by 0.03 units downwards until it was coincident with the eroded curve. If the final mass of the specimen was 1.0 units, the initial mass is 1.03 units, and the fraction flushed out during the tests is  $f_f = 0.03/1.03 = 2.9\%$ . The fraction flushed calculated by this method is summarized in Table 4-7.

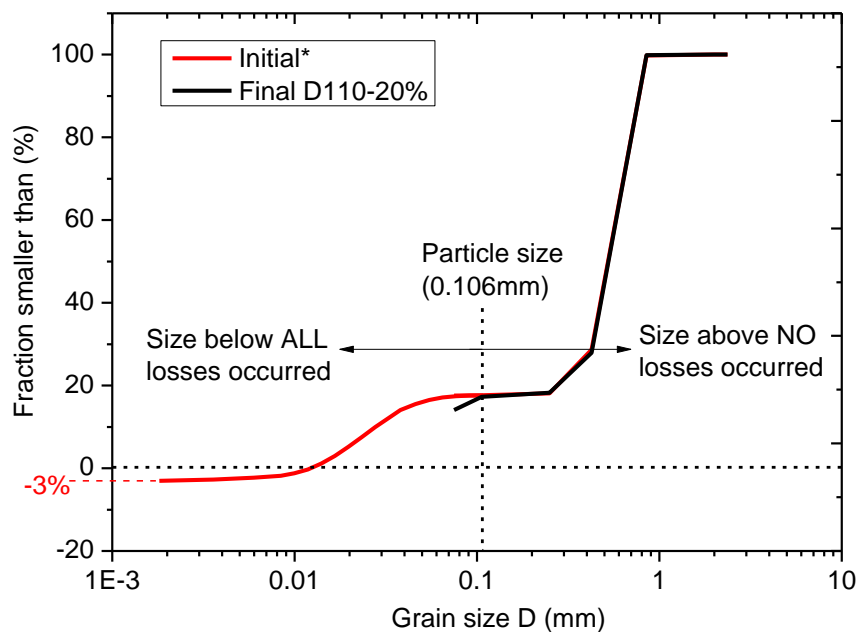


Figure 4-38 Fraction flushed in dense specimens

Table 4-5 Fraction flushed in the dense specimens

Test	Fraction flushed (%)
D110-20%	2.9
D150-20%	2.0
D190-20%	2.9
D220-20%	1.0

The change in the grain size distribution is more evident in the loose specimens (Figure 4-39 and Figure 4-41). The initial curve was stretched downwards by around 15% and 20% for the specimens with 20% and 35% of initial fines, respectively (Figure 4-40 and Figure 4-42). The fraction flushed for all the loose specimens is summarized in Table 4-6.

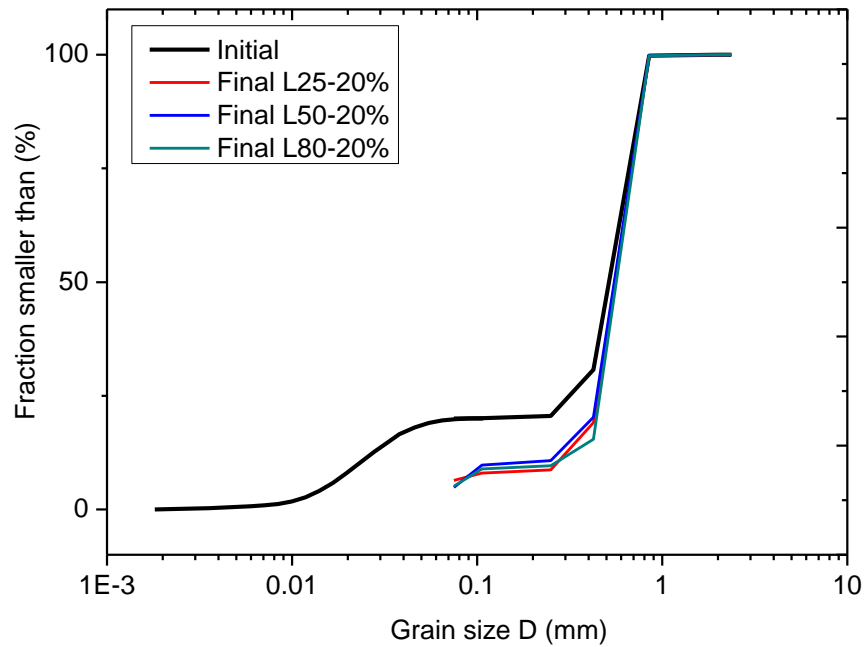


Figure 4-39 Grain size distribution of loose specimens with initial fines content of 20%

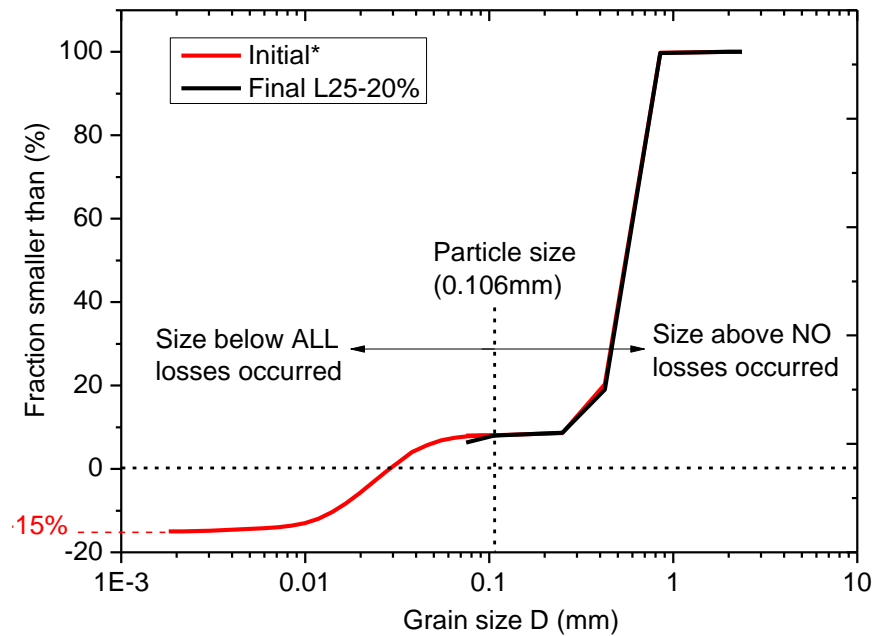


Figure 4-40 Fraction flushed in dense specimens with initial fines content of 20%

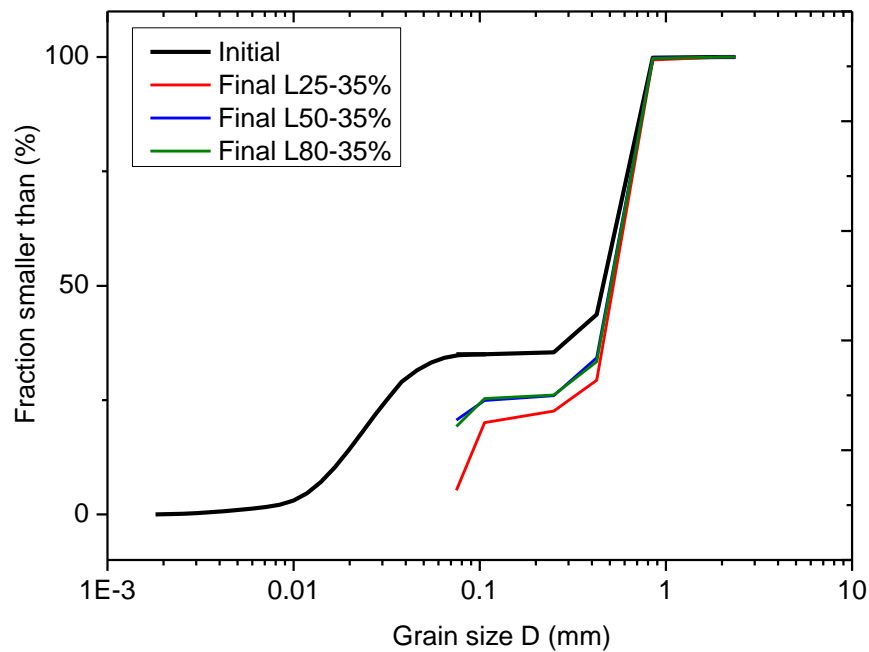


Figure 4-41 Grain size distribution of loose specimens with initial fines content of 35%

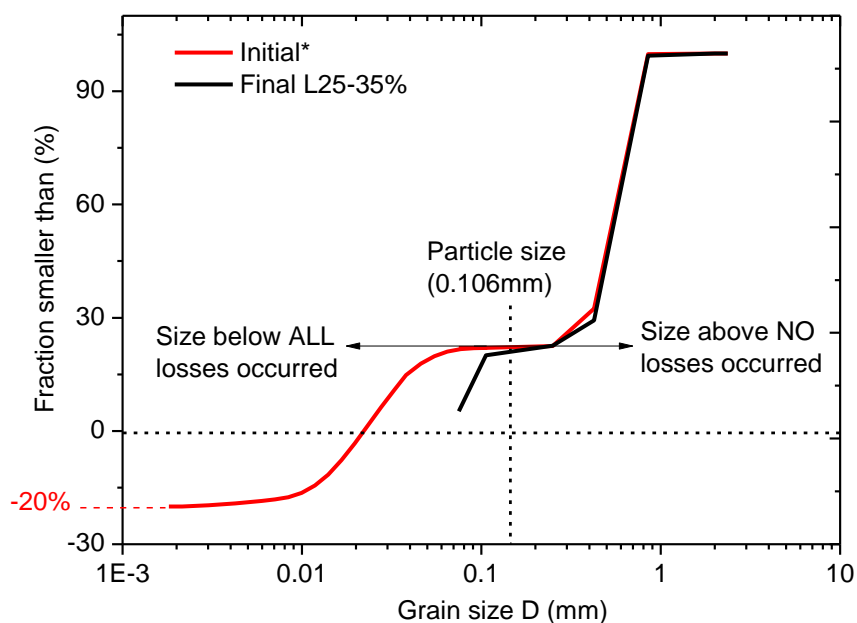


Figure 4-42 Fraction flushed in dense specimens with initial fines content of 35%

Table 4-6 Fraction flushed in the loose specimens

Test	Fraction flushed (%)
L25-20%	16.7
L50-20%	12.3
L80-20%	13.0
L25-35%	13.0
L50-35%	11.1
L80-35%	12.3

#### 4.10. Method of describing the shape of the PSD curve

The method of describing the shape of the grain size distribution curve was suggested by Kenney and Lau (1985) as explained previously. The shape curve (in the space  $H$  vs.  $F$ ) is independent of the grain size and depends only on the geometric shape of the grain size distribution curve.

Therefore, these curves describe the relationship between the constrictions made by the coarser grains and the fines that can move through them. Knowing the  $H$ - $F$  curve enables to determine the internal stability of the soil.

As explained in Figure 3-7, the soils before erosion are considered as internally unstable because their shape curves are in the zone for unstable (Kenney and Lau, 1985). Figure 4-43 shows the initial curve (black curve) and the curves of the dense specimens after erosion. As the amount of fines eroded is around 3%, there is insignificant difference from the original one, but the curves are closer to the zone for stable.

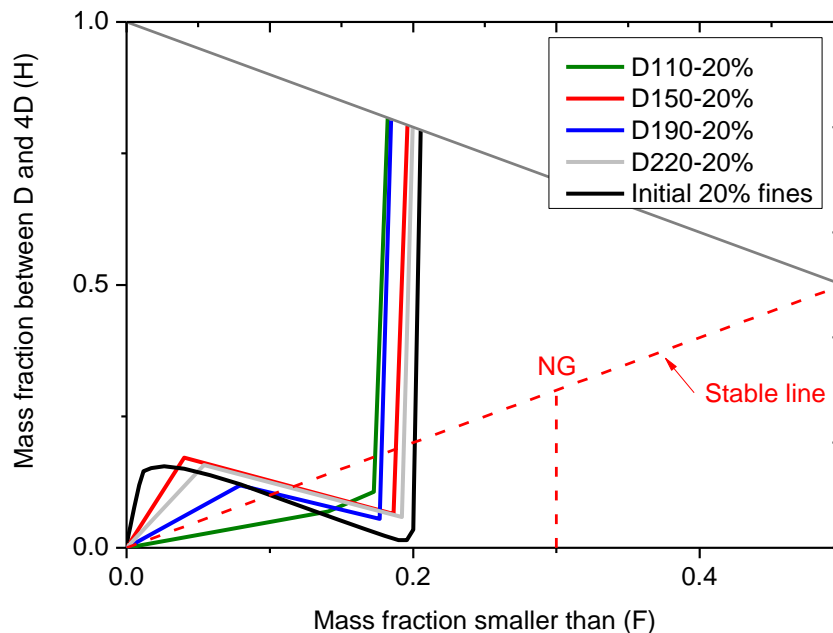


Figure 4-43  $H$  vs.  $F$  curves for the dense specimens

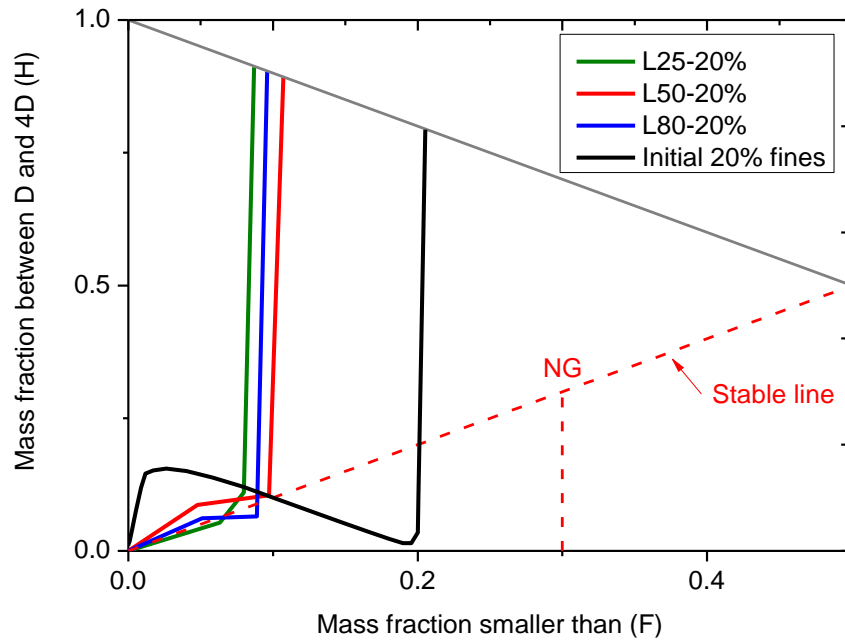


Figure 4-44 H vs. F curves for the loose specimens with 20% of initial fines

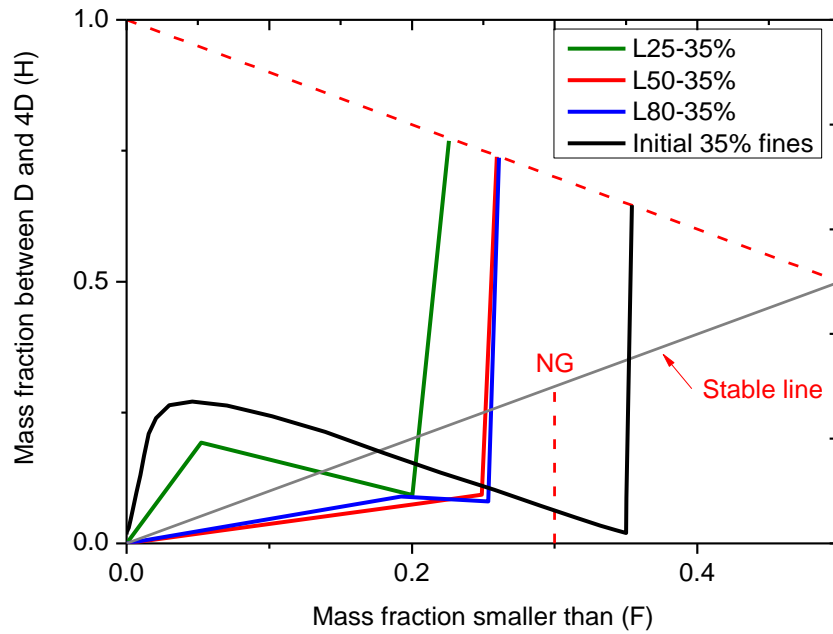


Figure 4-45 H vs. F curves for the loose specimens with 35% of initial fines

As for the loose specimens, the difference is more obvious. Figure 4-44 shows the shape curves for the soils with 20% of initial fines, which are located almost out of the unstable zone. This means that after the erosion all the particles which were considered as potentially erodible left the specimen. In Figure 4-45 the same tendency is observed, although there still are remaining fine particles which make the specimen internally unstable.

#### 4.11. Analysis and conclusions

By means of permeability tests using a chamber with hollows in the bottom plate enabled evaluation of the susceptibility to suffusion of a soil by evaluating the variation of its relative density, initial fines content, and seepage with different hydraulic gradients.

##### *4.11.1. Effects of the density*

The results show that the density of the soil is a determining factor for the resistance against suffusion. In dense specimens ( $D_r \approx 90\%$ ), the fines moved out from the matrix are around 10% of the total amount of the soil expelled from the loose specimens ( $D_r \approx 50\%$ ).

According to the variation of the characteristics along the experiments (Figure 4-1, Figure 4-12, Figure 4-16, Figure 4-20, Figure 4-24, Figure 4-29), it can be concluded that the first stages of infiltration have a greater effect on suffusion, after which a stable path is created for the passage of water, which does not produce a greater effect of erosion.

Table 4-7 summarizes the final results of each permeameter test. Additionally, Figure 4-46 shows a clear difference in the characteristics of the loose and dense tests where the vertical axes include values for amount of drained soil, coefficient of permeability, turbidity, and void ratios. The results for the loose specimens and dense specimens are presented at the left side and the right side of Figure 4-46, respectively, where considerably larger values are observed in the loose specimens. Therefore, the degree of erosion (suffusion) can be related to changes in the permeability, turbidity and void ratio.



Table 4-7 Summary of results for permeameter test

ID	Soil drained %	k  m/s	Turbidity  NTU	e	D <sub>r</sub>  %	e <sub>s</sub>	D <sub>rs</sub>  %
L25-35%	6.0	3.94E-05	7775	0.80	28.1	1.44	42.0
L50-35%	9.6	4.27E-05	6525	0.85	23.0	1.48	38.7
L80-35%	12.5	5.29E-05	15625	0.90	16.2	1.45	41.5
L25-20%	9.6	5.10E-05	10050	0.92	13.0	1.14	43.4
L50-20%	9.7	4.91E-05	6825	0.91	14.1	1.13	44.6
L80-20%	10.4	5.06E-05	10525	0.91	14.7	1.11	47.2
D110-20%	2.5	1.12E-05	1990	0.51	60.5	0.73	81.7
D150-20%	1.9	7.58E-06	1585	0.43	81.5	0.75	78.5
D190-20%	1.4	1.06E-05	2085	0.43	82.4	0.75	76.7
D220-20%	1.5	4.94E-06	2025	0.42	84.1	0.74	79.6

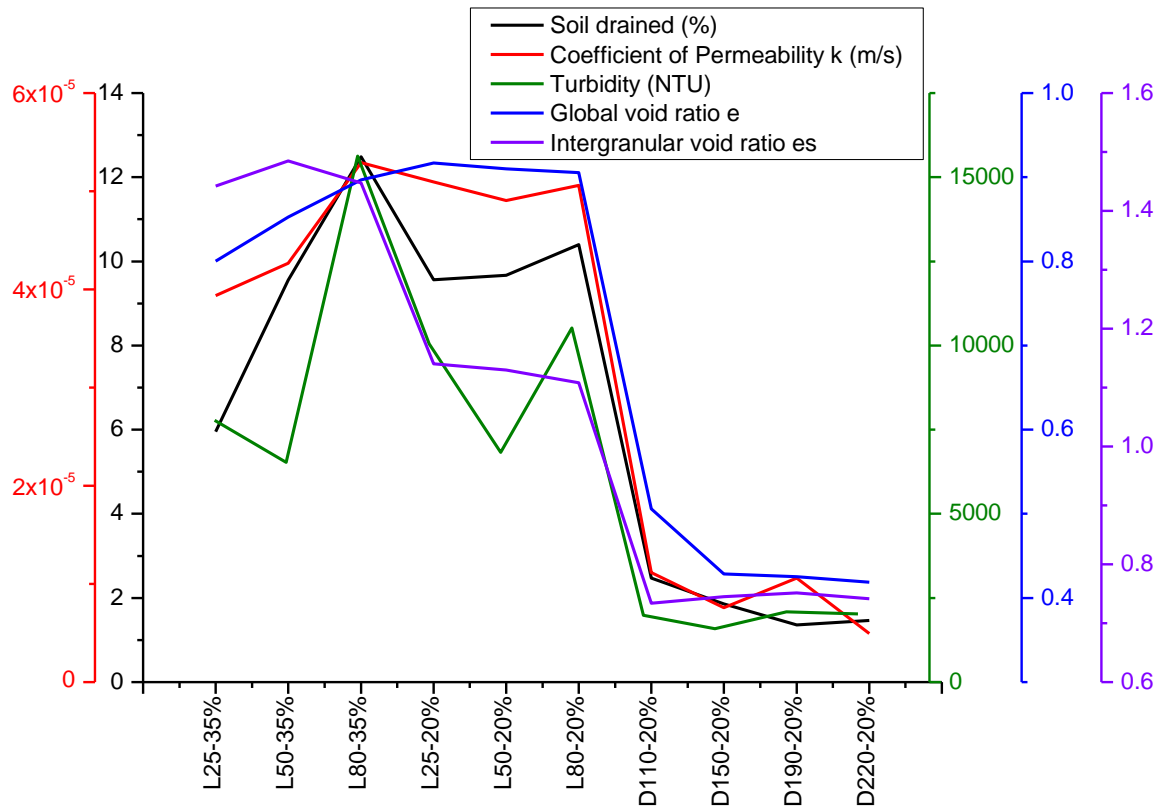


Figure 4-46 Summary of results

#### 4.11.2. Effects of the hydraulic gradient

Regarding to the hydraulic gradient, it has different effects depending on the initial relative density. In loose specimens the eroding effect is proportional to the hydraulic gradient, while in the dense specimens at higher hydraulic gradients the movement of particles is reduced. It is intuited that in the dense specimens, at very high hydraulic gradients the particles are moved so aggressively that it clogs the constrictions immediately. Yet, a middle hydraulic gradient moves the particles gently enough to displace them between constrictions without clogging.

#### 4.11.3. Effects of the initial fines content

In order to evaluate the effect of the initial fines content, specimens with the same density ( $D_r \approx 50\%$ ) but different initial percentage of DL clay (20% and 35%) were compared. The fines content influences the size of the pores and constrictions: A greater amount of fines

located in the intergranular space makes the size of constrictions larger and hence the influence of the hydraulic gradient is more perceptible.

There is a relation between the initial fines content and the hydraulic gradient: When the force of the water is low, it is easier to move the particles if there is less initial amount of these (because there is more separation between them and therefore weaker connections). But, at higher hydraulic gradients, the degree of erosion becomes governed by the force of water and not by the connectivity between particles (Figure 4-8).

#### *4.11.4. Grain size distribution*

The comparison of the grain size distribution between before and after the erosion by seepage, shows a reduction in the mass of the fines (particles with diameter lower than 0.106 mm), which are only the particles of DL clay. It means that the water seepage removes only the detached particles successfully, and the primary fabric remains in the specimen supporting the structure.

With the grain size distribution, it was also possible to estimate the amount of soil eroded (Figure 4-47). This figure can be compared with the results of total drained soil measured by oven drying (Figure 4-8). As the results obtained by the stretching method overestimate the amount of soil eroded, the comparison between the grain size distribution can be a reliable method to estimate the degree of erosion without keeping and measuring the particles drained out.

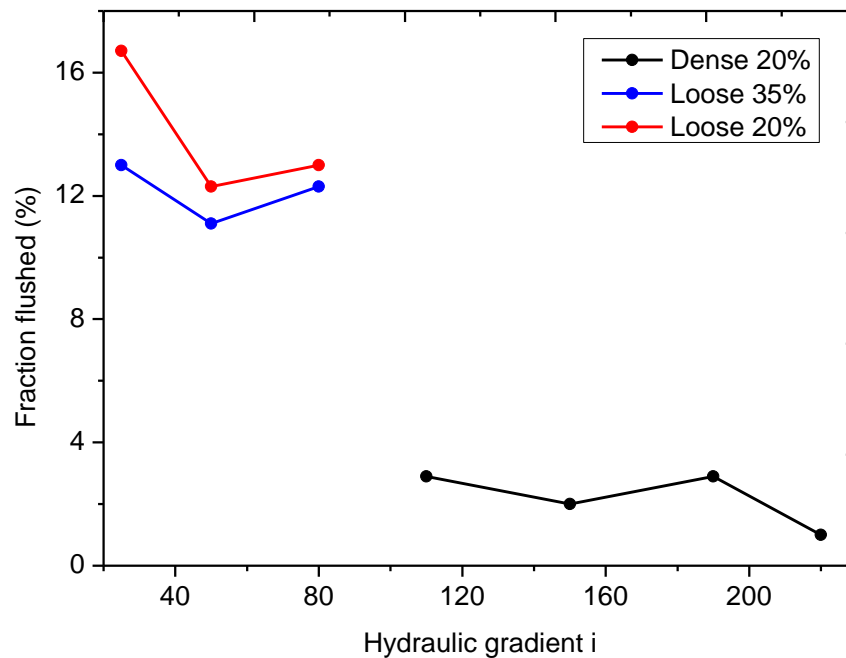


Figure 4-47 Fraction flushed vs. hydraulic gradient

#### 4.12. References

Head, K. H. (1985) Manual of Soil Laboratory Testing. Volume 2, Permeability, shear strength and compressibility tests.

Kenney, T.C. and Lau, D. (1985). Internal stability of granular filters. Canadian Geotechnical Journal, 22, 215 – 225. Can. Geotech. J. 45, 1303 – 1309.

Mitchell, J. K. (1976). Fundamentals of soil behavior, Wiley, New York.

Pazdro, Z. and Kozerski, B. (1990) Hydrogeologia ogólna. Wydawnictwa Geologiczne.

Terzaghi, K. and Peck, R.B. (1967) Soil Mechanics in Engineering Practice, Second Edition: John Wiley & Sons, New York.

## Chapter 5. Evaluation of the mechanical properties by hollow cylindrical torsional shear test

### 5.1. General

In order to evaluate the mechanical characteristics of soils subjected to suffusion, a series drained tests using the hollow cylindrical torsional shear apparatus have been carried out. The results of the tests explained previously in Chapter 3 are described and analyzed in this chapter. The experiments performed aim to evaluate the impact of the erosion by suffusion considering the variation of density, erosion degree and confining stress, as follows:

- Variation of density:
  - (a) Dense specimens  $D_r \approx 97\%$
  - (b) Medium dense specimens  $D_r \approx 75\%$
  - (c) Loose specimens  $D_r \approx 50\%$
  - (d) Dense and loose specimens with reduced density  $D_r = 95\%$  and  $D_r = 46\%$
- Variation of erosion degree
  - (a) Non-eroded tests
  - (b) Eroded before shearing
  - (c) Eroded before and during shearing
- Variation of the confining stress
  - (a)  $\sigma_z = \sigma_r = \sigma_\theta = 60kPa$
  - (b)  $\sigma_z = \sigma_r = \sigma_\theta = 150kPa$

The tests carried out are listed in Table 5-1.

Table 5-1 Torsional tests conditions

$\sigma_c$ (kPa)	Density	$\rho_d$ (g/cm <sup>3</sup> )	$D_r$ (%)	Erosion	ID
60	Dense	1.90	98	Non-eroded	D-NE-60
		1.90	98	Eroded before shearing	D-EbSH-60
		1.89	97	Eroded before and during shearing	D-Eb&dSH-60
		1.88	94	Non-eroded	D-NE-60 (Dr95)
	Medium	1.79	75	Non-eroded	M-NE-60
		1.78	74	Eroded before shearing	M-EbSH-60
		1.79	76	Eroded before and during shearing	M-Eb&dSH-60
	Loose	1.69	51	Non-eroded	L-NE-60
		1.68	51	Eroded before shearing	L-EbSH-60
		1.69	52	Eroded before and during shearing	L-Eb&dSH-60
		1.66	46	Non-eroded	L-NE-60 (Dr46)
150	Dense	1.90	98	Non-eroded	D-NE-150
		1.90	98	Eroded before shearing	D-EbSH-150
		1.89	97	Eroded before and during shearing	D-Eb&dSH-150
	Loose	1.70	55	Non-eroded	L-NE-150
		1.70	54	Eroded before shearing	L-EbSH-150
		1.70	54	Eroded before and during shearing	L-Eb&dSH-150

## 5.2. Eroded soil and turbidity

As explained previously, the value of turbidity is correlated with the amount of eroded soil. The cumulative percentage of eroded soil and the variation of turbidity are discussed below:

### 5.2.1. Specimens confined at $\sigma_z = \sigma_r = \sigma_\theta = 60\text{kPa}$

For the specimens confined at isotropic stress of 60 kPa, the pressure applied to the to the upper tank is 45kPa, equivalent to a hydraulic gradient of  $i = 50$ . Figure 5-1 shows the variation of the turbidity and the cumulative amount of eroded soil during the test in the dense specimen ( $D_r = 98\%$ ) eroded before shearing (D-EbSH-60). The turbidity reaches its maximum values with the first infiltrations and decreases through the continuous seepage (the same trend was observed in the one-dimensional columns permeability tests). The test was stopped when the turbidity reached around 100 NTU. The maximum amount of eroded soil in this test was 3.0% and the total volume of water passed was 4500 ml (3 tanks of water).

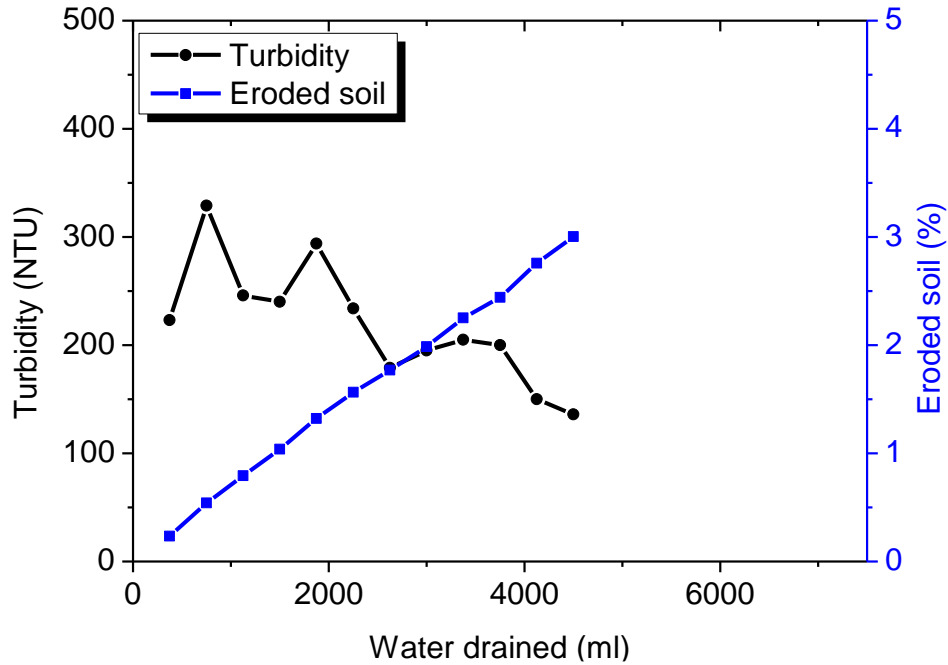


Figure 5-1 Eroded soil and turbidity. Dense eroded before shearing D-EbSH-60

The procedure for the tests eroded before and during shearing was explained in detail in the Chapter 3, 3.3.3 Test procedure. Basically the water seepage is applied to the specimen at different shear stress values (10, 20, 30 and 40 kPa) as shown in Figure 5-2. Firstly, the specimen is sheared until the specified value of shear stress, then after the application of small torsional cyclic loading (STCL) the specimen is maintained in creep, where the seepage is applied and the turbidity is measured until it reaches again lower values (around 100 NTU). After this the STCL is applied and the test continue to the next value of shear stress.

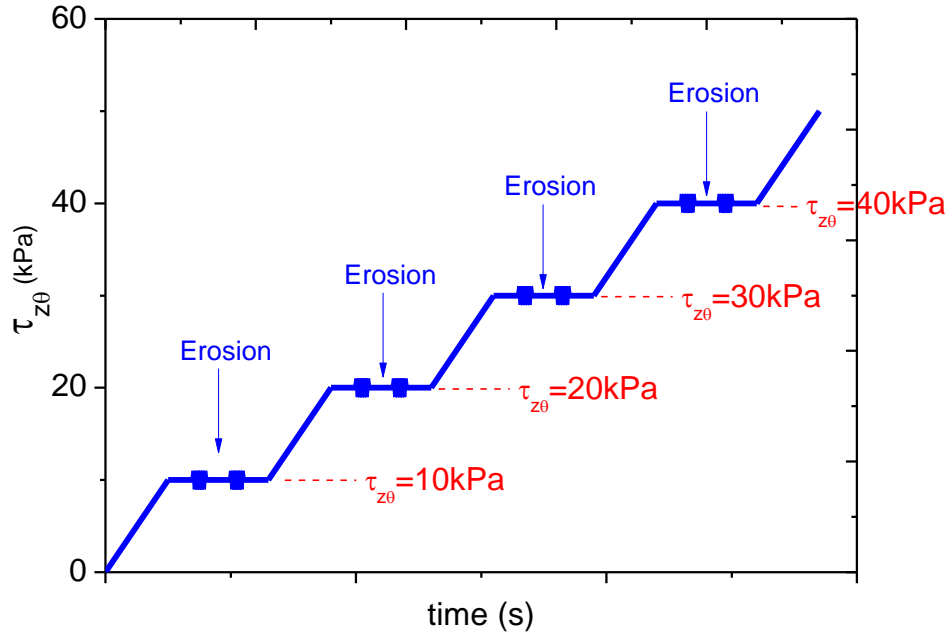


Figure 5-2 Schematic erosion procedure during torsional shearing

Referring to Figure 5-3, the variation of eroded soil and turbidity for the dense specimen ( $D_r = 97\%$ ) eroded before and during shearing is illustrated. A similar trend to specimen D-EbSH-60 is obtained before the shearing stage, in which the turbidity is higher at the beginning of the erosion and then decreases until reaching a value close to 100 NTU at 4500 ml, resulting in 2.6% of eroded soil.

After this point, torsional shear is applied up to  $\tau_{z\theta} = 10\text{kPa}$ . The turbidity value increases suddenly from 128 NTU to 293 NTU with the first cycle of water infiltration (375 ml). The turbidity value decreases to 127 NTU in the second cycle of water infiltration where the erosion was regarded insignificant. The specimen was sheared until the next shear stress of  $\tau_{z\theta} = 20\text{kPa}$ , where the same behavior was observed, as well as for  $\tau_{z\theta} = 30\text{kPa}$  and  $\tau_{z\theta} = 40\text{kPa}$ .



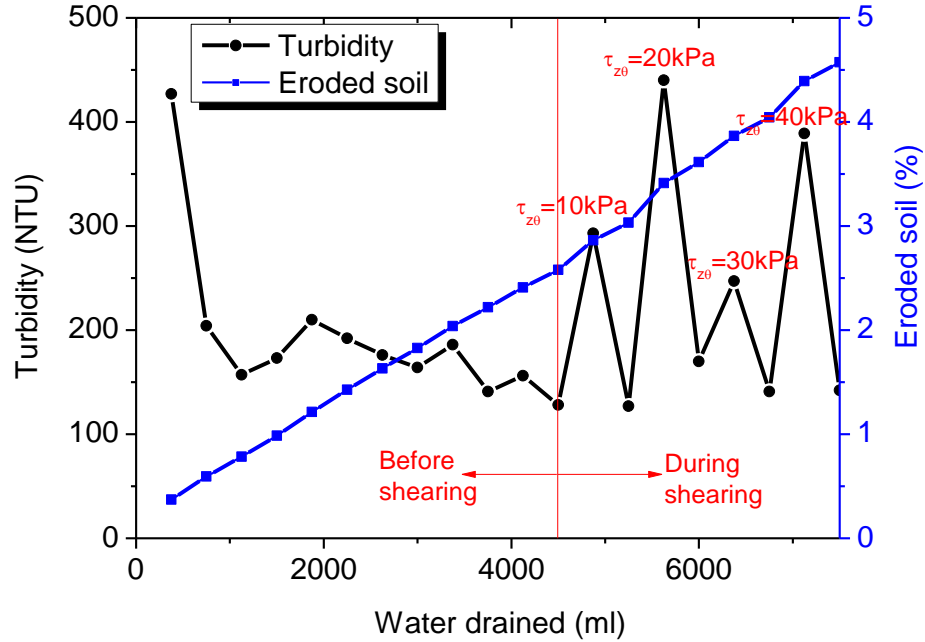


Figure 5-3 Eroded soil and turbidity. D-Eb&amp;dSH-60

In the medium dense specimens ( $D_r = 74\%$ ) the turbidity value is higher (around 550 NTU) compared to the dense specimens (around 425 NTU); more volume of water was needed to apply until the turbidity value decreased to a stable value. Specifically, 6000 ml of water was applied for these cases (4 tanks of water) (Figure 5-4).

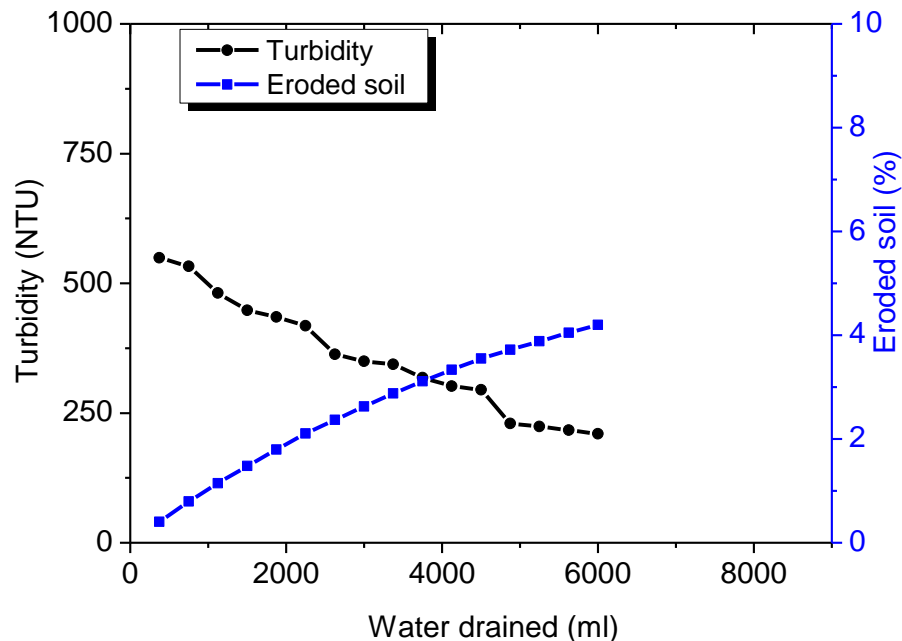


Figure 5-4 Eroded soil and turbidity. Medium eroded before shearing M-EbSH-60

A similar behavior is observed in the test eroded before and during shearing (Figure 5-5) compared to the dense specimen results. After the shearing at  $\tau_{z\theta} = 10\text{kPa}$  the first cycle of water induces an increase of the turbidity up to 901 NTU, and two more cycles of water infiltration were needed to reduce the turbidity value to the initial levels. After the erosion stage of  $\tau_{z\theta} = 20\text{kPa}$ , the shear stresses of  $\tau_{z\theta} = 30\text{kPa}$  and  $\tau_{z\theta} = 40\text{kPa}$  were applied but the turbidity value did not increase.

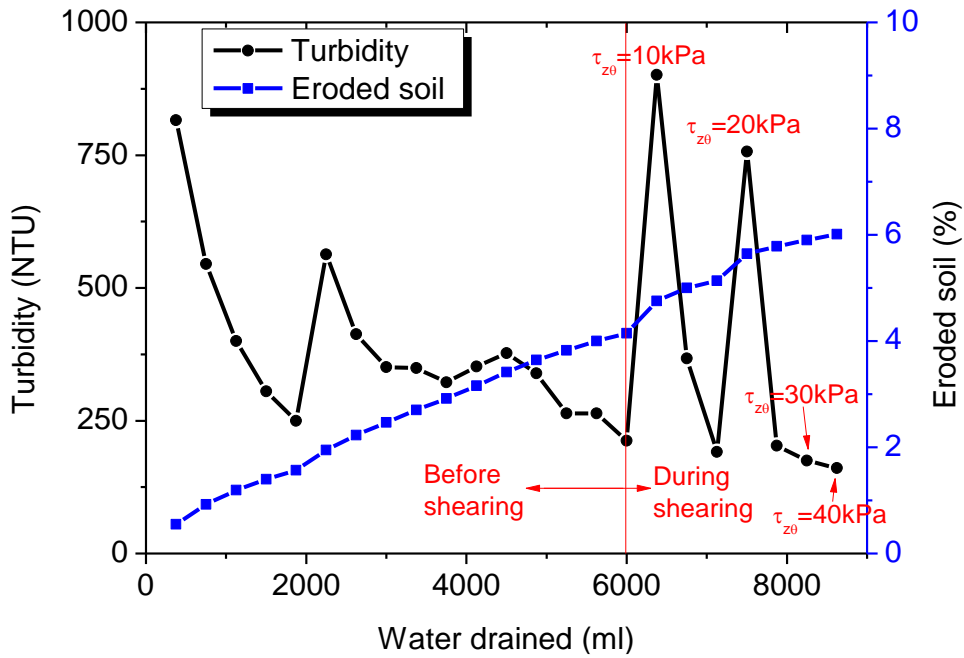


Figure 5-5 Eroded soil and turbidity. Medium eroded before and during shearing M-Eb&dSH-60

A similar trend is obtained in the loose specimens ( $D_r = 51\%$ ) (Figure 5-6 and Figure 5-7), but with higher turbidity values and amount of total eroded soil. Accordingly, it was necessary to infiltrate more water (6000 and 8625ml). The percentage of eroded soil obtained in the tests confined at 60 kPa is summarized in Table 5-2.

Table 5-2 Eroded soil in the tests confined at 60kPa

Density	Eroded soil before shearing	Eroded soil after shearing
Dense	3.0%	4.6%
Medium	4.2%	6.0%
Loose	6.1%	8.2%

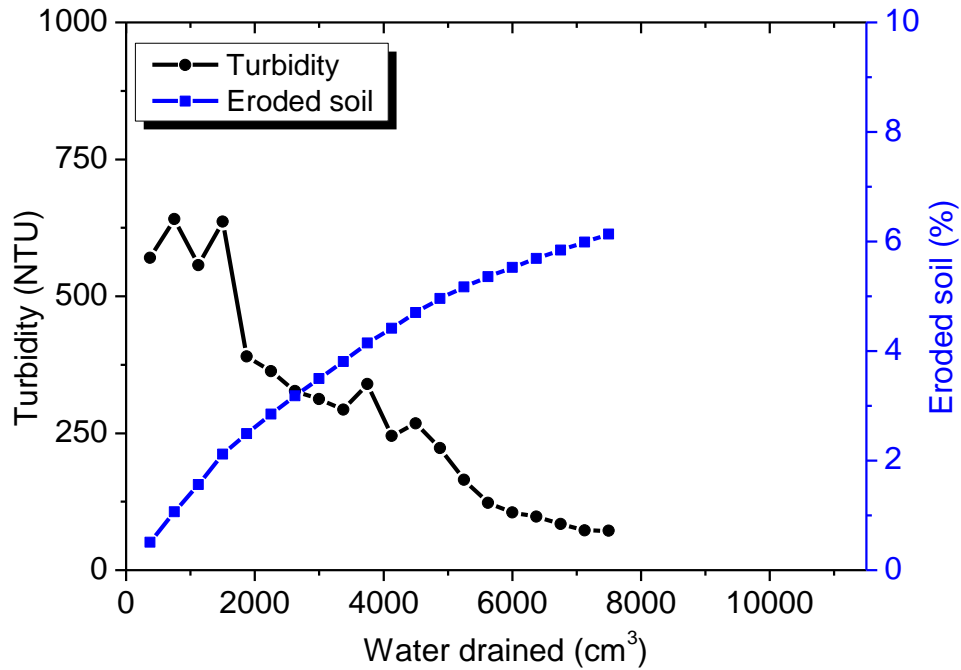


Figure 5-6 Eroded soil and turbidity. Loose eroded before shearing L-EbSH-60

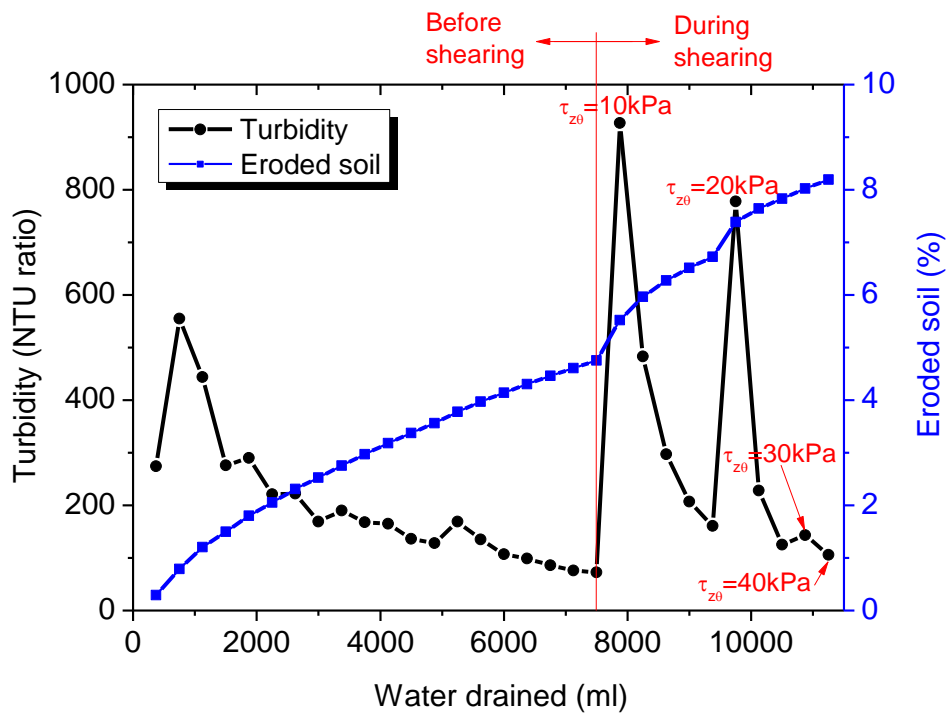


Figure 5-7 Eroded soil and turbidity. Loose eroded before and during shearing L-Eb&dSH-60

### 5.2.2. Specimens confined at $\sigma_z = \sigma_r = \sigma_\theta = 150\text{kPa}$

Some experiments were carried out at the higher confining pressure of 150 kPa using specimens with the extreme densities (dense and loose). These experiments were performed to compare the results with the specimens confined at 60 kPa, and so the same percentage of eroded soil was sought (similar values to Table 5-2). Therefore, the seepage was stopped when the same percentage of eroded soil was achieved without considering the turbidity value.

In the experiments confined at 60 kPa the pressure applied to the tank of water was 45 kPa, and so the effective stress in the specimen was around 15 kPa (at the top of the specimen, since the bottom tank is at atmospheric pressure). For the experiments confined at 150 kPa the same effective stress of 15 kPa was considered, i.e. for the first experiment executed (dense specimen ( $D_r = 98\%$ ) eroded before shearing), the pressure applied to the water was 135 kPa.

The turbidity obtained at the first cycle of water infiltration was 2907 NTU (Figure 5-8), which is considerably greater than that obtained for the similar specimen confined at a lower pressure level (223 NTU). As the same degree of erosion was achieved, the pressure was reduced to 45 kPa in the next cycle of water infiltration, with which the erosion induced was similar (2.8%).

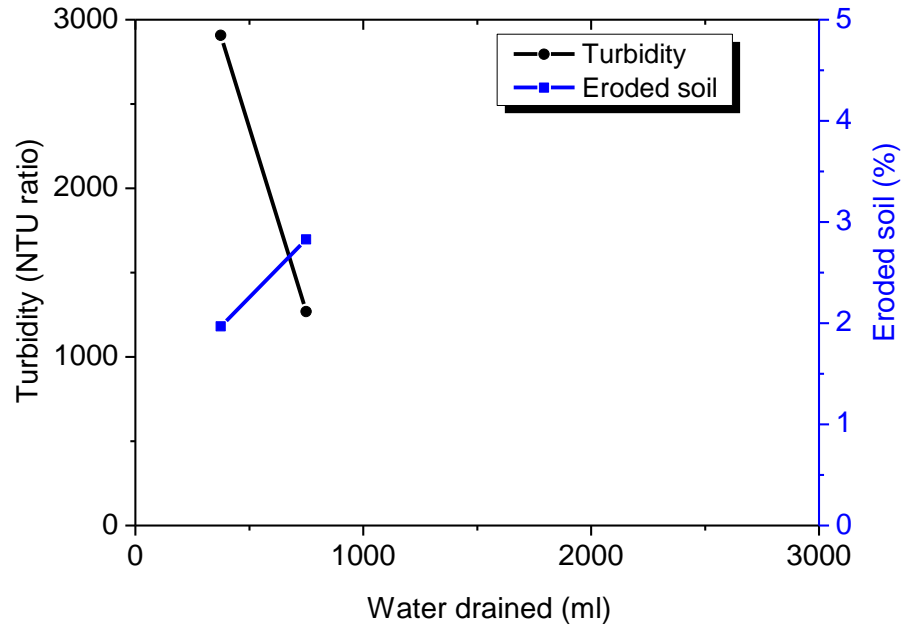


Figure 5-8 Eroded soil and turbidity. Dense eroded before shearing D-EbSH-150

Therefore, for the experiments performed afterwards the pressure applied to the water was kept 45 kPa as in the previous experiments. Figure 5-9 shows the results for the dense specimen eroded before and during shearing. The shearing started when the eroded soil was around 3%.

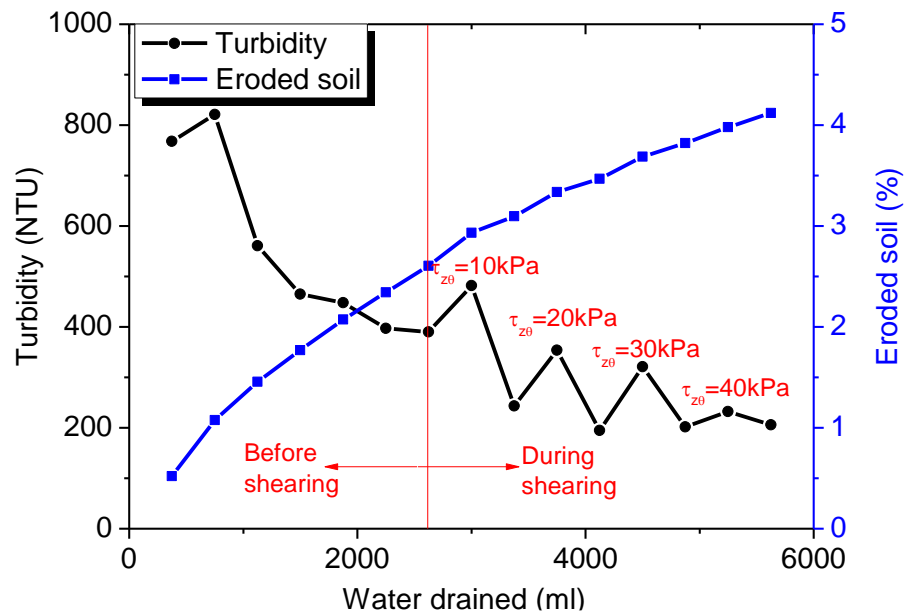


Figure 5-9 Eroded soil and turbidity. Dense eroded before and during shearing D-Eb&dSH-

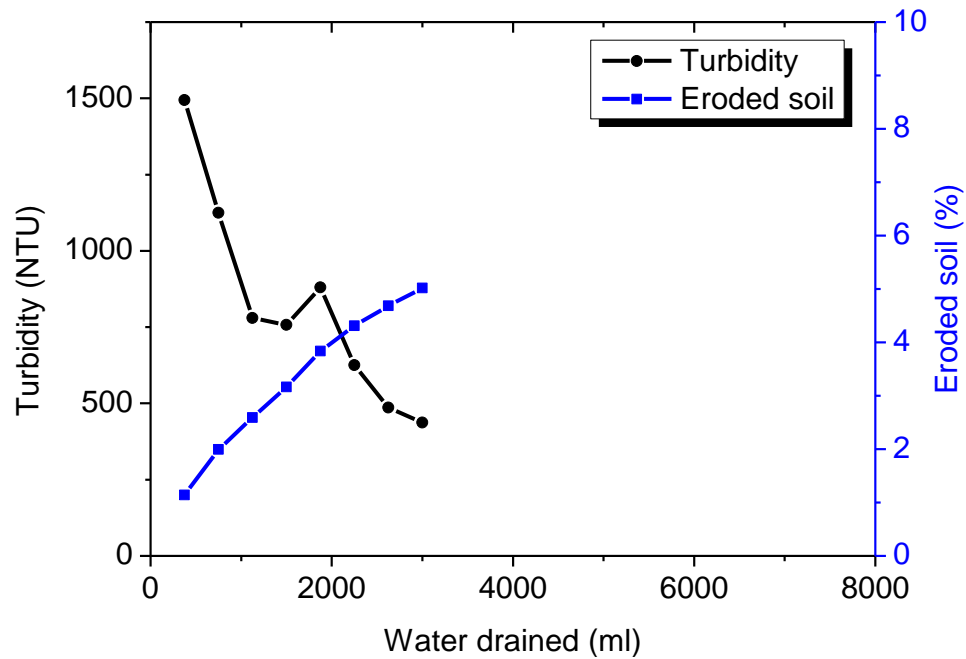


Figure 5-10 Eroded soil and turbidity. Loose eroded before shearing L-EbSH-150

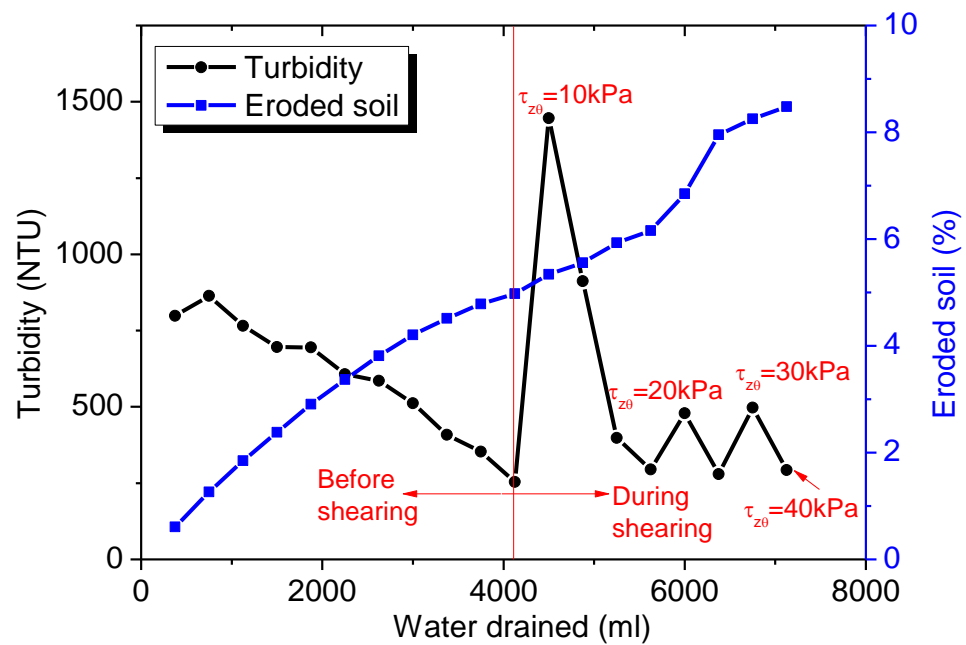


Figure 5-11 Eroded soil and turbidity. Loose eroded before and during shearing L-Eb&dSH-

Same procedure was repeated for the loose specimens. Their results are shown in Figure 5-10 and Figure 5-11, and the summary of the results for the experiments confined at 150 kPa is shown in Table 5-3.

Table 5-3 Eroded soil in the tests confined at 150kPa

Density	Eroded soil before shearing	Eroded soil after shearing
Dense	2.8%	4.1%
Loose	5.0%	8.5%

Figure 5-12 presents the total amount of soil eroded for all the test cases. It shows the comparison of the soil eroded in the specimens confined at 60 kPa (solid lines) and the specimens confined at 150 kPa (dashed lines).

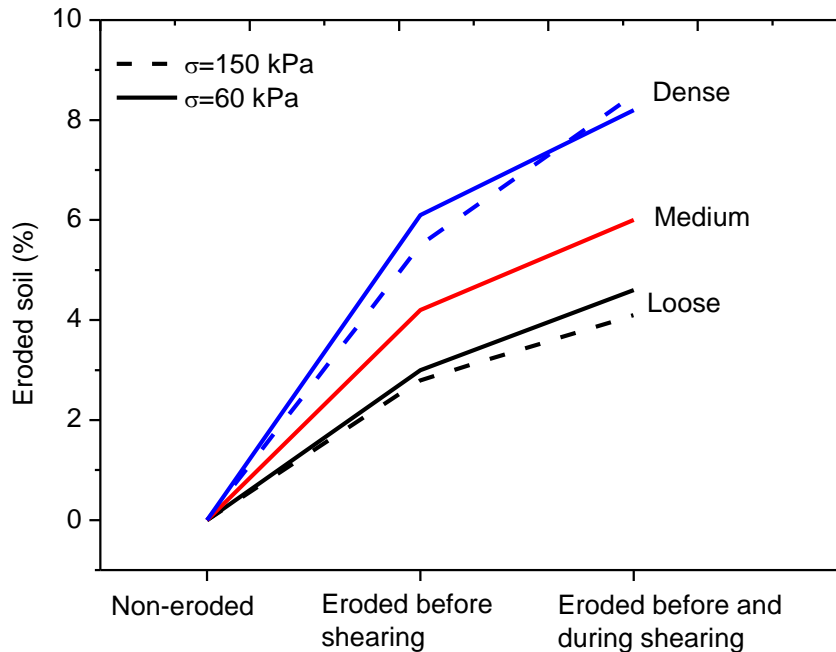


Figure 5-12 Final amount of eroded soil in all the experiments

### 5.2.3. Analysis

As mentioned previously, turbidity is related to the amount of eroded particles. Figure 5-13 shows the relationship between the value of turbidity and the corresponding slope of the curve of cumulative eroded soil, representing the increment of eroded particles. This slope is large at the beginning of the experiments when the turbidity is high, and decreases along the test down to near zero meaning that no more particles are being displaced out of the specimen.

In Figure 5-13 all the curves have similar trends: the value of turbidity is proportional to the increment of eroded soil. The variation in the slope of these curves is small but shows some trend depending on the density and confining pressure. The variation in turbidity value could be expressed as a function of the increment of eroded soil with a constant slope  $n$ . Figure 5-14 shows the variation of  $n$  at different confining pressures and relative densities. Note that the  $n$  value depends on the interval of data points in the horizontal axis (waver drained) (see Figure 5-11); however, a constant interval of the data points was used for all the experimental data presented here.

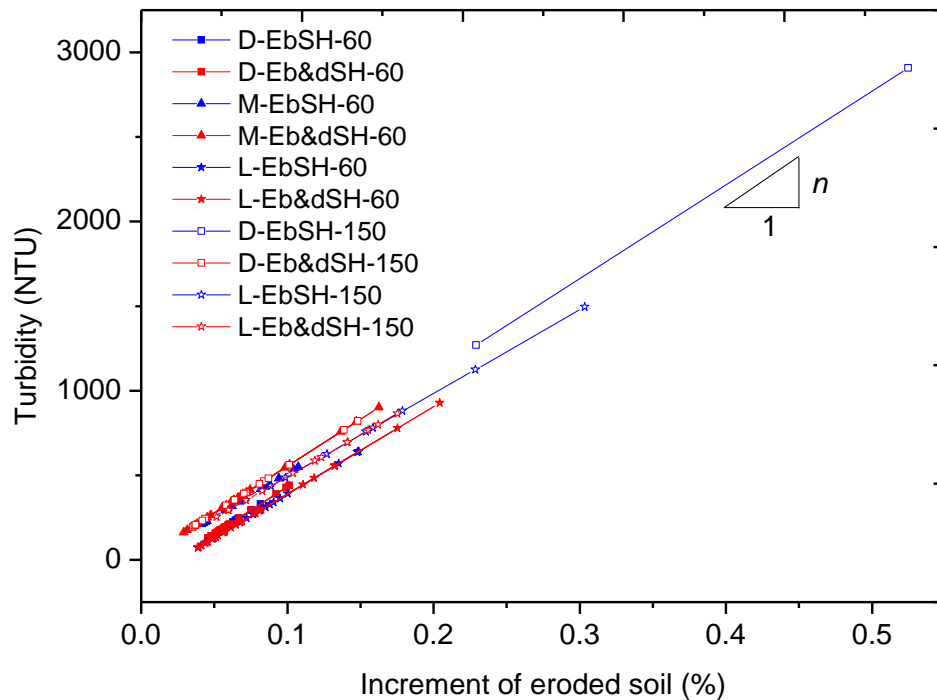


Figure 5-13 Turbidity vs. increment of eroded soil



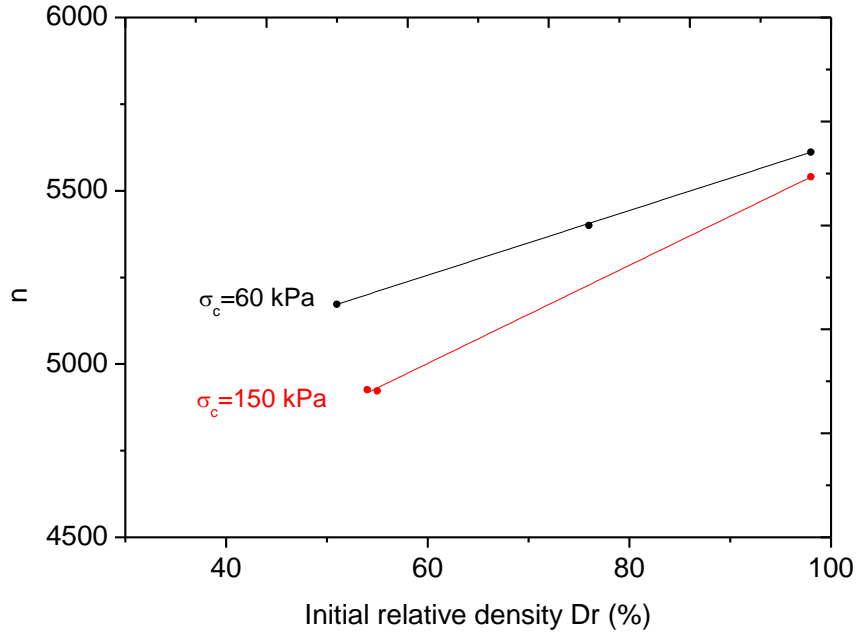


Figure 5-14 Increment of eroded soil with varying relative density and confining pressure

The lower the  $n$  value is, the greater the incremental amount of eroded soil becomes for a given value of turbidity. From Figure 5-14 it can be concluded that the increment of eroded soil in the loose specimens is higher than in that in the dense specimens. In addition, in the specimens confined at higher pressures, the increment is also larger. Therefore, the erosion seems to be easier if the density is low and the confining stress is high for a given value of turbidity.

### 5.3. Volumetric strain

#### 5.3.1. Specimens confined at $\sigma_z = \sigma_r = \sigma_\theta = 60 \text{ kPa}$

For all the specimens, the volumetric strain ( $e_{vol}$ ) increased during the increment of the confining pressure from 30 kPa (setup) to 60 kPa. In the same way, during the erosion process before shearing, the volumetric strain increased (shrinkage of the specimen) caused by the drainage of the fines. During the first stages of torsional shearing (0 to 40 kPa), the volumetric strain remains stable (Figure 5-15, Figure 5-16 and Figure 5-17).

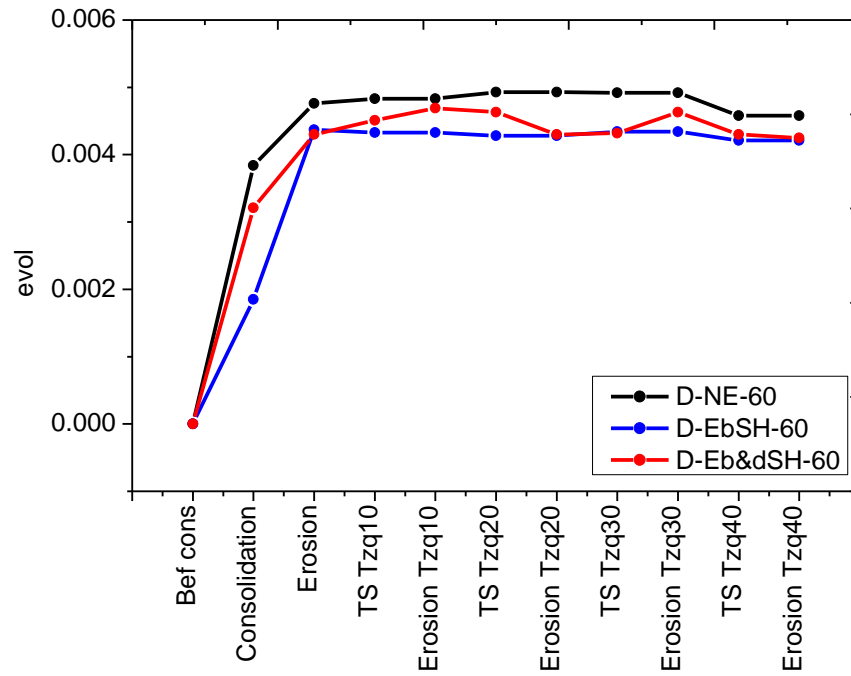


Figure 5-15 Volumetric strain Dense  $\sigma=60$  kPa

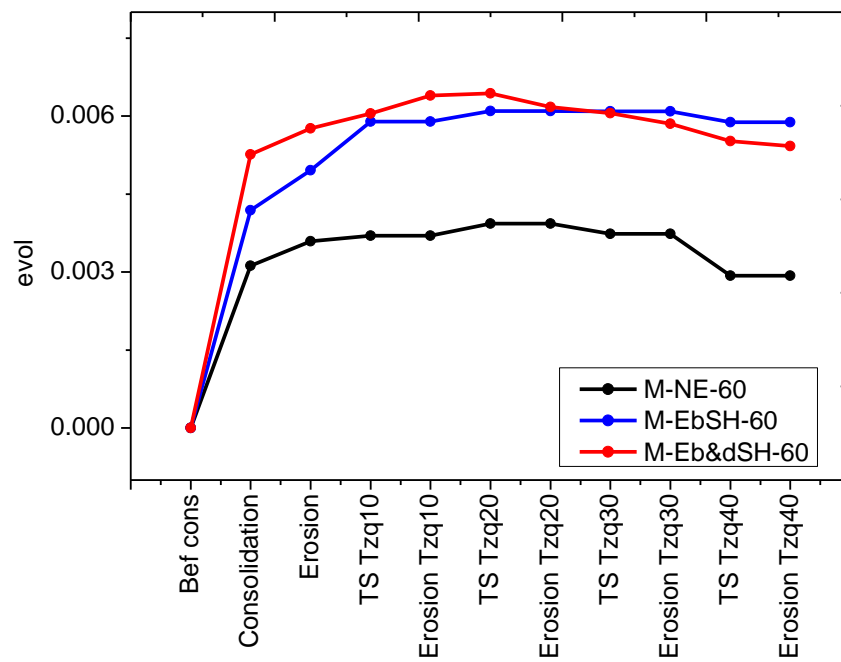
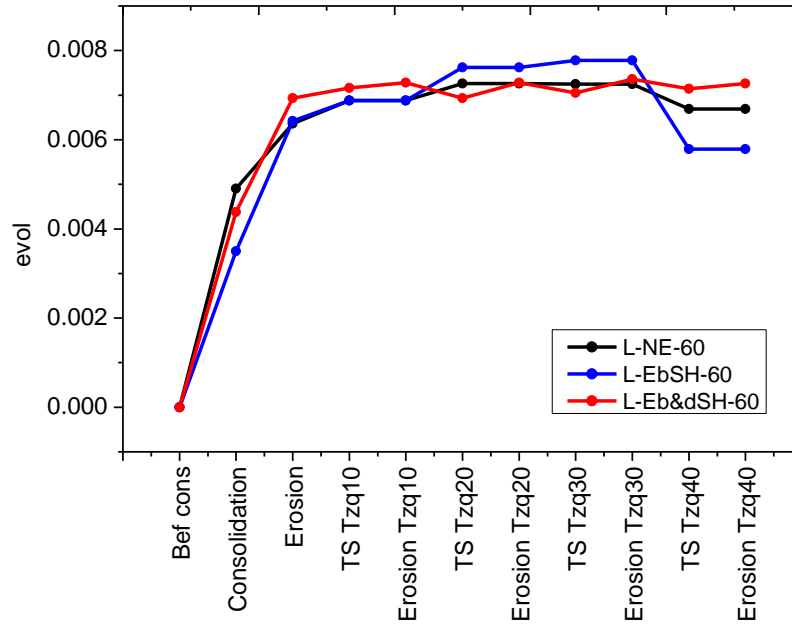
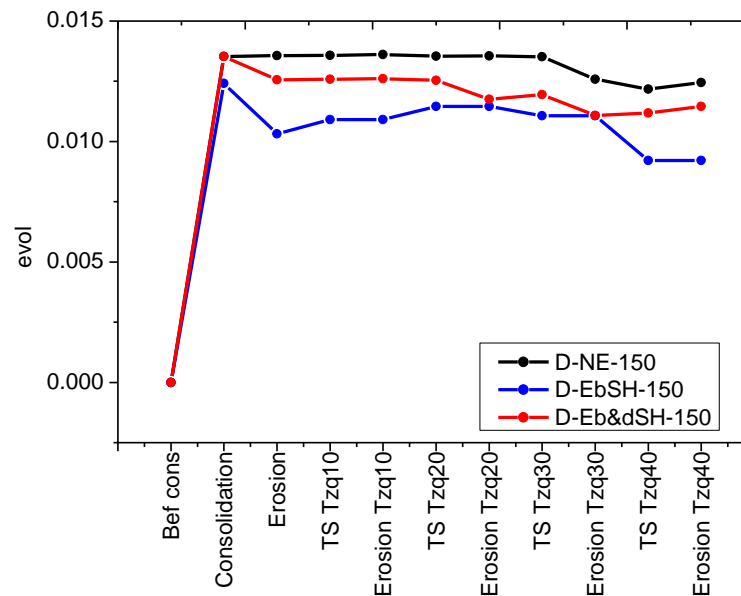


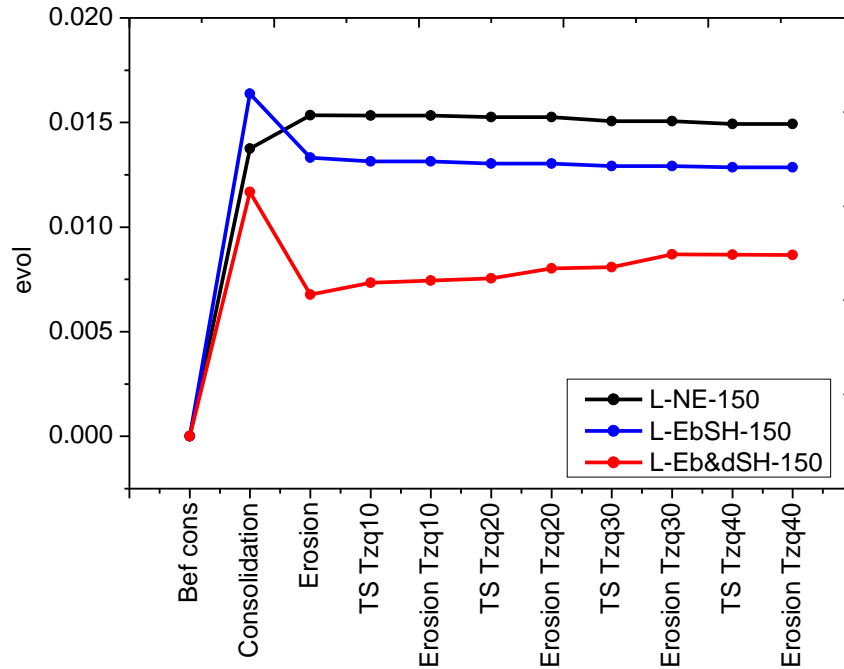
Figure 5-16 Volumetric strain Medium  $\sigma=60$  kPa

Figure 5-17 Volumetric strain Loose  $\sigma=60$  kPa

### 5.3.2. Specimens confined at $\sigma_z = \sigma_r = \sigma_\theta = 150$ kPa

The specimens confined at 150 kPa show a difference during the first erosion stage before shearing; their volumetric strain is slightly reduced during the initial seepage in the eroded tests. After this, the volumetric strain remains constant during the torsional shearing at small shear strains (Figure 5-18 and Figure 5-19).

Figure 5-18 Volumetric strain Dense  $\sigma=150$  kPa

Figure 5-19 Volumetric strain Loose  $\sigma=150$  kPa

### 5.3.3. Analysis

Figure 5-20 shows the variation of the volumetric strain in the specimens with maximum degree of erosion, i.e. eroded before and during shearing. During the torsional shearing, the volumetric strain remains constant for all the specimens; however, its value depends on the density in which the dense specimens contract to a lesser extent, compared with the looser specimens.

The specimens confined at the higher pressure (150 kPa) are more compressed isotropically, but exhibit insignificant changes in volume during shearing (Figure 5-20).

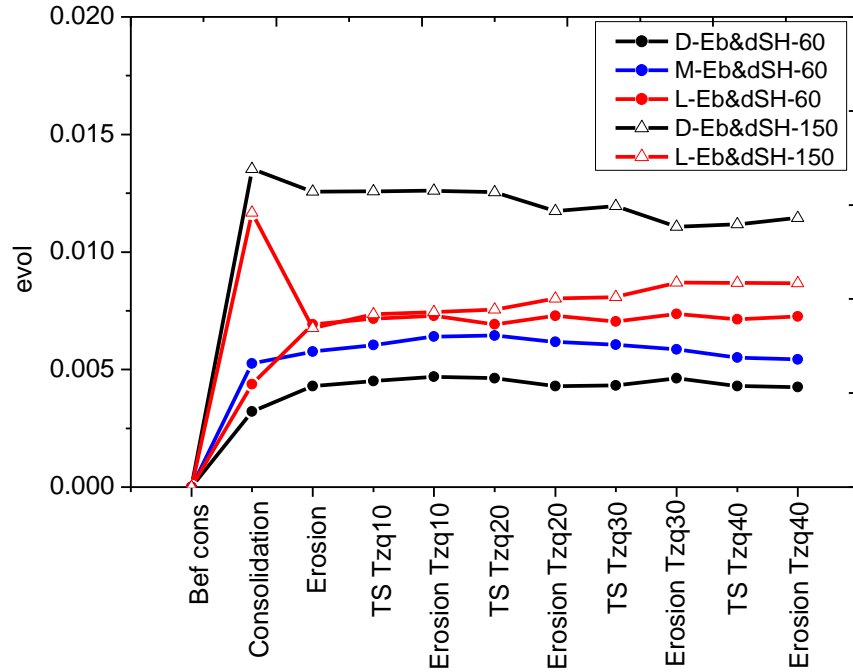


Figure 5-20 Comparison of volumetric strain for all the specimens with maximum erosion

#### 5.4. Global void ratio

##### 5.4.1. Specimens confined at $\sigma_z = \sigma_r = \sigma_\theta = 60kPa$

Figure 5-21, Figure 5-22 and Figure 5-23 show the variation of the global void ratio during consolidation, erosion and shearing. For the non-eroded specimens, the voids are reduced with increasing confining pressure, and remain constant during the first stages of torsional shearing (Black curves). For the eroded specimens, the voids are considerably increased during the seepage, confirming the expulsion of particles due to suffusion. For the specimens eroded before and during shearing, a stepwise increase in the void ratio can be observed in each water infiltration during torsional shearing (red curves).

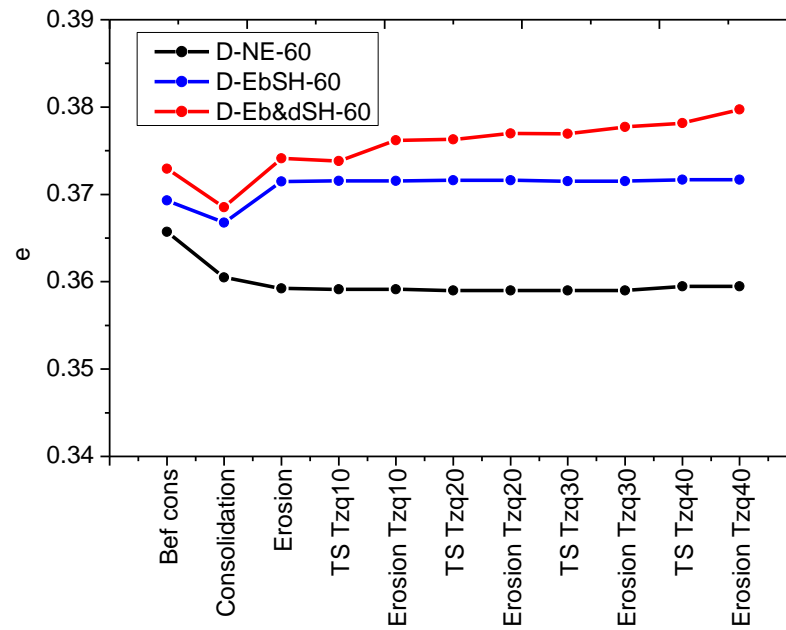


Figure 5-21 Global void ratio Dense  $\sigma=60$  kPa

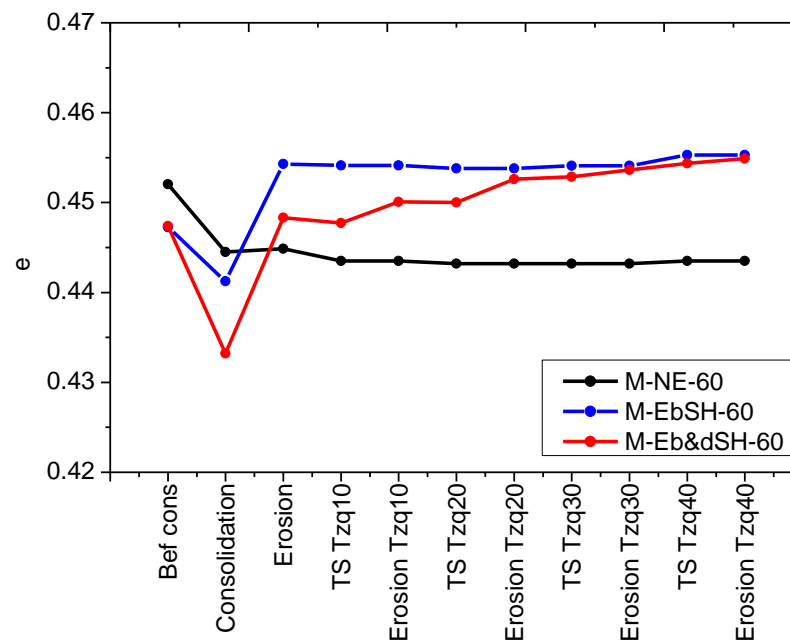
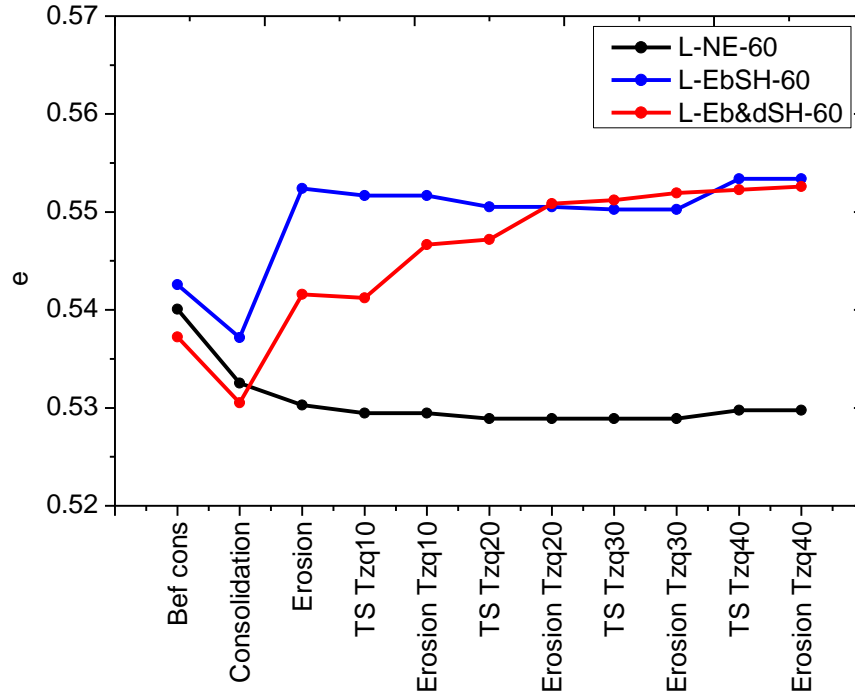
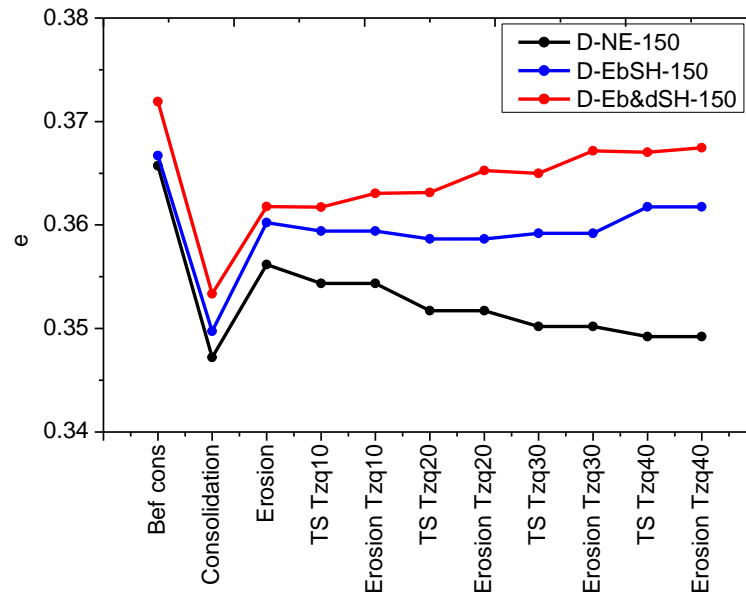


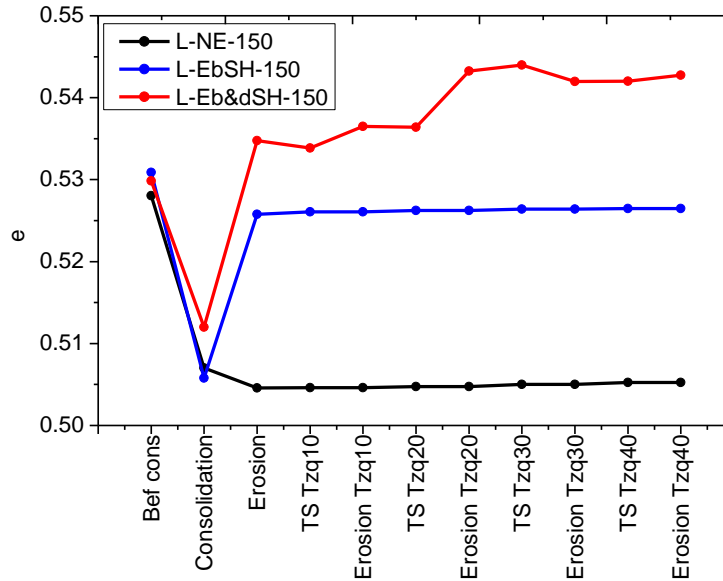
Figure 5-22 Global void ratio Medium  $\sigma=60$  kPa


 Figure 5-23 Global void ratio Loose  $\sigma=60$  kPa

#### 5.4.2. Specimens confined at $\sigma_z = \sigma_r = \sigma_\theta = 150$ kPa

For the specimens confined at 150 kPa, a similar behavior is exhibited (Figure 5-24 and Figure 5-25).


 Figure 5-24 Global void ratio Dense  $\sigma=150$  kPa

Figure 5-25 Global void ratio Loose  $\sigma=150$  kPa

#### 5.4.3. Analysis

Figure 5-26 shows the influence of the initial density of the specimens on the variation in void ratio during the test stages. As expected, the denser specimens have a smaller void ratio. However, the confining pressure does not influence the variation of void ratio, as the similar curves are observed for the specimens with same densities but different confining pressure.

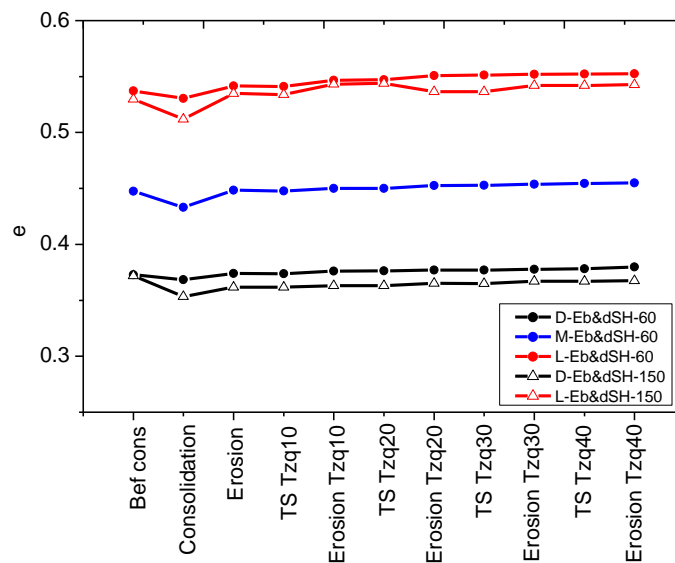


Figure 5-26 Comparison of the global void ratio for all the specimens with maximum erosion



### 5.5. Intergranular void ratio

As mentioned previously in Chapter 2, the intergranular void ratio ( $e_s$ ) is defined as the void ratio of the original coarser-grains matrix structure if the fines were removed from there. The intergranular void ratio can be used as an index of the active contacts of the primary fabric that support the stresses (Thevanayagam, 1998).

#### 5.5.1. Specimens confined at $\sigma_z = \sigma_r = \sigma_\theta = 60 \text{ kPa}$

Unlike the global void ratio, the intergranular void ratio ( $e_s$ ) decreases just slightly during increasing of confining pressure, which means that the voids made by the contacts between the coarse particles is unaffected, and that the change in the global void ratio is mostly because of the compression of the volume filled by fines.

The water seepage for erosion induces a decrease in  $e_s$ , this means that the intergranular spaces of the primary fabric are closing due to the escape of the detached particles. This reduction is more evident with lower density of the soil (Figure 5-27, Figure 5-28 and Figure 5-29).

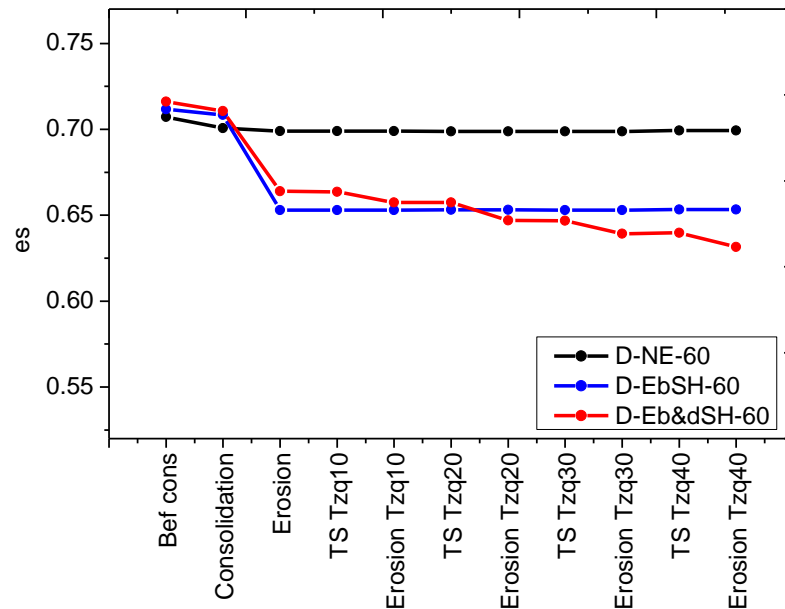


Figure 5-27 Intergranular void ratio Dense  $\sigma=60 \text{ kPa}$

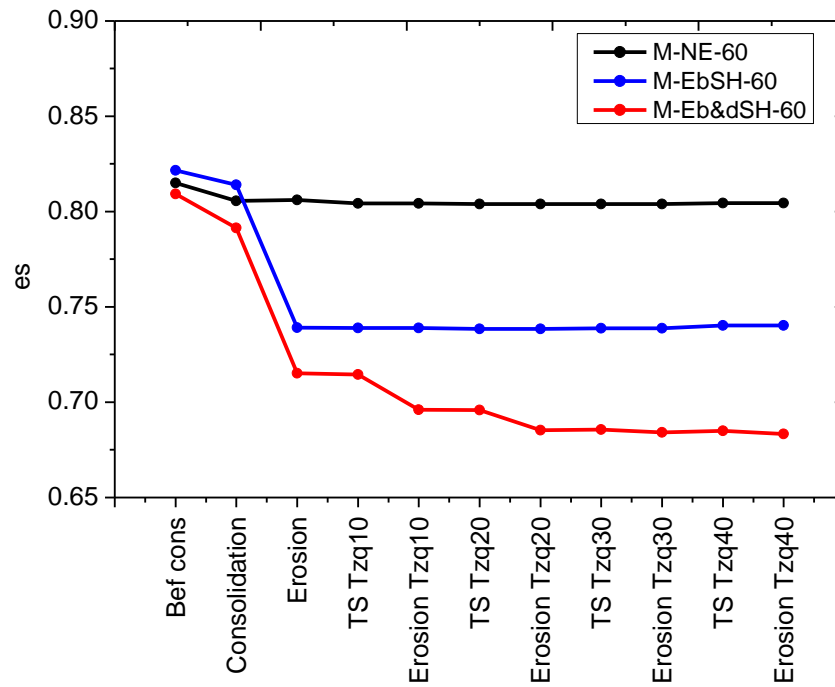


Figure 5-28 Intergranular void ratio Medium  $\sigma=60$  kPa

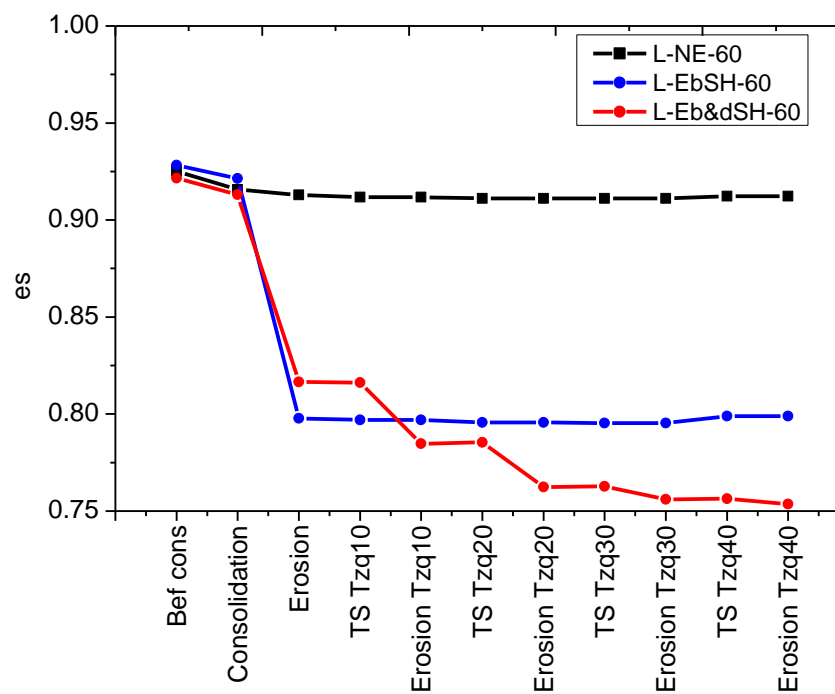


Figure 5-29 Intergranular void ratio Loose  $\sigma=60$  kPa

### 5.5.2. Specimens confined at $\sigma_z = \sigma_r = \sigma_\theta = 150 \text{ kPa}$

When the soil is confined at the higher pressure, the effect of seepage on the reduction in the pores made by the coarse grains is larger. Nevertheless, the size of the pores in the primary fabric is affected mostly by the erosion; this means that the fines located between the coarser particles contribute significantly to the size of pores.

It must be noted that the torsional shearing does not affect the variation of the intergranular void ratio, i.e. changes in  $e_s$  occur during water infiltration.

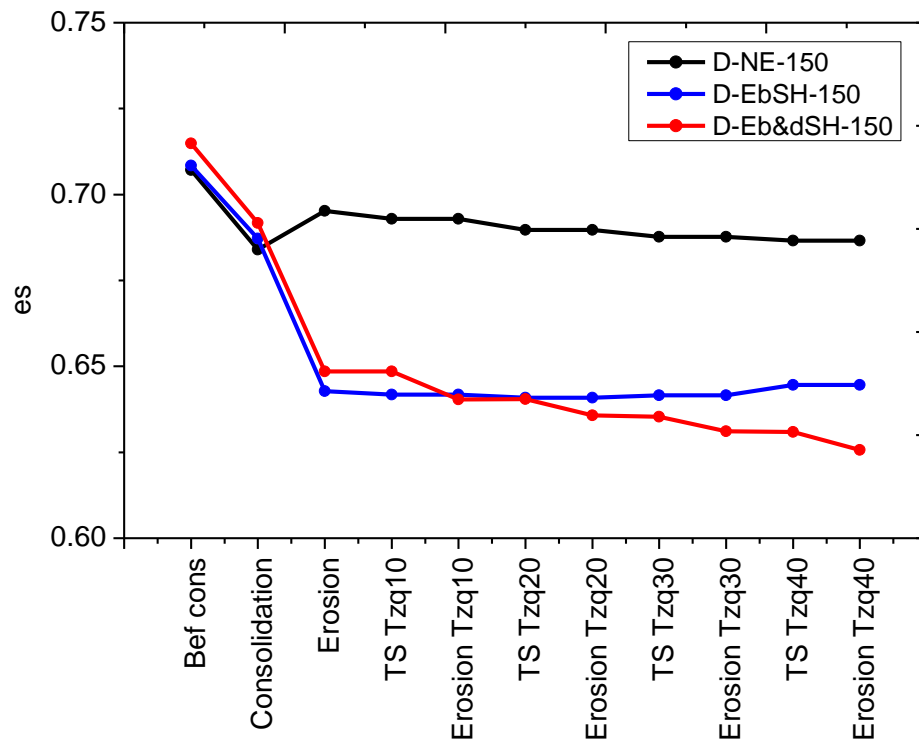
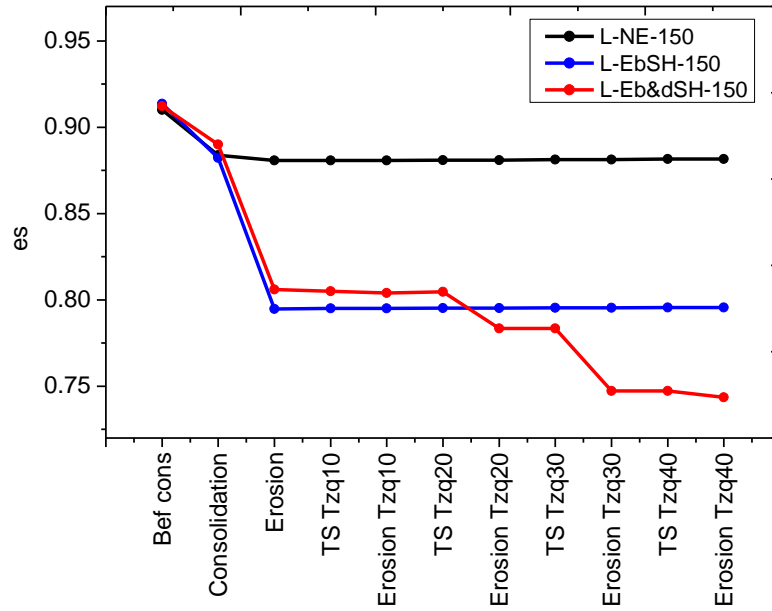


Figure 5-30 Intergranular void ratio Dense  $\sigma=150 \text{ kPa}$

Figure 5-31 Intergranular void ratio Loose  $\sigma=150$  kPa

### 5.5.3. Analysis

Figure 5-32 shows the variation in the intergranular void ratio of the specimens eroded. For the loose specimens the initial  $e_s$  value is larger, and the reduction of  $e_s$  during seepage is also larger than that for the dense soils. The difference in the confining pressure does not affect the variation of  $e_s$ .

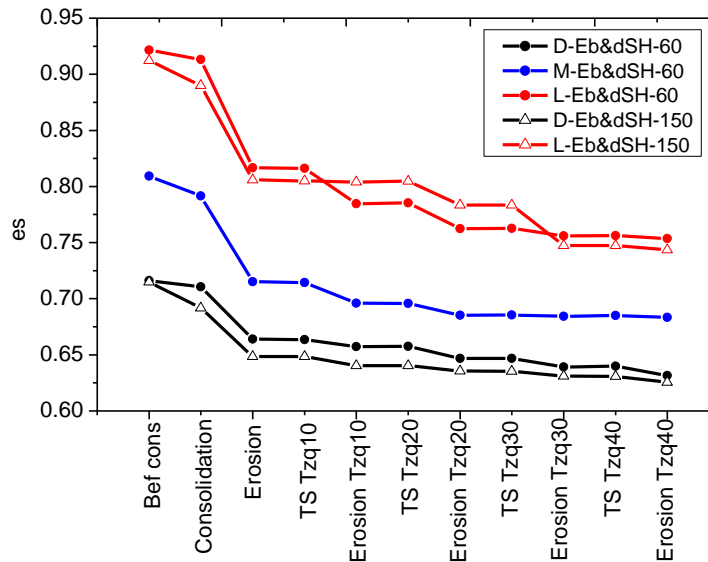


Figure 5-32 Comparison of the Intergranular void ratio for all the specimens max erosion

## 5.6. Relative Density

### 5.6.1. Specimens confined at $\sigma_z = \sigma_r = \sigma_\theta = 60 \text{ kPa}$

As a result of the variation in the global void ratio, the relative density rises with increasing confining pressure and decreases by the action of erosion (Figure 5-33, Figure 5-34 and Figure 5-35).

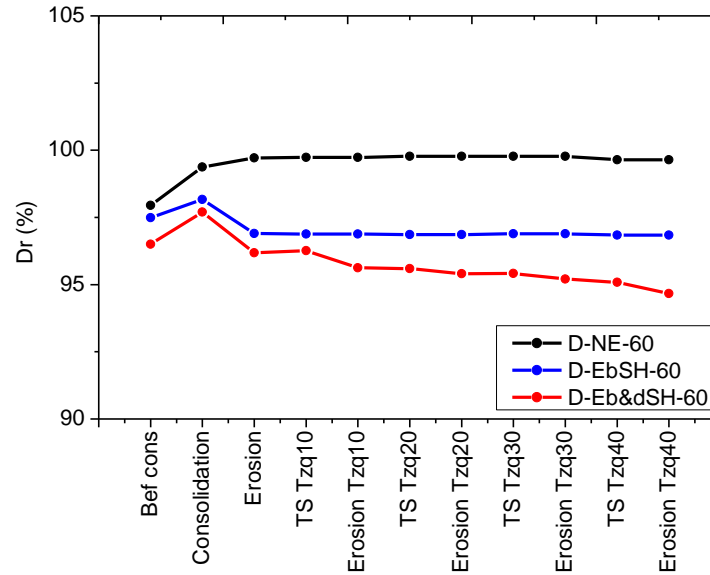


Figure 5-33 Relative density Dense  $\sigma=60 \text{ kPa}$

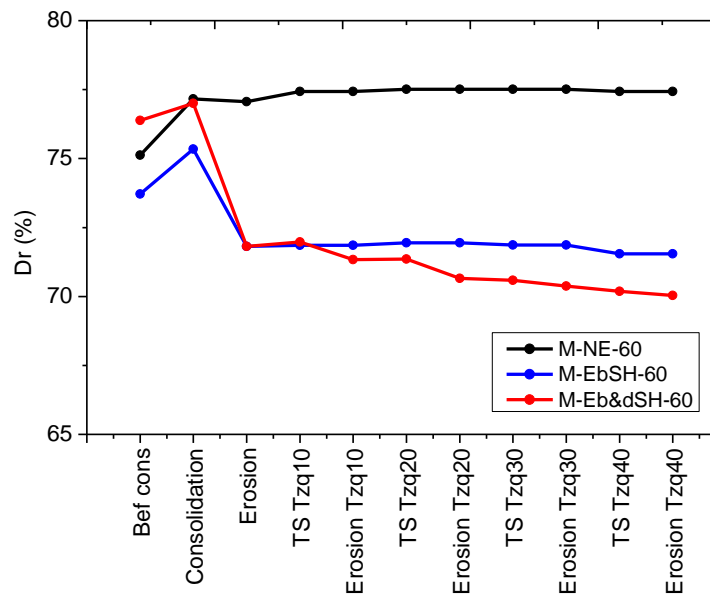


Figure 5-34 Relative density Medium  $\sigma=60 \text{ kPa}$

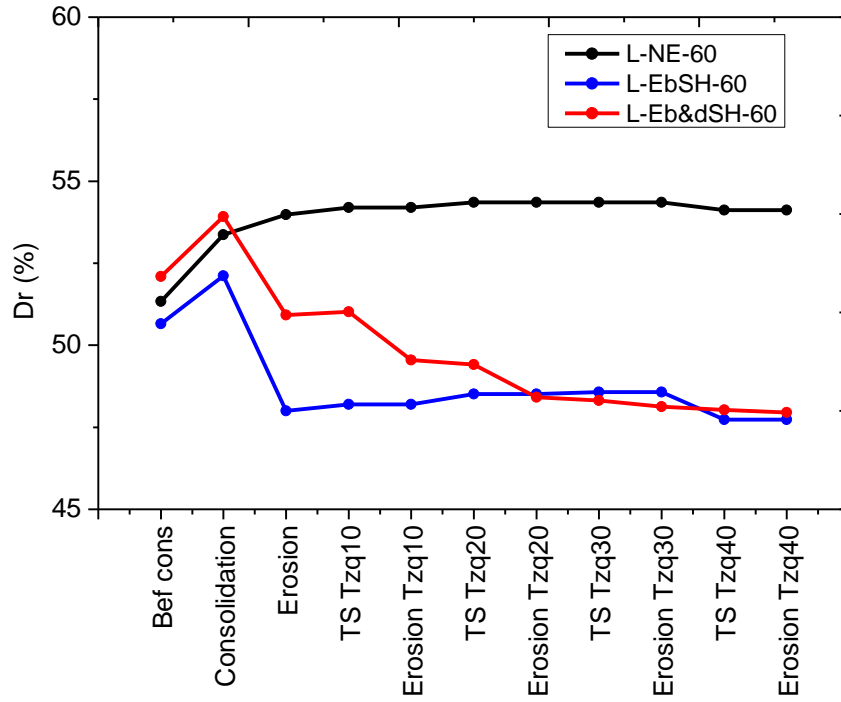


Figure 5-35 Relative density Loose  $\sigma=60$  kPa

#### 5.6.2. Specimens confined at $\sigma_z = \sigma_r = \sigma_\theta = 150$ kPa

Likewise, the specimens confined at 150 kPa present the same behavior (Figure 5-36, Figure 5-37).

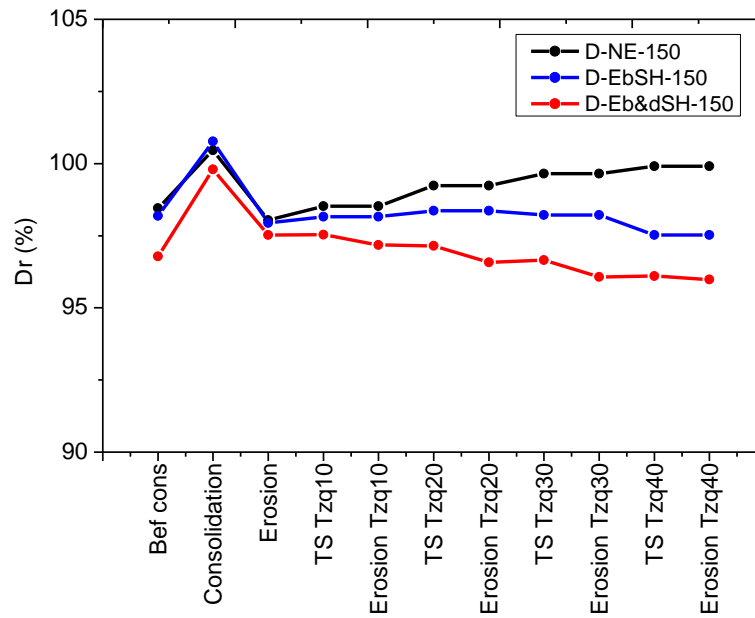
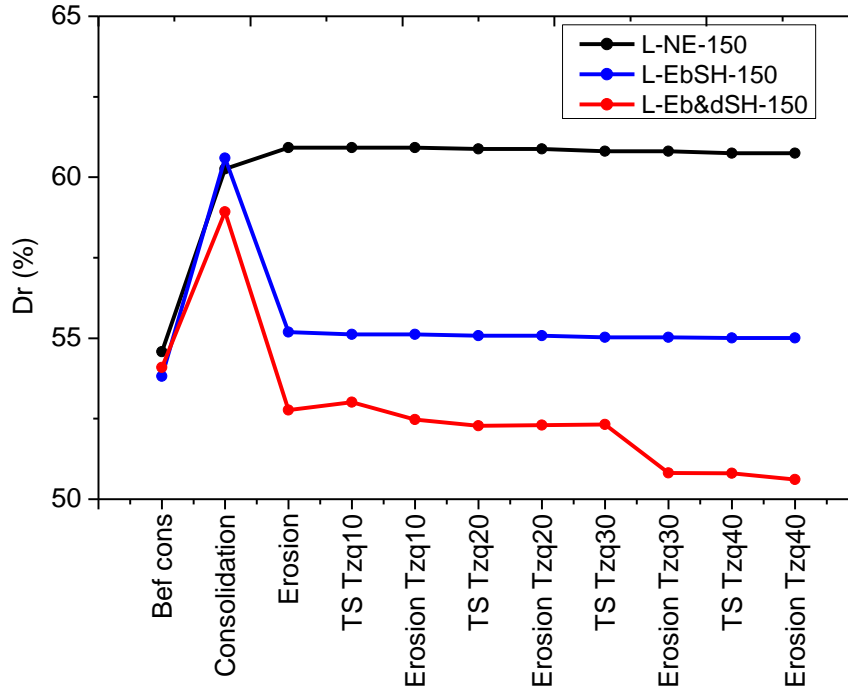


Figure 5-36 Relative density Dense  $\sigma=150$  kPa


 Figure 5-37 Relative density Loose  $\sigma=150$  kPa

### 5.6.3. Analysis

The relative density ( $D_r$ ) is influenced to some extent by the confining pressure, but the erosion seems to have a greater impact on  $D_r$  (Figure 5-38).

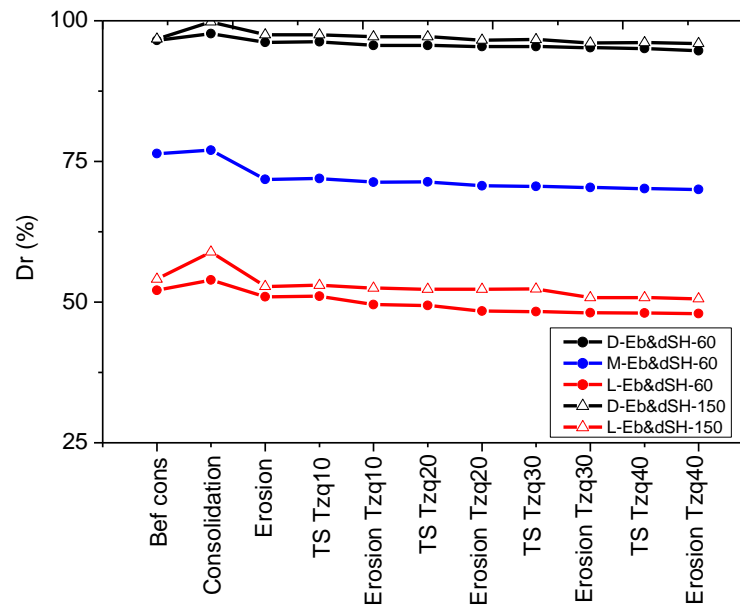


Figure 5-38 Comparison of the relative density for all the specimens with maximum erosion

## 5.7. Intergranular Relative Density

### 5.7.1. Specimens confined at $\sigma_z = \sigma_r = \sigma_\theta = 60 \text{ kPa}$

Contrary to the global relative density, the intergranular relative density ( $D_{rs}$ ) increases because of the particles eroded out of the specimen. Since the  $D_{rs}$  value does not consider the reduction in fines due to the erosion, the increment in  $D_{rs}$  is just because of the reduction in the volume of the primary fabric (Figure 5-39, Figure 5-40 and Figure 5-41).

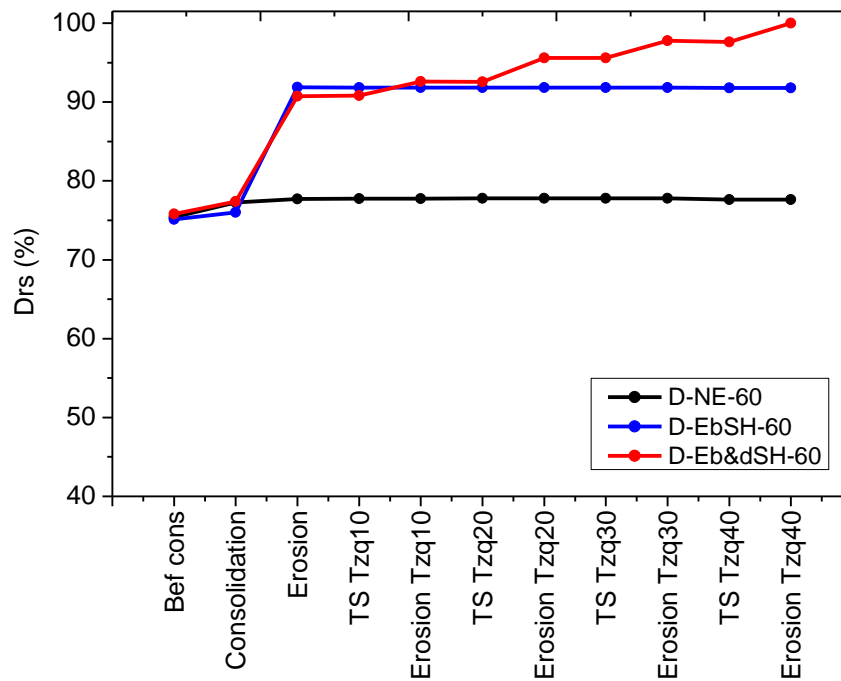


Figure 5-39 Intergranular Relative density Dense  $\sigma=60 \text{ kPa}$



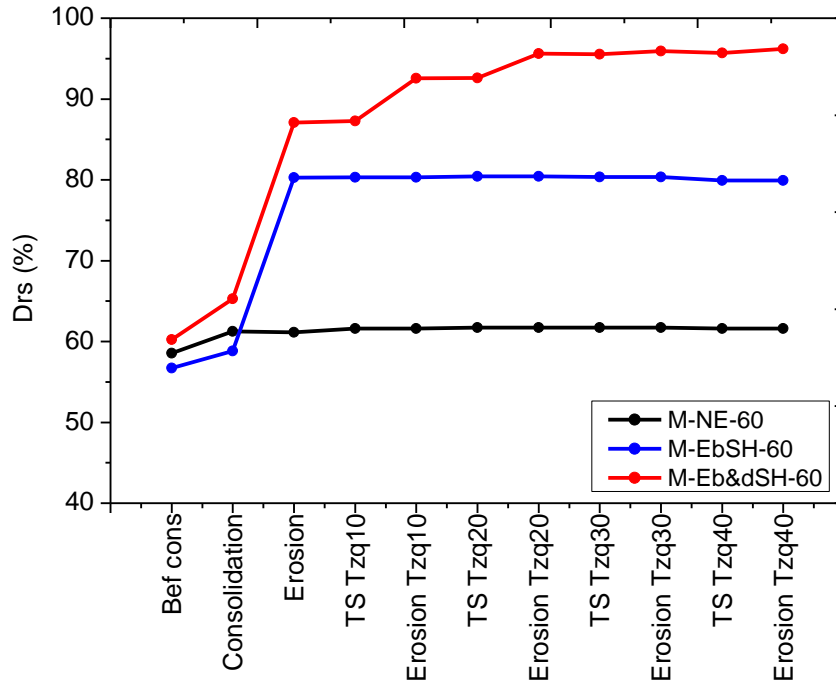


Figure 5-40 Intergranular Relative density Medium  $\sigma=60$  kPa

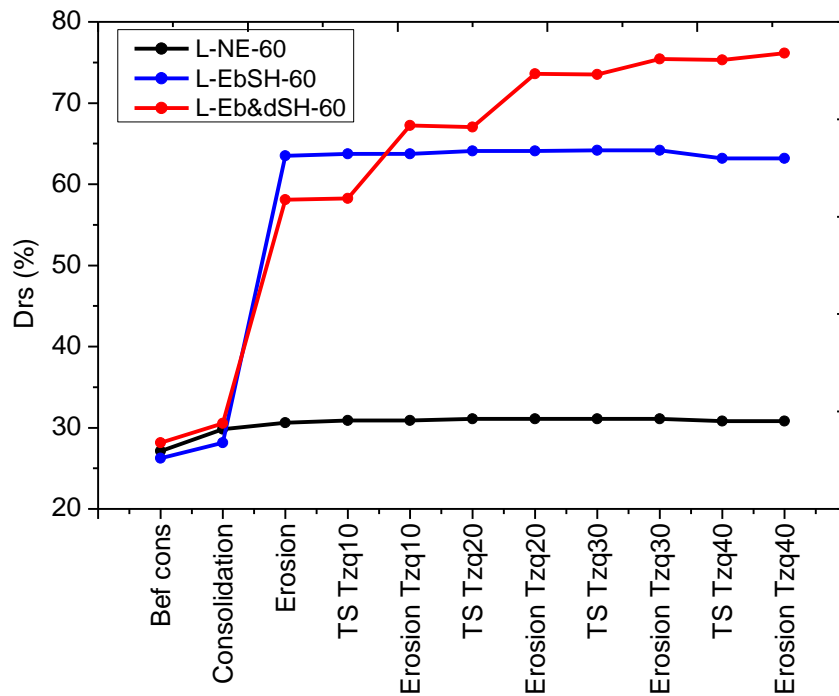
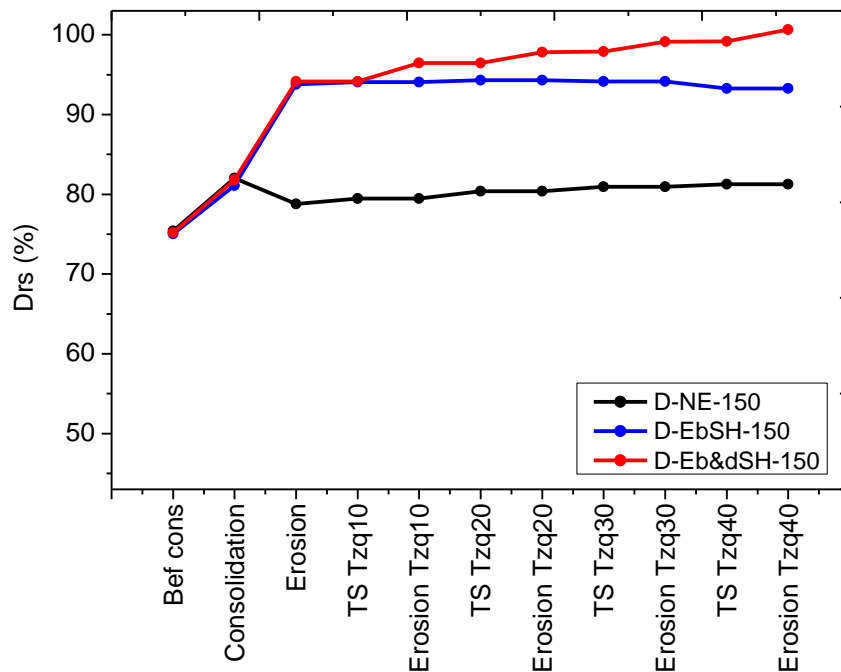
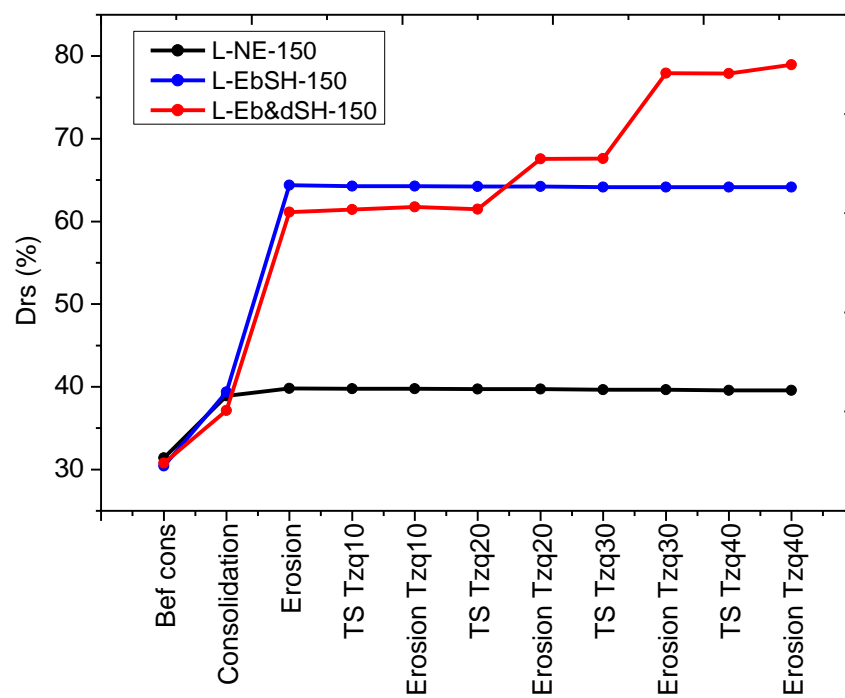


Figure 5-41 Intergranular Relative density Loose  $\sigma=60$  kPa

5.7.2. Specimens confined at  $\sigma_z = \sigma_r = \sigma_\theta = 150 \text{ kPa}$ Figure 5-42 Intergranular Relative density Dense  $\sigma=150 \text{ kPa}$ Figure 5-43 Intergranular Relative density Loose  $\sigma=150 \text{ kPa}$

### 5.7.3. Analysis

The rise in the density of the loose specimens is larger compared with that of the dense ones mainly due to the initial density and also the greater amount of eroded particles in the loose specimens (Figure 5-12 Final amount of eroded soil in all the experiments). Since more fines left the original matrix, the coarser grains decrease the distance between the particles and therefore a greater reduction in volume is observed (Figure 5-44).

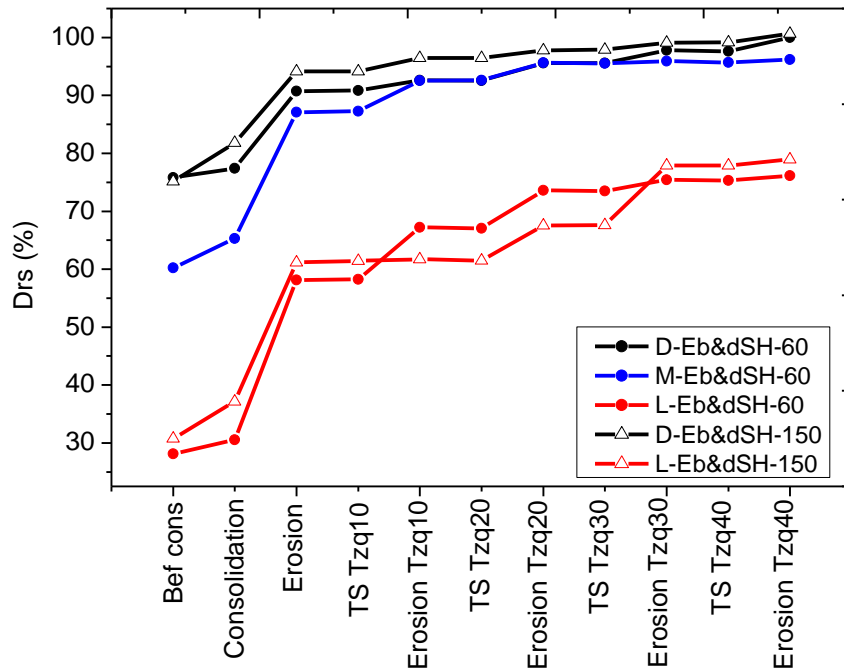


Figure 5-44 Comparison of the intergranular relative density for all the specimens with maximum erosion

## 5.8. Shear strength

### 5.8.1. Specimens confined at $\sigma_z = \sigma_r = \sigma_\theta = 60 \text{ kPa}$

Figure 5-45 shows the shear stress-strain relationship for the dense specimens confined at 60 kPa. The eroded specimens exhibit a slight decrease (compared with the non-eroded specimen) of the peak shear stress and the slope of the initial curves referring to the tangential shear modulus. The same trend is observed in the medium-dense and loose specimens, but the magnitude of reduction is relatively larger (Figure 5-46 and Figure 5-47).

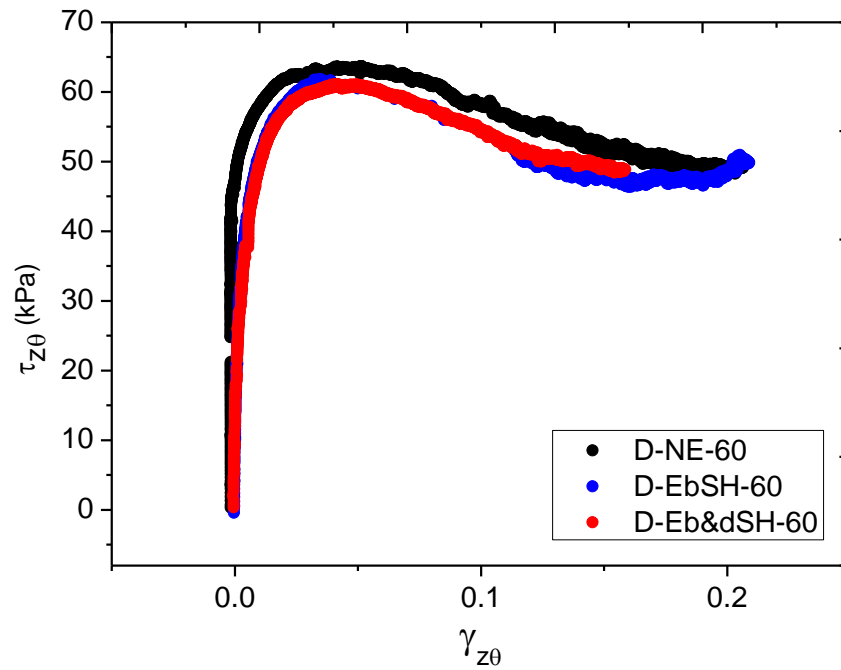


Figure 5-45 Stress-strain relationship for dense specimens confined at 60 kPa

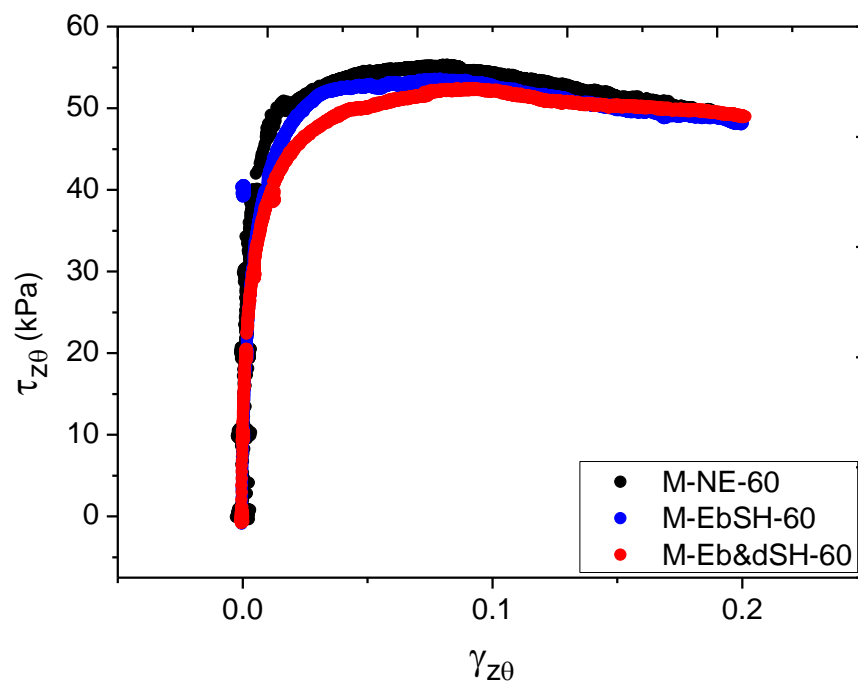


Figure 5-46 Stress-strain relationship for medium-dense specimens confined at 60 kPa

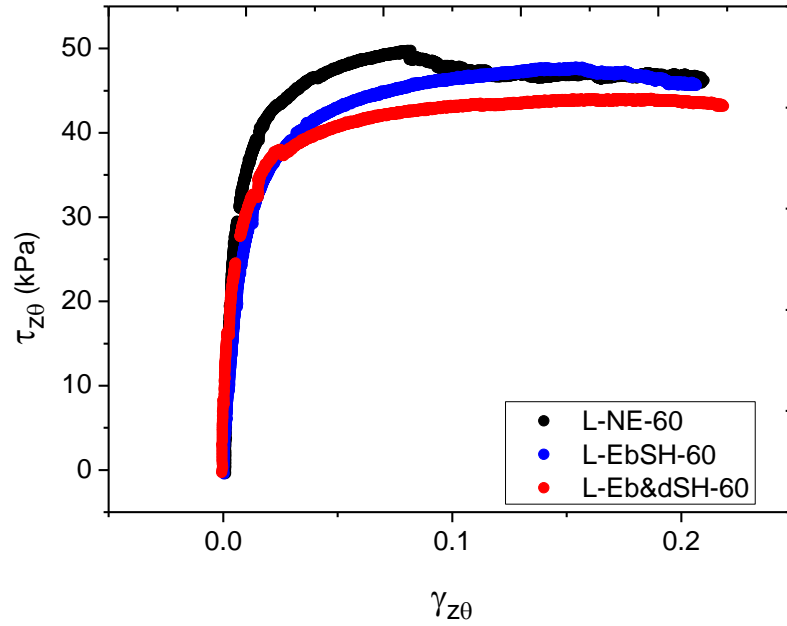


Figure 5-47 Stress-strain relationship for loose specimens confined at 60 kPa

#### 5.8.2. Specimens confined at $\sigma_z = \sigma_r = \sigma_\theta = 150 \text{ kPa}$

In the case of the specimens confined at 150 kPa, the reduction in shear strength is observed only in the loose specimens due to their larger percentage of particles eroded (Figure 5-48 and Figure 5-49).

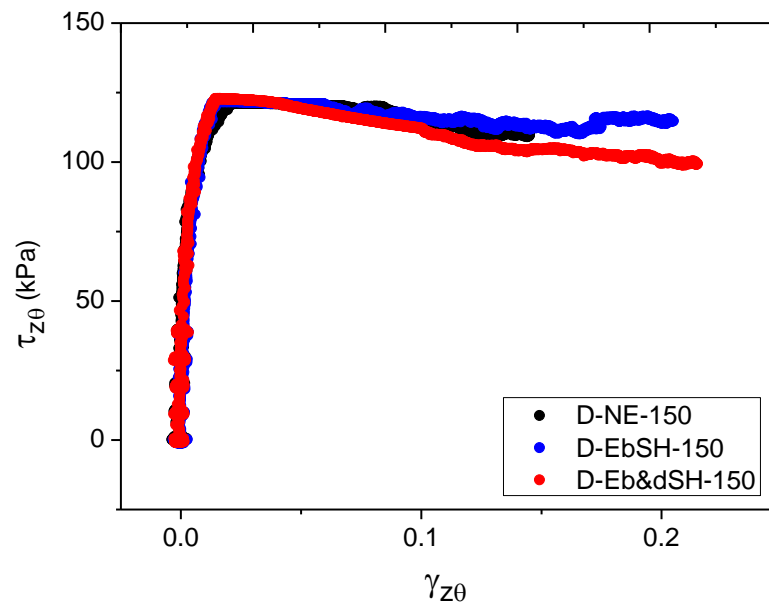


Figure 5-48 Stress-strain relationship for dense specimens confined at 150 kPa

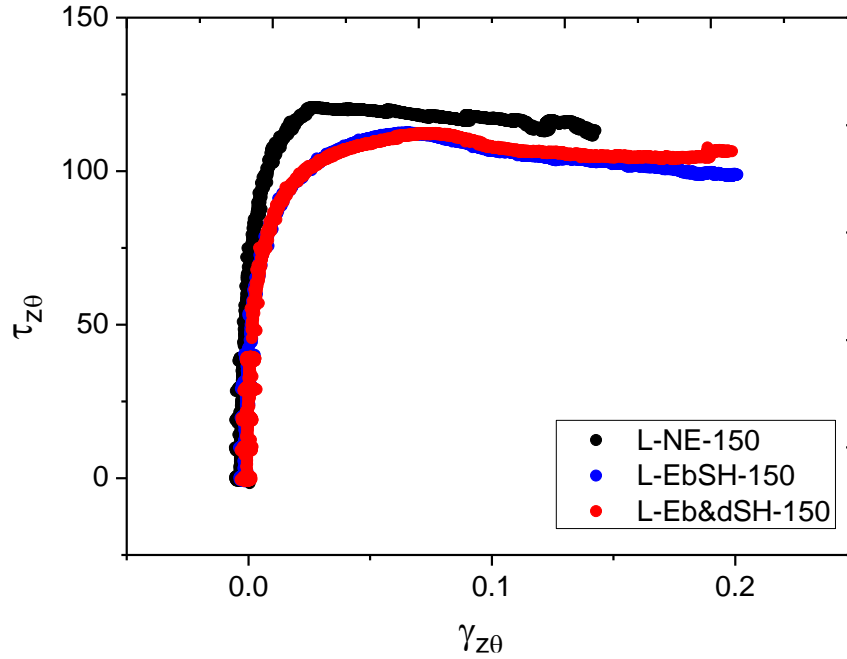


Figure 5-49 Stress-strain relationship for loose specimens confined at 150 kPa

### 5.8.3. Non-eroded specimens with lower density

The previous results show a lower shear strength in the eroded cases, and this reduction can be a result of the reduced density due to the particle removal, the disturbance of the microstructure due to the suffusion, or a combination of both. In order to verify the cause of this behavior, two additional non-eroded tests with a lower density were performed.

In the dense specimen eroded before and during shearing, the initial relative density of  $D_r = 97\%$  decreased to  $D_r = 95\%$ ; thus, a specimen with initial relative density of  $D_r = 94\%$  and final relative density of  $D_r = 95\%$  after consolidation was sheared with no erosion (Figure 5-50).

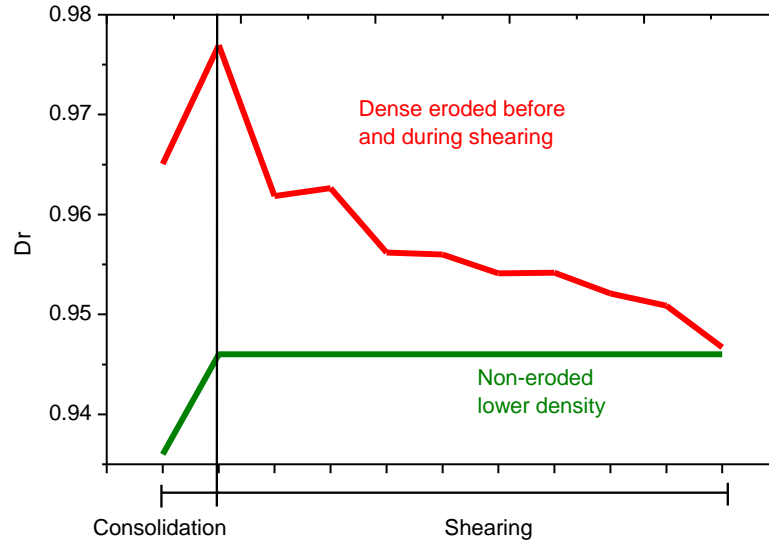


Figure 5-50 Relative density variation of the dense specimens

Figure 5-51 shows the relationship between shear stress and shear strain of the specimen non-eroded with lower density  $D_r = 95\%$  (Green curve). Although the green curve has the same density with the eroded test cases, it reaches almost the same peak shear stress as the densest specimen, this can be observed in detail in Figure 5-52.

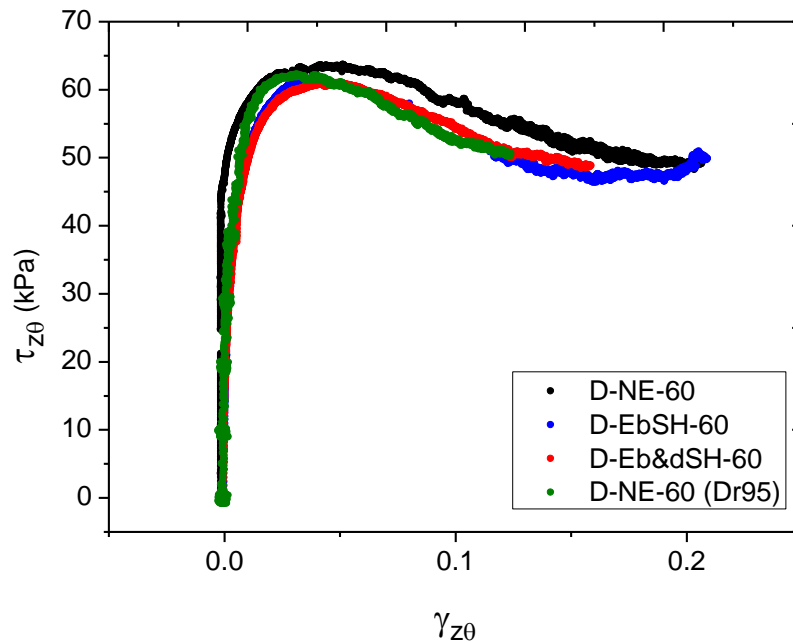


Figure 5-51 Comparison of the stress-strain relationship for Dense specimens confined at 60 kPa

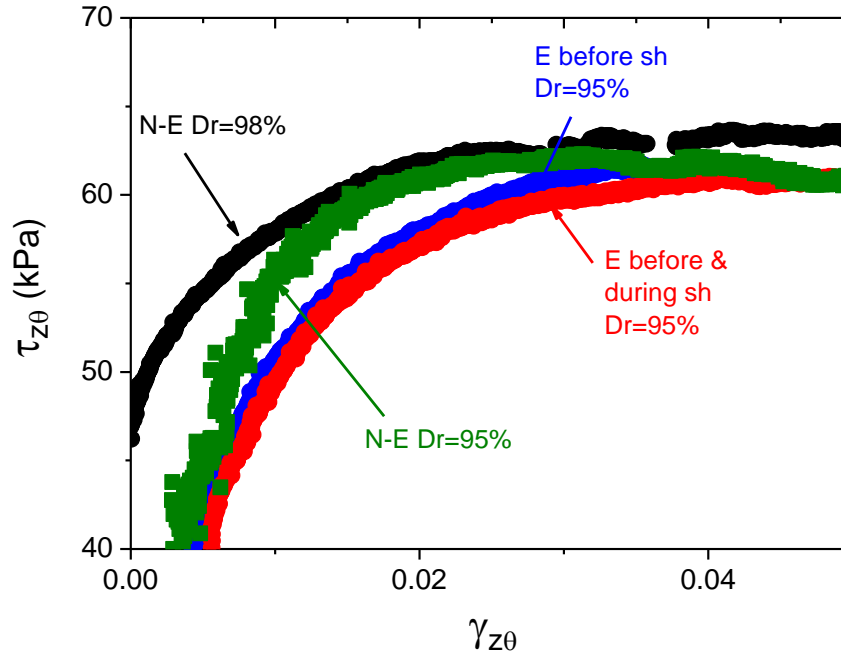


Figure 5-52 Detail of  $\tau_{peak}$  for dense specimens confined at 60 kPa

Therefore, the reduction in the peak shear stress can be caused by the disturbance of the particles due to the water seepage for erosion. Nevertheless, the residual shear strength is coincident with the eroded specimens and the tangential shear modulus is also reduced.

For the dense specimens the reduction in the relative density is insignificant due to the small percentage of particles eroded. For this reason, a loose specimen non-eroded with lower density was carried out. In this case, the initial relative density of the specimen eroded before and during shearing was  $D_r = 52\%$  and was reduced to  $D_r = 48\%$  due to erosion. Then a non-eroded specimen with initial relative density of  $D_r = 46\%$  and final  $D_r = 48\%$  was tested (Figure 5-53).

In Figure 5-54 although the green and red curves have the same density, the difference in the maximum shear stress can be noted, but their residual strength is very similar. The shear strength between the two non-eroded tests (Black and green curves) has similar shear modulus (slope of the curve) and peak shear strength although they have a difference in relative density of 6% (also see Figure 5-55).



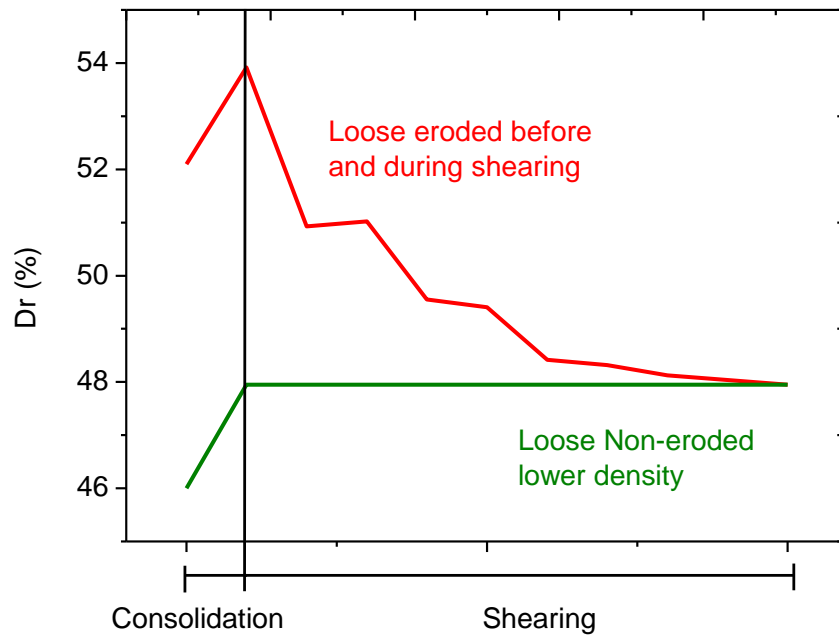


Figure 5-53 Relative density variation of the loose specimens

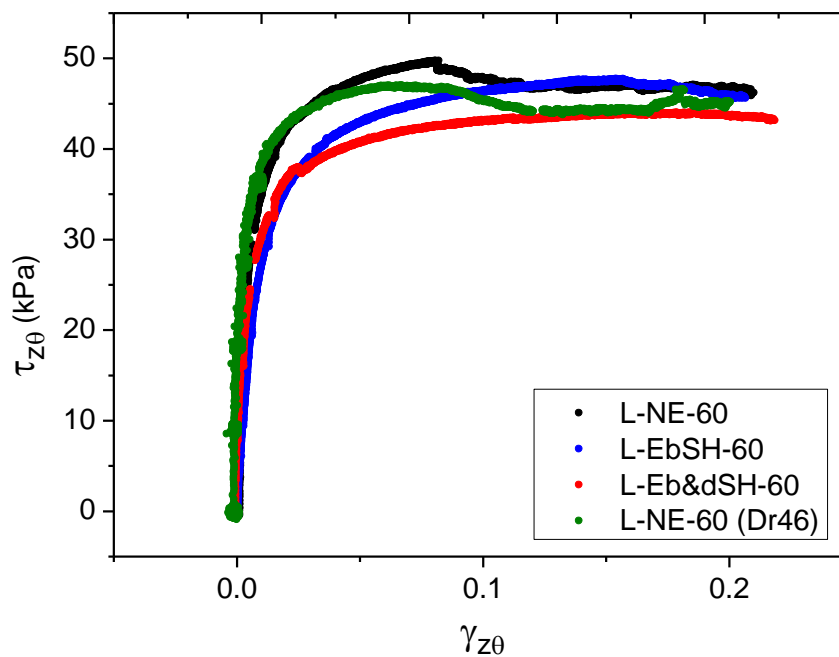


Figure 5-54 Comparison of the stress-strain relationship for Loose specimens confined at 60 kPa

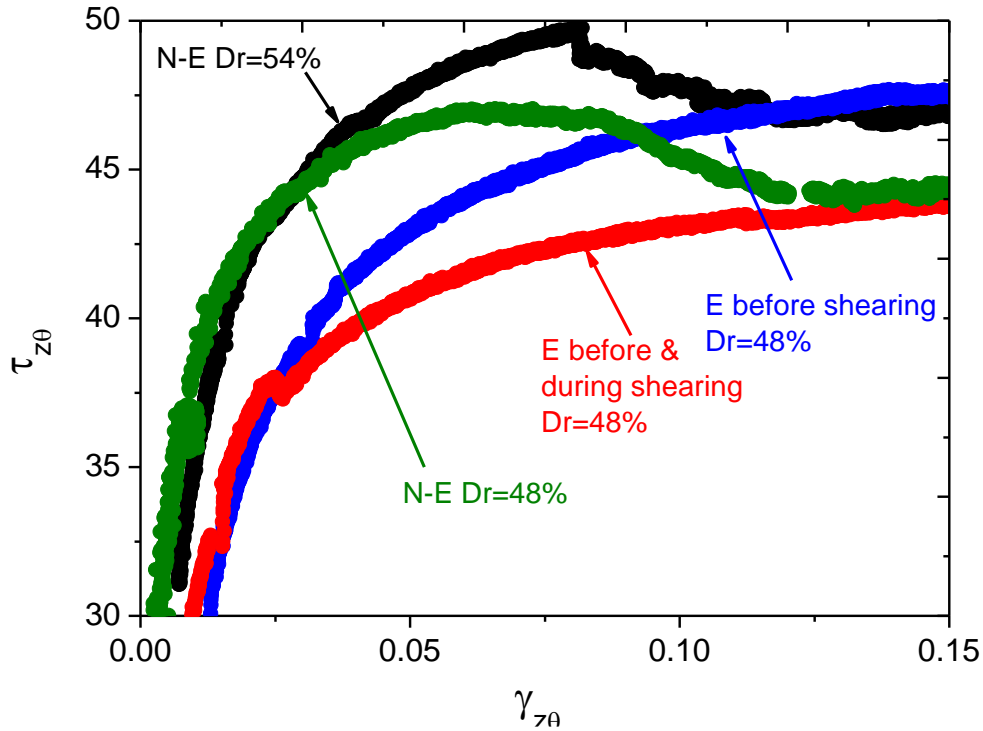


Figure 5-55 Detail of  $\tau_{peak}$  for loose specimens confined at 60 kPa

#### 5.8.4. Analysis

Figure 5-56 shows the comparison of all the specimens sheared; it is remarkable that the specimens confined at a higher pressure also exhibit a larger peak shear stress. Furthermore, the dense specimens without erosion present a typical curve for a dense specimen with an accentuated peak prior to a residual stress. The eroded specimens exhibit a softer response similar to the behavior of a loose soil, and do not show a clear peak.

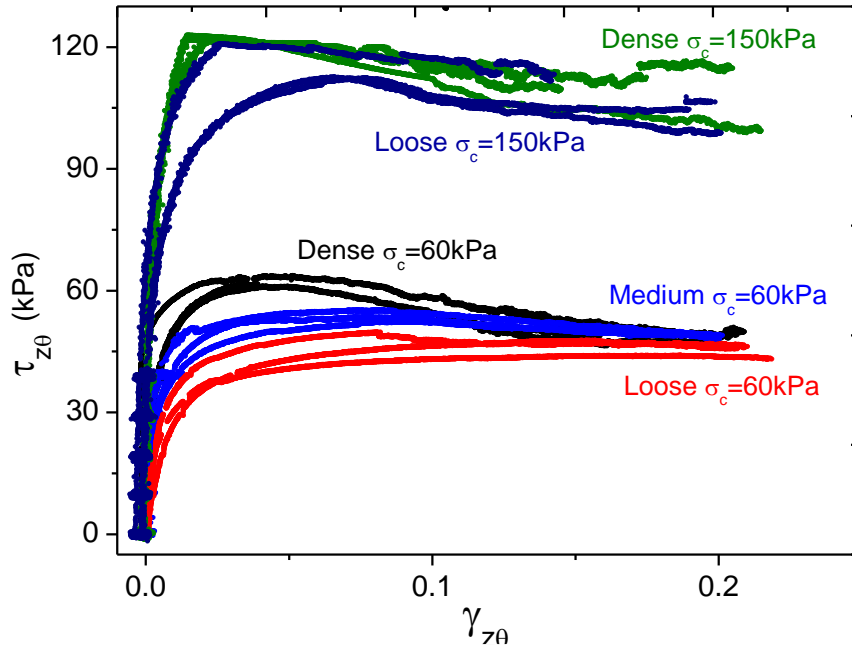


Figure 5-56 Comparison of the shear stress strain curves of all the specimens

Figure 5-57 shows the variation in the maximum shear stress for the specimens confined at 60 kPa at different erosion degrees. In the dense specimens (black points) the strength was reduced by 3% and 4% in the eroded tests with respect to the non-eroded test. In addition, the black triangle symbol, that shows the peak shear stress for the non-eroded specimen with reduced density, shows a decrease by 2%, while the specimen eroded with the same density exhibited a reduction of 4%.

Therefore, the reduction of shear strength can be attributed to the action of the seepage, causing a disturbance in the soil structure, and added to the reduction of relative density due to the fines expelled out of the specimen during seepage.

The reduction in the peak shear stress is larger (3% and 5%) for medium-dense specimens (blue points), and even larger for the loose specimens (3% and 11%) with 2% of reduction in the non-eroded specimen with lower density. This confirms that the reduction of the shear

strength is influenced by the reduction in density due to erosion, mainly because of the destabilization of the soil structure due to the suffusion.

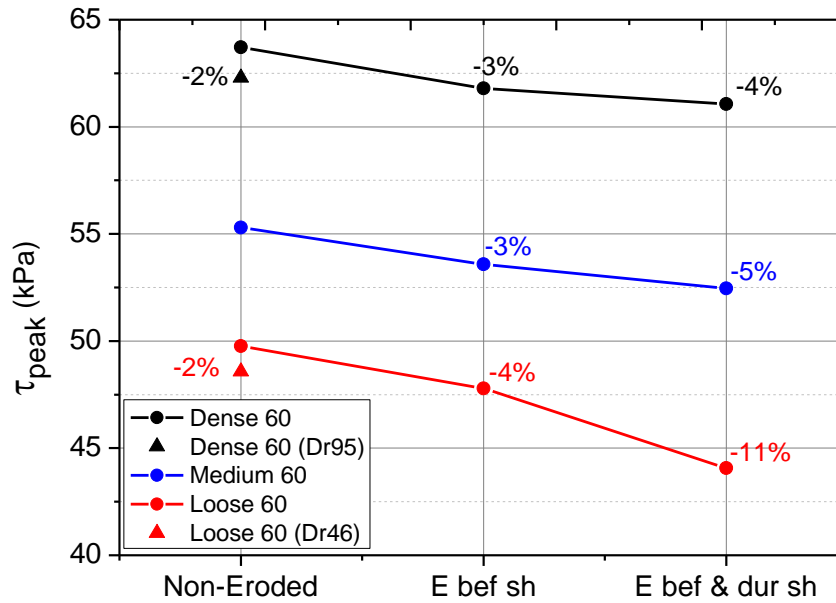


Figure 5-57  $\tau_{peak}$  variation for the specimens confined at 60 kPa

In the dense specimens at a higher confining pressure the reduction is almost imperceptible, this can be attributed to the small degree of erosion observed in these specimens. The structures of the specimens are highly stable due to the stronger contact force between particles, and so the erosion seems to have nearly no effect on the strength. In the loose specimens the reduction is 7% in both eroded cases; although the reduction is higher, there is insignificant reduction due to the erosion during shearing (Figure 5-58).

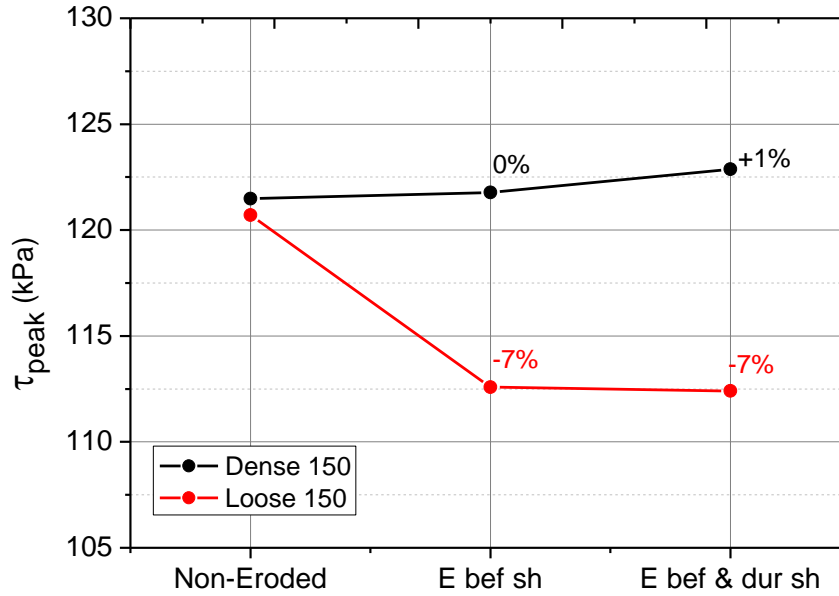
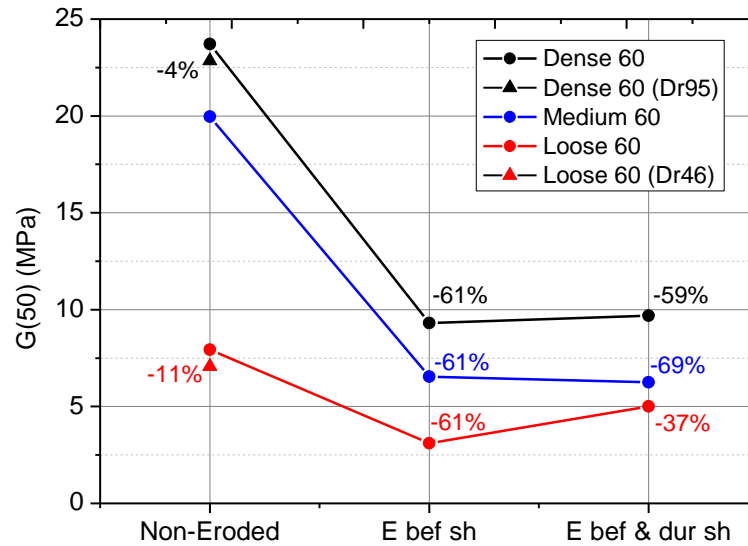
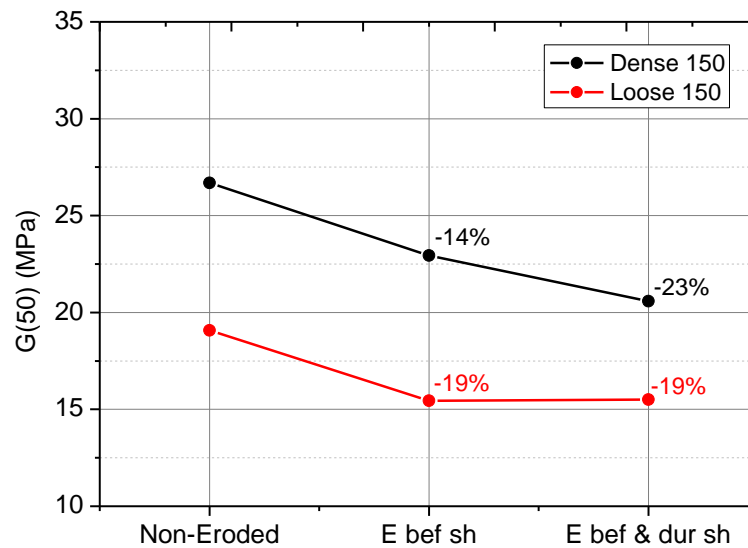


Figure 5-58  $\tau_{peak}$  variation for the specimens confined at 150 kPa

In the same way, the tangent shear modulus also exhibits a reduction in the eroded cases compared with the non-eroded specimens (Figure 5-59 and Figure 5-60). The triangles in Figure 5-59 are the values of the non-eroded specimens with lower densities; their values are just slightly reduced compared with the non-eroded specimens with larger densities, but are significantly higher than that obtained by the eroded specimens with the same density. The finding proves that the reduction of the shear modulus is mainly due to the action of erosion, and not caused by the reduction of the density, since the fine particles drained during the erosion do not contribute to the transmission of stresses.

Figure 5-59  $G_{50}$  variation for the specimens confined at 60 kPaFigure 5-60  $G_{50}$  variation for the specimens confined at 150 kPa

Thevanayagam (1998) stated that the shear strength of a silty sand can be divided into three groups considering the roles of the fines in the matrix. The first case (case 1) refers to the silty sands with high densities, where  $e_s$  (intergranular void ratio) is less than  $e_{max,HS}$  (maximum void ratio of the host sand); in this case most of the fines are confined in the pores, and the shear strength is primarily derived from the friction along the primary fabric. For the second case (case 2), where  $e_s \approx e_{max,HS}$ , the shear strength is derived from a combination of friction along the coarser-grain contacts and the fines. The soils grouped in

case 2 have low densities, where  $e_s > e_{max,HS}$ , and the shear strength is significantly affected by the presence of fines.

Considering the relationship between the intergranular void ratio of the silty sand and the intergranular void ratio of the primary fabrics, the specimens tested can be classified into case 1 for the dense and medium-dense specimens, and case 2 for the loose specimens (Table 5-4).

Table 5-4 Classification of the specimens tested, according to the role of fines

Density	Dr (%)	ID	Case
Dense	98	D-NE-60	1
	98	D-EbSH-60	1
	97	D-Eb&dSH-60	1
	95	D-NE-60 (Dr95)	1
Medium	75	M-NE-60	1
	74	M-EbSH-60	1
	76	M-Eb&dSH-60	1
Loose	51	L-NE-60	2
	51	L-EbSH-60	2
	52	L-Eb&dSH-60	2
	46	L-NE-60 (Dr46)	2
Dense	98	D-NE-150	1
	98	D-EbSH-150	1
	97	D-Eb&dSH-150	1
Loose	55	L-NE-150	2
	54	L-EbSH-150	2
	54	L-Eb&dSH-150	2

This classification is consequent with the shear strength behavior shown from Figure 5-45 to Figure 5-49. In the dense specimens (case 1), most of the fines are restricted in the intergranular spaces made by the primary fabric. Although there are some fines eroded the shear strength is taken mostly by the primary fabric; therefore, the reduction of the peak stress is small in the eroded cases (Figure 5-61 (a)). In the loose specimens (case 2) “the coarser-grain skeleton by itself is unstable. Some of the fines may be acting as secondary

load transfer vehicles between some of the coarser grains, while the rest of the fines are still confined to the intergranular voids. The shear strength is derived from a combination of friction along the coarser-grain contacts and along the fines” (Thevanayagam, 1998). This explains the reduction of the shear strength in the loose cases, because the fine particles drained by the erosion are originally transmitting stresses in conjunction with the primary fabric, and therefore when the erosion takes place the shear strength is affected (Figure 5-61 (b)).

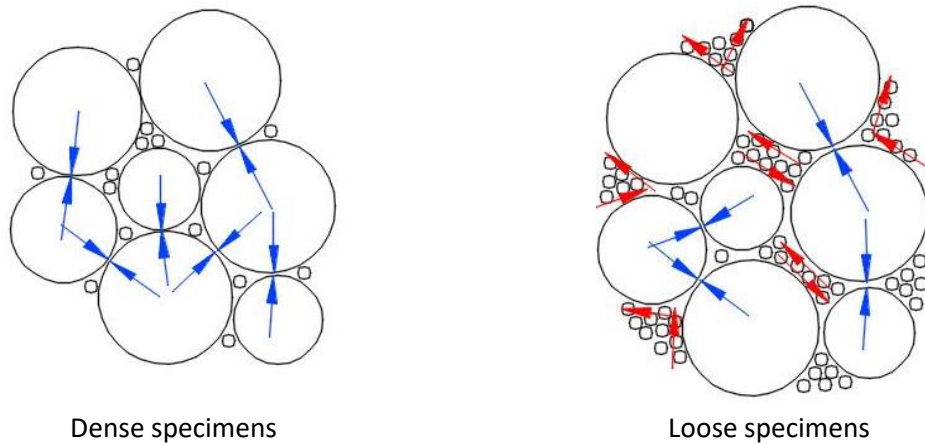


Figure 5-61 Shear stress transmission

## 5.9. Small strain Shear Modulus

### 5.9.1. Specimens confined at $\sigma_z = \sigma_r = \sigma_\theta = 60kPa$

As previously mentioned in Section 3.3.3, cyclic torsional loading at small-strain levels ( $\gamma_{z\theta} < 0.001\%$ ) were applied at different stages during the tests in order to estimate the shear modulus  $G$ . Table 5-5 shows the measurement of  $G$  in each test; for the eroded cases  $G$  is determined before and after erosion during torsional shearing.



Table 5-5 Measurement of G by STCL during the tests

	Non-eroded	Eroded before shearing	Eroded before and during shearing
Before water infiltration	X	X	X
After water infiltration or erosion	X	X	X
TS $\tau=10\text{kPa}$	X	X	X
Erosion at $\tau=10\text{kPa}$	-	-	X
TS $\tau=20\text{kPa}$	X	X	X
Erosion at $\tau=20\text{kPa}$	-	-	X
TS $\tau=30\text{kPa}$	X	X	X
Erosion at $\tau=30\text{kPa}$	-	-	X
TS $\tau=40\text{kPa}$	X	X	X
Erosion at $\tau=40\text{kPa}$		-	X

Figure 5-62 shows the variation of G along the tests in loose specimens confined at 60 kPa. For all the cases (eroded and non-eroded) G decreases with the first water infiltration, which refers to the measurement after the erosion before shearing in eroded cases, and after saturation in the non-eroded cases.

After this point, in the non-eroded specimen (black curve) the shear modulus increase at a constant rate during torsional shearing. The specimen eroded before shearing (blue line) also present a rise in G during torsional shearing, although its values are lower than in the non-eroded cases, product of the initial erosion.

The case eroded before and during shearing (red curve) exhibits the same trend as the blue curve before shearing. After this, the value of  $G$  is reduced during the first erosion seepage (at  $\tau = 10\text{kPa}$ ), causing a permanent difference with respect to the non-eroded  $G$  values.

It must be noted that the non-eroded specimen with reduced density ( $D_r = 46\%$ ) (green curve) has almost the same values as the non-eroded specimen with  $D_r = 51\%$  (black curve). Although the green and red curves have the same relative density, the shear modulus values differ substantially, proving that the erosion has an unfavorable effect with respect to the shear strength of the soil.

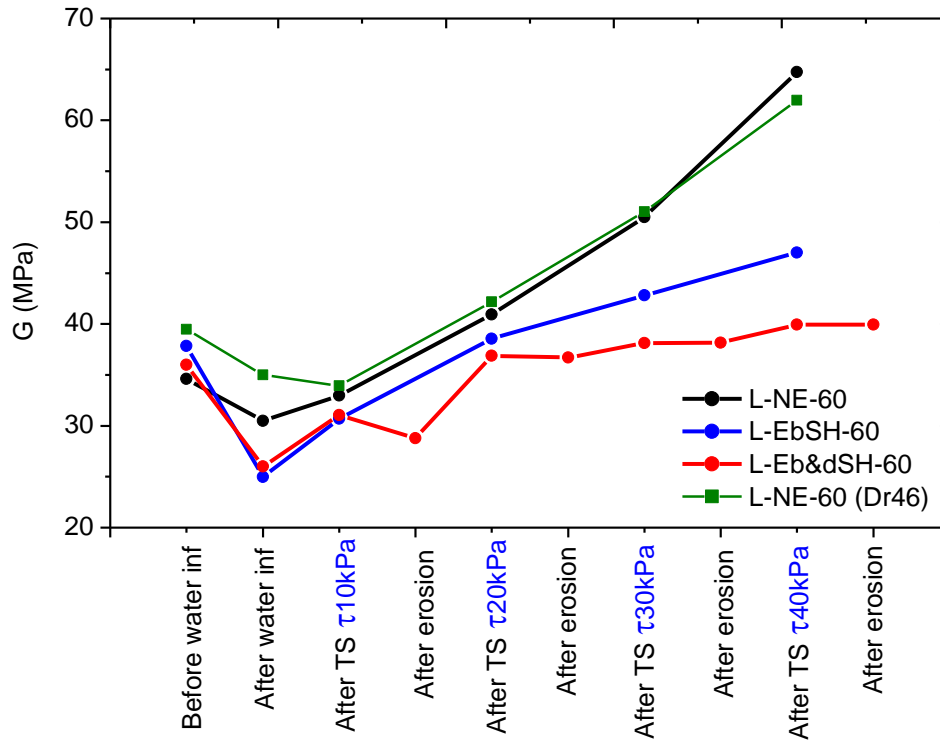


Figure 5-62 G variation of loose specimens confined at 60 kPa

In order to minimize the effects of density, the shear modulus has been plotted as a function of the void ratio proposed by Hardin and Richart (1963) (Figure 5-63) (explained in detail in

the section 2.5.1 Void ratio function  $f(e)$ ). Although the overall  $G$  values are reduced, there is still a reduction of the shear modulus after the erosion stages, where the strength is reduced by the erosion process alone and not because of the reduction of density due to the fines moved out of the matrix.

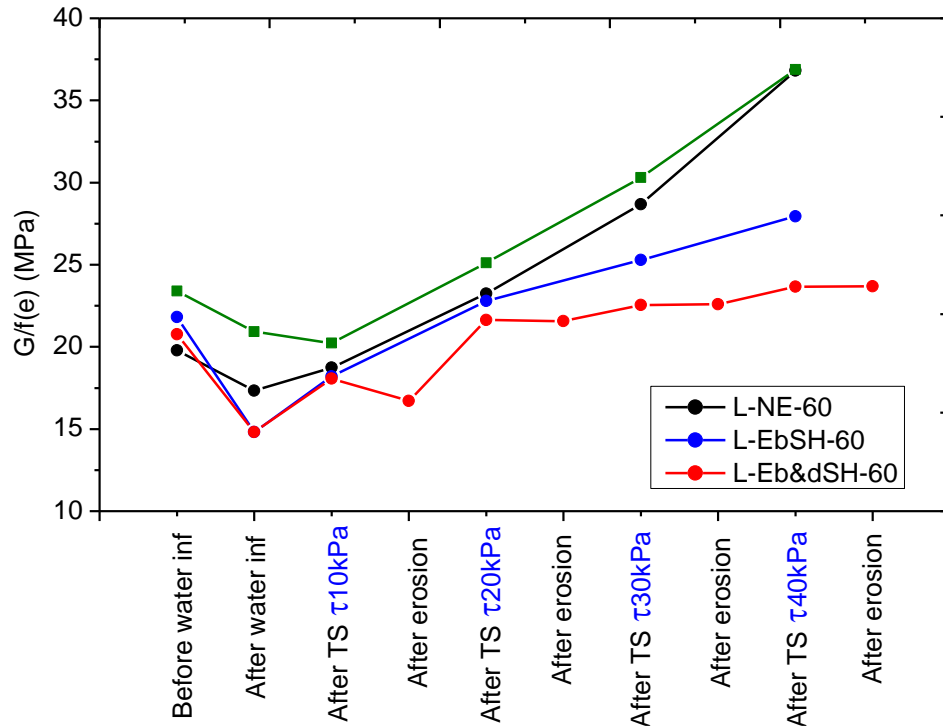


Figure 5-63  $G/f(e)$  variation of Loose specimens confined at 60 kPa

As explained previously (Figure 5-61) the shear stresses can be transmitted mainly by the primary fabric or a combination of contacts between the fines and primary fabric. Assuming that in the loose case just the coarser-grain fabric supports the stresses, the variation of the shear modulus has been plotted in terms of the void ratio function, but considering the intergranular void ratio  $e_s$ . The results are shown in Figure 5-64; a larger difference between the eroded and the non-eroded tests can be appreciated.

Figure 5-65, Figure 5-66 and Figure 5-67 show the variation of  $G$ ,  $G/f(e)$  and  $G/f(e_s)$  for the dense specimens confined at 60 kPa, where the reduction of  $G$  after the erosion stages is

observed. Unlike the loose specimens, the shear modulus does not increase during the torsional shearing for the non-eroded specimens.

A similar behavior is observed for the medium-dense specimens (Figure 5-68, Figure 5-69, Figure 5-70).

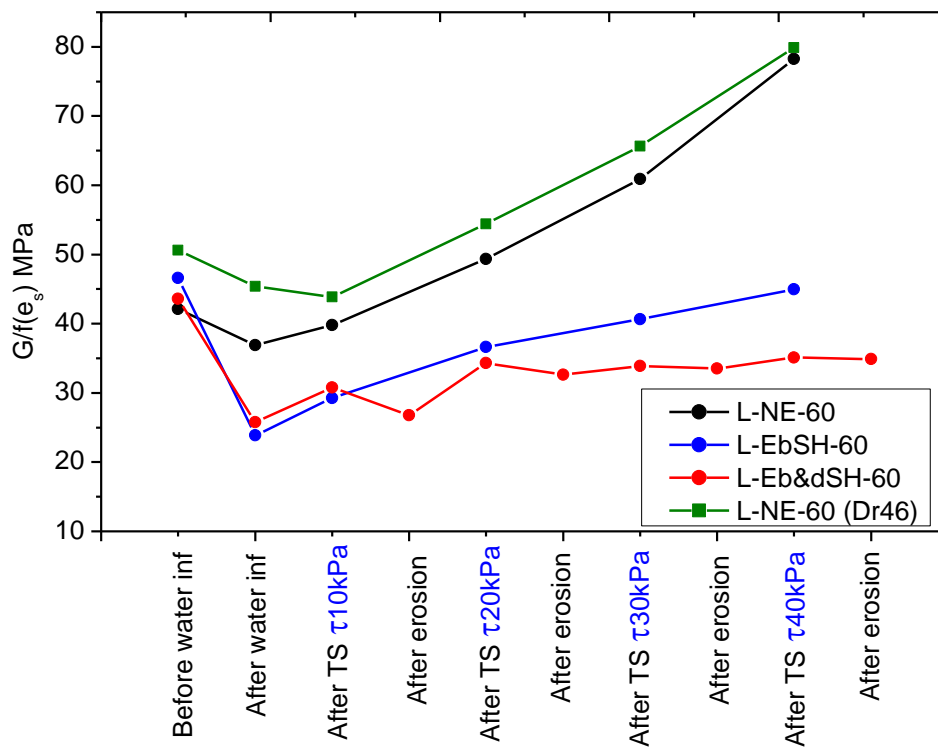


Figure 5-64  $G/f(e_s)$  variation of loose specimens confined at 60 kPa

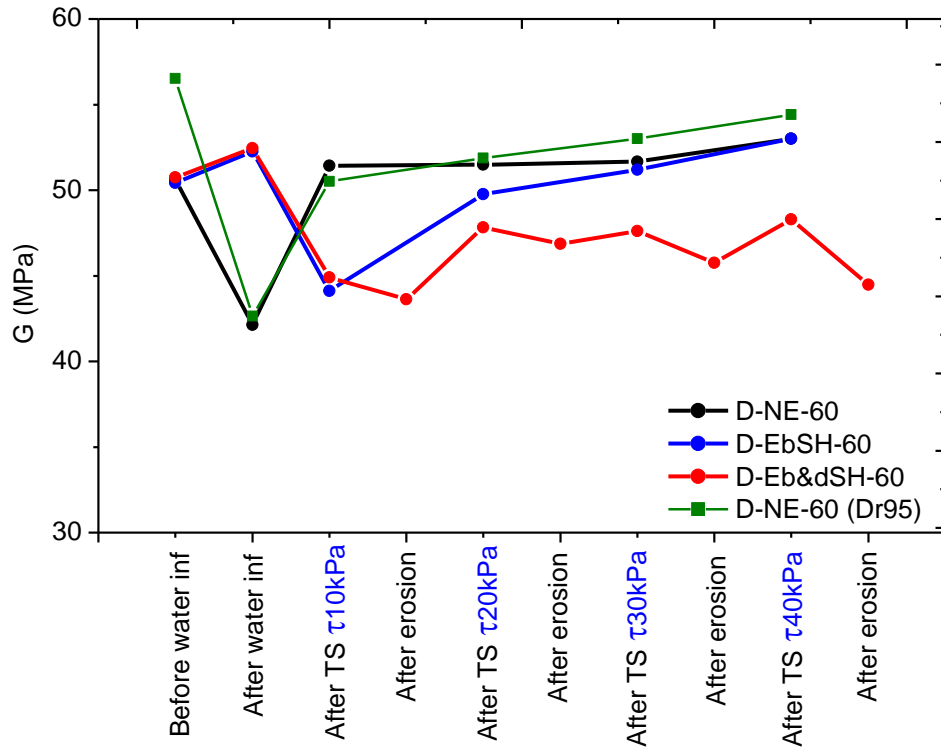
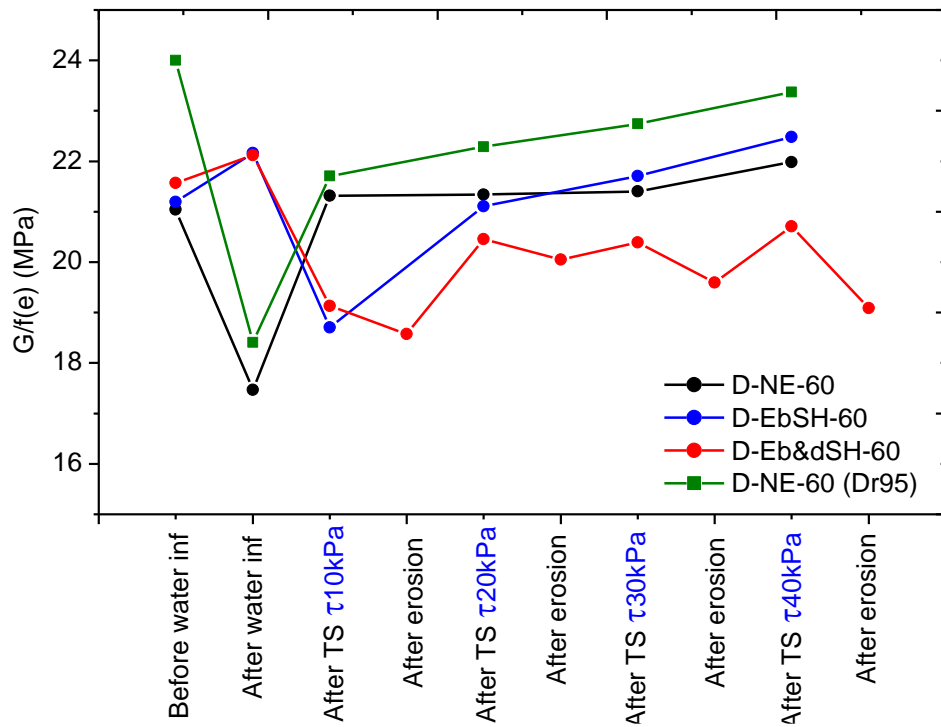
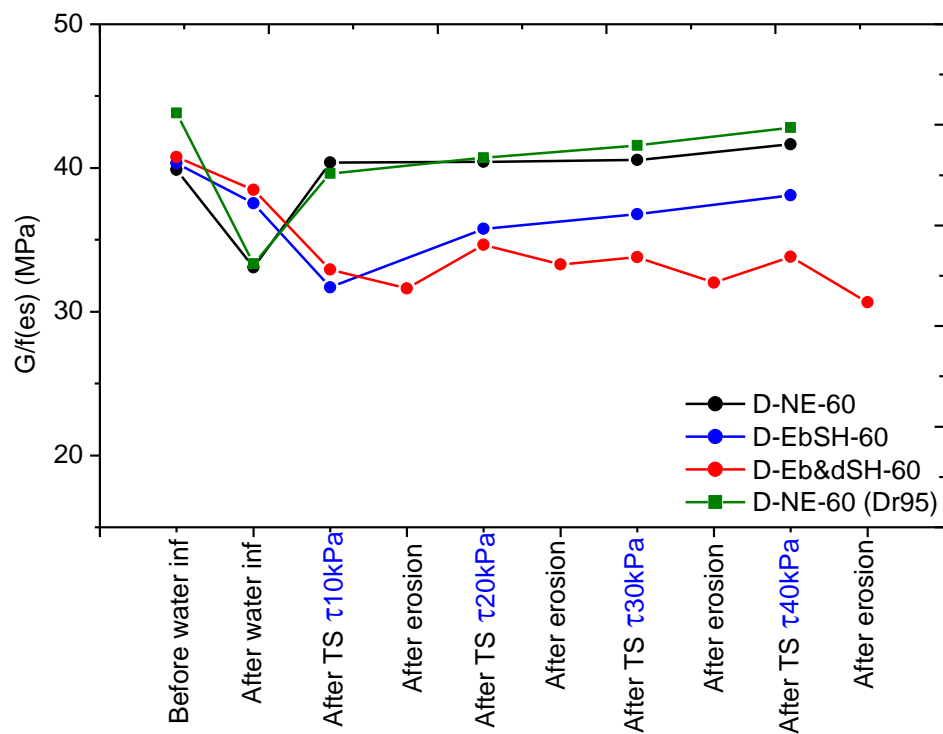
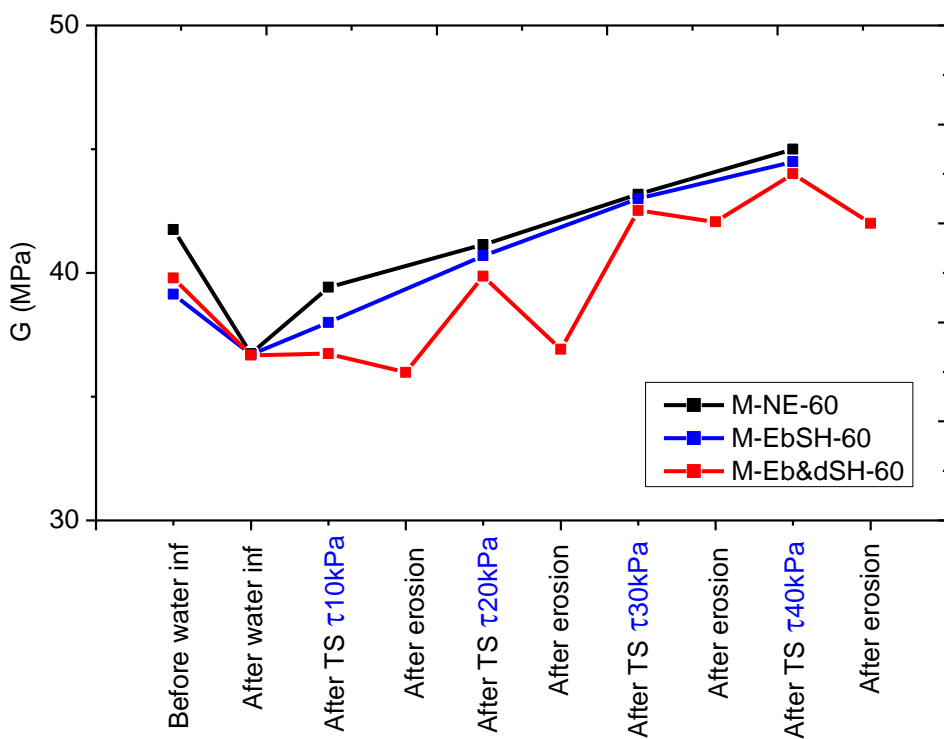


Figure 5-65 G variation of dense specimens confined at 60 kPa

Figure 5-66  $G/f(e)$  variation of dense specimens confined at 60 kPa

Figure 5-67  $G/f(e_s)$  variation of dense specimens confined at 60 kPaFigure 5-68  $G$  variation of medium-dense specimens confined at 60 kPa

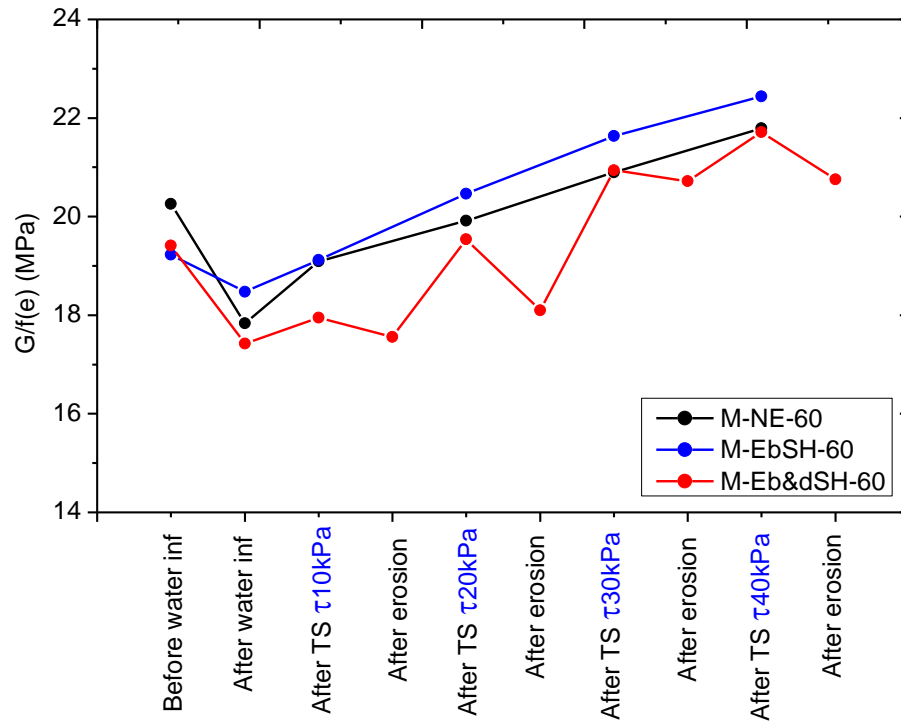


Figure 5-69  $G/f(e)$  variation of medium-dense specimens confined at 60 kPa

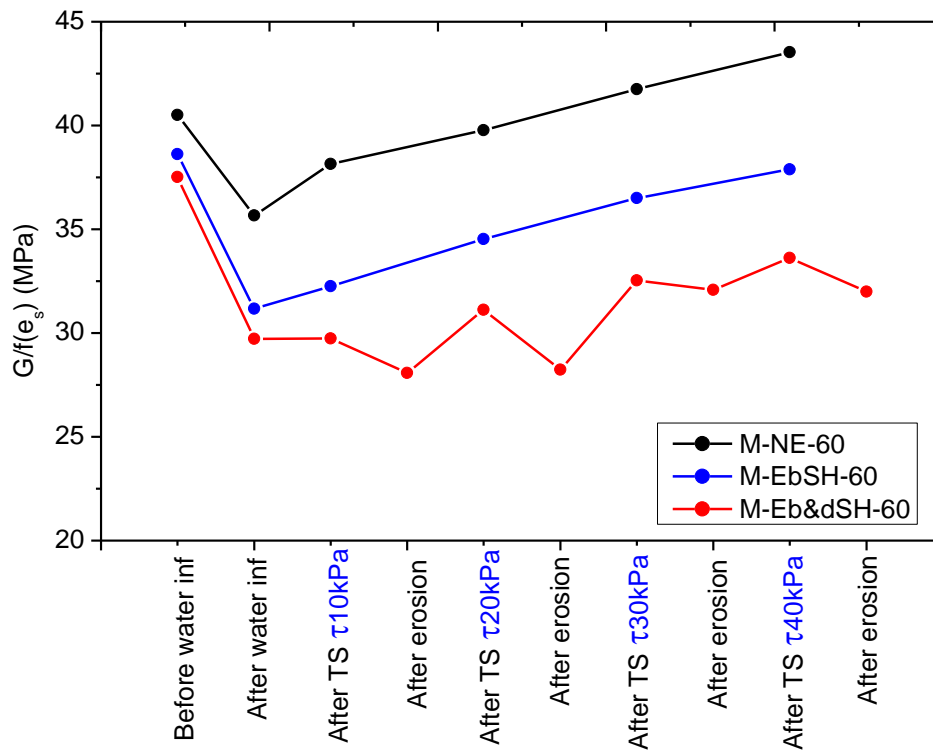


Figure 5-70  $G/f(e_s)$  variation of medium-dense specimens confined at 60 kPa

### 5.9.2. Specimens confined at $\sigma_z = \sigma_r = \sigma_\theta = 150 \text{ kPa}$

Similar to the variation of the shear modulus in the specimens confined at 60 kPa, the specimens confined at 150 kPa show a reduction of  $G$  in the eroded cases and specifically in the eroded stages, compared with the values obtained in the specimens without erosion. Moreover, as expected, the shear modulus values are higher than the ones obtained in the specimens confined at 60 kPa (Figure 5-71 to Figure 5-76).

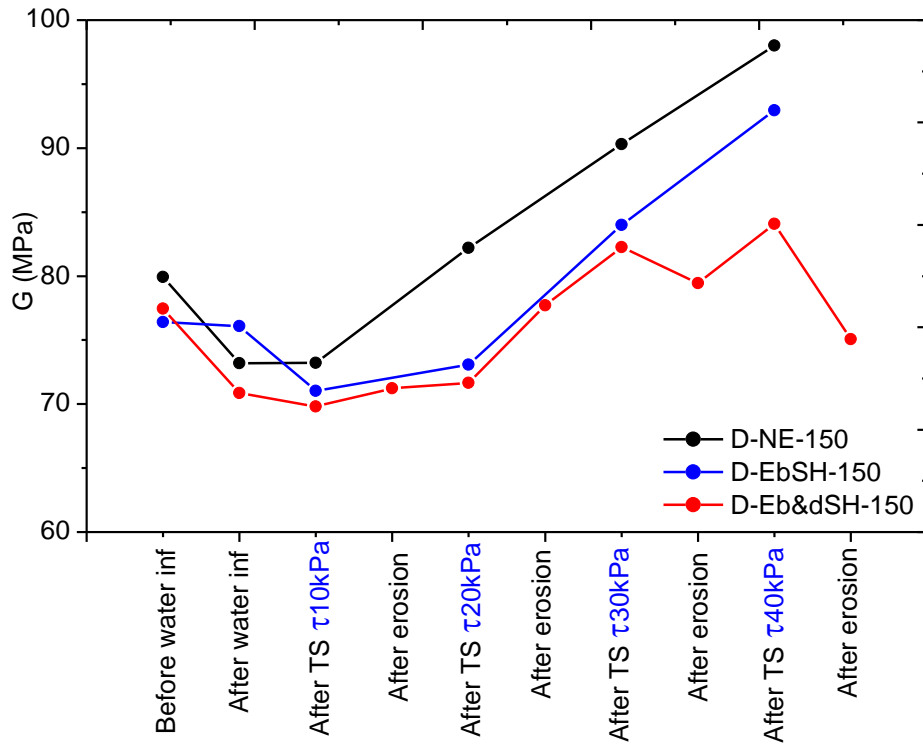


Figure 5-71  $G$  variation of dense specimens confined at 150 kPa



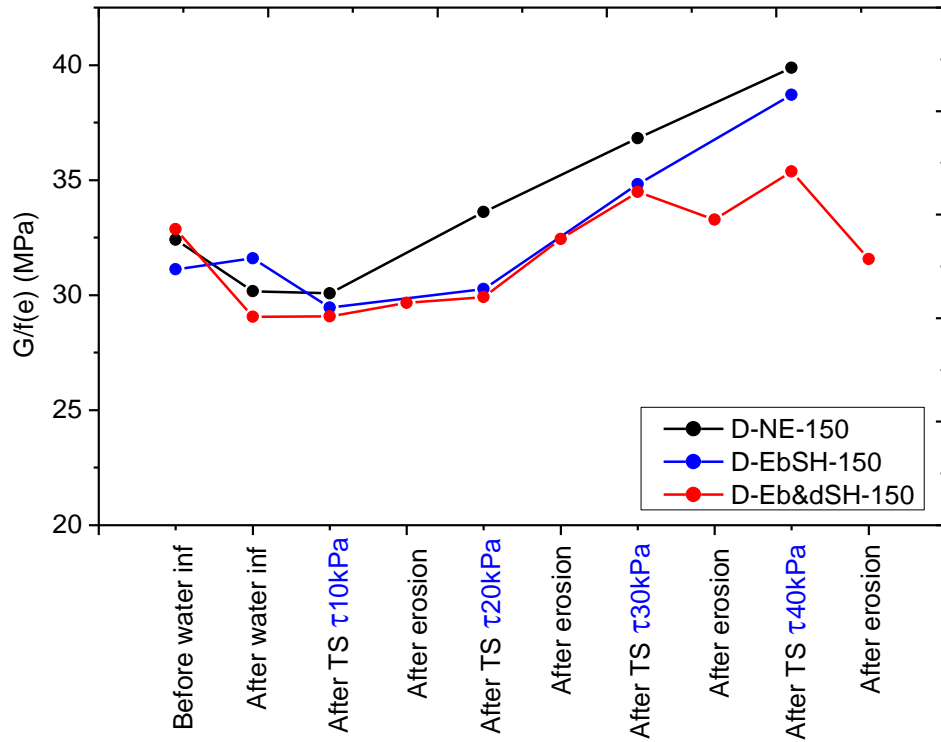


Figure 5-72  $G/f(e)$  variation of dense specimens confined at 150 kPa

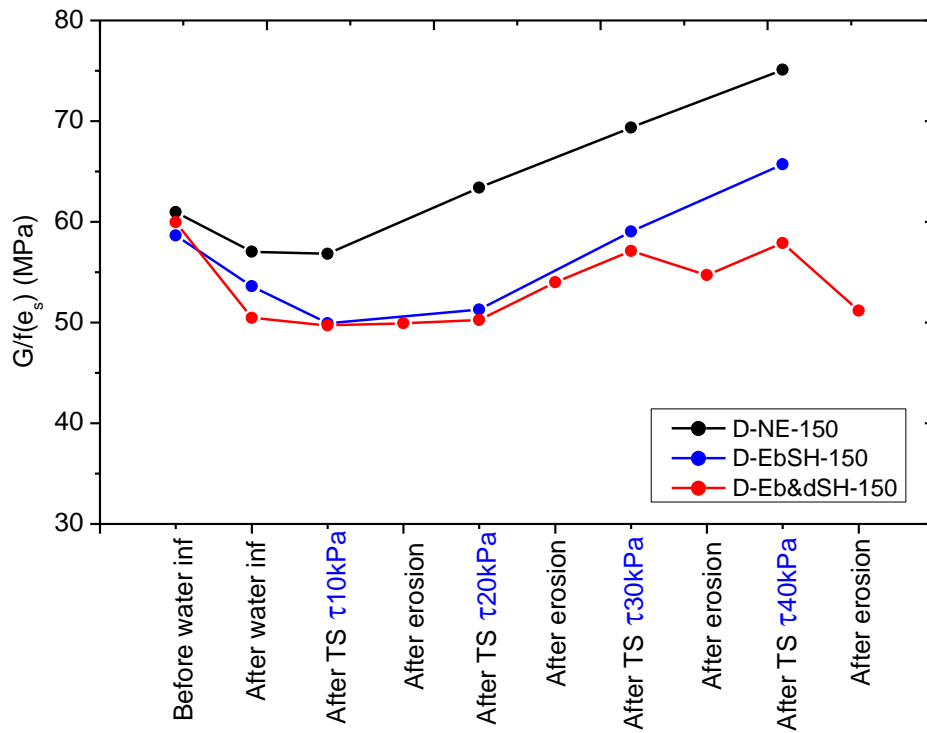
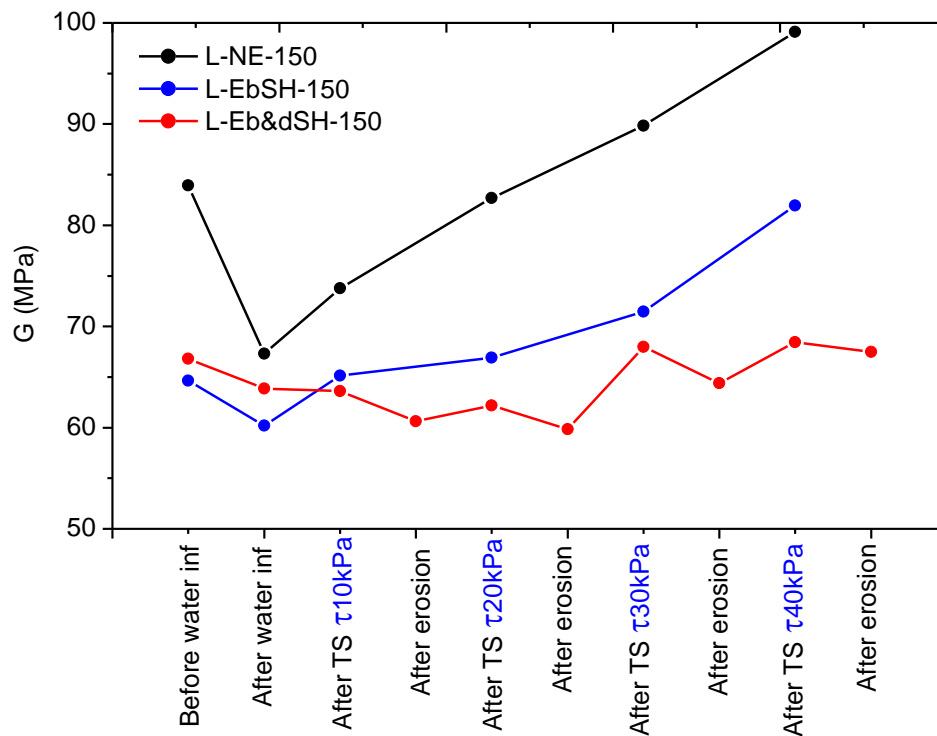
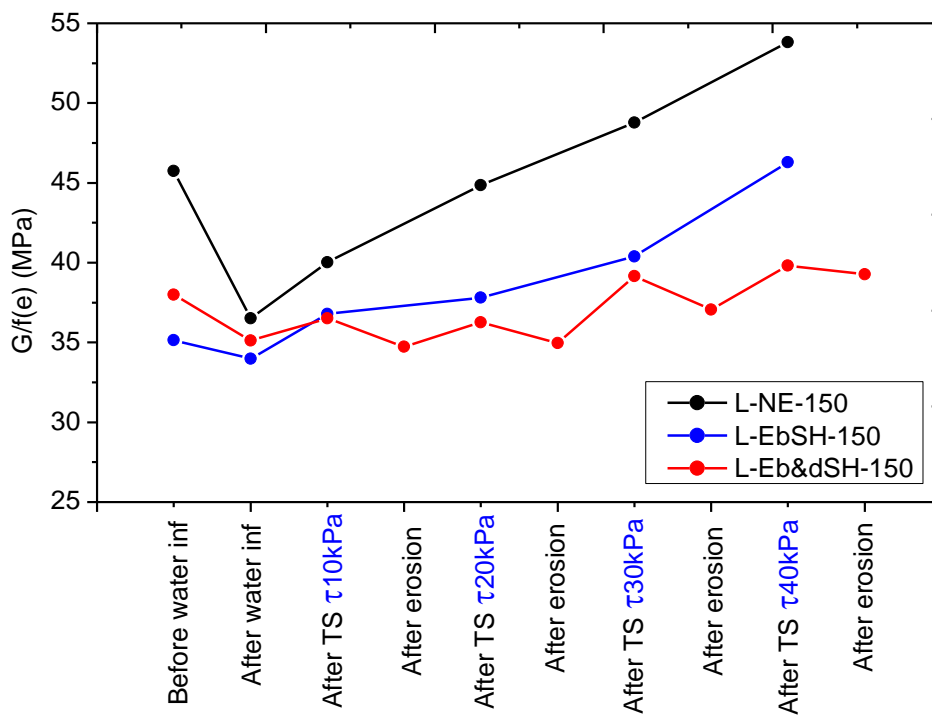


Figure 5-73  $G/f(e_s)$  variation of dense specimens confined at 150 kPa

Figure 5-74  $G$  variation of loose specimens confined at 150 kPaFigure 5-75  $G/f(e)$  variation of loose specimens confined at 150 kPa

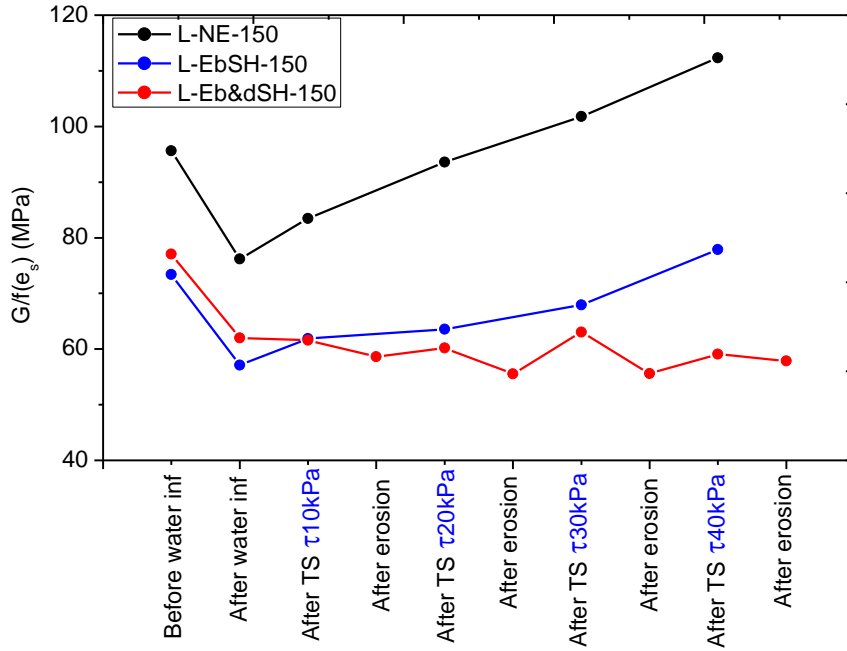


Figure 5-76  $G/f(e_s)$  variation of loose specimens confined at 150 kPa

### 5.9.3. Analysis

#### a. Influence of the confining stress:

As explained previously, the shear modulus experiences a reduction after the water infiltration stages in which the erosion is induced. This reduction is conserved throughout the test signifying a permanent reduction in the shear strength if the erosion process has been taken place just before the torsional shearing, or a combination of erosion before and during the shearing.

The initial confining stress also affects the strength of the soil. In Figure 5-77 the variation of the shear modulus normalized by a function of the intergranular void ratio is displayed for the dense specimens confined at 60 kPa and 150 kPa. The intergranular void ratio is used to normalize the  $G$  because it is the parameter that better describes the stresses transmission inside the soil matrix. In addition, Thevanayagam (1998) suggests that for soils classified into case 1 (high densities) “the intergranular void ratio  $e_s$  may be a suitable index to characterize the shear strength of a silty sand”.

It can be observed that the shear strength in the specimens confined at 150 kPa is higher than the values of the specimens confined at 60 kPa. This is consequent of the idea that the shear strength is derived from the friction along the primary fabric contacts, and if the particles are subjected to higher pressures, the inter-particle forces at contacts will be stronger.

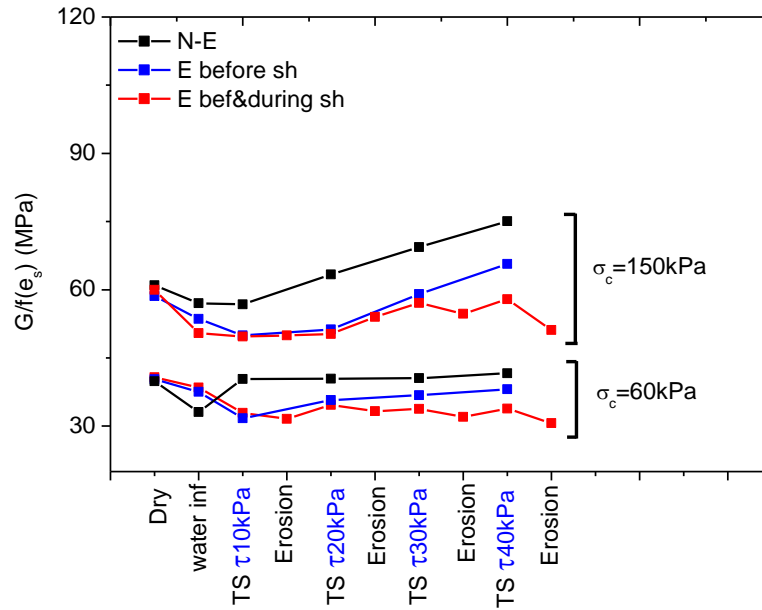


Figure 5-77 Comparison of  $G/f(e_s)$  in dense specimens

The loose specimens also exhibit a larger resistance at a higher pressure (Figure 5-78). However, the  $G$  values for the loose specimens are significantly higher than those for the dense specimens, which is perhaps counter intuitive. A possible explanation to this behavior is stated by Thevanayagam (1998) for soils with low densities: *“When the initial confining stress is increased, it may result in compaction of the finer grains at the contacts due to high compressibility at large  $e_f$  (interfine void ratio), and it may increase the coarser-grain contacts compared to a specimen of the same silty sand at the same void ratio at a low confining stress. Hence, the strength may also become sensitive to confining stress”*. Therefore, the sensitivity of the loose soils to the confining stress is larger than that of the dense soils. For this reason, the increment of shear strength is also larger at high confining pressures.

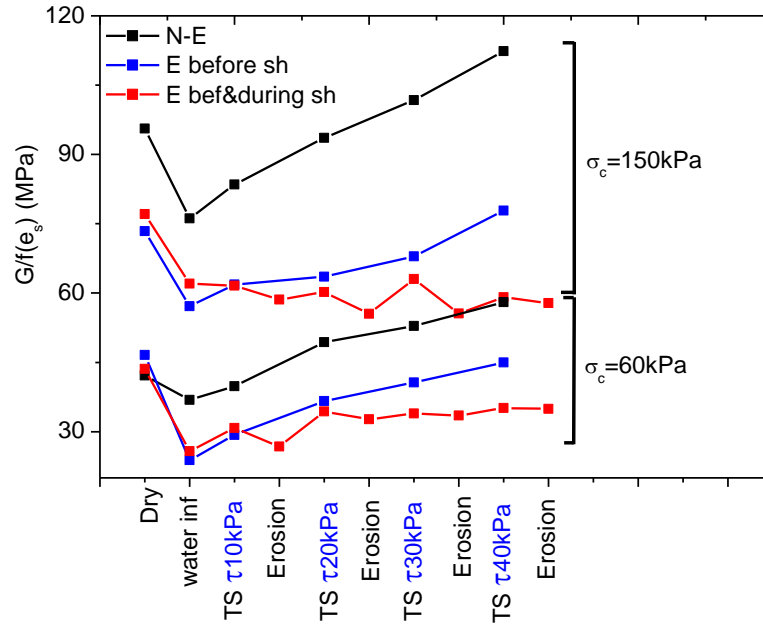
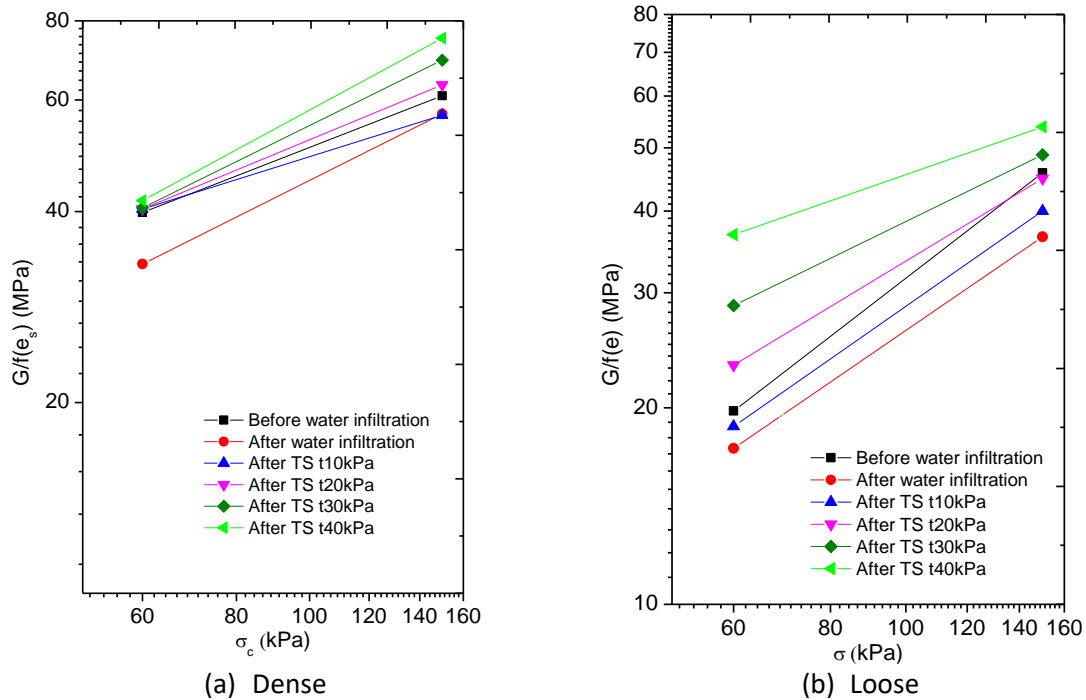

 Figure 5-78 Comparison of  $G/f(e_s)$  in loose specimens

Figure 5-79 to Figure 5-81 show the linear relationships between  $G/f(e_s)$  for dense specimens and  $G/f(e)$  for loose specimens, and the confining pressure on full logarithmic plot, at the different stages during the tests.


 Figure 5-79 Variation of  $G$  at different confining pressures, in specimens non-eroded

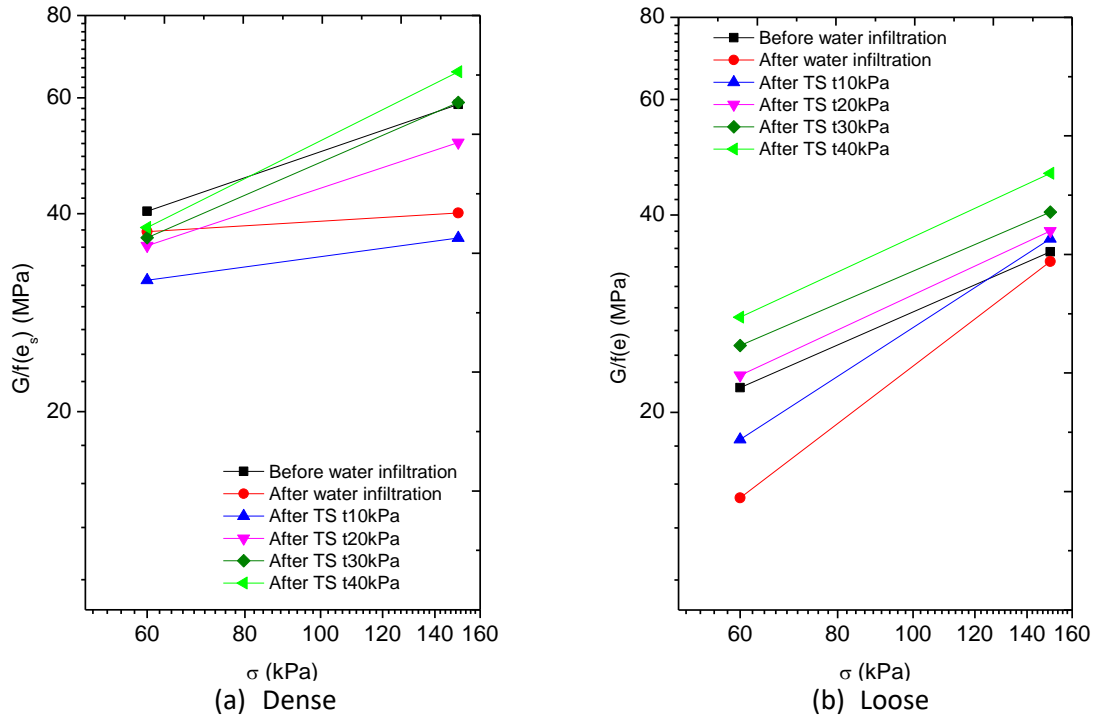


Figure 5-80 Variation of  $G$  at different confining pressures, in specimens eroded before shearing

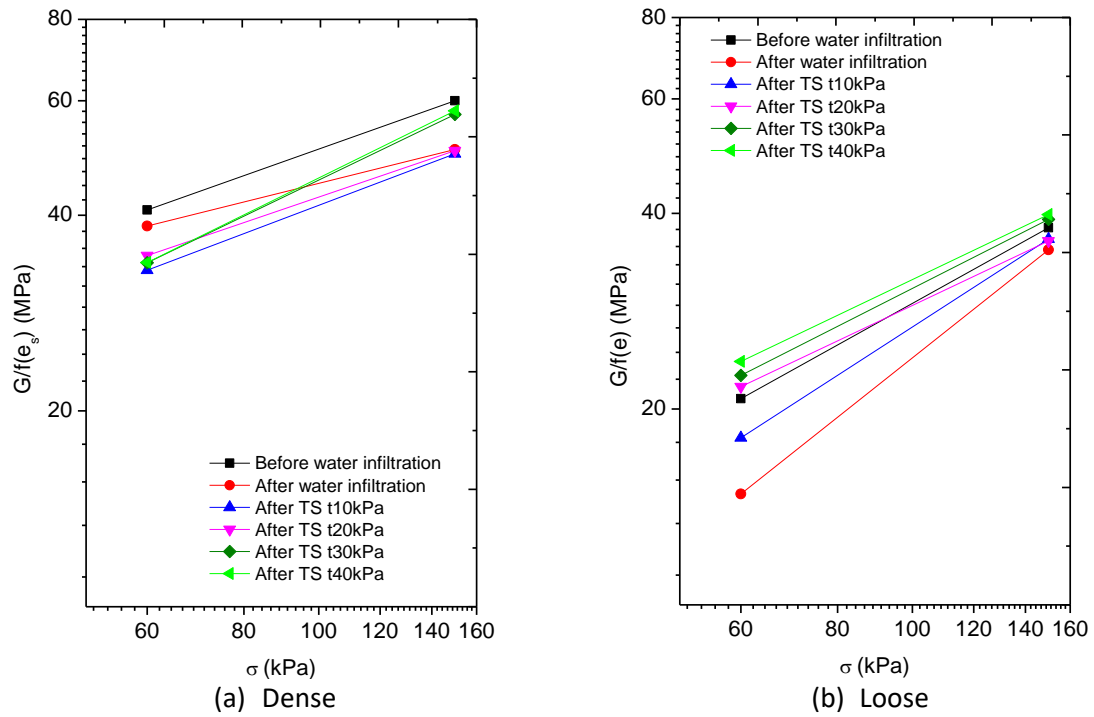


Figure 5-81 Variation of  $G$  at different confining pressures, in specimens eroded before and during shearing

From the previous figures  $G/f(e_s)$  can be expressed in a function of  $\sigma'_c{}^m$ , with  $m$  being the slope of the curve  $G/f(e_s) - \sigma'_c$  in logarithmic plot. The  $m$  value varies depending on the density and the stage in the test (Figure 5-82); it tends to decrease in the loose specimens and increase in the dense specimens.

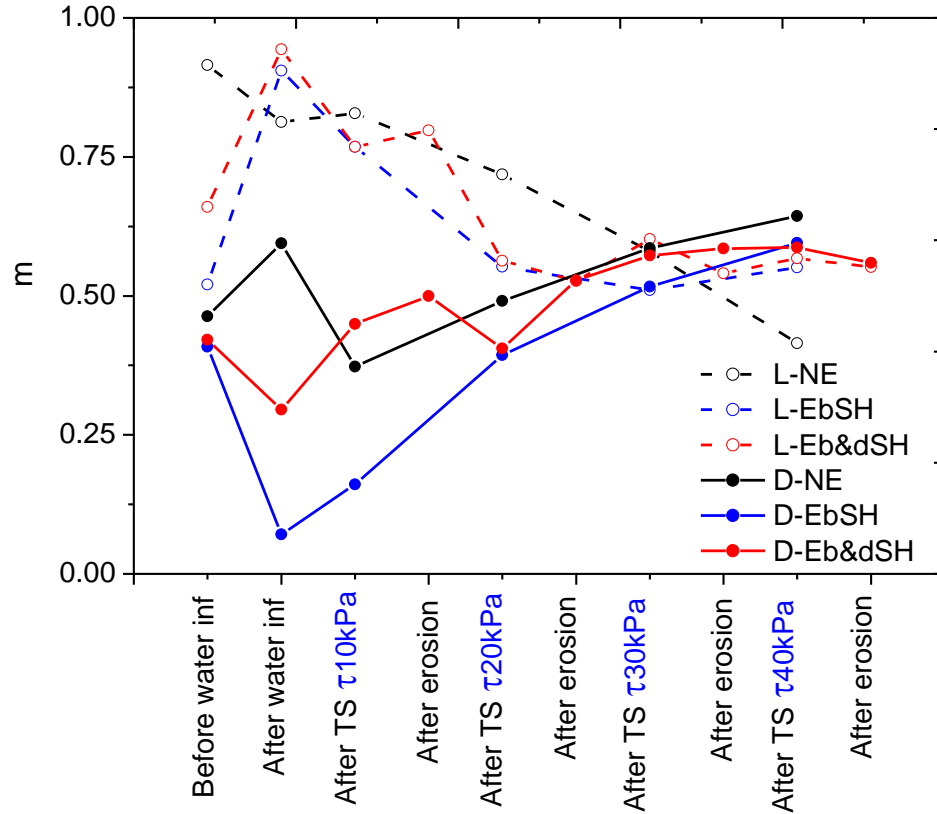
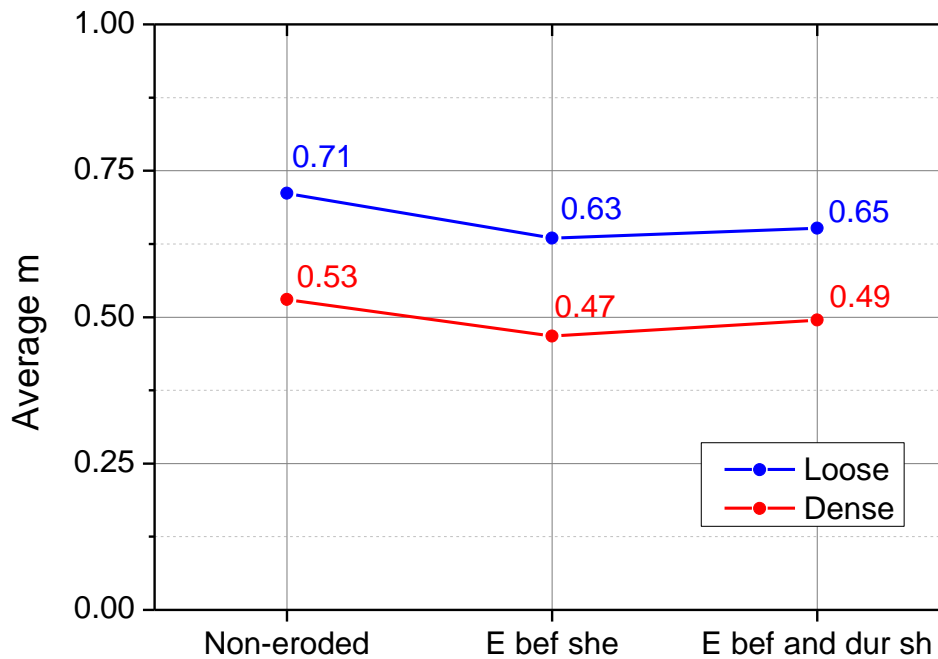


Figure 5-82 Variation of  $m$  for loose and dense specimens

The average slope  $m$  for loose and dense specimens is shown in Figure 5-83. The averaged  $m$  values are larger in loose specimens (0.67 to 0.77) compared with the dense specimens (0.47 to 0.53). The  $m$  value for dense specimens is similar to the values found for Toyoura sand  $m \approx 0.5$  (HongNam and Koseki, 2005; Yang, 2015).

Additionally, the specimens eroded exhibit lower values of  $m$  compared with the specimens not subjected to erosion.

Figure 5-83 Average  $m$  for loose and dense specimens

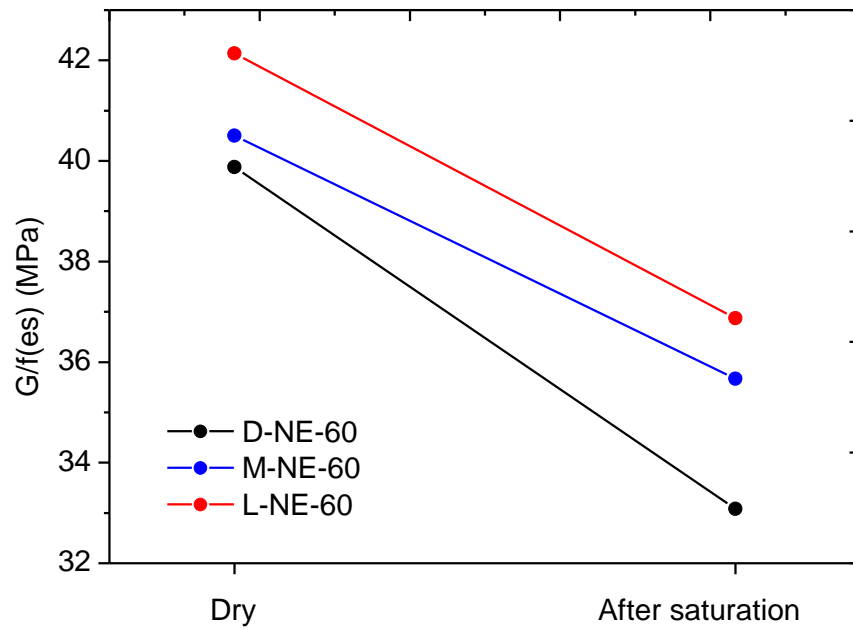
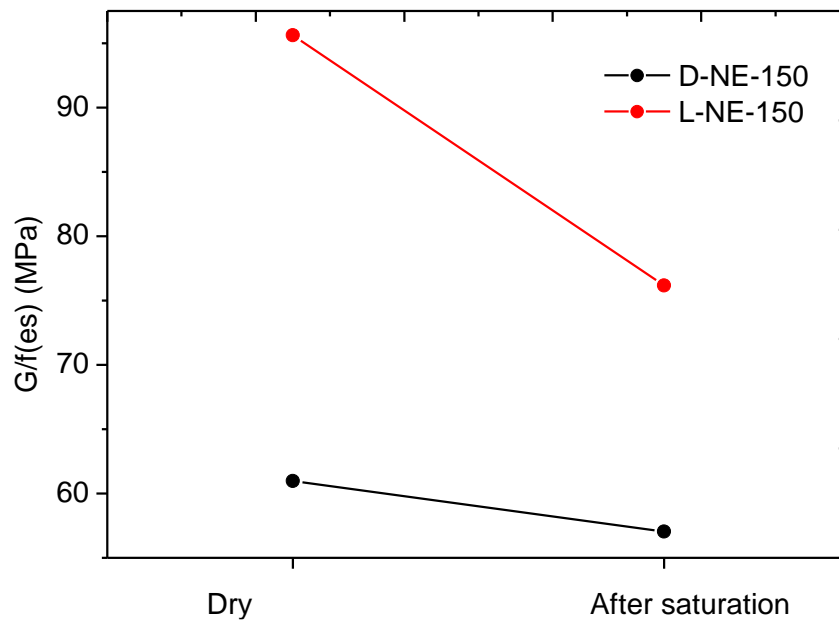
b. Influence of the detached particles on the stiffness:

In the analysis of the results of shear strength in the subsection 5.8.4 it was suggested that the fines (or detached particles) may have an influence in the strength depending on the relative density of the soil; the looser the soil is, the primary fabric skeleton is unstable by itself and the detached particles may act at some extent as transfer of loads. This behavior is also observed from the results of small strain stiffness.

When  $G$  is normalized with a function of intergranular void ratio  $e_s$ , it is assumed that only the primary fabric is acting in the stiffness. If the global void ratio  $e$  is used in the normalization it is considered that all the fines are contributing to the stiffness.

However, in the loose specimens it is unknown the percentage of fines contributing to the stiffness. If it is considered that only the primary fabric supports of stresses, the soils with all the densities normalized with the intergranular void ratio  $e_s$  would have the same values of  $G/f(e_s)$ . Nevertheless, the values of  $G$  normalized in the stages before shearing don't fit in the same point as it is shown in Figure 5-84 and Figure 5-85 (during shearing the difference is even higher so this analysis will be only focused in the variation before shearing).



Figure 5-84  $G/f(e_s)$  before shearing of specimens confined at 60 kPaFigure 5-85  $G/f(e_s)$  before shearing of specimens confined at 150 kPa

The difference in the values of  $G/f(e_s)$  show that some amount of fines is contributing to the stiffness in the looser specimens. The shear modulus  $G$  of medium-dense and loose soils was normalized considering various amounts of detached particles acting in the structure until

the values completely fit with the  $G/f(e_s)$  of the dense specimens (assuming that in the dense specimens 0% of the detached particles is contributing).

Figure 5-86 shows the estimated amount of detached particles that possibly act in the structure of the soil. The looser the soil is the greater the amount of detached particles contributing to the load transfer, and the percentage of fines acting is also dependent to the confining stress, if the particles are confined at higher pressures the structure of the soil will probably have more influence of the fines (Figure 5-87).

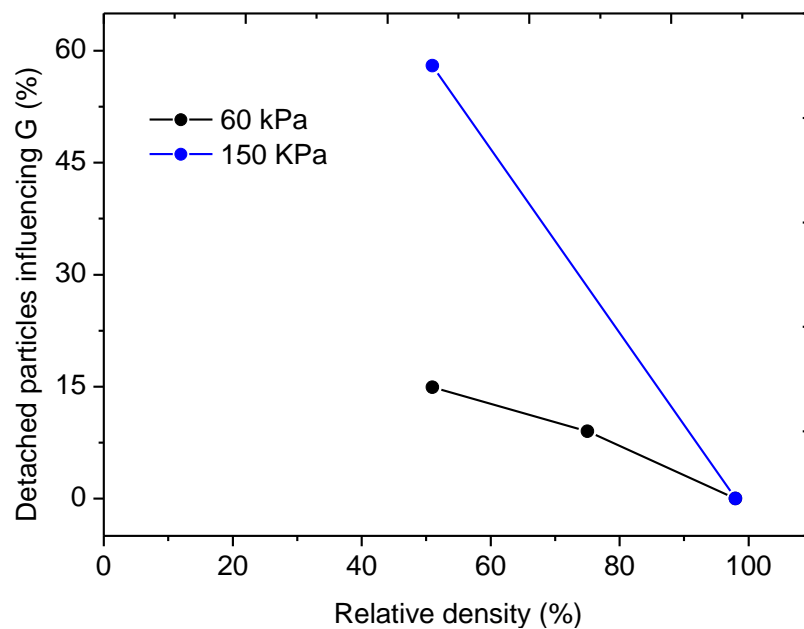


Figure 5-86 Estimation of the amount of detached particles acting on the structure

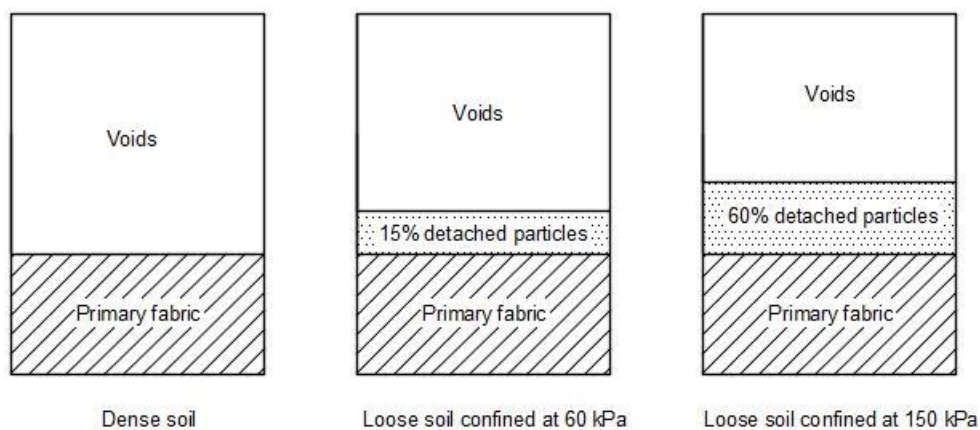


Figure 5-87 Influence of the detached particles on the structure

### 5.10. Strength parameters

The Mohr-Coulomb circles representing the peak states (solid curves) and critical states (dashed curves) and their respective envelopes and strength properties are shown from Figure 5-88 to Figure 5-93.

The critical state is defined as: “After large shear-induced volume change, a soil under given effective confining stress will arrive ultimately at unique final water content or void ratio that is independent of its initial state. At this state, the interlocking achieved by densification is gone in the case of dense soils, the metastable structure of loose soils has collapsed and the soil is fully destructured. A well-defined strength value is reached at this state, and is often referred to as the critical state strength” (Mitchell, 1976). The critical state can be considered a fundamental state, and it can be used as a reference state to explain the effect of relative density, and various stress paths on strength properties of soils (Schofield and Wroth, 1968)

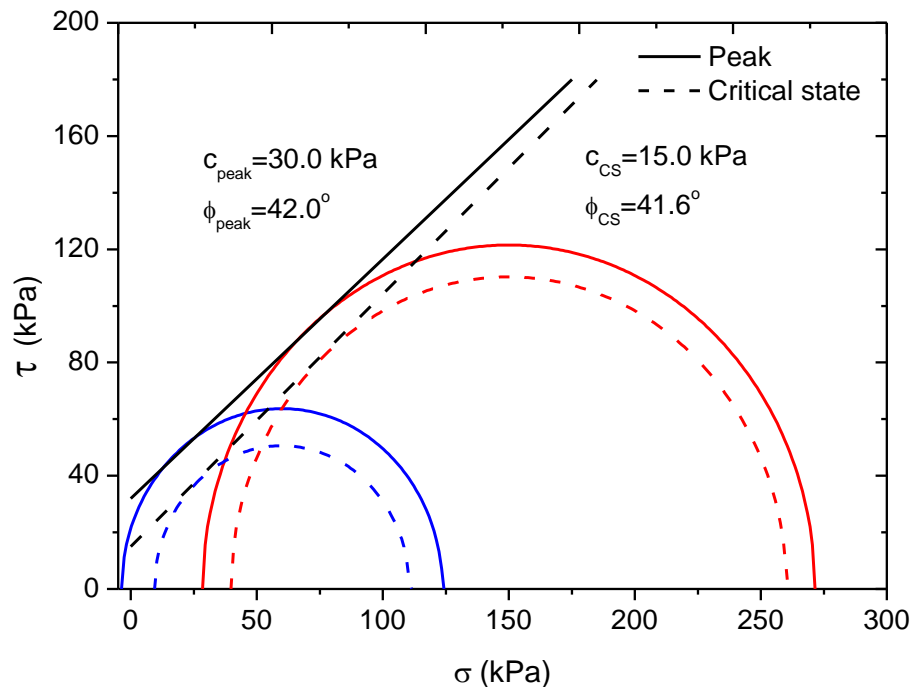


Figure 5-88 Peak strength and critical states for dense specimens non-eroded

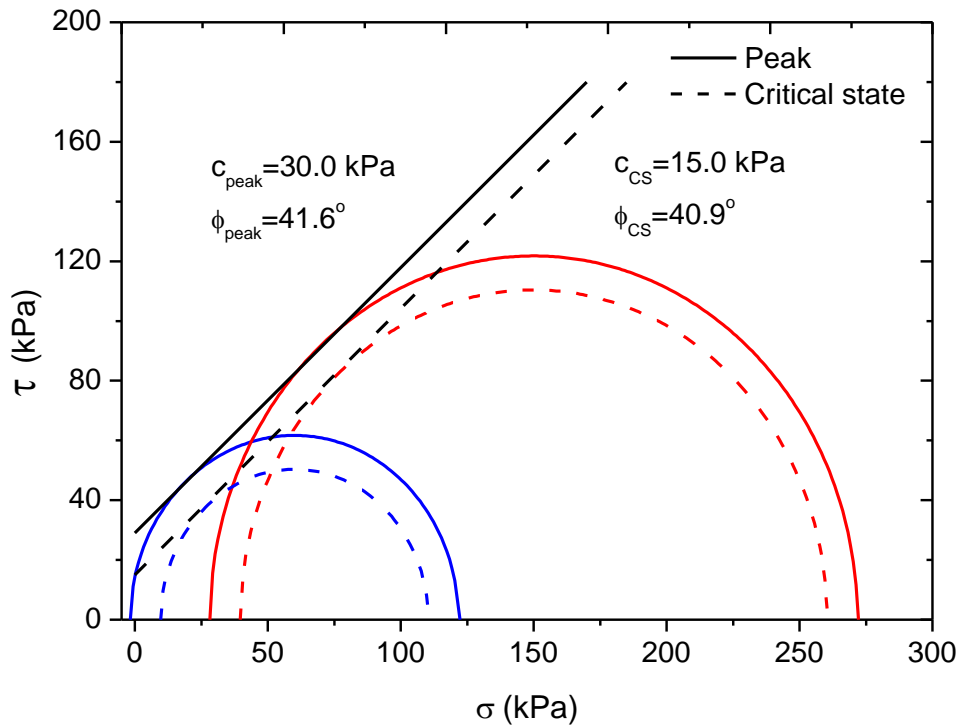


Figure 5-89 Peak strength and critical states for dense specimens eroded before shearing

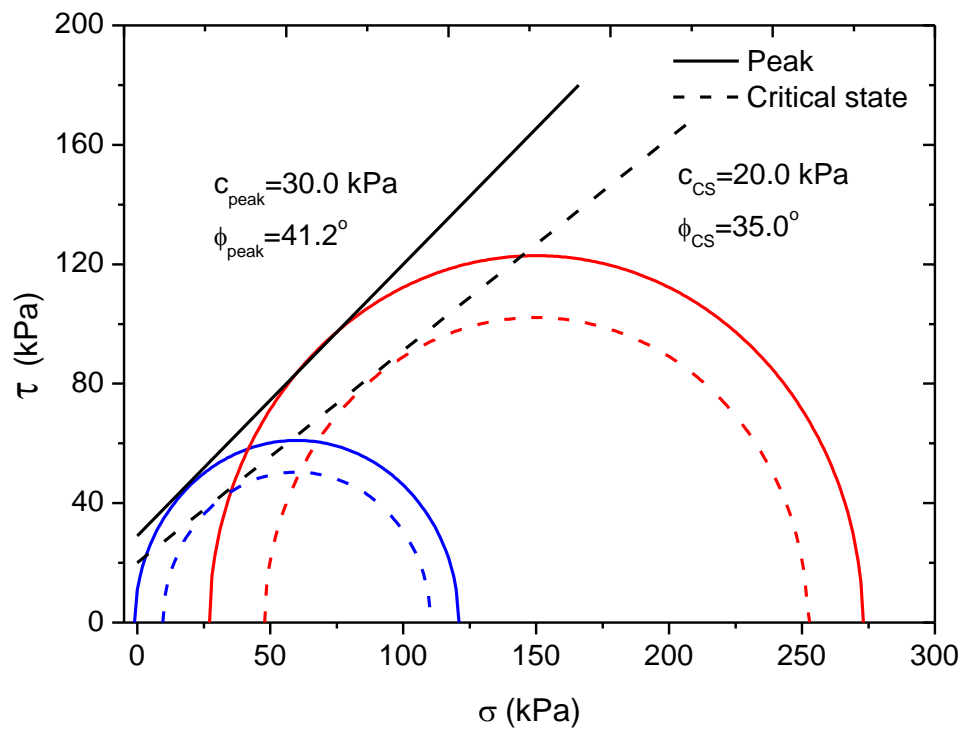


Figure 5-90 Peak strength and critical states for dense specimens eroded before and during shearing

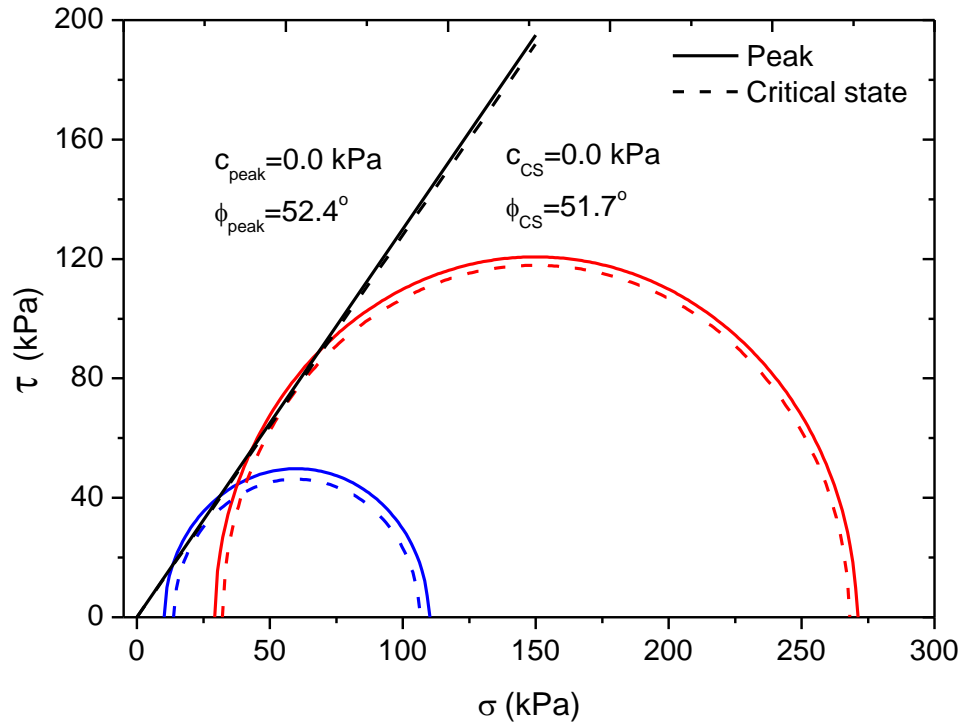


Figure 5-91 Peak strength and critical states for loose specimens non-eroded

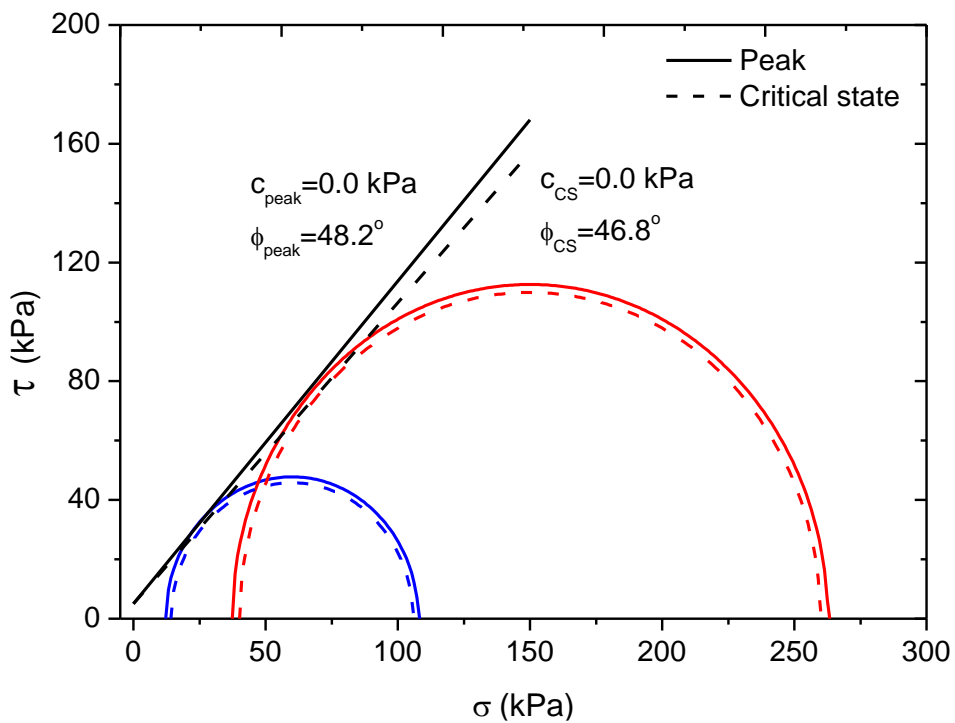


Figure 5-92 Peak strength and critical states for loose specimens eroded before shearing

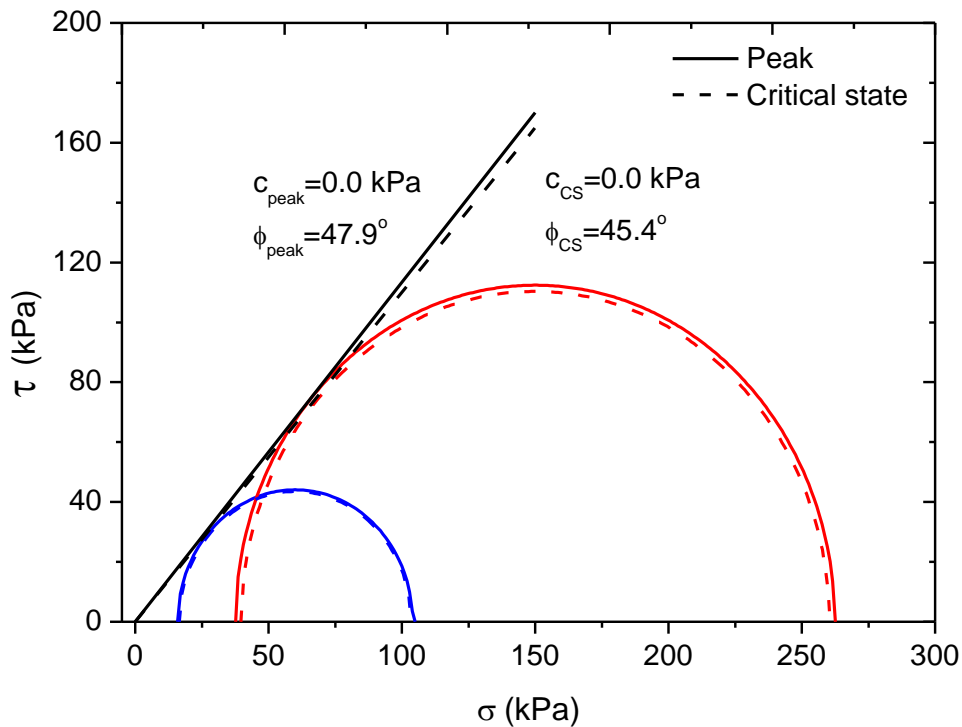


Figure 5-93 Peak strength and critical states for loose specimens eroded before and during shearing

For dense specimens the peak friction angle consists in part of internal rolling and sliding friction between grains and in part of interlocking of particles (Taylor, 1948). In specimens with high relative densities the peak strength is greater than the critical state strength in which the soil deforms under sustained loading at constant volume (Mitchell, 1976), this can be observed in the previous figures as the reduction in size of the Mohr-Coulomb circles and consequently the reduction of the friction angle. In loose soils the peak friction angle normally coincides with the critical state friction angle and there is no peak in the stress-strain curve (Mitchell, 1976). The Mohr-Coulomb circles for the loose specimens have similar sizes as it can be observed from Figure 5-91 to Figure 5-93.

The summary of the strength parameters is shown in Table 5-6 as the tests performed were under a drained condition, the total and effective stresses are the same. The variation of the friction angle on peak and critical states is shown in Figure 5-94. There is a reduction of the friction angle in the eroded specimens, compared to the specimens not subjected to erosion.

Table 5-6 Summary of strength parameters

		$c_{\text{peak}}$ (kPa)	$\phi_{\text{peak}}$ (°)	$c_{\text{CS}}$ (kPa)	$\phi_{\text{CS}}$ (°)
Dense	Non-eroded	30.0	42.0	15.0	41.6
	Eroded before shearing	30.0	41.6	15.0	40.9
	Eroded before and during shearing	30.0	41.2	20.0	35.0
Loose	Non-eroded	0.0	52.4	0.0	51.7
	Eroded before shearing	0.0	48.2	0.0	46.8
	Eroded before and during shearing	0.0	47.9	0.0	45.4

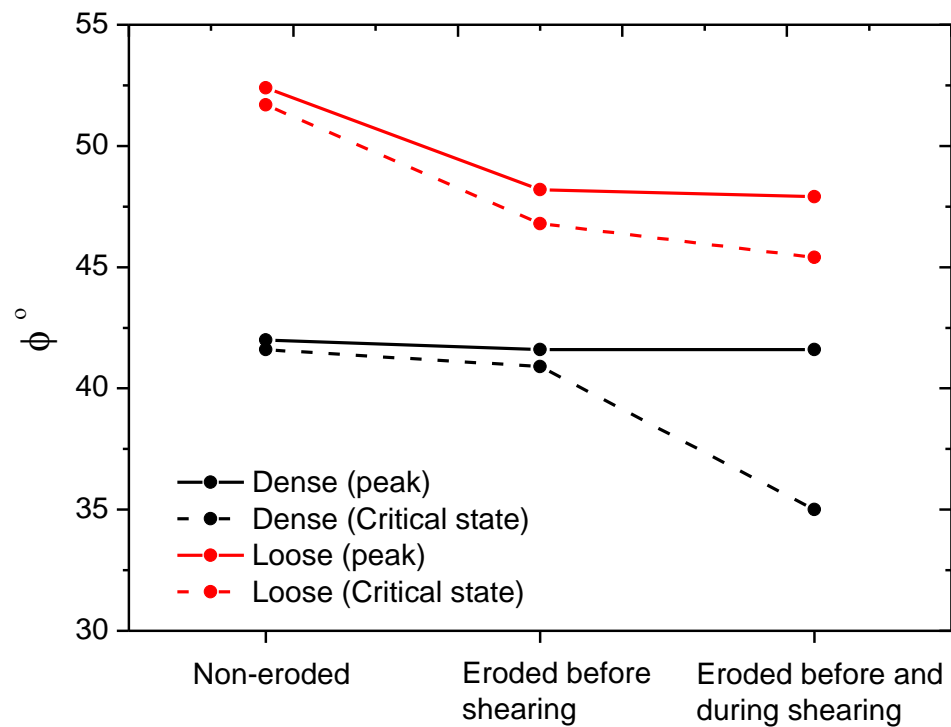


Figure 5-94 Variation of the peak and critical state friction angle

The critical state lines for dense and loose specimens have been determined as regression curves of the shear stress at critical state; they have similar values of slope around 0.74 and 0.75 (Figure 5-95). Thus, the critical state ratio for specimens with any relative density can be approximated to be  $slope = 0.75$ .

The relationship between the void ratio and mean effective stress at failure could not be calculated in this study because the clip gauges are detached at large strains to avoid failure of clip gauges.

The comparison of the peak shear stresses and the critical state line CSL is shown in Figure 5-96. The dense specimens are above the CSL, while the loose specimens coincide with the CSL.

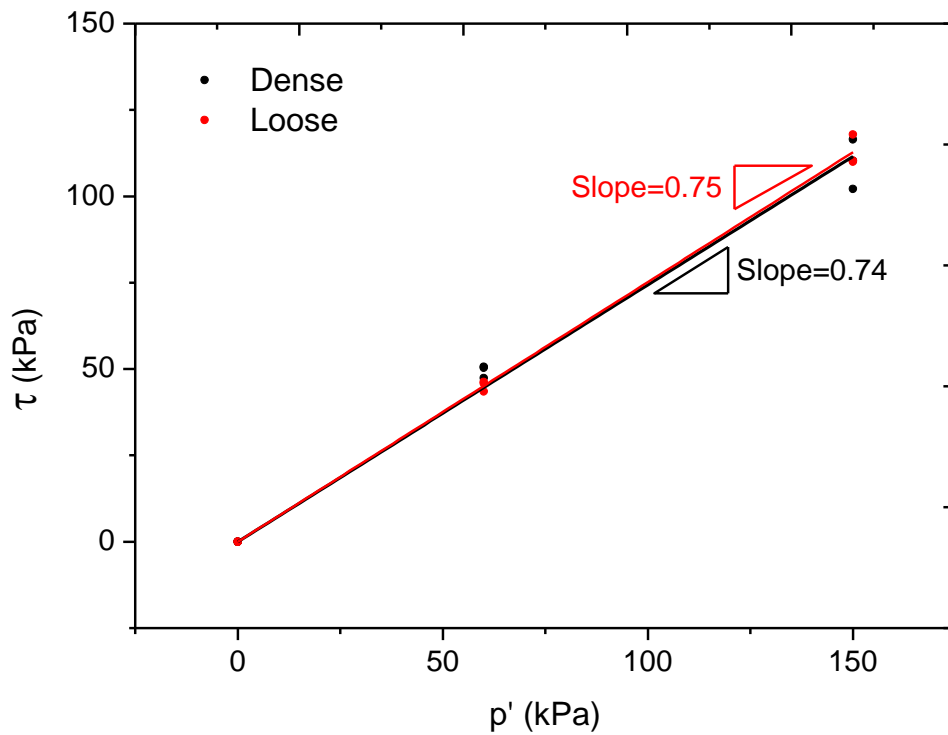


Figure 5-95 Critical state lines for dense and loose specimens



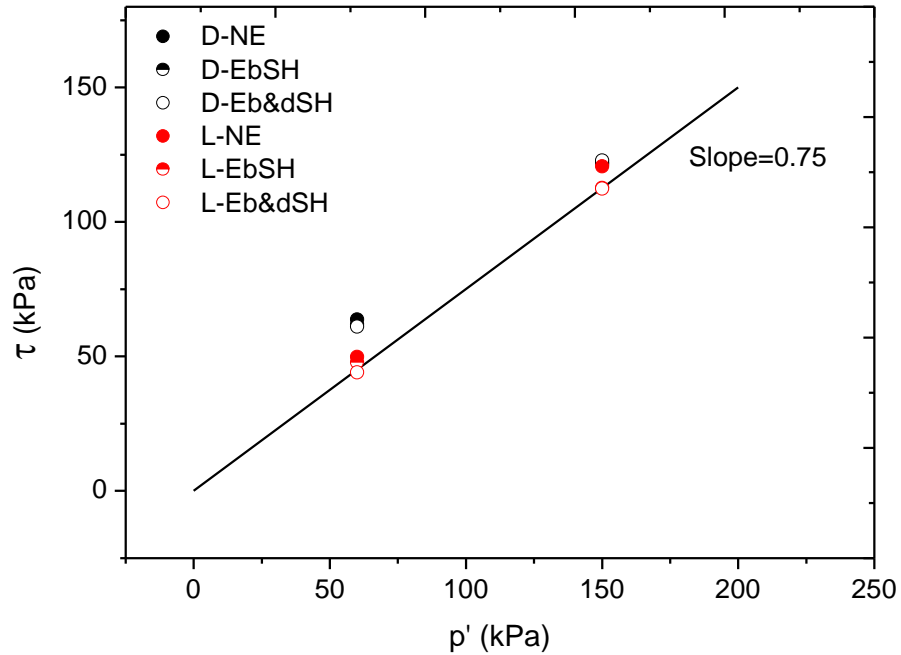


Figure 5-96 Comparison of the peak shear stresses and the critical state line

#### 5.11. Image analysis

After the tests, the particles content and distribution along the specimens were studied through microscope images and their image analysis. Small samples (Figure 5-98) at 5 different heights in the specimen (Figure 5-97) were taken, at different sites diametric distribution, in order to obtain more reliable data.

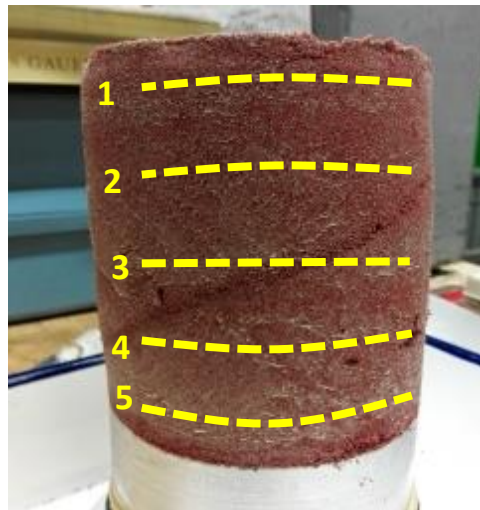


Figure 5-97 Location of the images taken in the specimen



Figure 5-98 Samples for image analysis

Using a Digital Microscope 3R-MSM025S (Figure 5-99) precise images of the particles were taken (Figure 5-100).



Figure 5-99 Digital microscope

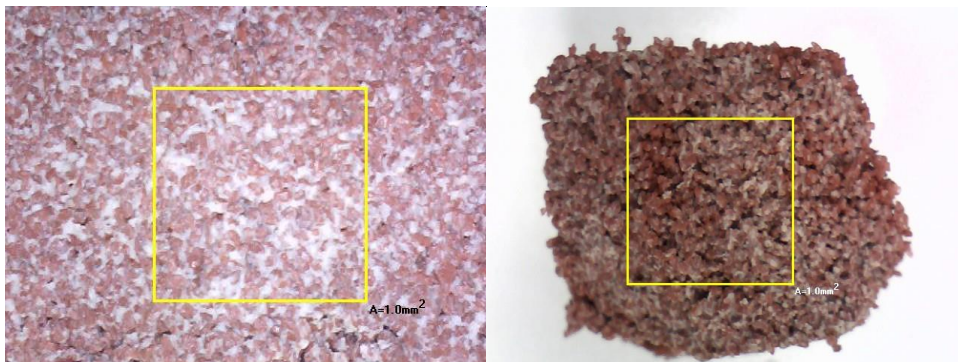


Figure 5-100 Microscope images

The microscope images of a non-eroded and an eroded soil show clearly the particles having different colors (red and white). In the non-eroded specimen there is a large amount of white particles (DL clay or detached particles), while in the eroded soil most of the particles are just red (Silica sand or primary fabric) (Figure 5-101).

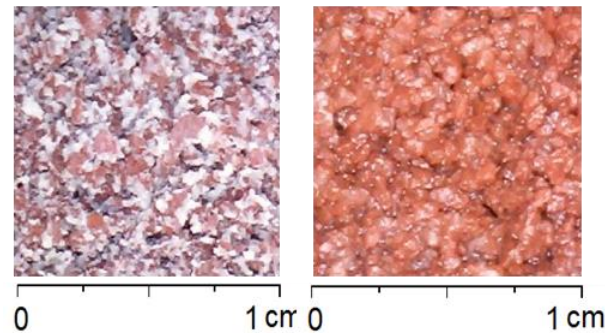


Figure 5-101 Microscope images of a non-eroded soil (left) and eroded soil (right).

In order to analyze the content of particles, and differentiate the primary fabric (Silica sand color red) and the detached particles (DL Clay whitish), the software Image J was used, which is an open-source software for the analysis of images (Figure 5-102).

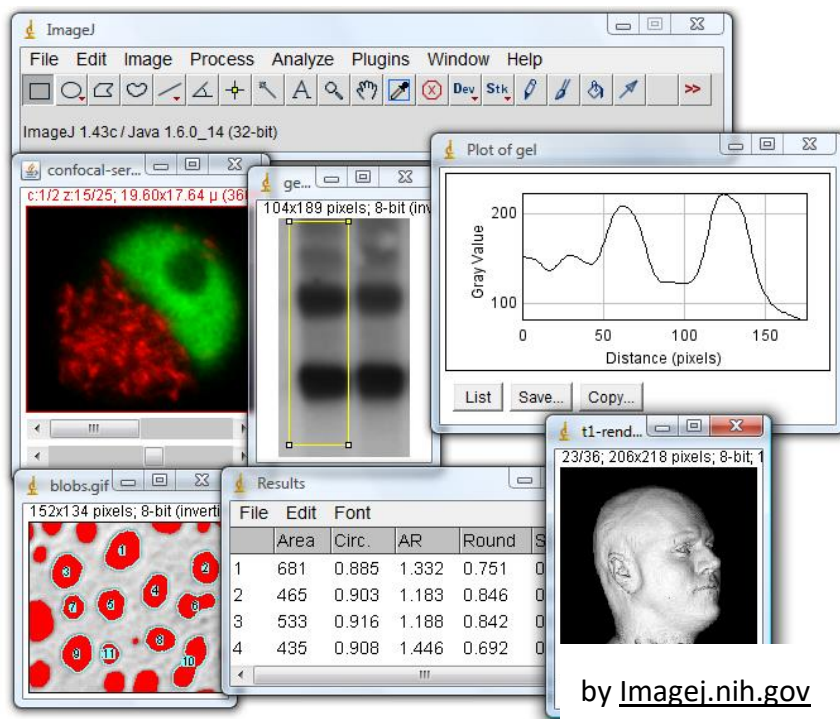


Figure 5-102 ImageJ software

Using the Image J the brightness can be analyzed; therefore the particles with low brightness can be attributed to voids, the brightest to the fines, and the moderate brightness to the primary fabric (Figure 5-103 and Figure 5-104).

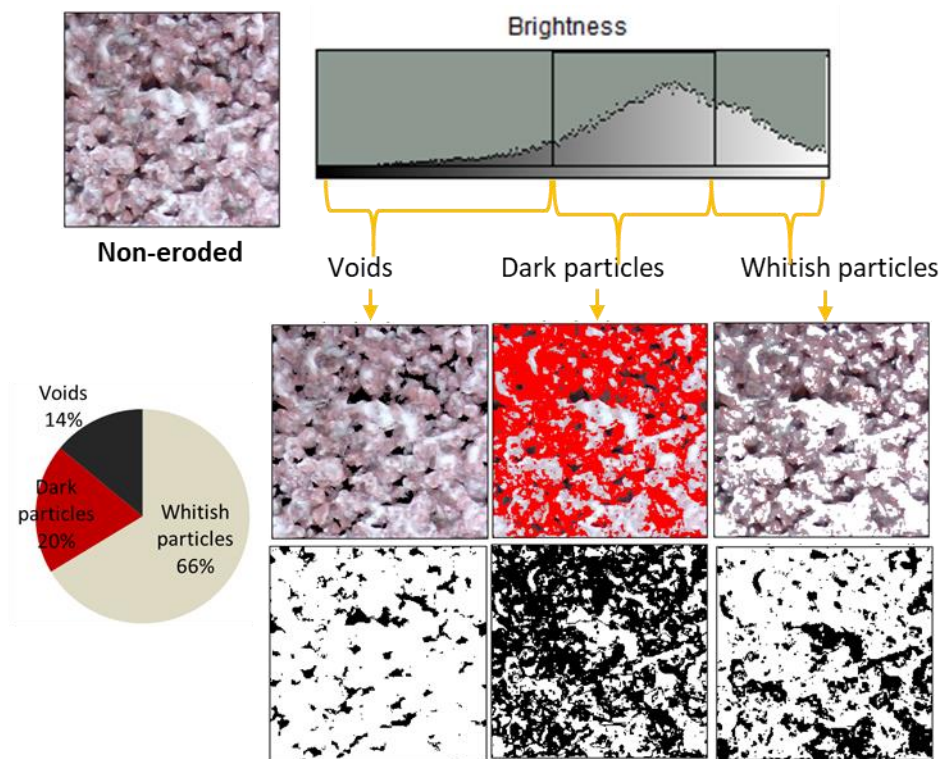


Figure 5-103 Image analysis of a non-eroded sample

It is possible to measure the percentage of each group in the image, relating it to the amount of particles. For instance, in the non-eroded sample the amount of whitish particles or fines is 66% (Figure 5-103) and in the eroded sample the amount of fines is 32% (Figure 5-104). Nevertheless, the area of detached particles could be overestimated because they could be covering the surface of some primary fabric particles.

The area of voids can be measured; however, the accuracy seems not sufficient because the darkness of the void depends on its depth, e.g. if the void is too shallow it may have the same brightness as a silica sand grain. For this reason, the area of voids has not been analyzed.



Although the estimation of the detached particles by image analysis is not precise enough and cannot be used for a quantitative analysis, it can still be used for a qualitative evaluation of erosion.

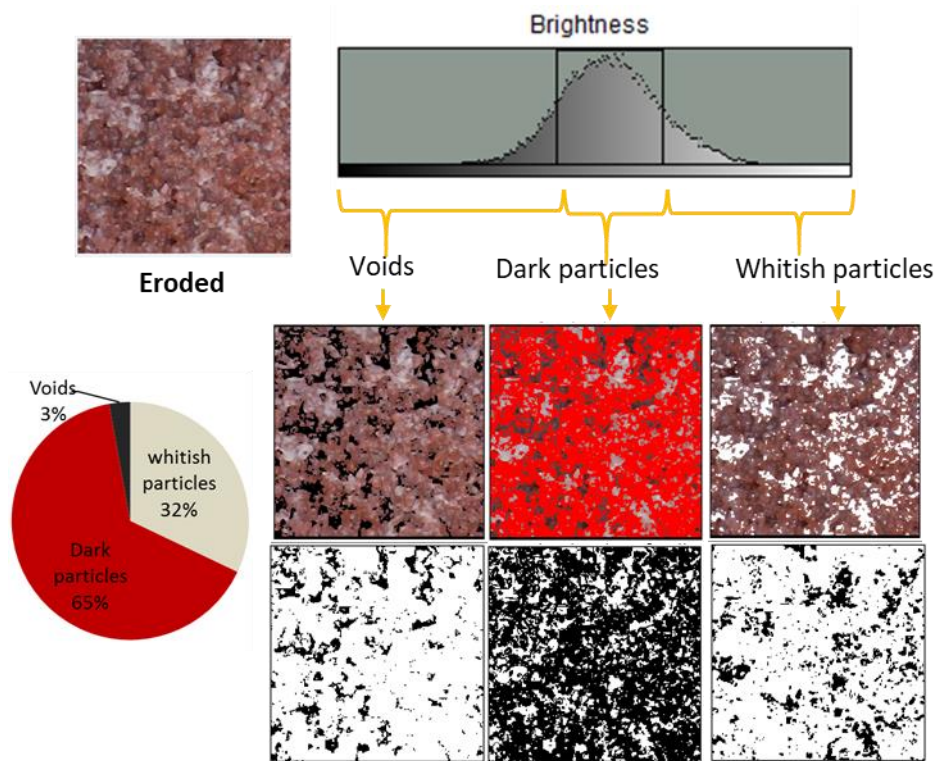


Figure 5-104 Image analysis of an eroded sample

Therefore, it is possible to make a correlation of the percentage of whitish particles measured by ImageJ and the amount of fines in the soil (Figure 5-105). The calibration is shown in Figure 5-106.

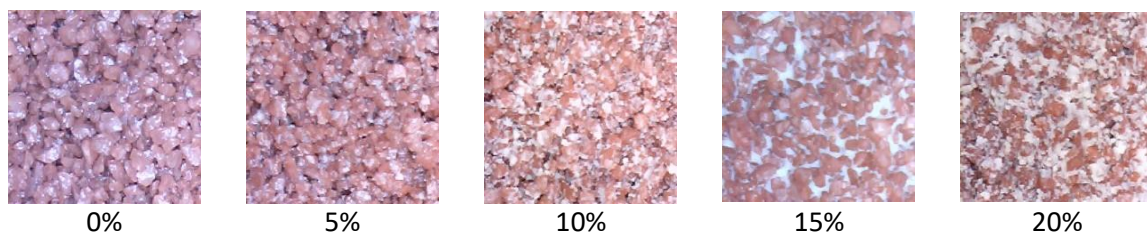


Figure 5-105 Microscope images of soils with different fines content

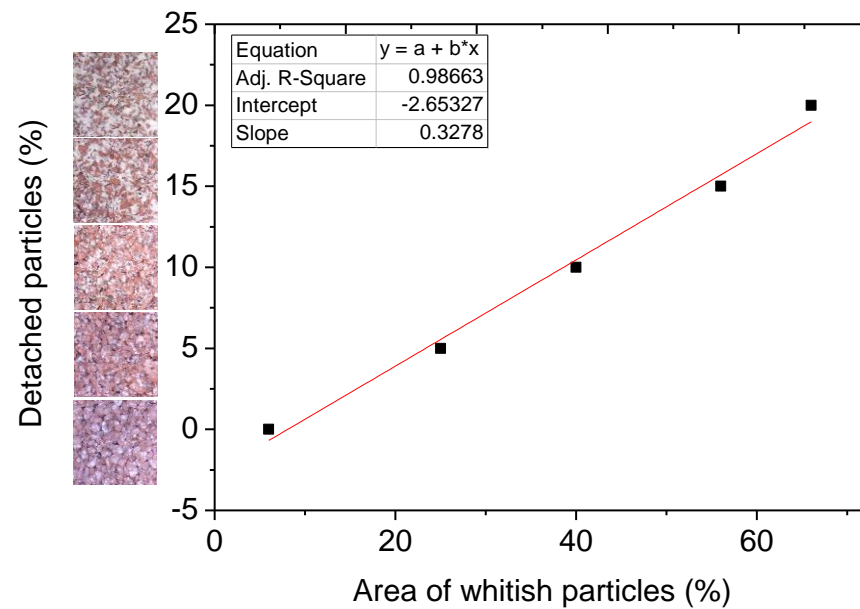


Figure 5-106 Calibration for image analysis

#### 5.11.1. Specimens confined at $\sigma_z = \sigma_r = \sigma_\theta = 60kPa$

The results of the amount of particles eroded out of the specimen are shown from Figure 5-107 to Figure 5-111. Additionally, the microscope image corresponding to each point in the extreme cases: For the non-eroded in the left side and for the eroded before and during shearing in the right side. As it is known, the initial percentage of detached particles is 20% for all the specimens, in the dense specimens there is a considerable erosion of the fines (around 10%), and as expected the non-eroded specimens show around 0% of eroded particles (Figure 5-107).

The medium-dense specimens also present erosion of around 10% of the particles (Figure 5-108). For the loose specimens, in the most eroded case, almost 20% of the particles were eroded (Figure 5-109).

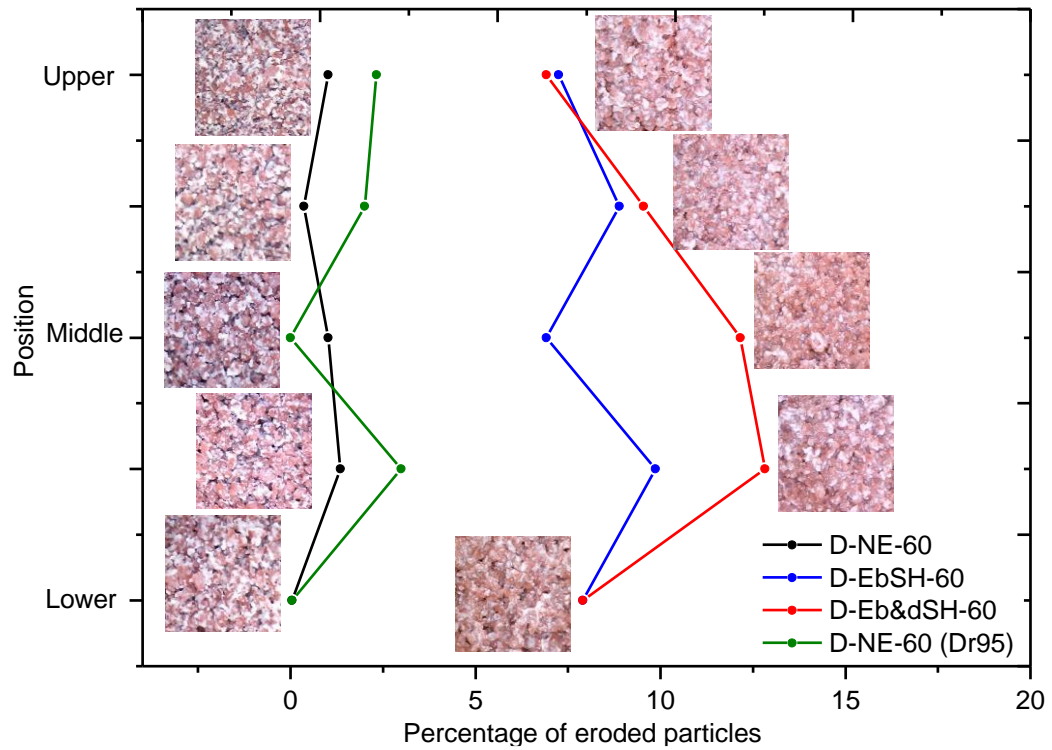


Figure 5-107 Percentage of eroded fines for the dense specimens confined at 60 kPa

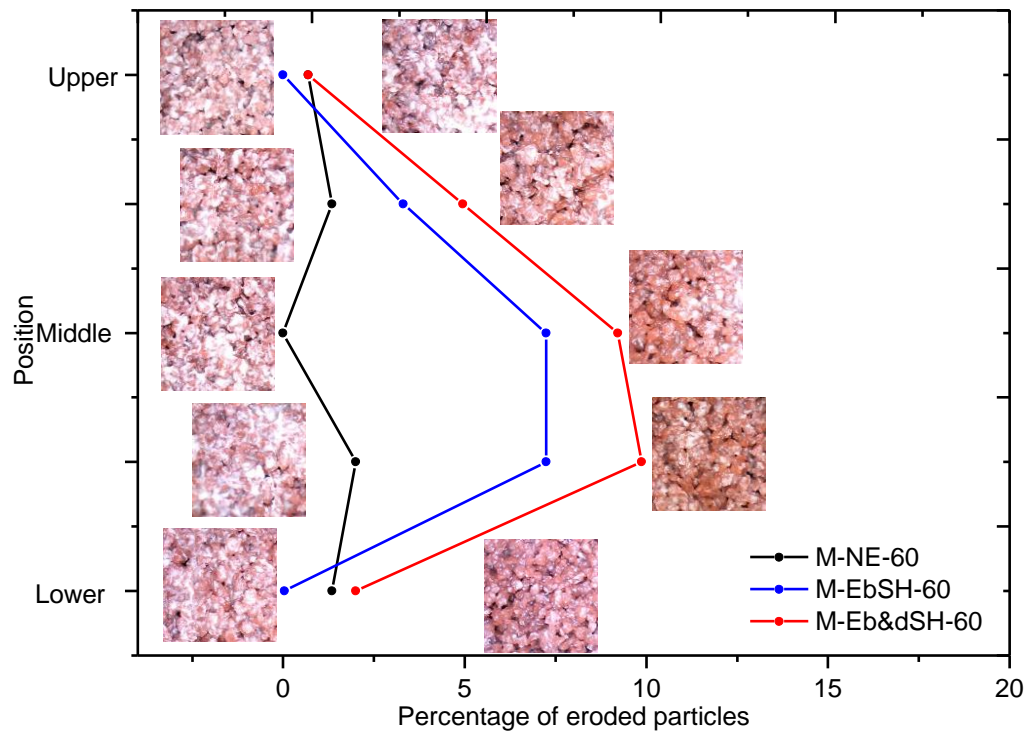


Figure 5-108 Percentage of eroded fines for the medium-dense specimens confined at 60 kPa

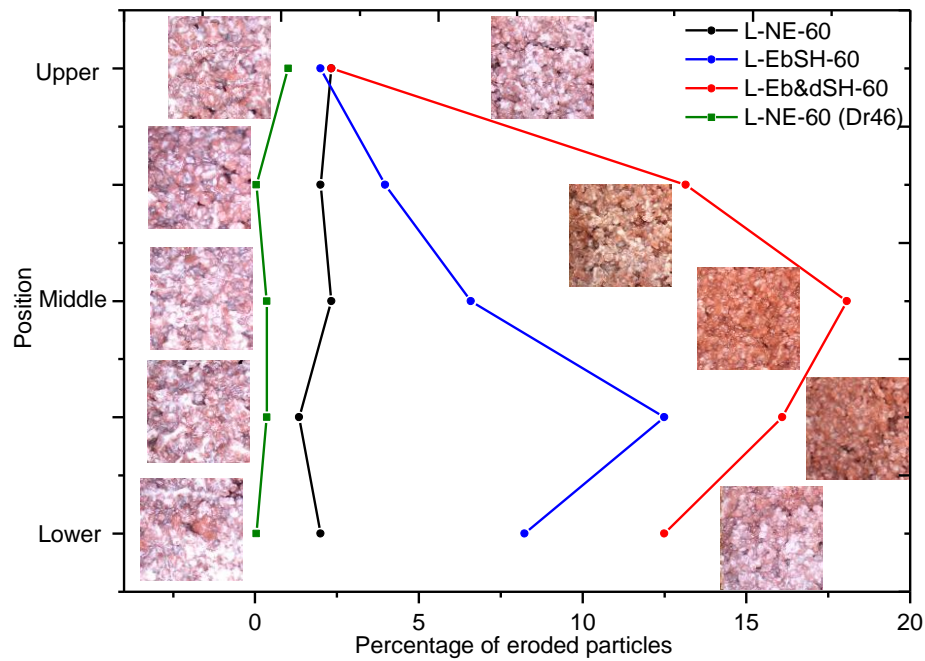


Figure 5-109 Percentage of eroded fines for the loose specimens confined at 60 kPa

#### 5.11.2. Specimens confined at $\sigma_z = \sigma_r = \sigma_\theta = 150 \text{ kPa}$

For the specimens confined at 150 kPa a similar trend is exhibited (Figure 5-110 and Figure 5-111).

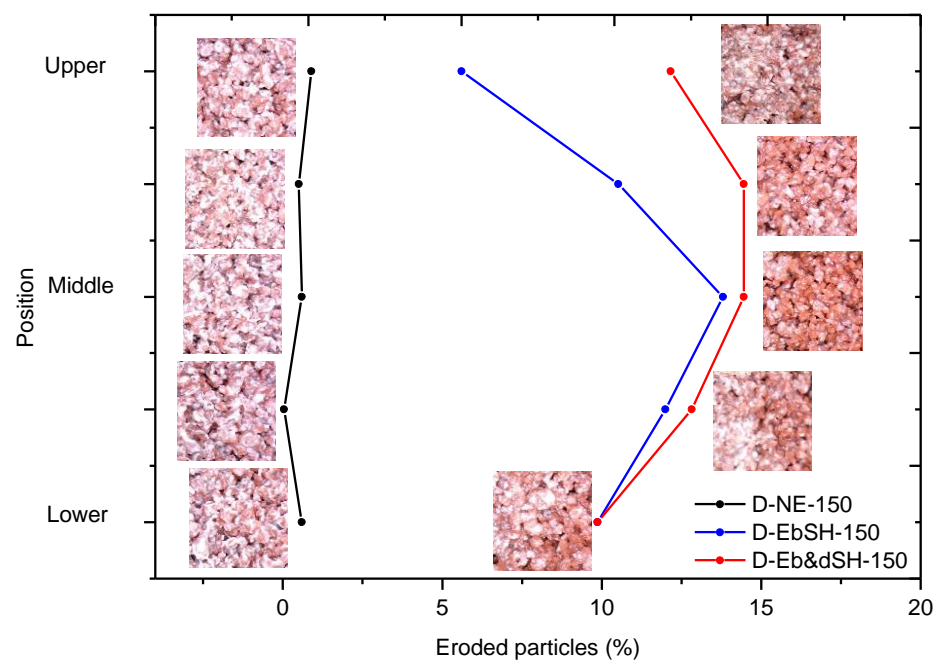


Figure 5-110 Percentage of eroded fines for the dense specimens confined at 150 kPa



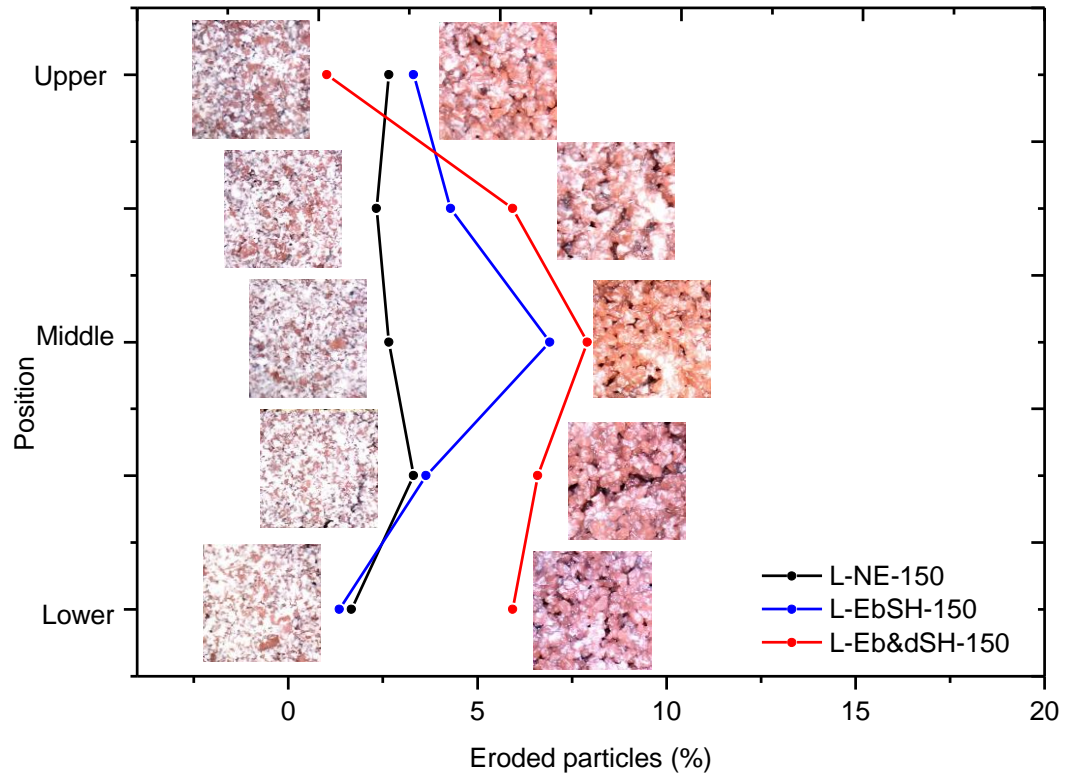


Figure 5-111 Percentage of eroded fines for the loose specimens confined at 150 kPa

### 5.11.3. Void ratio variation at various heights in the specimen

The general trend in the variation of the percentage of fines, is that the maximum erosion or amount of displaced fines is concentrated at the middle height of the specimen. In order to understand this behavior, the void ratio was calculated according to the individual data recorded by the three clip gauges used (Figure 5-112).

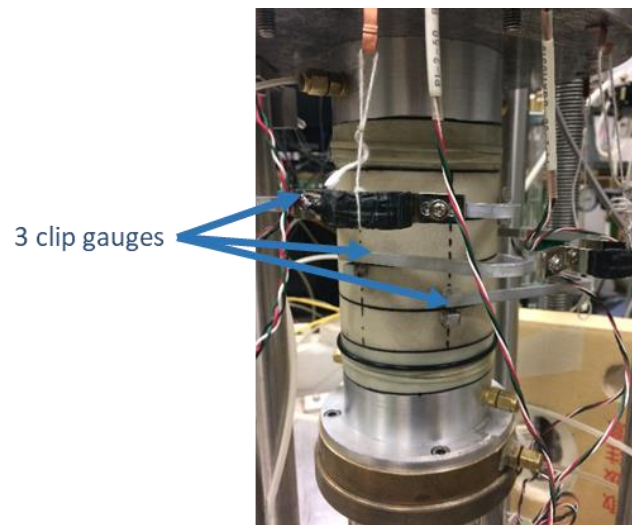


Figure 5-112 Position of the clip gauges

The variation of the void ratio can be determined at the upper, middle and lower part of the specimen. Figure 5-113 shows the void ratio variation of the loose specimens at the three locations of the clip gauges. The maximum void ratio is observed at the mid-height of the specimen, due to the constraint effect of the membrane attached to the pedestal and the top cap in the bottom and upper parts. This explains that the migration of the fines is mainly from the middle zones. Also, the void ratio increases accordingly to the degree of erosion, and it is larger in the most eroded soil (red points).

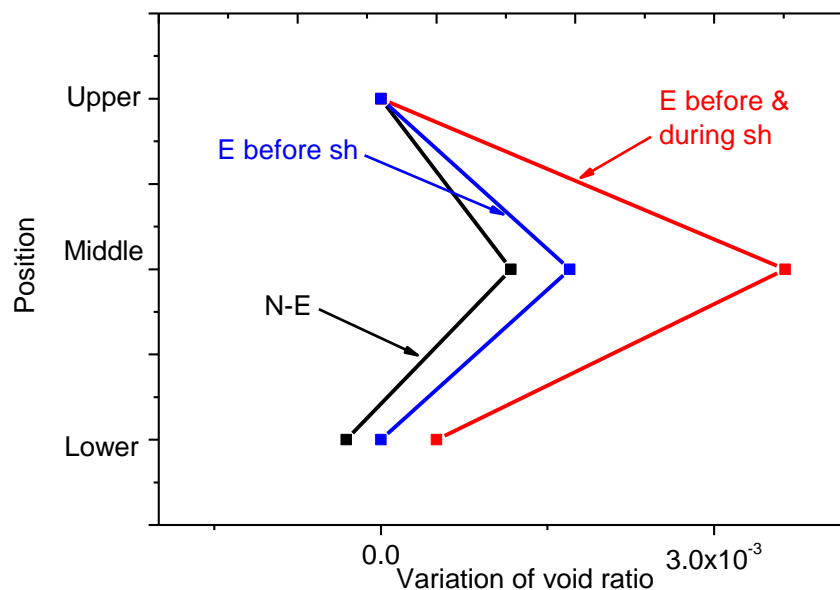


Figure 5-113 Void ratio variation at various heights

The previous analysis (Figure 5-107 to Figure 5-111) show the estimated amount of fines at the three parts in the specimen after finishing the test. A possible explanation for the lower degree of erosion at the bottom part is that the fines that are in this zone at the final stage were not originally in that place, which means that they come from the upper parts of the specimen.

The flow of the particles eroded is plotted in Figure 5-114 to Figure 5-118. The flow is considerably larger in the lower part because the water is infiltrated from the top and drained from the bottom pedestal.

The flow also depends on the degree of erosion, it remains constant nearly zero in the specimens non-eroded and in the eroded specimens the flow of the particles is larger as expected.

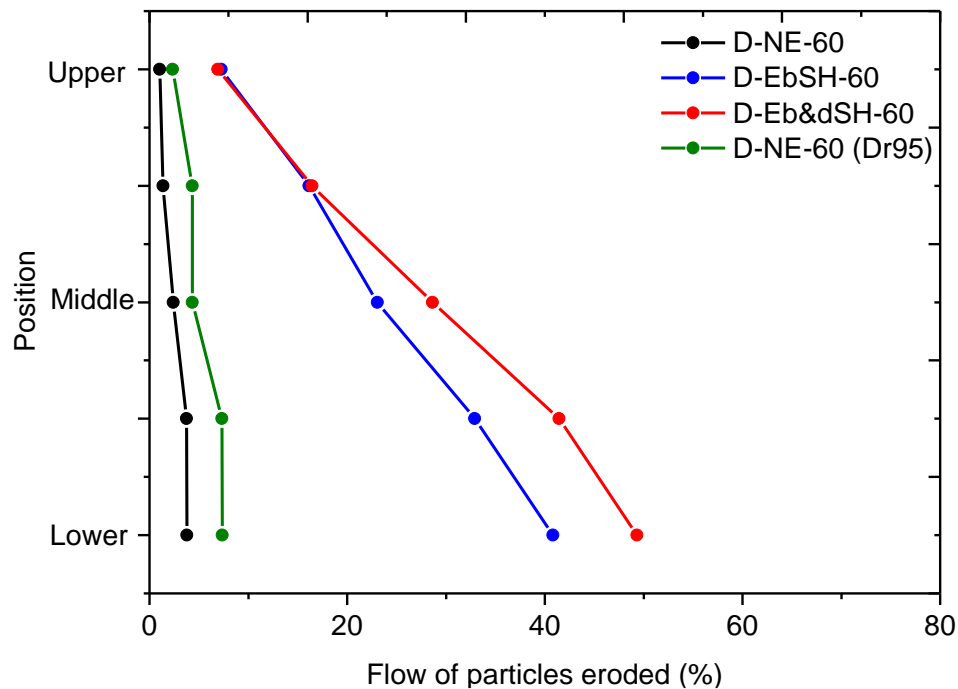


Figure 5-114 Flow of particles eroded for the dense specimens confined at 60 kPa

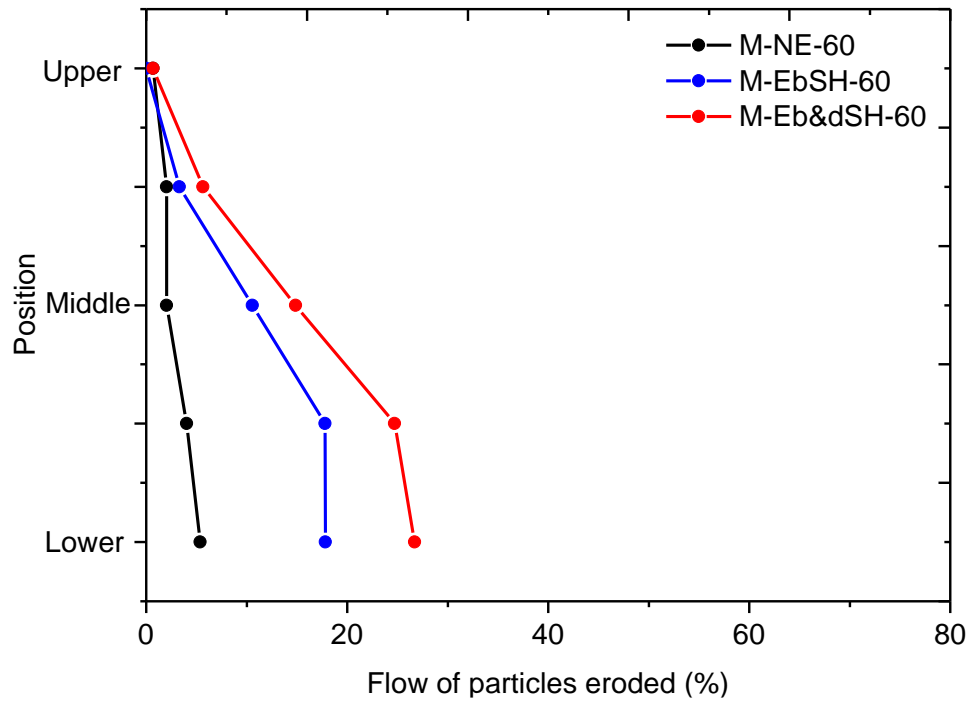


Figure 5-115 Flow of particles eroded for the medium dense specimens confined at 60 kPa

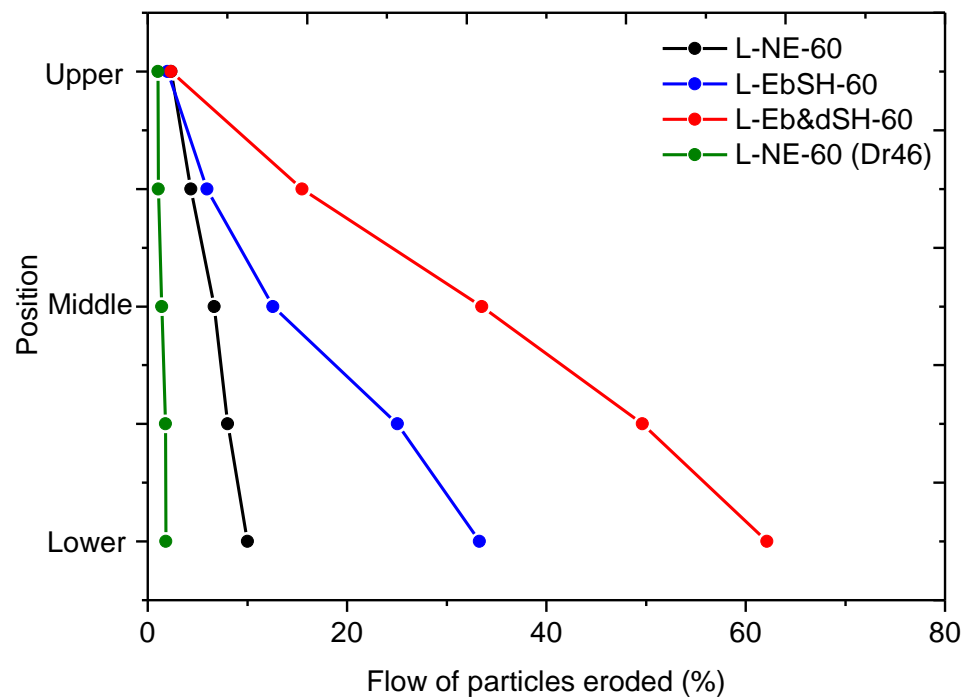


Figure 5-116 Flow of particles eroded for the loose specimens confined at 60 kPa

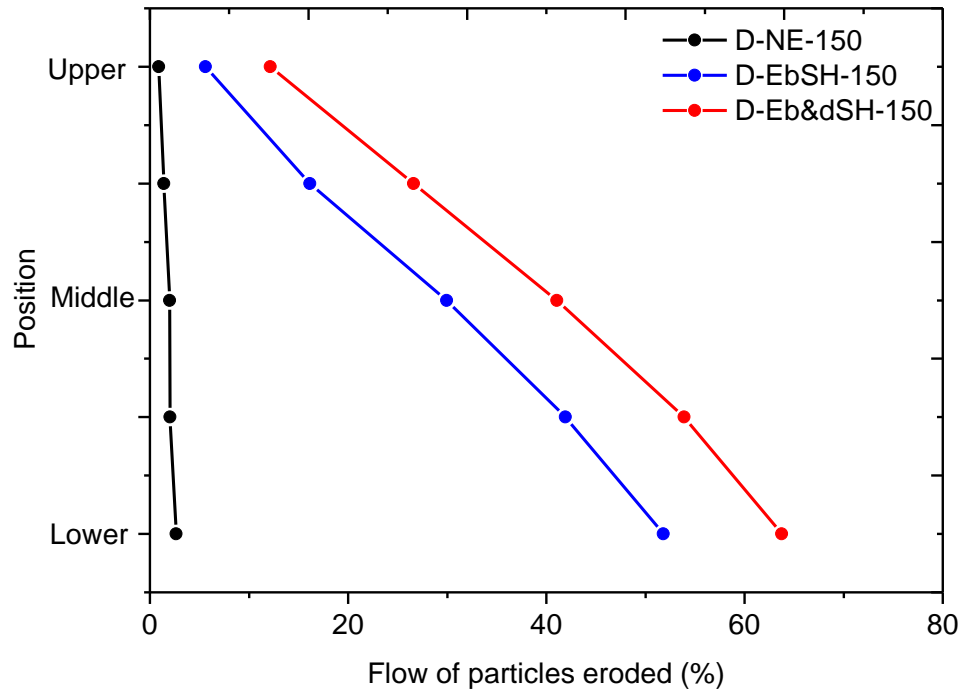


Figure 5-117 Flow of particles eroded for the dense specimens confined at 150 kPa

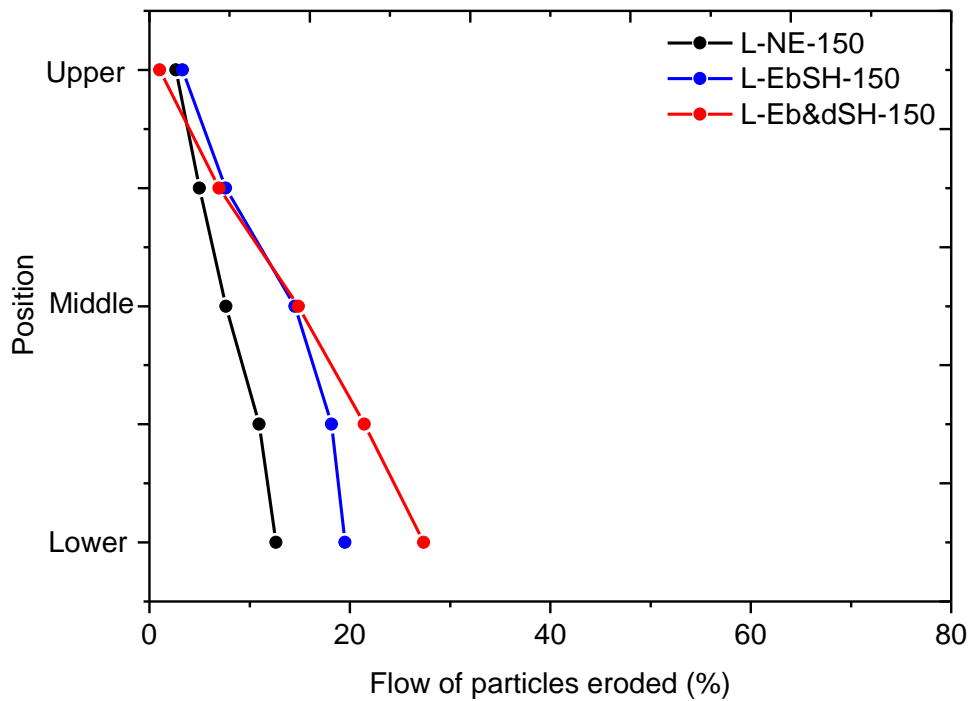


Figure 5-118 Flow of particles eroded for the loose specimens confined at 150 kPa

## 5.12. Analysis and conclusions

### 5.12.1. Effects of the torsional shear in the degree of erosion

Referring to the variation of eroded soil and turbidity (see Figure 5-3 to Figure 5-11), there is a considerable rise in the turbidity of the water that pass through the specimen after small increments in the shear strain. In order to evaluate this behavior, the results for the loose specimen eroded before and during shearing with confining stress of 60 kPa (L-Eb&dSh-60) are analyzed below.

Figure 5-119 shows that after applying torsion up to  $\tau_{z\theta} = 10\text{kPa}$  the turbidity value increases from 73 NTU to 927 NTU, meaning a rise of almost 13 times; a similar response is observed at  $\tau_{z\theta} = 20\text{kPa}$ , and at a less extent at  $\tau_{z\theta} = 30\text{kPa}$  and  $\tau_{z\theta} = 40\text{kPa}$ .

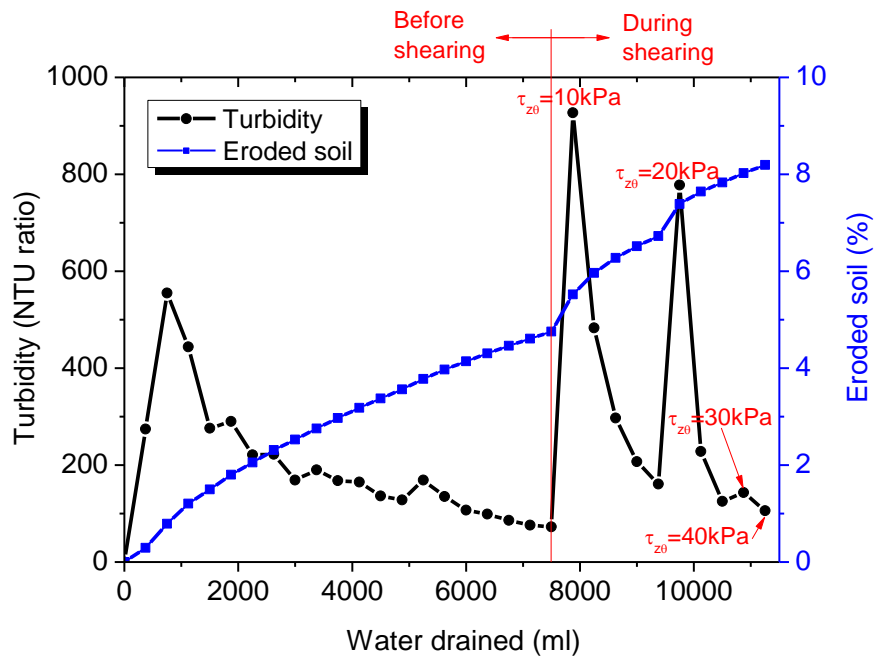


Figure 5-119 Turbidity and eroded soil of L-Eb&dSH-60 (same as Figure 5-7)

However, the values of volumetric strain  $\varepsilon_{vol}$ , global void ratio  $e$  and intergranular void ratio  $e_s$  do not present any significant change during the increments of shear stress, as it can be observed in the hatched areas in Figure 5-120. Likewise, the global relative density and intergranular relative density remain constant during this stage (Figure 5-122).

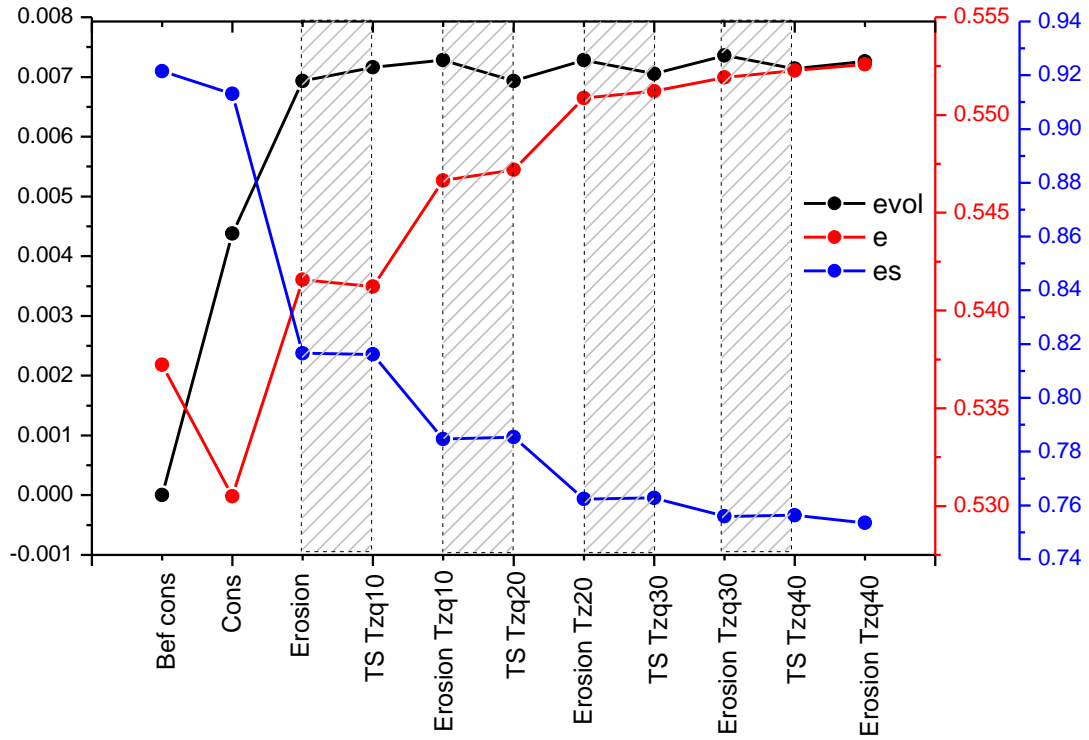
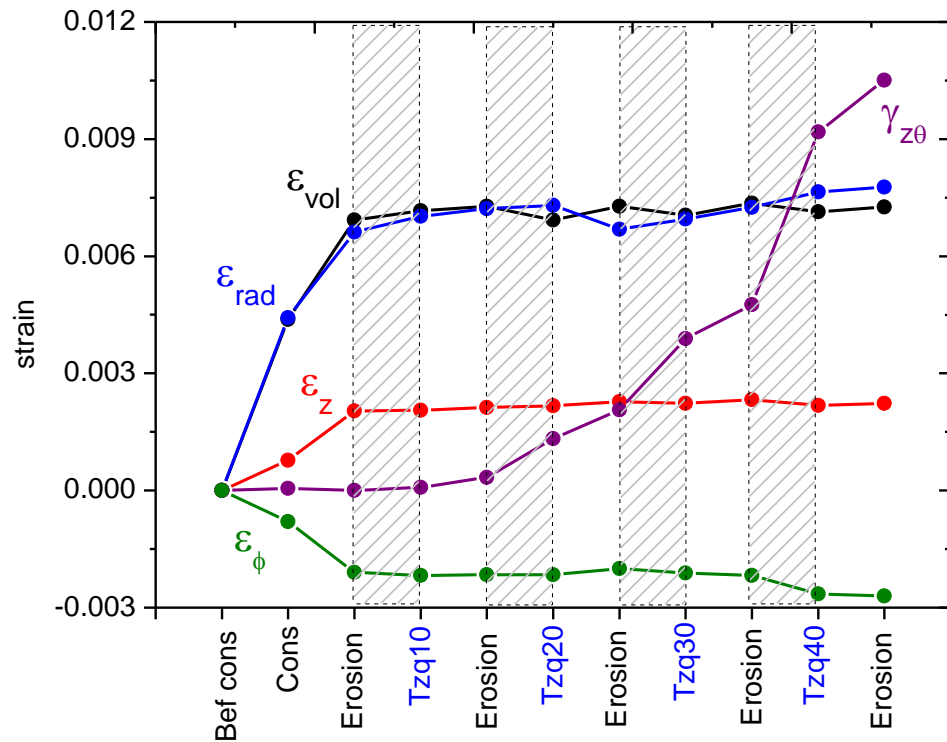
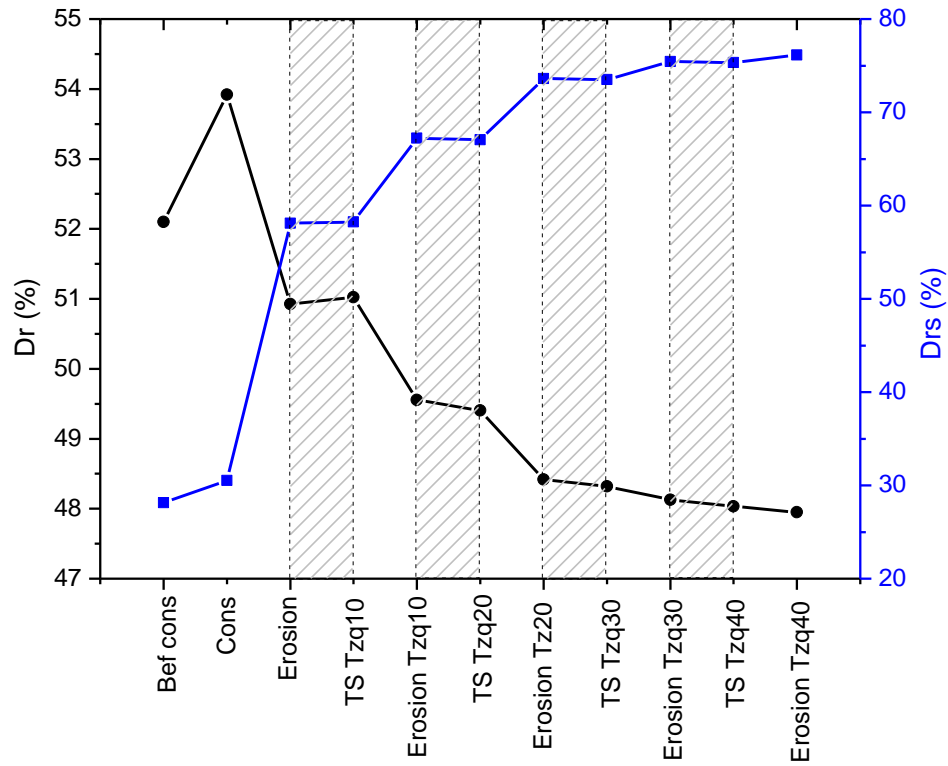

 Figure 5-120 Variation of  $\epsilon_{vol}$ ,  $e$  and  $e_s$  of L-Eb&dSH-60


Figure 5-121 Variation of  $\varepsilon_{vol}$ ,  $e$  and  $e_s$  of L-Eb&dSH-60Figure 5-122 Variation of  $D_r$  and  $D_{rs}$  of L-Eb&dSH-60

The increment of eroded particles after the small steps of torsional shearing might be due to rearrangement of particles induced by the shear strain, allowing the movement of fines through new constrictions (Figure 5-123).

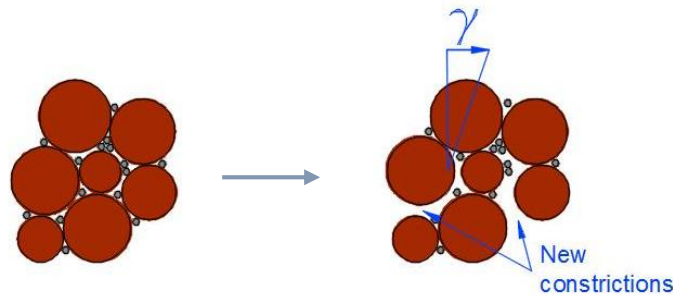


Figure 5-123 Arrangement of particles before and after torsional shearing



### 5.12.2. Effects of the density and degree of erosion

In spite of the erosion, the volumetric strain remains practically constant during the erosion stages in the torsional shearing (Figure 5-120 black curve). A possible explanation to this is that the migration of soil particles generates a structure with higher void ratio (Figure 5-127), and the channels left do not collapse easily (Figure 5-124).

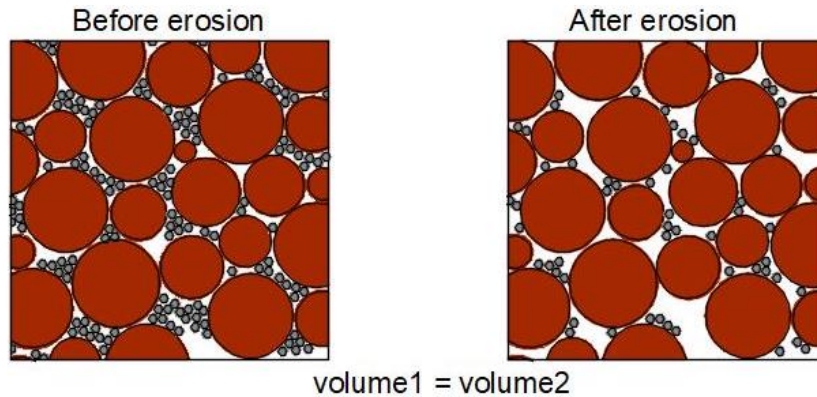


Figure 5-124 Arrangement of particles before and after erosion

This consideration has a counterproductive effect on the soil strength:  $\tau_{max}$  (Figure 5-125),  $G_{tan}$  (Figure 5-126), and  $G$  by STCL (Figure 5-62 to Figure 5-76). The specimens subjected to erosion present a reduction in their strength.

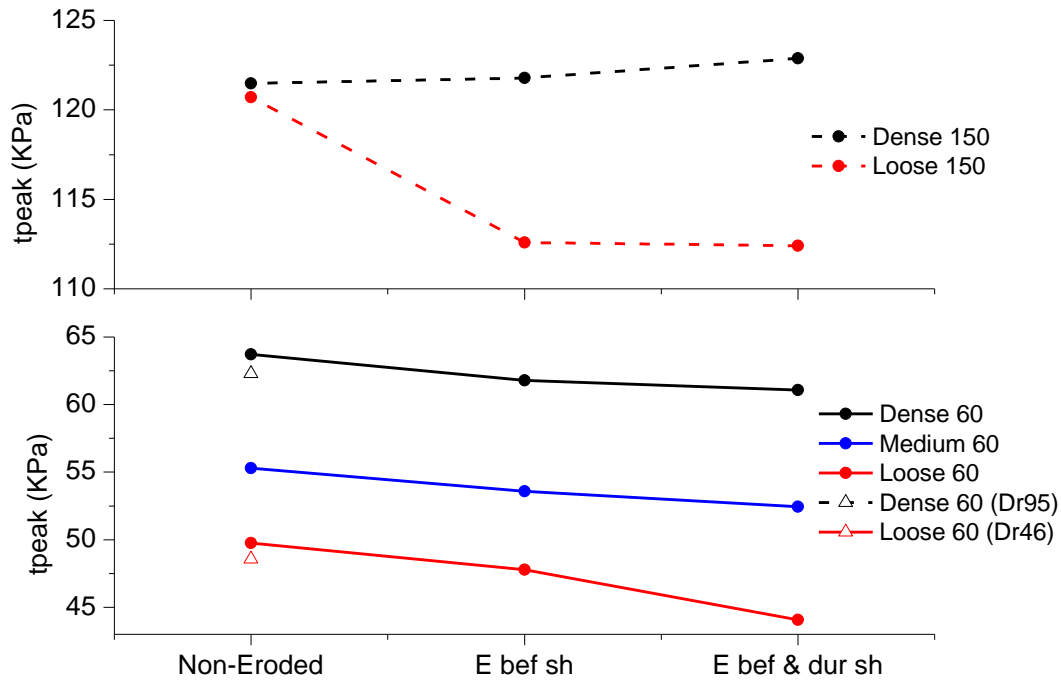


Figure 5-125 Variation of peak shear stress

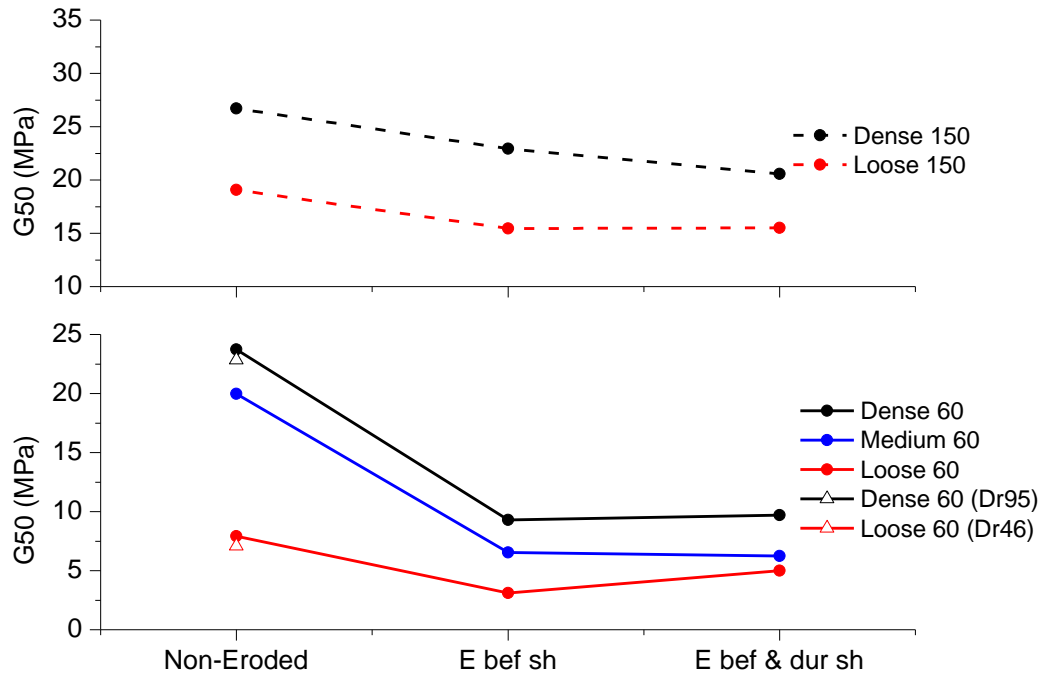


Figure 5-126 Variation of shear modulus

In theory, just the primary fabric transmits stresses and supports loads, and the fines are considered to move freely between the pores and do not support loads. Thus, if only the fine particles are eroded and the intergranular relative density increases after the erosion takes place (Figure 5-130) the reduction of the strength might be due to the open channels generated by internal erosion by suffusion. Thus, the detached particles or fines do contribute to the strength of the soil and their internal movements destabilize the structure.

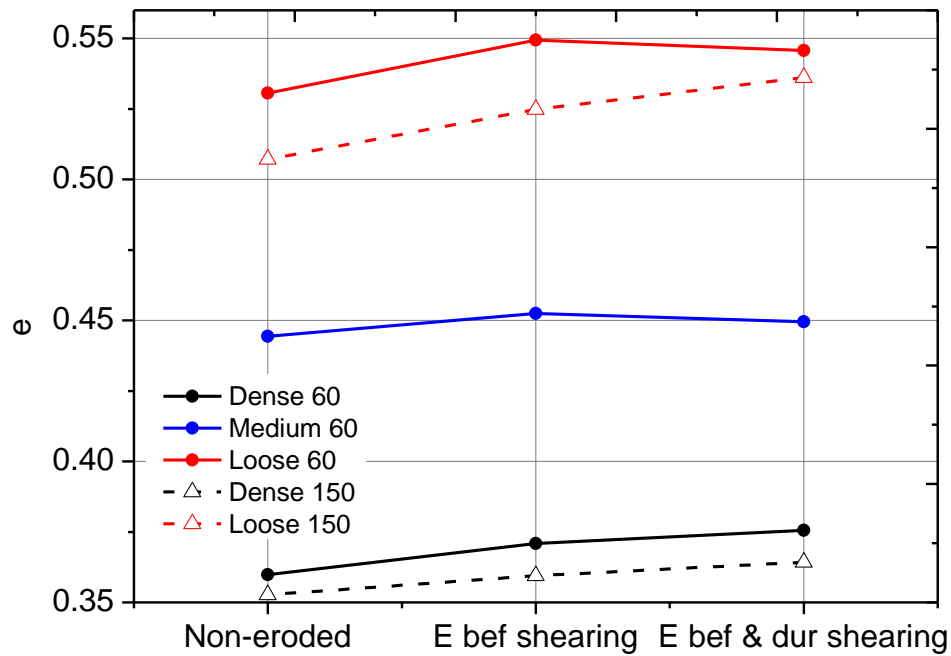


Figure 5-127 Average void ratio

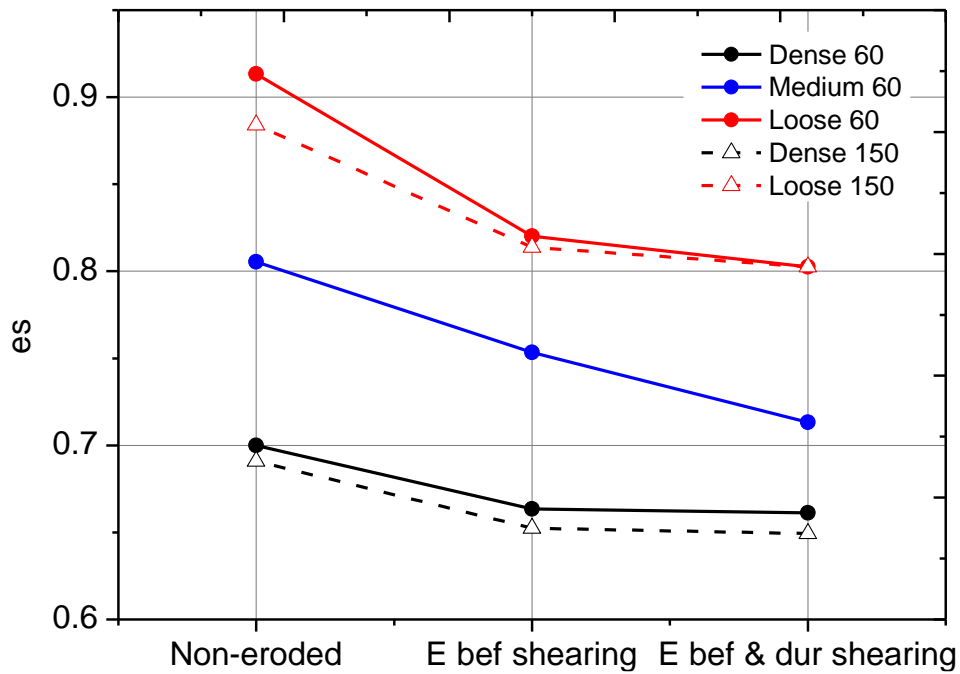


Figure 5-128 Average intergranular void ratio

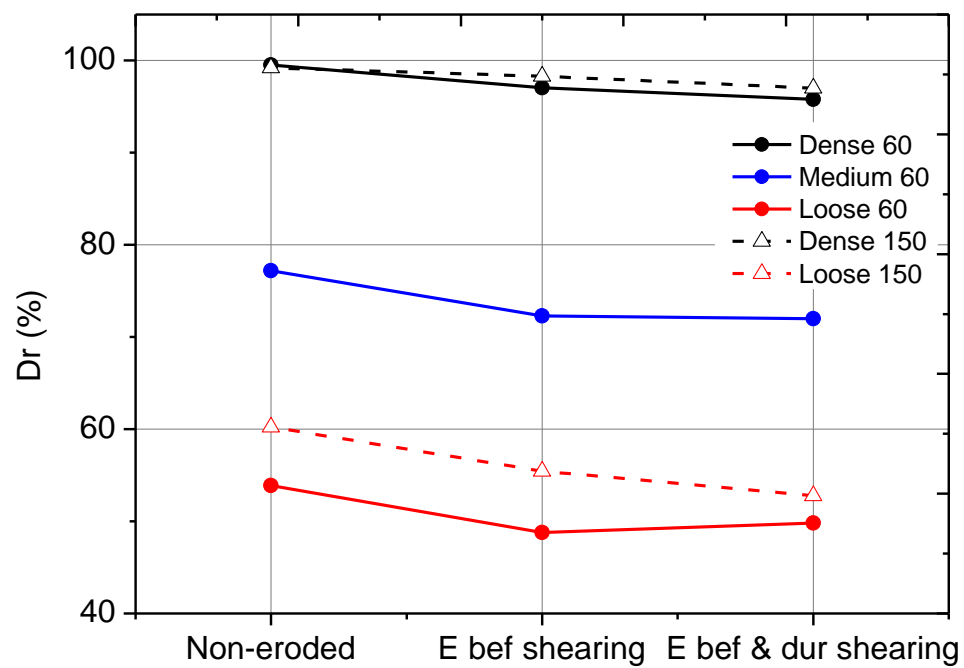


Figure 5-129 Average relative density

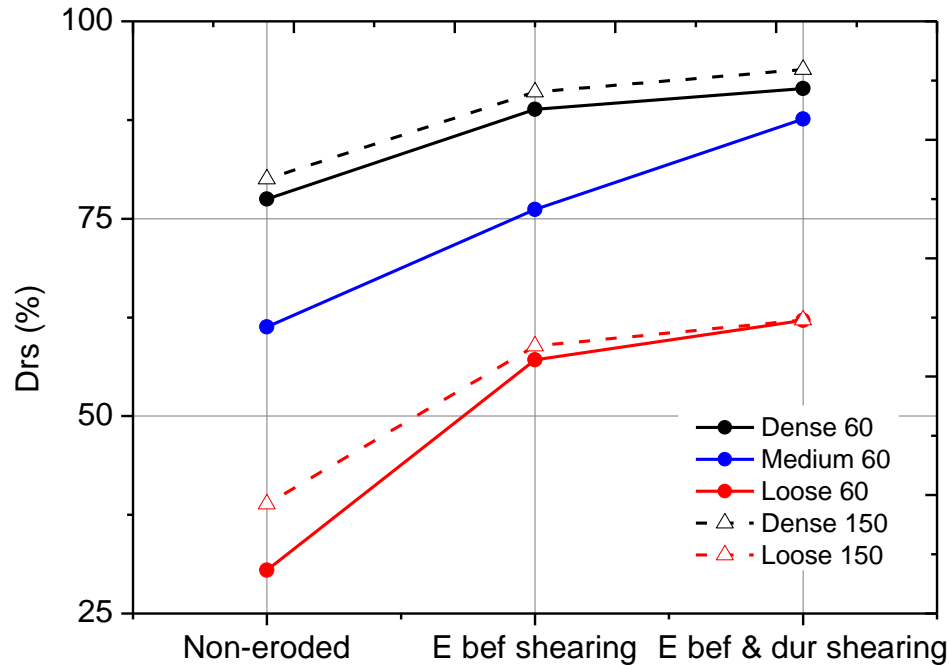


Figure 5-130 Average intergranular relative density

The assumption of the destabilization of the structure due to the erosion is confirmed by the tests using non-eroded specimens with the same density but different erosion degree. The strength is higher in a specimen with no erosion than that in a specimen eroded with the same density (Figure 5-125 and Figure 5-126).

In addition, the soil strength is reduced to a lesser extent for the dense specimens (compared with the loose specimens); hence, in the dense soils the stress transmission is given mostly (but not totally) by the primary fabric, while in the loose soils the fines play a more important role in the strength.

### 5.12.3. Effects of the confining pressure

In the soils confined at higher stresses the soil strength is larger than in the specimens confined at lower stresses. Additionally, after erosion their resistance did not decreased in a greater extent in spite of having the same percentage of eroded particles and same relative

densities  $D_r$  and  $D_{rs}$  (Figure 5-129 and Figure 5-130) than the specimens tested at low confining stress. Thus, the confining pressure also plays a contribution to the strength of a soil that has been eroded.

Contrary to what was initially expected, it was not necessary to apply seepage with a greater hydraulic gradient to erode the fines of the specimens confined to greater pressures. The same hydraulic gradient is needed to erode the same amount of particles with the specimens confined at different pressures. According to this, it is verified that the transmission of stresses is given only by the large particles and for this reason the fines can be easily moved between pores regardless of the confining pressure. But during torsional shearing the fines contribute to the resistance of the soil (Figure 5-131).

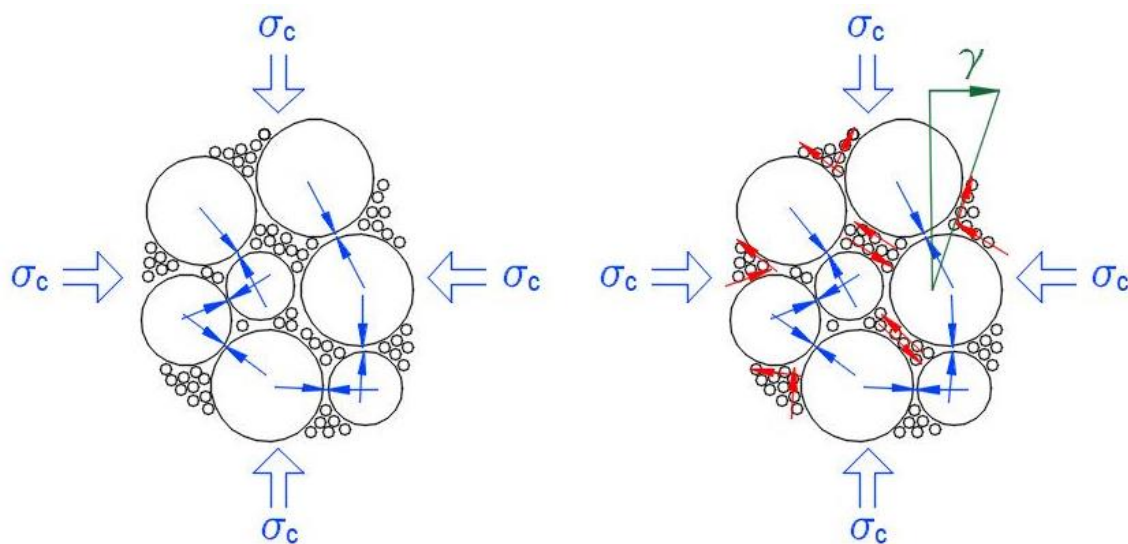


Figure 5-131 Transmission of stresses. Before shearing (left) During torsional shearing (right)

### 5.13. References

Ferreira, T., Rasband, W. ImageJ User Guide IJ 1.46r.

Hach company. (2013). 2100 Series Laboratory Turbidimeters. LIT2498 Rev 4.

HongNam, H., Koseki, J. (2005). Quasi-elastic deformation properties of Toyoura sand in cyclic triaxial and torsional loadings. *Soils and Foundations*, 45(5): 19-38.

Hardin, B. O., and Richart, F. E. J. (1963). Elastic wave velocities in granular soils. *J. Soils Mechanics and Foundation, Div.*, 89(1), 33 – 65.

Yang, Y. (2015). Evaluation of mechanical properties of sand subjected to piping effect. Doctor of engineering thesis. The University of Tokyo.

Schofield, A., and Wroth, C. P. (1968). *Critical state soil mechanics*. McGraw-Hill, London.

Taylor, D.W. (1948). *Fundamentals of soil mechanics*, Wiley, New York.

Thevanayagam, S. (1998). *Journal of geotechnical and geoenvironmental engineering*, 124(6), 479 – 491.





## Chapter 6. Conclusions and Recommendations

Suffusion and many other manifestations of internal erosion in soils are the causes for landslides and failure of structures subjected to water seepage. Although various studies have been conducted to study the internal erosion phenomenon, there are still many uncertainties about this mechanism and how it affects the soils.

The aim of this research is to generate suffused soils in laboratory using internally stable soils. Modified apparatuses for permeability and torsional tests that allow suffusion have been employed to study the soil properties and understand how the erosion process is developed.

Some factors that influence the response of the soil has been studied such as density, hydraulic gradient, confining pressure, and degree of erosion. The findings and conclusions of this research are summarized below.

### 6.1. Conclusions

Two kinds of experiments were carried out in this study, and the conclusions for each of them are presented separately as follows:

#### *6.1.1. One-dimensional column permeability test*

- One of the main objectives of this study was to achieve the generation of suffusion to a soil in laboratory. In order to enhance the amount of eroded particles, soils defined as internally stable were tested; as a result, these soils let their fine particles outside from the specimen when seepage was applied. The migration of particles did not follow a specific path along the internal structure of the soil, but moved gradually in various channels through the voids between the coarse-grain matrix. Therefore, it can be considered that the specimens were successfully subjected to suffusion.

- Previous research suggest that the erodability of the soil is only conditioned by the grain size distribution (Kenney and Lau, 1985). However, it was found in this study that the erodability of a soil is also influenced by additional factors such as the density, initial fines content, and hydraulic gradient.
- The density of the soil is a determining factor for the resistance against suffusion. In dense specimens, the fines that moved out from the matrix are around 10% of the total amount expelled in the loose specimens.
- The first stages of infiltration have a greater effect on suffusion, after which a stable path is created for the passage of water, which does not produce a greater eroding effect.
- The hydraulic gradient has different effects on suffusion depending on the initial relative density. In loose specimens the eroding effect is proportional to the hydraulic gradient, while in the dense specimens at higher hydraulic gradients the movement of particles is reduced. It is presumed that in the dense specimens, at very high hydraulic gradients the particles are moved so aggressively that they clog the constrictions immediately. Yet, a middle hydraulic gradient moved the particles gently enough to displace them between constrictions without clogging.
- The fines content influences the size of the pores and constrictions: a greater amount of fines located in the intergranular space leads to greater constrictions and hence the influence of the hydraulic gradient is more perceptible.
- The turbidity of the water is proportional to the weight of drained particles. It can be used to estimate the degree of erosion.

#### *6.1.2. Hollow cylindrical torsional shear test*

- The specimens subjected to erosion exhibit a reduction in their strength: peak shear stress, and shear modulus (G50 and small strain stiffness G).

- The friction angle is also reduced in the eroded soils; however, the reduction is larger in the loose specimens compared with the dense specimens.
- The shear strength of a soil is reduced by the action of suffusion, not only because of a reduction in density, but also because of the movement of fines. The reduction of the strength might be due to the open channels generated by internal erosion by suffusion. Thus, the detached particles or fines contribute to the strength of the soil and their internal movements destabilize the structure.
- In dense specimens, the shear strength is mainly derived from the friction along the contacts of primary fabric. The soil strength is reduced to a lesser extent in the dense specimens (compared with the loose specimens). Hence, in the dense soils the stress transmission is mainly due to the primary fabric, while in the loose soils the fines play a more important role in the strength.
- In loose specimens the shear strength is resulting from a combination of friction along the primary fabric contacts and along the detached particles. Nevertheless, at low densities the shear strength is affected by the presence of fines, the primary fabric supports most of the stresses.
- The contribution of the detached particles in the stiffness is dependent on the confining stress; if the particles are confined at higher pressures the structure of the soil will probably have more influence of the fines.
- As in the loose specimens, the number of the intergranular contacts is lower than that in the dense specimens, and the sensitivity to the confining stress is larger in consequence.
- The shear strain induces a rearrangement of particles, and hence increases the erosion degree: the increment of eroded particles after the small steps of torsional shearing might be due to a rearrangement of particles induced by the shear strain, allowing the movement of fines through new constrictions.

- Soil with lower relative density and higher confining stress are more susceptible to erosion.
- The same hydraulic gradient is needed to erode the same amount of particles the specimens confined at different pressures. Based on this, it is verified that the transmission of stresses is given only by the large particles, and for this reason the fines can be easily moved between pores regardless of the confining pressure level. But during torsional shearing, the fines contribute to the resistance of the soil.

## 6.2. Recommendations for future research

- The soil used for this research was a combination of Silica Sand No. 5 and DL Clay. This soil was considered to be internally unstable, however a large percentage of fines stayed inside the specimen after the water infiltration, possibly because of the clogging of constrictions. For future research, a soil with a primary fabric with grains of larger diameters can be used so that the size of the constrictions can be larger and allow the migration of the fines more easily.
- The measurement of the volume change is limited during torsional shearing because the clip gauges detach themselves when large torsional strains happen, and therefore it could not be estimated accurately along the complete process of shearing. It can be studied in an alternative way to measure the strains when the apparatus rotation is large.
- The specimens confined at higher stresses (150 kPa) were eroded with the same water pressure (45 kPa) than the specimens confined at 60 kPa. The initial selection of this hydraulic pressure was not to exceed the stresses applied externally in the chamber. However, for the specimens confined at 150 kPa, higher hydraulic gradients could have been applied (large enough not to exceed the confining pressure), but because the objective of this study was about comparing specimens confined at

different pressures with the same number of eroded particles, only small hydraulic gradients were applied. For future research, soils subjected to larger confining pressures and therefore higher hydraulic gradients can be studied, so that the percentage of erosion achieved can be larger.

- This research was focused on the erosion before the shearing stage and during the shearing at small shear strain. The effect of the erosion only at shearing or at larger shear strains can be assessed.